Transport and statistics of anyons in the quantum Hall regime

Pierre Glidic

Université Paris Cité

École doctorale n°564 Physique en Île-de-France (EDPIF)
Centre de Nanosciences et de Nanotechnologies (C2N, UMR 9001)

Transport and statistics of anyons in the quantum Hall regime

Par Pierre GLIDIC

Thèse de doctorat de PHYSIQUE

Dirigée par Frédéric PIERRE
Et par Anne ANTHORE

Présentée et soutenue publiquement le 24/11/2023

Devant un jury composé de :

Pascal DEGIOVANNI	Directeur de recherche	LPENS	Président, Rapporteur
Erwann BOCQUILLON	Professeur associé	Université de Cologne	Rapporteur
Mitali BANERJEE	Professeure assisante	EPFL	Examinatrice
Bernd ROSENOW	Professeur	Université Paris Cité	Examinatrice
Frédéric PIERRE	Directeur de recherche	C2N - CNRS	Directeur de thèse
Anne ANTHORE	Professeure	Université Paris Cité - C2N	Directrice de thèse

Abstract/Résumé

Title: Transport and statistics of anyons in the quantum Hall regime.

Key words: Condensed matter physics, Mesoscopic physics, Quantum transport, Two dimensional electron gas, Integer quantum Hall effect, Fractional quantum Hall effect, Anyons, Fractional statistics, Edge magneto plasmons

Abstract: In this PhD work, we experimentally study the exotic properties of quasiparticles in two-dimensional quantum Hall conductors. "Anyons" quasiparticles, resulting from Coulomb interactions in low dimensional systems, are unconventional excitations with fractional charge and exchange statistics intermediate between fermions and bosons.

The fractional quantum Hall regime where current only flows along chiral one-dimensional edge channels is a good platform to implement such exotic physics. Accordingly, quantum Hall anyon quasiparticles and their potential applications for quantum computing have triggered intense theoretical and experimental work in the last four decades but it is only very recently that strong signatures of their non-trivial exchange statistics were found. Here, such anyons are specifically investigated in "source-analyzer" setups, which combine several Quantum Point Contact constrictions in series and which have recently been identified as a versatile platform to probe this exotic physics.

First, an unconventional "Andreev-like" reflection of anyons is demonstrated in the emblematic $\nu = 1/3$ Laughlin fractional quantum Hall regime. This process involves an incident anyon of charge $e/3$ impinging on a tunnel barrier that favors the transfer of charge e. The incident quasiparticle is converted into a transmitted quasiparticle of charge e and a simultaneously reflected quasihole of charge $-2e/3$.

Then, signatures of anyon non-trivial exchange statistics are measured both in the $\nu = 1/3$ Laughlin state and in the more complex $\nu = 2/5$ Jain state through auto- and cross-correlations of current.

Finally, noise signatures of unconventional excitations are investigated in the $\nu = 2$ integer quantum Hall regime where inter-channel interactions fractionalize electronic excitations into one slow neutral mode and one fast charged mode. The last part of this thesis clarifies the link between the cross-correlations of current fluctuations and the anyonic statistics of the fractional charges propagating in the integer quantum Hall edges.

Titre: Transport et statistiques d'anyons dans le régime de l'effet Hall quantique.

Mots clefs : Physique de l'état condensé, Physique mésoscopique, Transport quantique, Gaz bidimensionnels d'électrons, Effet Hall quantique entier, Effet Hall quantique fractionnaire, Anyons, Statistique d'échange fractionnaire, Magneto plasmons de bords

Résumé: Cette thèse de doctorat étudie expérimentalement les propriétés exotiques des quasi-particules dans des conducteurs bidimensionnels en régime d'effet Hall quantique. Sous l'effet des interactions coulombiennes dans des systèmes de basse dimensionnalité, des excitations non conventionnelles peuvent apparaître : des "anyons", dotés d'une charge fractionnaire et d'une statistique d'échange intermédiaire entre celle des fermions et celle des bosons.

L'effet Hall quantique fractionnaire (EHQF), où le courant électrique circule de manière chirale le long de canaux de bord unidimensionnels, constitue un système adapté à l'étude d'une telle physique exotique. Ainsi, durant ces quatre dernières décennies, les quasi-particules anyoniques de l'EHQF et leurs potentielles applications en informatique quantique ont suscité d'intenses études théoriques et expérimentales dans de tels systèmes. Mais ce n'est que très récemment que des signatures expérimentales claires de leur statistique d'échange non triviale ont été mises en évidence. Dans ce travail de thèse, ces anyons sont spécifiquement étudiés dans une géométrie de type "source-analyseur", qui combine plusieurs contacts ponctuels quantiques mis en série et qui a récemment été identifiée comme un dispositif très riche pour sonder cette physique exotique.

Tout d'abord, nous mettons expérimentalement en évidence un processus de transport non conventionnel de type "réflexion d'Andreev" dans l'EHQF à un facteur de remplissage $\nu = 1/3$. Dans un tel régime dit "de Laughlin", ce processus met en jeu une quasi-particule de charge $e/3$ arrivant sur une barrière tunnel réglée pour favoriser de transfert de charge e. La quasi-particule incidente est alors convertie en une quasi-particule transmise, de charge e, et un quasi-trou de charge $-2e/3$ simultanément réfléchi.

Dans un second temps, des signatures expérimentales d'une statistique d'échange anyonique sont mesurées via le bruit de grenaille d'une part dans la fraction de Laughlin $\nu = 1/3$ et d'autre part dans la fraction de Jain $\nu = 2/5$.

Enfin, ces même signature d'excitations non conventionnelles sont étudiées dans l'effet Hall quantique entier, à $\nu = 2$, dans lequel les excitations électroniques sont fractionnées sous l'effet des interactions inter-canaux en un mode neutre lent et un mode chargé rapide. La dernière partie de cette thèse clarifie le lien entre les corrélations croisées des fluctuations de courant et la statistique anyonique des charges fractionnaires dans des canaux de bords en régime Hall quantique entier.

Remerciements

Ces trois années de doctorat n'auraient assurément pas pu se dérouler aussi agréablement sans le concours d'un grand nombre de personnes. Avant de plonger dans le grand bain des quasiparticules anyoniques, je tiens donc à remercier en quelques lignes toutes celles et tous ceux qui ont permis que ma thèse se déroule si bien.

Avant tout et par-dessus tout, commençons par remercier mon directeur et ma directrice de thèse. Anne et Fred, je n'aurais pas pu imaginer avoir de meilleurs guides. Que ce soit à distance, pendant le premier confinement, ou les mains dans le cambouis de la manip', votre excellence scientifique et votre rigueur m'ont toujours énormément inspiré ; et je compte bien poursuivre mon parcours fort de toutes les connaissances et de l'exigence que j'ai appris à vos côtés. Merci d'avoir si bien encadré ma thèse !

Je remercie très chaleureusement mes compagnons de manip' avec lesquels je suis resté de longues heures devant Labview et Mathematica. Olivier, tout d'abord, qui, à peine revenu de Finlande, a découvert avec moi les joies et les peines de l'effet Hall quantique fractionnaire et qui m'a initié aux codes de la recherche académique en matière condensée. Puis je remercie Colin, mon co-thésard PCéen, avec qui, au-delà de l'effet Kondo, nous avons exploré les Alpes (Zurich dans le froid, Aussois dans le froid aussi puis Grenoble en pleine canicule et avec un petit coup de chartreuse). Et enfin, un grand merci à Ivana qui a rendu très agréable ma dernière année de thèse et qui m'a également donné de très précieux conseils.

Les autres membres de l'équipe QPC m'ont aussi été d'un grand soutien pendant ces trois ans. Hadrien qui m'a fait découvrir le labo et m'a gentiment prodigué des conseils très utiles, Abdel avec qui j'ai écumé la salle blanche et qui a été d'une grande aide pour la manip, Yosuke et Alexandre grâce à qui j'ai passé une très bonne fin de thèse et les stagiaires qui ont animé le bureau Amel et Clément.

Ces trois années auraient aussi été bien plus terne sans la présence des autres membres de l'équipe Phynano. Merci Dominique d'égayer le couloir tout comme Rebeca, à qui je dois d'avoir pu continuer ma thèse quelques semaines après mon contrat. Merci infiniment Rebeca. Merci aussi à Ulf, Antonella, Yong (pour nos discussions très stimulantes à midi), Guillemin, Jean-Christophe, Hervé et tous les stagiaires, thésards et post-doc avec qui j'ai passé d'excellentes soirées : Everton, Léo, Guillaume, Yuanzho, Aurélien, Mario, Sambit, Gaia, Jorge, Liam, Jean-Baptiste et tous les autres.

Je remercie aussi toutes les personnes remarquables avec qui j'ai eu de très stimulantes discussions et de très franches rigolades au laboratoire, en école d'été et en conférence. Je remercie particulièrement François, mon "parrain académique" qui est toujours de bons conseils, ainsi que Loic, mais aussi Christophe et Dimitri qui ont développé une grosse partie théorique

de ma thèse. Je ne peux malheureusement pas être exhaustif, mais je remercie chaleureusement tous les membres de la communauté méso grâce à qui j'ai beaucoup appris.

Enfin, je ne saurais conclure ces lignes sans remercier tout particulièrement ma famille, mes amis de longue date et mes professeurs qui, tous, ont contribué au succès de ces trois années de doctorat. Merci infiniment à tous !

Contents

List of abbreviations

2DEG : Two-Dimensional Electron Gas
CF : Composite Fermions
EMP : Edge Magneto-Plasmons
FQHE : Fractional Quantum Hall Effect
FWHM : Full Width at Half Maximum
HEMT : High-Electron-Mobility Transistor
IQHE : Integer Quantum Hall Effect
LL : Landau Level
MBE : Molecular Beam Epitaxy
PSD : Power Spectral Density
QPC : Quantum Point Contact
SBS : Strong Back-Scattering
SEM : Scanning Electron Microscopy
TLL : Tomonaga Luttinger Liquid
WBS : Weak Back-Scattering

List of Figures

List of Tables

Résumé en français

Ce manuscrit de thèse présente des avancées expérimentales pour la compréhension de la nature de quasi-particules appelées « anyons » dans des circuits mésoscopiques. La physique mésoscopique traite des objets de taille intermédiaire entre l'échelle atomique, décrite par la mécanique quantique, et le monde macroscopique, décrit par la physique classique. À cette échelle, un grand nombre de particules en interaction, chacune obéissant aux règles de la physique quantique, peut conduire à l'apparition de nouveaux phénomènes exotiques. La compréhension de ces phénomènes et les fonctionnalités potentielles qui en découlent, en particulier pour les futures applications en nanoélectronique, font partie des objectifs de ce champ de la physique.

L'effet Hall quantique est un exemple paradigmatique de cette physique exotique. En effet, dans le cas des systèmes bidimensionnel à basse température soumis à un fort champ magnétique perpendiculaire, une quantification exacte de la résistance de Hall à des valeurs entières ou fractionnaires de h/e^2 est observée, accompagnée d'une résistance longitudinale nulle. Le courant circule alors uniquement de manière chirale le long de canaux unidimensionnels aux bords de l'échantillon.

Les propriétés de transport des porteurs de charge dans ce régime Hall quantique ont dès lors suscité un intérêt considérable pour de nombreux domaines, de la métrologie à l'étude de problèmes de la physique de la matière condensée tels que la théorie des liquides de Luttinger ou encore l'effet Kondo. Mais outre ces applications, la physique de l'effet Hall quantique est en elle-même très riche et intrigante. En particulier, les excitations naturelles dans l'effet Hall quantique fractionnaire (EHQF) portent une fraction de la charge élémentaire e et la théorie prédit que leur statistique d'échange est intermédiaire entre celle des fermions et celle des bosons. Alors que ces systèmes sont largement étudiés depuis trois décennies, ce n'est que récemment que deux expériences complémentaires, l'une utilisant un interféromètre de Fabry-Perot, l'autre une géométrie de « collisionneur » mésoscopique, ont fourni les premières signatures convaincantes d'une telle statistique anyonique.

Cette thèse explore expérimentalement la nature et les propriétés de transport de ces quasi-particules fractionnaires en suivant la seconde approche. Dans les circuits considérés, une ou deux sources créent des faisceaux de quasi-particules anyoniques qui s'écoulent vers un « analyseur » où ils entrent en collision. Cette géométrie a ainsi été nommée *collisionneur* ou *source-analyseur*. D'abord proposée par B. Rosenow, I.P. Levkivskyi et B.I. Halperin [1], elle a été mise en œuvre pour la première fois par H. Bartolomei *et al.* [2] puis a récemment suscité des progrès théoriques et expérimentaux intenses. Ce travail de thèse s'inscrit donc dans les avancées récentes de ce sujet en effervescence.

Le manuscrit suivant est divisé en deux parties : la première vise à décrire les éléments nécessaires pour comprendre la physique de ces systèmes. La seconde présente les trois principaux résultats expérimentaux obtenus lors de ce travail.

Concepts généraux et éléments théoriques

La première partie de cette thèse a pour objectif de décrire d'une part le cadre général dans lequel elle s'inscrit et d'autre part les principaux éléments théoriques de l'effet Hall quantique.

Le premier chapitre fournit tout d'abord les notions nécessaires à la compréhension de la suite du manuscrit. En premier lieu, le concept d'anyon est présenté. Alors que dans les systèmes à trois dimensions, les particules sont soit des fermions, soit des bosons, les anyons se développent dans des systèmes de plus basse dimensionnalité, et se caractérisent par une statistique d'échange non conventionnelle, distincte de celle des fermions et des bosons. Dans le cas d'anyons abélien l'échange adiabatique de deux de ces quasi-particules indiscernables leur fait acquérir une phase d'échange θ dont la valeur est comprise entre 0 et π.

$$|\Psi_1\Psi_2\rangle = e^{i\theta}\,|\Psi_2\Psi_1\rangle \tag{1}$$

Après avoir décrit les particularités de ces quasi-particules exotiques (notamment leur charge et leur statistique fractionnaires), la suite du chapitre présente le système physique utilisé pour l'étude de telles quasi-particules : un gaz bidimentionnel (« gaz 2D ») d'électrons. Dans notre cas, le gaz d'électrons utilisé apparaît dans une hétérostructure, à l'interface entre une couche de GaAs et une couche de AlGaAs. La densité de ce gaz est contrôlable, via des grilles métalliques, par effet de champ et l'on peut dès lors concevoir des circuits basés sur des paires de telles grilles, formant un « Contact ponctuel quantique » (CPQ) qui agit comme un séparateur de faisceau de quasi-particules dont la transmission et la réflexion sont ajustables.

Enfin, la fin de ce premier chapitre est dédiée à la présentation des fluctuations de courant et de leurs corrélations (le « bruit » de courant). En particulier, cette partie de la thèse décrit le *bruit de grenaille* dans ces systèmes, causé par la granularité des porteurs de charge constituant le courant. La mesure de ce bruit permet en effet de déduire la charge des quasi-particules impliquées dans les processus de transport et constitue l'observable principale utilisée dans cette thèse pour explorer les propriétés non conventionnelles des anyons.

Le second chapitre donne les éléments théoriques principaux décrivant l'effet Hall quantique, dans lequel les anyons apparaissent. À basse température et sous l'effet d'un intense champ magnétique perpendiculaire au gaz 2D, la conductance transverse G_{H} est quantifiée selon des valeurs entières ou fractionnaires de e^2/h et le transport ne se produit plus que selon des *canaux de bord* chiraux parfaitement conducteurs.

Tout d'abord, le cas de l'effet Hall quantique entier où G_{H} est un multiple entier de e^2/h ($G_{\mathrm{H}} = \nu e^2/h$ avec ν le *facteur de remplissage*) est discuté. Dans ce cas, les porteurs de charges naturels de ce système sont des électrons conventionnels et les caractéristiques des canaux de bord ainsi que celle du « bulk » (partie centrale isolante de l'échantillon) sont bien décrites par de tels fermions sans interactions.

En revanche, le cas où le facteur de remplissage ν est fractionnaire non entier requiert une description plus complexe présentée dans la suite de ce chapitre. Les interactions coulombiennes ont en effet une importance considérable dans ce cas. Le chapitre se focalise sur le cas simple dit « de Laughlin » où $\nu = 1/m$ (m étant un entier impair), pour lequel les excitations de plus faible énergie dans le « bulk » de l'échantillon sont des anyons dont la charge vaut e/m et la phase d'échange θ/m. Puis, comme cette thèse étudie les propriétés de telles quasi-particules à travers leur dynamique dans les canaux de bord, la fin de ce chapitre présente la physique des porteurs de charge au bord de l'échantillon, qui est décrite par le modèle de liquide de Luttinger.

Les résultats expérimentaux de cette thèse sont ensuite présentés dans les chapitres suivants.

Mise en évidence d'un processus de réflexion de type Andreev à $\nu = 1/3$

En premier lieu, le troisième chapitre présente le premier résultat central de cette thèse mettant en évidence un phénomène de transport appelé « diffusion de type Andreev », dans le cas d'un facteur de remplissage $\nu = 1/3$. Dans ce processus, une quasi-particule incidente de charge $e/3$ arrive sur un contact ponctuel quantique (CPQ) en régime de forte rétrodiffusion et est convertie à la fois en une charge e transmise et en un trou rétrodiffusé, de charge de $-2e/3$. Il en résulte des corrélations croisées négatives entre les courants en sortie, et leur valeur quantitative donne accès à la charge des porteurs considérés. Les mesures de bruit présentées dans ce chapitre démontrent ce phénomène et sont robustes sur une plage de températures allant de $T = 15$ mK à $T = 60$ mK. Par contraste, lorsque les CPQ sont réglés dans des régimes différents, les corrélations croisées sont légèrement positives, ce qui souligne la spécificité de ce processus non trivial.

Singulièrement, ce mécanisme de réflexion d'Andreev ne conserve ni le nombre ni la nature des excitations, ce qui contraste fortement avec l'image habituelle de séparateur de faisceau des CPQ et ouvre ainsi une nouvelle perspective concernant d'autres expériences proposées, analogues à celle de l'optique quantique mais mettant en jeu des anyons. Compte tenu de la multiplicité des charges fractionnaires accessibles en réglant les CPQ ou le facteur de remplissage fractionnaire, cette observation pourrait se généraliser en une famille élargie de processus similaires.

Signatures d'une phase d'échange anyonique dans l'effet Hall quantique fractionnaire

Le quatrième et le cinquième chapitres présentent des observations révélant la statistique d'échange non triviale de quasi-particules anyoniques à travers des mesures de bruit. Dans un système « collisionneur », la phase d'échange θ est liée à un processus de tressage entre d'une part une paire quasi-particule-quasitrou créée à un CPQ et d'autre part des anyons incidents créés par des sources en amont. À $\nu = 1/3$, le quatrième chapitre montre que la phase d'échange se manifeste à travers trois indicateurs distincts :

- premièrement, la présence de fortes corrélations croisées négatives, en contraste marqué avec le signal légèrement positif observé pour les fermions à $\nu = 2$;
- deuxièmement, la dépendance des corrélations croisées avec l'asymétrie de réglage entre les sources, à la différence du processus Andreev précédemment étudié;
- enfin, des autocorrélations super-poissonniennes, nettement plus élevées que le signal attendu dans un l'image d'une simple partition des faisceaux incidents;

Dans le canal interne de la fraction $\nu = 2/5$, des corrélations croisées négatives, indiquent également la présence d'un processus de tressage sous-jacent impliquant des anyons. Cependant, leur valeur quantitative suggère que ce type de fractions plus complexes pourrait présenter des caractéristiques supplémentaires que la théorie ne décrit pas encore complètement.

Signatures de statistique anyonique dans l'effet Hall quantique entier

Enfin, le dernier chapitre de cette thèse s'intéresse à un système « collisionneur » similaire mais dans le cas de l'effet Hall quantique entier en présence d'interactions coulombiennes. En effet, du fait des interactions entre canaux de bord, les électrons injectés au niveau des sources peuvent se convertir en des excitations collectives appelées *magnéto-plasmons de bord* (MPB). Dans le cas considéré, il en résulte des charges fractionnaires se propageant le long des canaux entiers et dont la statistique d'échange est également prédite anyonique par la théorie. Après avoir démontré la présence de telles charges fractionnaire dans ce système, des corrélations croisées négatives entre les faisceaux en sortie du système « collisionneur » sont mesurées dans le cas de faisceaux incident dilués. Ce signal indique le caractère anyonique des charges fractionnaires le long des canaux entiers. Par ailleurs, au-delà de ce régime dilué, un bon accord est trouvé entre les mesures et la théorie des magnéto-plasmons de bord.

Cette première étude expérimentale de MPB dans une configuration « collisionneur » ouvre la voie à la création et à l'étude d'anyons dans le régime quantique de Hall entier, plus facilement accessible que le régime fractionnaire.

Perspectives

Ainsi, avec ces trois résultats expérimentaux principaux, ce travail de thèse apporte de nouvelles connaissances sur les processus de transport et la statistique d'échange des anyons. Ces accomplissements ouvrent également d'importantes perspectives parmi lesquels l'étude approfondie de processus de type Andreev avec de nouvelles charges encore inexplorées, la compréhension fine du processus de tressage d'anyons dans des fractions plus complexes et l'utilisation d'anyons dans l'effet Hall quantique entier, plus facilement contrôlable.

Par ailleurs, les résultats de cette thèse contribuent aux étapes nécessaires pour atteindre l'objectif de long terme consistant à manipuler des anyons non abélien, qui sont de bons candidats pour mettre en œuvre des qubits topologiquement protégés.

General Introduction

This thesis manuscript reports on experimental advances in the understanding of the nature of quasiparticle nature in mesoscopic circuits.

Mesoscopic physics is the field of condensed matter physics dealing with objects of length scales intermediate between the atomic scale, described by quantum mechanics, and the macroscopic world, described by classical physics. In the mesoscopic world, a large number of interacting particles following the rules of quantum physics may lead to new exotic phenomena. The understanding of such phenomena and the potential functionalities to be derived from them - particularly for future nanoelectronics applications - are arguably among the goals of mesoscopic physics.

The quantum Hall effect is a paradigmatic example of such exotic physics. With improvements in semiconductor engineering, materials with very few defects and in which electrons are confined in two dimensions can now be designed and used as conductors. Regimes where the transport is not affected by scattering with impurities or phonons are now accessible, giving rise to intriguing effects. In particular, for two-dimensional systems at a low temperature under a high perpendicular magnetic field, Von Klitzing *et al.* observed in 1980 an exact quantization of the Hall resistance at integer values of h/e^2, accompanied by a vanishing longitudinal resistance. This discovery was followed in the subsequent years by the evidence of fractional values of h/e^2 within cleaner samples. In this regime, the transport properties of carriers have raised considerable interest as current flows along chiral unidimensional channels at the sample edges. The universality and precision of the quantum Hall effect are such that, since 1990, it has been employed in metrology to set the international standard for the Ohm, with an accuracy better than one billionth. Moreover, it has revealed to be a very versatile platform for studying many condensed matter problems such as the Luttinger liquid theory or the Kondo effect.

Besides these applications, the physics of the quantum Hall effect is in itself very rich and intriguing. In particular, the natural bulk excitations in the fractional quantum Hall (FQH) effect carry a fractional charge and were also predicted to have fractional exchange statistics, intermediate between fermions and bosons. After a long quest for experimental evidence of this fractional exchange statistics, two recent and complementary experiments using either a Fabry-Perot interferometer or a "mesoscopic collider" geometry gave first convincing signatures.

The main objective of this thesis is to experimentally explore the nature and the transport properties of fractional quasiparticles in the quantum Hall effect following the second approach. This is done in circuits composed of one or two sources, creating beams of quasiparticles that flow up to an "analyzer" where the beams "collide". Accordingly, the considered geometry is called "collider" or "source-analyzer". This setup, proposed by B. Rosenow, I.P. Levkivskyi and B.I. Halperin [1] and first implemented by H. Bartolomei *et al.* in Gwendal Feve's group, [2] has recently triggered intense theoretical and experimental progress. This thesis work is part of the recent advances in this effervescent topic.

The following manuscript is divided into two main parts: the first one aims to introduce the elements necessary to understand the physics of such systems. The second one presents the three main experimental results obtained during this Ph.D. work.

Chapter 1

Introduction

This Ph.D. thesis work focuses on the unconventional properties of quasiparticles emerging from strongly correlated charge carriers in low-dimensional systems. These quasiparticles called *anyons* will be specifically investigated in two-dimensional systems, through electrical transport and current noise measurements in mesoscopic circuits. In this introductory chapter, we aim to address the general concepts largely used in the remainder of the manuscript.

This chapter begins by presenting the basics of anyon statistics. The two-dimensional electron gas AlGaAs|GaAs heterostructure used in this thesis to study these anyons is discussed. As this thesis aims to investigate anyons through transport measurements, we then describe the electrical transport in one-dimensional channels connecting reservoirs. Finally, we present the key ideas about the noise in such mesoscopic conductors, since it constitutes the main observable used in the present work.

1.1 Anyons and their unconventional properties

In three-dimensional systems, particles and elementary excitations fall into two categories: *bosons*, obeying the Bose-Einstein statistics, and *fermions*, obeying the Fermi-Dirac statistics. This classification depends on the quantum exchange phase θ accumulated by the many-body wave-function $\Psi(\vec{r}_i)$ of the system when two indistinguishable particles at respective positions $\vec{r}_1$ and $\vec{r}_2$, are exchanged (see Fig. 1.1a). For bosons, $\theta = 0$ while for fermions, $\theta = \pi$, which corresponds to the standard commutation relations (symmetric for bosons leading to a $+1$ factor and antisymmetric for fermions with a -1 factor):

$$\begin{aligned}\Psi(\vec{r}_1)\Psi(\vec{r}_2) &= e^{i\theta}\Psi(\vec{r}_2)\Psi(\vec{r}_1) \\ &= \begin{cases} +\Psi(\vec{r}_2)\Psi(\vec{r}_1) & \text{if } \theta = 0 \\ -\Psi(\vec{r}_2)\Psi(\vec{r}_1) & \text{if } \theta = \pi \end{cases}\end{aligned} \tag{1.1}$$

However, this simple classification involving only fermionic or bosonic statistics is no longer exhaustive in lower dimensions. Indeed, due to spatial confinement, topological constraints emerge for the path used to exchange quasiparticles. Hence, when swapped, these quasiparticles accumulate an exchange phase intermediate between that of fermions and bosons [3, 4]. Therefore, they were accordingly coined *any-ons* (*any* because they can have any intermediate statistics) [5]. Mathematically, this interchange or the winding of one quasiparticle around the other is an operation called "braiding", described by the so-called "braid group" [6].

This work focuses on abelian anyons, obeying $\Psi(\vec{r}_1)\Psi(\vec{r}_2) = e^{i\theta}\Psi(\vec{r}_2)\Psi(\vec{r}_1)$ with $\theta \in [0, \pi]$ but note that the more complex non-abelian anyons[1] have been predicted to be good candidates for engineering topologically protected states relevant in quantum information [3]. In that case, the braiding is not described by an exchange phase but rather by a unitary transformation acting on a set of degenerate states. In the past years, experiments on the $e/4$ tunneling charge across a QPC [7] and observations of half-integer thermal Hall conductance [8] corroborated the predictions for non-abelian anyons in the $\nu = 5/2$ case.

Now, let us discuss in more detail why intermediate anyonic exchange statistics are only possible in 2D and 1D. We consider a particle A adiabatically moving along a closed path $\mathcal{C}$ around another identical particle B of the same nature in the (xy) plane. This process can be described by a translation operator $\mathcal{T}$ and one can show that $\mathcal{T}$ is equivalent to two successive permutations (or exchange) operators $\mathcal{P}$ i.e. $\mathcal{T} = \mathcal{P}^2$ [9], see Fig. 1.1a.

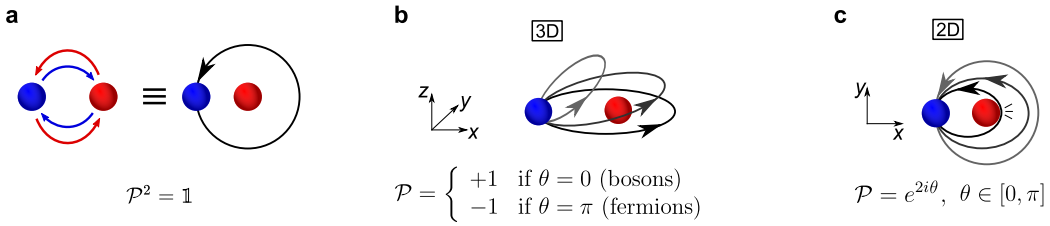

Figure 1.1: **Exchange statistics.**
a A double exchange between two identical particles (blue and red dots) is topologically equivalent to the round trip of one of them around the other.
b In 3D, the path can be continuously shrunk and reduced to a single point. So a double exchange is equivalent to identity. The exchange phase can only have two values 0 or π.
c In 2D, the path is topologically constrained so the exchange phase can take any intermediate value: $\theta \in [0, \pi]$

In three dimensions (Fig. 1.1b), one can always continuously shrink the closed path into a point-like path $\mathcal{C}'$ thanks to the vertical direction z. A double exchange is then topologically equivalent to a single point and one has $\mathcal{T}(\mathcal{C}) = \mathcal{T}(\mathcal{C}') = \mathbb{1}$ i.e. $\mathcal{P}^2 = \mathbb{1}$ [9]. Hence, the exchange quantum-mechanical operator $\mathcal{P}$ has two eigenvalues λ_i (the two square roots of unity) which respectively correspond to fermionic ($\lambda_\mathrm{F} = e^{i\pi} = -1$) and bosonic ($\lambda_\mathrm{B} = e^0 = 1$) statistics. We then recover the commutation relations (1.1).

On the contrary, in two dimensions (Fig. 1.1c), it is not possible to shrink the closed path $\mathcal{C}$ without crossing the other particle. In the simplest abelian case, the double exchange is no longer described by the two square roots of unity and the double exchange gives [9]:

$$\Psi(\vec{r}_1)\Psi(\vec{r}_2) = e^{2i\theta}\Psi(\vec{r}_2)\Psi(\vec{r}_1) \tag{1.2}$$

with $\theta \in [0, \pi]$.

This explains why involved quasiparticles end up having an intermediate exchange statistics between those of fermions and bosons.

Up to now, anyons have only been experimentally observed in two-dimensional systems set in the fractional quantum Hall (FQH) regime that will be described in Chapter 2. In that case,

[1] i.e. for which interchange is mathematically described by a non-abelian group

the involved anyons are quasiparticles with fractional charge [10, 11] leading to unconventional transport processes like an Andreev-like reflection studied in Chapter 3. This thesis aims to study the rich and unconventional physics of such quasiparticles through electrical transport and noise measurement in mesoscopic devices. Let us now describe the confined systems in which anyons emerge.

1.2 Experimental platform to study anyon physics

This section describes the experimental implementation of the low-dimensional conductor used in this work to study the exotic properties of anyons.

1.2.1 Two dimensional electron gas

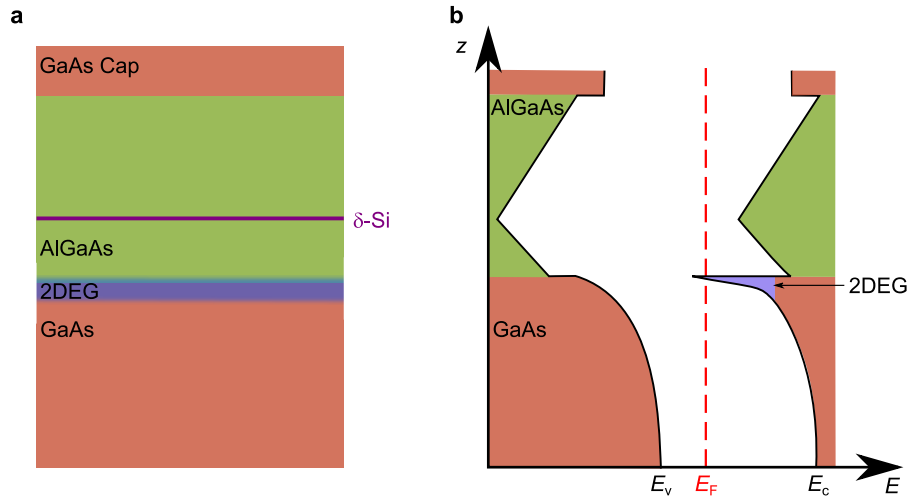

Figure 1.2: **2DEG in a AlGaAs|GaAs heterostructure.** The 2DEG (blue) is formed at the interface of AlGaAs and GaAs.
a Side view of the heterostructure: a stack of a GaAs layer, a n-doped AlGaAs layer with Si dopants (purple line), and a GaAs cap (used to avoid a deep oxidation).
b Corresponding energy diagram. The dashed line denotes the Fermi energy E_F. Continuous lines display the top of the valance band and the bottom of the conduction band (of respective energy E_v and E_c).

In mesoscopic physics, two-dimensional (2D) systems constitute a very rich platform to study the emergence of correlated states of matter. They allow to implement low-dimensional coherent conductors tunable by field effect. For instance, during the past decades, graphene [12] has become one of the most emblematic examples of such 2D systems. However, engineering well-controlled mesoscopic circuits from it has remained experimentally challenging for a long time, in spite of remarkable advances in the past few years (see e.g. [13, 14, 15, 16]).

In this thesis, we use well-controlled two-dimensional electron gas (2DEG) localized at the interface between a GaAs layer and an AlGaAs layer (see Figure 1.2a). Due to the similar lattice constants of these two layers and the remote Si-doping, their interface has few defects. As the Fermi energy in the AlGaAs layer is larger than the one in GaAs, Si-donors in the n-doped AlGaAs will ionize, creating free electrons moving toward the minimum of energy. After

equilibration, a triangular quantum well appears at the interface (see Fig. 1.2b), trapping the electrons that happen to be confined in the z vertical direction, in the ground state of the well. The resulting gas of electrons, locked in the z-position but free to move in the (xy) plane, is therefore bidimensional.

The samples used in this thesis have been grown by U. Gennser and A. Cavanna using Molecular-Beam Epitaxy (MBE) techniques. MBE is used to grow AlGaAs crystalline structure on a GaAs substrate, by evaporating gallium arsenic and a given proportion of aluminum. This process is performed in an ultra-high vacuum chamber (to minimize pollution) and it gives a growth accuracy better than a single atomic layer. The first sample measured during this thesis work (used in Chapters 3, 4, and 5) has a density $n = 1.2 \times 10^{11}$ cm^{-2} and a mobility $\mu = 1.8 \times 10^{6}$ cm^2 V^{-1} s^{-1}. The 2DEG is at 142 nm depth and the Si-dopants lie 67 nm below the surface. The second sample, discussed in Chapter 6, uses a 2DEG buried 95 nm below the surface, with density 2.5×10^{11} cm^{-2} and mobility 2.5×10^{6} cm^2 V^{-1} s^{-1}.

1.2.2 Edge states and Quantum Point Contact

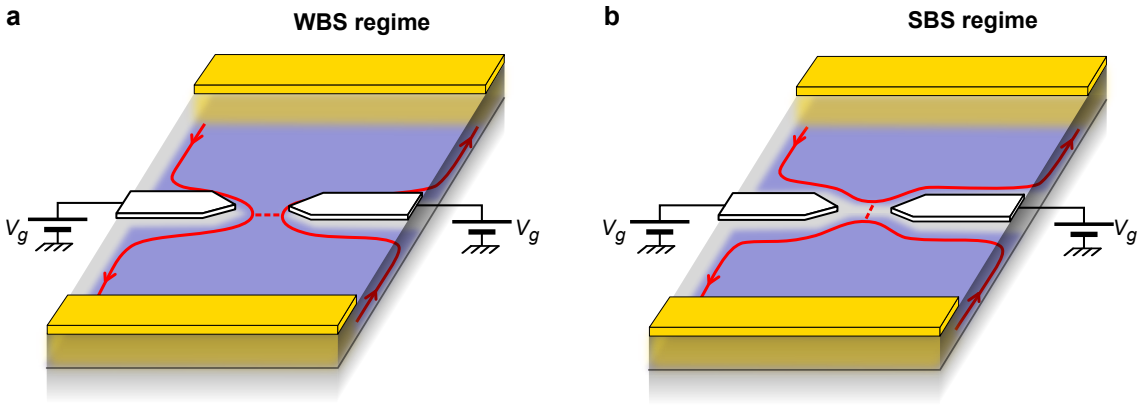

Figure 1.3: **Schematics of a QPC in WBS and SBS regimes.**
Ohmic contacts (yellow) are connected to the 2DEG (displayed as a buried blue layer) allowing the current to flow unidimensionally along chiral channels (red lines with arrows). When a negative bias voltage V_g is applied on the QPC gates (white), the 2DEG is progressively depleted, which allows to tune the fraction of current crossing the QPC. Panel (a) illustrates the weak back-scattering (WBS) regime and panel (b) the strong back-scattering (SBS) regime.

Two-dimensional electron gas can host anyons in the quantum Hall effect. As will be discussed in detail in Chapter 2, the electrical transport only occurs within one-dimensional chiral channels along the edges of the sample. By designing the path of these channels, one can implement mesoscopic circuits allowing to investigate the transport properties of the quasiparticles.

In particular, the elementary building block of such a mesoscopic circuit is the so-called quantum point contact (QPC) [17]. It consists of a pair of metallic gates deposited on the surface of the sample (see Fig. 1.3). Their geometry, with sharp tips pointing at each other, allows to gradually reduce the separation between the counter-propagating channels on either side of the constriction.

By applying a negative voltage V_g on gates, electrons in the buried 2DEG will be progressively depleted by field effect. The induced constriction results in a potential barrier whose shape can be determined by the gate geometry and the applied gate voltage [18]. In the standard picture, a (quasi)particle impinging on this barrier will either be back-scattered or transmitted through the QPC.

Therefore, in essence, a QPC plays the role of a "beam-splitter" of electrons, with a tunable transmission $\tau \in [0, 1]$, defined as the ratio between the impinging current and the current transmitted through the constriction. However, we will see in this thesis that this standard "beam-splitter" picture does not always hold.

In this thesis, the QPCs are mostly set in one of the two extreme regimes of *strong backscattering* (SBS) for which most of the current is reflected ($\tau \ll 1$) and of *weak backscattering* (WBS) for which most of the current is transmitted ($1 - \tau \ll 1$), as pictured in Fig. 1.3a and b respectively.

1.3 Electronic transport in coherent conductors

Let us now briefly address the general framework describing the electrical transport in short coherent conductors directly connected to a voltage source and in the absence of interactions.

We consider the situation of two reservoirs (left and right) connected by N one-dimensional conductors referred to as *conducting channels*. The respective temperatures $T_{\mathrm{L(R)}}$, voltage bias $V_{\mathrm{L(R)}}$ (or the chemical potentials $\mu_{\mathrm{L(R)}}$) of the left and right reservoirs drive the flow of heat and electricity along the channels (see Figure 1.4).

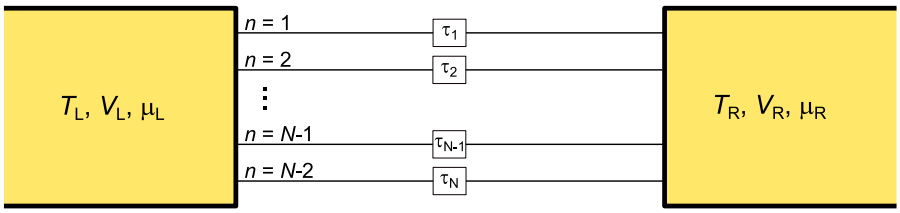

Figure 1.4: **Coherent conductor description in the Landauer-Büttiker-Martin framework.**
Two reservoirs (yellow squares), left and right, are connected by N one-dimensional channels of transmission probability τ_n.

The theoretical description of electrical transport in such channels was pioneered by Landauer [19]. Then, several experiments [20, 17, 21] prompted its refinement [22, 23], giving finally the *Landauer-Büttiker-Martin formalism*.

1.3.1 Current in a single channel without scatterer

In the ideal case of a single channel without defect, the current I of free electrons is given by the product between the elementary charge e and the number of electrons crossing a section of the channel $\int \frac{dk}{2\pi} v(k) f(k)$, where k is the wave vector amplitude and v the velocity of carriers. f is the Fermi-Dirac distribution of energy ϵ, i.e. $f(\epsilon) = \dfrac{1}{1 + \exp\left\{\frac{\epsilon - \mu}{k_B T}\right\}}$, with k_B the Boltzmann constant. Note that here we consider the case of a spin-polarized system.

For free electrons, ϵ is purely kinetic (i.e. $\partial E/\partial k = \hbar v$) and the current from the left (right) reservoir $I_{\mathrm{L(R)}}$ reduces to:

$$I_{\mathrm{L(R)}} = \frac{e}{h}\int d\epsilon f_{\mathrm{L(R)}}(\epsilon - \mu_{\mathrm{L(R)}}) \tag{1.3}$$

and, if one applies a bias V between the two contacts (i.e. $eV = \mu_{\mathrm{L}} - \mu_{\mathrm{R}}$), a net current I flows from the left to the right reservoir [22]:

$$\boxed{I = I_{\mathrm{L}} - I_{\mathrm{R}} = \frac{e}{h}\int_{\epsilon} d\epsilon \left[f_{\mathrm{L}}(\epsilon - \mu_{\mathrm{L}}) - f_{\mathrm{R}}(\epsilon - \mu_{\mathrm{R}})\right] = \frac{e}{h}(\mu_{\mathrm{L}} - \mu_{\mathrm{R}}) = \frac{e^2}{h}V} \tag{1.4}$$

This is the famous Landauer formula for a single spin-polarized ballistic (i.e. without scattering) channel.

The conductance $G = I/V$ of the considered channel is therefore precisely the quantum of conductance G_{K}:

$$G_{\mathrm{K}} = \frac{e^2}{h} \tag{1.5}$$

One can alternatively define the quantum of resistance $R_{\mathrm{K}} = h/e^2 \simeq 25.8$ kΩ, also referred as the *von Klitzing constant* and which is only characterized by the universal constants e and h.

1.3.2 Generalization: Landauer-Büttiker scattering formalism

In general, the N channels connecting the two reservoirs have defects acting like scatterers on which electrons are either reflected or transmitted. The reflection and transmission probabilities from incoming channels to outgoing channels can be encoded in the so-called scattering matrix $\boldsymbol{S}$ [22]. Defining the transmission probability of channel n by τ_n (see Fig. 1.4), the reasoning performed in the previous section generalizes and, as the conductances of independent channels add up, the total conductance G between the two reservoirs reads, when τ_n does not depend on ϵ:

$$G = \frac{e^2}{h}\sum_{n=1}^{N}\tau_n \quad , \tag{1.6}$$

finally leading to

$$\boxed{I = \frac{e}{h}\int_{\epsilon} d\epsilon \left[f_{\mathrm{L}}(\epsilon - \mu_{\mathrm{L}}) - f_{\mathrm{R}}(\epsilon - \mu_{\mathrm{R}})\right]\sum_{n=1}^{N}\tau_n = \frac{e^2}{h}V\sum_{n=1}^{N}\tau_n} \tag{1.7}$$

1.4 Noise in mesoscopic conductors: a rich source of information

Most of the measurements constituting the core experimental results of this thesis are measurements of the current *shot noise*. Indeed, the noise, i.e. the fluctuations of current around its mean value, carries strong insights about the nature of quasiparticles (charge, statistics...) and their transport properties in mesoscopic systems: "the noise is the signal" [24]. This section briefly defines the considered quantities and describes the different sources of noise in mesoscopic conductors.

1.4.1 Correlation function

We consider the current $I(t)$, which can be written as the sum of a mean value $\langle I \rangle$ and fluctuations around this mean value $\delta I(t)$: $I(t) = \langle I \rangle + \delta I(t)$ [25] (see Fig. 1.5a). These fluctuations result from random processes and can therefore be described by a random variable X (e.g. a Poissonian distribution). As X depends on time, correlations between two successive processes can carry information on the system [24].

We define the time-dependent correlation function g_{XY} between two random variables X and Y (at respective times t_1 and t_2) as:

$$g_{XY}(t_1, t_2) = \langle X(t_1)Y(t_2) \rangle \tag{1.8}$$

In particular, for an ergodic stationary process[2] which only depends on $\tau \equiv t_1 - t_2$, the auto-correlations of currents g_{II} reads:

$$g_{II}(\tau) = \langle \delta I(0)\delta I(\tau) \rangle \tag{1.9}$$

We can then define the spectral density of current fluctuations S_{II} as the Fourier transform of the auto-correlation function:

$$\boxed{S_{II}(\omega) = 2\int_{-\infty}^{+\infty} g_{II}(\tau)e^{i\omega\tau}d\tau} \tag{1.10}$$

Experimentally, measurements in this Ph.D. work are voltage fluctuations detected thanks to home-made high-electron-mobility transistors (HEMT) cryogenic amplifiers [26, 27, 28]. Hence, in practice, current fluctuations δI are converted into voltage fluctuations δV thanks to an output impedance $Z(\omega)$ combining the sample Hall resistance R_{H} and the resistance of a LC tank circuit: $\delta V = Z(\omega)\delta I$. After amplification and integration over a bandwidth $\Delta\omega$ centered on the resonance frequency of a tank circuit (0.86 MHz), we then measure:

$$\langle \delta V^2 \rangle = \int_{\Delta\omega} \frac{S_{VV}}{2\pi} d\omega = \int_{\Delta\omega} \frac{S_{II}Z^2(\omega)}{2\pi} d\omega \tag{1.11}$$

from which we finally deduce the spectral density of current noise S_{II}. More details concerning the noise measurement setup and the amplification chain are given in Appendix B.

Let us now turn to the main sources of noise in mesoscopic conductors. Their relative contributions to the total power spectral density of current are summarized in Figure 1.5b.

1.4.2 Thermal Noise

At finite temperature T, the thermal agitation of carriers is the source of noise in such systems that we will first consider. It is also referred to as the *Johnson-Nyquist noise* [30, 31]. For a conductor of conductance G, this agitation leads to a power density of current fluctuations following the Nyquist formula [32]:

$$S_{II} = 4k_{\mathrm{B}}TG \tag{1.12}$$

Importantly, note that this is a white noise (i.e. independent of the frequency $f = \omega/(2\pi)$) in the low-frequency regime $f \leq k_{\mathrm{B}}T/h$ and note also that it is present even when the system is at equilibrium.

[2] in that case temporal averaging corresponds to statistical averaging

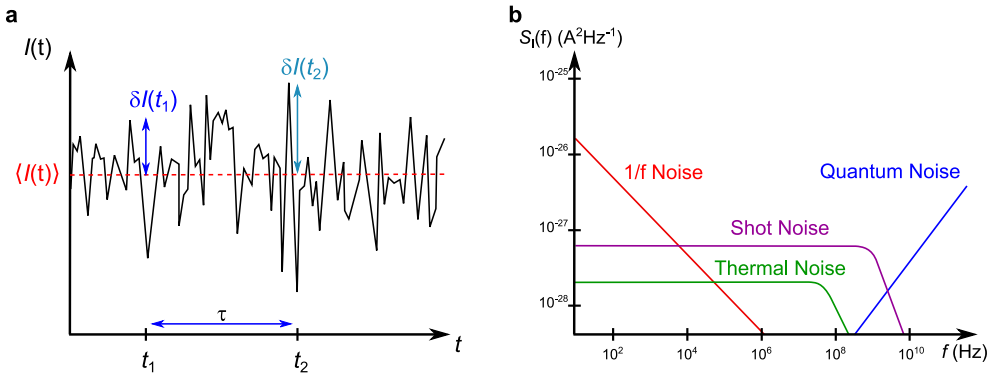

Figure 1.5: **Fluctuations of current and sources of noise.**
a Current $I(t)$ presents fluctuations $\delta I(t)$ around a mean value $\langle I \rangle$
b Different sources of noise amplitude versus frequency, adapted from the review [29]

1.4.3 The $1/f$ Noise

In mesoscopic conductors, another source of noise called the $1/f$ noise or "pink noise" may appear. It is believed to be linked to the interactions between carriers and defects in the sample [33, 34, 29]. Charges can indeed be trapped, absorbed and emitted by such conductor impurities (which are sets of discrete energy levels), leading to a power spectral density of current fluctuations typically proportional to:

$$S_{II} \propto \frac{I^2}{f} \tag{1.13}$$

In this thesis work, as the $1/f$ noise is not the signal of interest, we choose to amplify the signal at frequencies for which it is negligible ~ 1 MHz (with a tank circuit resonance frequency of 0.86 MHz). Thus, in this frequency range, the signal is dominated by neither the irrelevant $1/f$ noise (mostly due to the amplifier in our case), nor by the quantum noise [35, 29, 36] (induced by quantum fluctuations of the electric fields) because we remain in the low-frequency limit $f \ll k_B T/h \simeq 200$ MHz at $T = 10$ mK.

1.4.4 The shot noise

The so-called *shot-noise* is a source of noise carrying information about the nature of quasiparticles and constitutes the signal of interest of this Ph.D. work. Shot noise consists of fluctuations of current due to the granularity of charges (i.e. the fact that they propagate as discrete packets). Unlike the thermal noise, it is induced when the system is out of equilibrium.

Schottky's classical approach

Shot noise was first introduced by Schottky [37] in the classical case of N randomly tunneling particles of charge q during time τ, generating fluctuations δI around the mean value of current $\langle I \rangle$. $\langle \delta I^2 \rangle$ is then directly proportional to the variance $\langle N^2 \rangle$. For such a Poissonian emission, the variance and mean value are equal, so the noise S_I is the mean number of emitted electrons $q\langle I \rangle$ during the measurement time $\tau = 2/\delta f$:

$$S_I = \frac{\langle \delta I^2 \rangle}{\delta f} = 2q\langle I \rangle \tag{1.14}$$

Landauer-Büttiker-Martin's description of low-frequency shot noise in quantum conductors

A similar noise appears in quantum coherent conductors and has been described by Landauer, Büttiker and Martin [25, 38, 39, 40]. As it will be largely used in the remainder of the manuscript, it is interesting to give the key elements of the derivation of the shot noise expression for electrons.

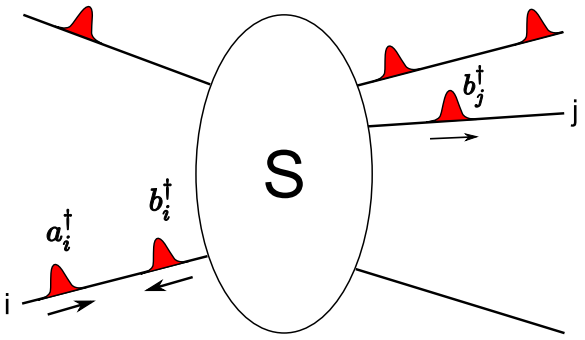

Figure 1.6: **Landauer-Büttiker scattering picture.**
N leads (black lines) are connected to a scatterer (white area). Incoming (outgoing) electronic modes (red packets) in channel i are created by operator $a^\dagger$ ($b^\dagger$) and destroyed by operator a (b). The scattering matrix $\boldsymbol{S}$ characterizes the scatterer by linking these operators.

In a coherent quantum conductor, we consider N reservoirs connected to a scatterer (typically a QPC) via N leads [3]. Each lead contains several incoming and outgoing quasiparticles as illustrated in Fig. 1.6. For $i, j \in [\![1, N]\!]$, we aim to determine the expression of the symmetrized correlations function between the fluctuations of the current operators in leads i and j:

$$\frac{1}{2}\langle \delta\hat{I}_i(t)\delta\hat{I}_j(t') + \delta\hat{I}_j(t')\delta\hat{I}_i(t)\rangle \tag{1.15}$$

The quasiparticle modes in the leads are described by the creation and annihilation operators $a_i^\dagger$ and $b_i^\dagger$ which respectively create an incoming and an outgoing electronic mode in lead i. The scattering matrix $\boldsymbol{S} = (s_{i,j})_{i,j\in[\![1,N]\!]}$ connects these operators as follows:

$$b_i^\dagger = \sum_j s_{i,j} a_j^\dagger \quad , \tag{1.16}$$

where the matrix element $s_{i,j}$ describes the probability amplitude for an incoming mode of lead j to be transferred (transmitted or back-scattered) into an outgoing mode in lead i. In the Fourier space, the current operators $\hat{I}_i$ and the power spectral density $S_{i,j}$ can respectively be expressed as:

$$\hat{I}_i(\omega) = \frac{e}{\hbar}\int d\epsilon \sum_{j,k} a_j(\epsilon) M_{j,k}(i, \epsilon, \epsilon + \hbar\omega) a_k(\epsilon) \tag{1.17}$$

$$S_{i,j}(\omega) = \frac{1}{4\pi\delta(\omega + \omega')}\langle \delta\hat{I}_i(\omega)\delta\hat{I}_j(\omega') + \delta\hat{I}_j(\omega')\delta\hat{I}_i(\omega)\rangle \tag{1.18}$$

[3] Here we only consider one channel per lead because in the QHE the scattering mostly remains in the same channel. However, one can generalize this reasoning to M channels per lead.

where $M_{j,k}$ are the matrix elements defined by $M_{j,k}(i,\epsilon,\epsilon+\hbar\omega) = \mathbb{1}\delta_{i,j}\delta_{i,k} - s^{\dagger}_{i,j}(\epsilon)s_{i,k}(\epsilon+\hbar\omega)$ In the considered limit $\omega \ll k_{\mathrm{B}}T/\hbar$, this reduces to the zero-frequency shot noise which can be expressed in the following compact form [25]:

$$S_{i,j} = \frac{e^2}{\hbar}\sum_{k,l}\int \{d\epsilon M_{j,k}(i,\epsilon,\epsilon)M_{j,k}(j,\epsilon,\epsilon)\left[f_k(1-f_l)+f_l(1-f_k)\right]\} \tag{1.19}$$

Non-interacting noise expression for the geometry used in this Ph.D. work

In this thesis and throughout the manuscript, the investigated geometry consists of QPCs of transmission τ (generally defined as the ratio between transmitted and injected currents) connected to four ohmic contact reservoirs by 1D chiral leads (two incoming and two outgoing) of conductance G_{H}. The configuration is displayed in Fig. 1.7a. All ohmic contacts are set at the same temperature T so the out-of-equilibrium situation is realized by applying a DC-voltage bias V on one ohmic contact.

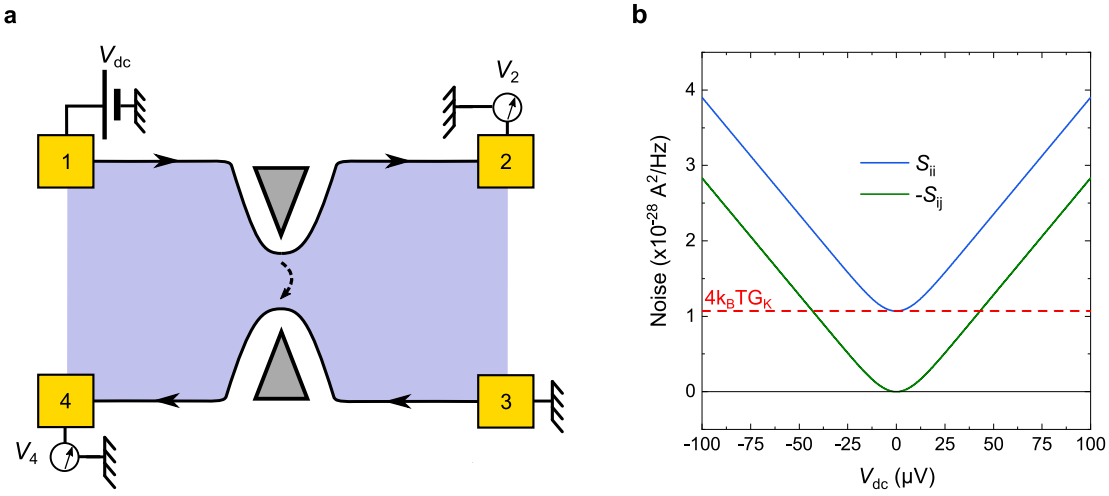

Figure 1.7: **Shot noise on a single QPC.**
a Typical geometry used in this thesis. Four ohmic contacts (yellow) labeled $1\ldots4$ are connected to a QPC defined by metallic split gates (pair of facing triangles) via 1D chiral channels (black lines with arrows). A DC-voltage bias V_{dc} is applied on contact 1 and measurements are made on contact 2 and 4.
b Auto- (blue line) and opposite of cross-correlation shot noise induced by a bias voltage V_{dc} on a QPC at $T = 50$ mK. The red dashed line indicates the thermal noise contribution.

In such a case, the Landauer-Büttiker prediction of the power spectral density of current in outgoing lead i reads [25]:

$$\boxed{S_{ii} = 4k_{\mathrm{B}}TG_{\mathrm{K}} + 2e\tau(1-\tau)G_{\mathrm{K}}V\left[\coth\left(\frac{eV}{2k_{\mathrm{B}}T}\right) - \frac{2k_{\mathrm{B}}T}{eV}\right]} \tag{1.20}$$

It corresponds to the *auto-correlations* of current fluctuations (see Fig. 1.7b). The first term $4k_{\mathrm{B}}TG_{\mathrm{K}}$ is the thermal noise contribution. To specifically probe the shot noise contribution to auto-correlations and to systematically remove the fixed noise added by the amplification chain, we will prefer using the *excess auto-correlations noise* $\Delta S_{ii}(V) \equiv S_{ii}(V) - S_{ii}(0)$.

Similarly, the power spectral density of current between the outgoing lead i and $j \neq i$ reads:

$$\boxed{S_{ij} = -2e\tau(1-\tau)G_{\mathrm{K}}V\left[\coth\left(\frac{eV}{2k_{\mathrm{B}}T}\right) - \frac{2k_{\mathrm{B}}T}{eV}\right]} \tag{1.21}$$

It corresponds to the *cross-correlations* of current fluctuations between leads i and j (see Fig. 1.7b) and is negative for free electrons (it probes anti-correlations). Remarkably, the contribution of thermal noise vanishes in the case of cross-correlations which constitutes a more direct signal to specifically investigate the shot noise.

The typical shapes of auto-correlations and of the opposite of cross-correlations are plotted in Fig. 1.7b, at $T = 50$ mK. The effect of temperature is only visible at low bias with a "thermal rounding" of the curve, while at large bias the slopes are the same for all temperatures.

Note that this formula is valid for electronic excitations but it has been phenomenologically extended for decades to channels of conductance νG_{K} (ν being a fractional filling factor and G_{K} the quantum of conductance) with unconventional excitations of fractional charge e^* [10, 11, 41].

With all these introductory details and prerequisites discussed, we can now briefly summarize the experimental investigation of this thesis and give the outlook of this manuscript.

1.5 Experimental investigation in this PhD thesis

In this Ph.D. thesis, we performed three experiments to explore transport and statistics properties of "anyon" quasiparticles via shot noise signature in the "source-analyzer" set-up. This geometry consists of several QPCs in series: one (or several) upstream constriction is used for creating a beam of quasiparticles while another one is used as an analyzer to induce shot noise and investigate the unconventional properties of the impinging quasiparticles. In this section, we address the key points of the three experiments.

1.5.1 Andreev-like scattering

The goal of the first experiment is to demonstrate an unconventional transport process occurring when the source and the analyzer do not naturally transmit the same kind of charges. In particular, when an incident diluted beam of $e/3$-charged quasiparticles impinges on the analyzer QPC tuned to transmit e-charged quasielectrons, a so-called *Andreev-like* reflection process is predicted to happen [42]: the incident $e/3$ charge is converted into a transmitted charge e and a simultaneously reflected quasihole of charge $-2e/3$ (see Fig. 1.8a).

While an earlier experiment with long source-analyzer paths previously showed mitigated results [43], we straightforwardly demonstrate this process through simultaneously measured auto- and cross-correlations of the outgoing currents [44]. It opens a path to the study into a larger family of Andreev-like processes involving other types of fractional charges.

1.5.2 Signature of anyon statistics

In a clean two-dimensional electron gas, quasiparticles may appear and acquire an unconventional exchange phase when swapped, corresponding to an exchange statistics intermediate

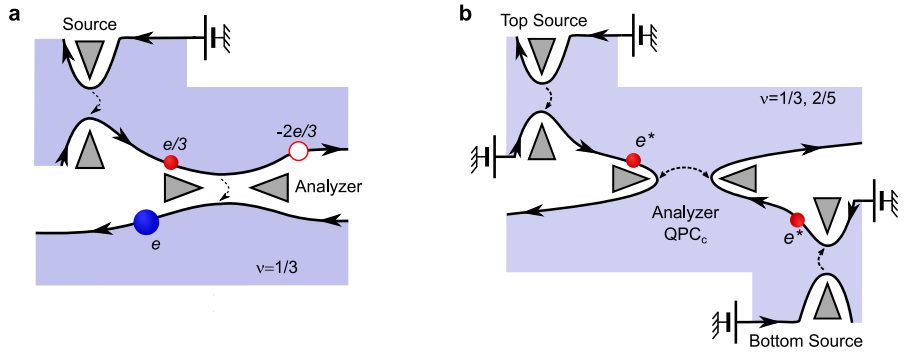

Figure 1.8: **Illustration of the first two experiments.**
a Implementation of the first experiment. A source QPC creates a beam of $e/3$ quasiparticles impinging on an analyzer QPC where they are converted into a transmitted charge e and a back-scattered $-2e/3$ quasihole.
b Implementation of the second experiment. Two diluted beams of anyons impinge on a central QPC. The cross-correlations between the two outgoing beams give information on their braiding statistics.

between fermions and bosons. After a long quest for experimental markers of such unconventional exchange phase, it is only recently that experiments presented convincing signatures of anyon statistics [45, 2].

During this thesis work, a second experiment performed in a source-analyzer device also aimed to demonstrate the unconventional exchange statistics of anyon quasiparticles and to clarify the meaning of noise signatures in such systems. When two diluted beams impinge on a central analyzer QPC set at high transmission (in the WBS regime, see Fig. 1.8b), negative cross-correlations were found and attributed to anyon statistics at both filling factors $\nu = 1/3$ and $\nu = 2/5$, in agreement with theory [1, 46, 47] in the $\nu = 1/3$ case. The cross-correlation dependence on the source imbalance as well as super-Poissonian auto-correlations in outgoing currents were demonstrated as complementary signatures of the anyon unconventional exchange phase. Finally, our work brings insights into the meaning of quantitative results recently obtained in several experiments [48, 49, 50].

1.5.3 Noise investigation of fractionalized quasiparticles

The third experiment performed during this Ph.D. work focuses on the behavior of fractional charges along IQHE channels in a source-analyzer setup. Indeed, interactions between conducting chiral channels may split an injected electron into two modes, hence fractionalizing its charge (see Fig. 1.9). Non-zero cross-correlations in such systems are observed, in marked contrast with the vanishing signal expected for free electrons. These signatures match with the edge magneto-plasmon (EMP) prediction and, in the particular regime of high source transmissions (WBS), the found signal is predicted to result from a non-trivial anyon statistics of the fractional charges along the IQHE channel. A connection between the observed signal and the predicted anyon exchange phase of the fractional charges is established.

This third experiment opens a path to the study of anyon statistics from the fractionalization of simple and well-controlled electron modes.

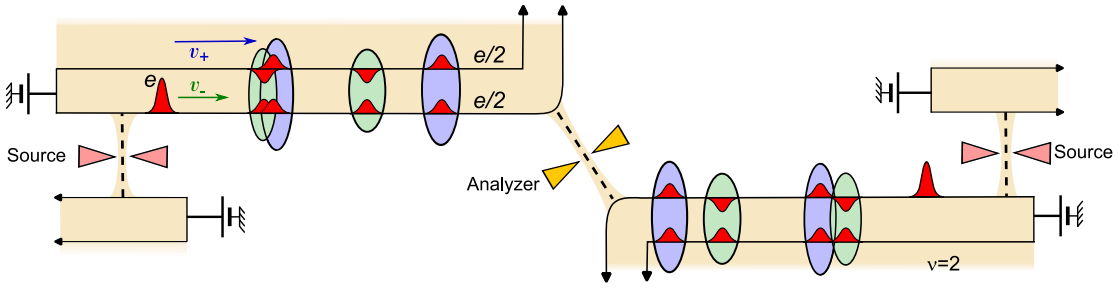

Figure 1.9: **Illustration of the third experiment.**
At $\nu = 2$, electrons (red wave packets facing up) injected by opposite source QPCs fractionalize into charges e/2 (smaller wave packets) that impinge on a central QPC. The outgoing cross-correlations allow us to investigate the statistics of the incident fractional charges.

1.6 Outlook of the manuscript

The preceding description of the experimental investigation carried out in this thesis reflects the organization of this manuscript.

First, a description of the integer and fractional quantum Hall effect is given in Chapter 2. It brings to the reader the key theoretical insights into this widely used effect and aims to summarize the present understanding of exotic excitations hosted in such systems.

Chapter 3 addresses the demonstration of Andreev-like scattering performed during this Ph.D. work. It discusses the specificity of this process and highlights the contrast with the trivial partition of electron beams in the QPC.

The investigation of unconventional anyon statistics in source analyzer set-up is reported in Chapters 4 and 5 at respective filling factors $\nu = 1/3$ and $\nu = 2/5$. The physical *braiding process* responsible for the signal is presented first. Then, we discuss the different markers of anyon statistics obtained in such systems as well as their quantitative meaning.

Finally, the last Chapter 6 presents the experimental results obtained for fractional charges in a source-analyzer set-up set at $\nu = 2$. After demonstrating the electron fractionalization due to inter-channel interactions, the cross-correlations of currents are investigated, compared to the edge magneto-plasmon (EMP) description and, in the particular regime of diluted beams, connected to the anyonic exchange phase of the resulting fractional charges.

Chapter 2

The Quantum Hall Effect

The quantum Hall effect (QHE) takes place at low temperatures when a two-dimensional conductor is immersed into an intense perpendicular magnetic field **B**.

It was discovered in 1980, when von Klitzing *et al.* observed in a bidimensional Si-MOSFET unexplained plateaus in the Hall resistance R_{H}, associated with a zero longitudinal Hall resistance [51]. Moreover, these plateaus were precisely quantized into integer fractions of the quantum of resistance:

$$R_{\mathrm{H}} = \frac{h}{\nu e^2}, \quad \nu \in \mathbb{N}. \tag{2.1}$$

Two years later, the same experiment performed in a high mobility AlGasAs|AlGaAs heterostructure demonstrated the existence of fractional values of ν [52].

These two Nobel prize-awarded observations, respectively coined integer quantum Hall effect (IQHE) and fractional quantum Hall effect (FQHE), gave rise to a vast field of theoretical and experimental research in condensed matter physics, still very active nowadays.

While their experimental manifestations are similar, their theoretical descriptions are based on different pictures. Indeed, IQHE only requires free electrons, with standard Fermi statistics distributed in Landau Levels (LL). In contrast, the theory of FQHE takes into account Coulomb interactions and describes excitations with exotic fractional charge and statistics, intermediate between fermions and bosons.

This chapter aims to concisely describe the theoretical pictures of IQHE and FQHE. A brief description of the IQHE physics is first given. Then, we give the basics concerning Laughlin picture of FQHE, with a description of the associated bulk exotic quasiparticles, with fractional charge and exchange statistics. The more complex hierarchical Jain series involving copropagating edge channels is then addressed, using the composite fermion picture. Finally, we describe the physics taking place at the edges in such a system, whose transport properties are described by the Tomonaga–Luttinger liquid (TLL) theory.

2.1 The integer quantum Hall effect (IQHE)

2.1.1 Landau Levels

When a two-dimensional electron gas (2DEG) is placed in a strong perpendicular magnetic field at low temperature, electron trajectories are curved due to the Lorentz force and follow cyclotron orbits. Orbiting electrons constitute a quantum harmonic oscillator, described by the following Hamiltonian:

$$\mathcal{H} = \frac{1}{2m^*}(\mathbf{p} - e\mathbf{A})^2 \tag{2.2}$$

where $\mathbf{p}$ is the momentum, m^* the effective mass of the electron ($m^* = 0.07m_e$ in GaAs [53]) and $\mathbf{A}$ is the magnetic vector potential.

Solving the Schrodinger equation $\mathcal{H}|\Psi\rangle = E|\Psi\rangle$ gives the eigenenergies E_n of the system, which are quantized: $E_n = (n + 1/2)\hbar\omega_c$, $n \in \mathbb{N}$. $\omega_c = eB/m^*$ is the cyclotron pulsation. A set of quantized orbitals with the same n is called a *Landau level* (LL). Note that the eigenfunctions Ψ_n of this system have the form :

$$\Psi_n(x, y) = C_n e^{ik_x x} e^{\frac{(y-y_0)^2}{2l_B^2}} \mathrm{H}_n(y - y_0) \tag{2.3}$$

with (x, y) the spatial coordinates, C_n a normalization constant, $l_B = \sqrt{h/(eB)}$ the magnetic length, and (H_n) Hermite polynomials.

Landau levels are highly degenerate because the arrangement of the center of the cyclotron orbits throughout the surface of the 2DEG can be achieved in many different ways (mathematically, there are multiple valid solutions). The degeneracy g, i.e. the maximal number of valid solutions, is equal to the number of flux quanta in the surface S:

$$g = n_\Phi = \frac{BS}{\Phi_0} = \frac{eBS}{h} \tag{2.4}$$

where $\Phi_0 = h/e$ is the flux quantum.

The relevant parameter describing the system is therefore the *filling factor* ν which is defined as the number of electrons N per flux quantum:

$$\boxed{\nu = \frac{N}{n_\Phi} = \frac{hn_{2\mathrm{D}}}{eB}} \tag{2.5}$$

with $n_{2\mathrm{D}}$ the density of electrons in the 2DEG sample. Consequently, tuning the magnetic field applied on a sample with a given density $n_{2\mathrm{D}}$ allows to sequentially fill the Landau levels and therefore to tune the filling factor.

2.1.2 Edge States

A real sample is subject to a confinement potential $V(x)$ bending the Landau levels at the edge of the sample (see Fig. 2.1a). The resulting electric field gives rise to a dissimilarity between transport along the edges and transport in the bulk of the sample. This distinction can be seen through the group velocity v_n of electrons in the n^{th} LL. v_n can be written using the energy dependence with the position along the x axis in the sample as follows:

$$v_n = -\frac{1}{eB}\frac{\partial E_n}{\partial x} \tag{2.6}$$

In the bulk, as $E_n(x)$ is constant, the group velocity is null and electrons do not contribute to transport. By contrast, at the edge of the sample, electrons have a finite group velocity v_n and therefore contribute to the total current. Note that v_n have opposite signs on opposite edges, indicating the chirality of the system.

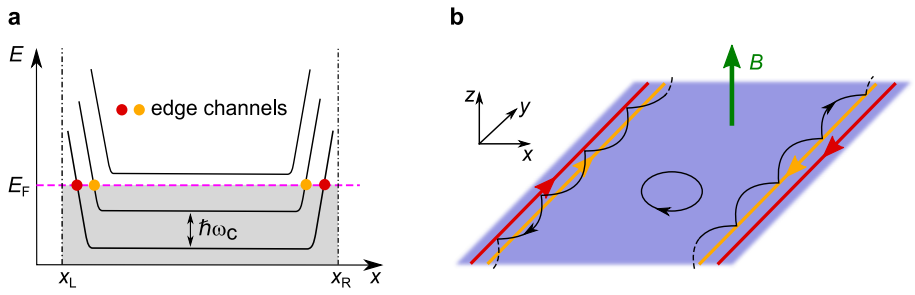

Figure 2.1: **Chiral edge channels in the IQHE.**
a Landau levels, bent due to the confining potential, cross the Fermi energy near the edge of the sample (at position x_L and x_R). Low-energy excitations which solely contribute to transport are only possible in edge channels (red and yellow dots).
b Semi-classical picture: only the edge electrons that cannot complete full orbits contribute to transport through successive bounces off the sample edge.

Another qualitative and maybe more intuitive way to tackle this problem is based on the semi-classical description of electron motion in the sample. At the edges of the sample, electrons cannot complete their cyclotron orbit and can propagate in a chiral manner along the borders by successive bounces (see Figure 2.1b). In the bulk, on the contrary, electrons perform full orbits (if their mean free path is larger than the typical perimeter of an orbit) and do not propagate in the longitudinal direction.

A full quantitative treatment performed by Halperin [54] explains the transport along the edges as a consequence of gapless edge excitations, where the occupied LLs cross the Fermi energy because of the confinement potential (see Fig. 2.1a). In contrast, the available bulk states have a finite energy gap (the cyclotron gap) and therefore do not contribute at low voltages and temperatures.

2.1.3 Disorder and percolation

The presence of disorder, composed of impurities randomly distributed in the sample, is a central ingredient to explain the presence of Hall resistance plateaus in the IQHE. Figure 2.2 illustrates the role and implication of disorder with the example of the transition between $\nu = 2$ (a) and $\nu = 1$ (c).

Indeed, impurities induce a random potential V_{imp} (pictured as curves on LL in the graphs of Figure 2.2) which leads to the emergence of local minima of potential in the sample. The electrons are therefore enclosed in equipotential loops (see top schemes of Figure 2.2) around impurities and the Fermi energy can lie between two successive LLs. If the loops do not connect the opposite edges (Figure 2.2a,c), the enclosed bulk electrons do not contribute to transport, leaving R_H on a plateau (see inset in graph of Figure 2.2b).

In contrast, when the highest LL is sufficiently (but not totally) filled the electrons percolate, i.e. they can transversely cross the sample by hopping from loop to loop (Figure 2.2b). Hence, in this situation, the bulk is not insulating anymore, and the Hall resistance changes, which corresponds to a transition between plateaus (inset in Figure 2.2b).

Let us now turn to the more complex fractional quantum Hall effect.

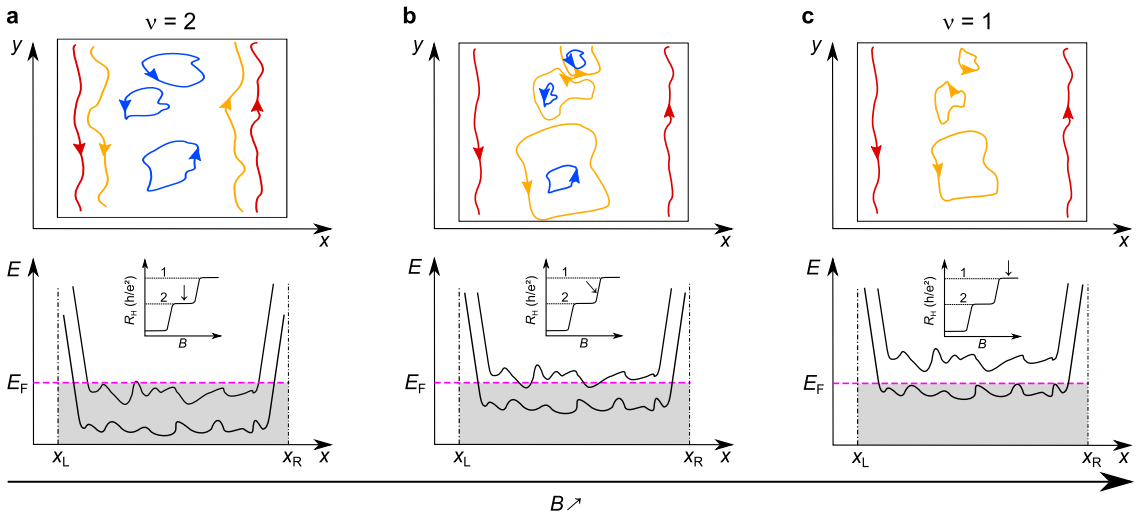

Figure 2.2: **The role of disorder in the IQHE.** In the top row are shown the equipotential lines in the sample.
a (c) For a completely filled LL $\nu = 2$ ($\nu = 1$), the edge channels are disconnected, and bulk electrons cannot flow transversely by hopping from the too-small equipotential loops. The transverse resistance (inset) is on a plateau.
b For partially filled LL, equipotential loops are big enough to allow electrons to hop from one edge to the other. The transverse resistance (inset) is intermediate between two plateaus.

2.2 Laughlin picture of the fractional quantum Hall effect

The results of this thesis work largely concern the fractional quantum Hall effect (FQHE). FQHE appears in very clean 2DEGs, with high mobility, and is characterized by a fractional filling factor: $\nu = p/n$ (with $p, n \in \mathbb{N}^\star$). Note that odd denominators are more easily observed in experiments. The fraction explored during this Ph.D. work concerns the case $\nu < 1$, for which only the first LL is partially filled.

The theoretical picture describing this effect is essentially based on Coulomb interactions in the conductor, while we only consider free fermions in the IQHE. This section aims to give a brief overview of the FQHE theory.

First, let us focus on the $\nu = 1/(2m+1)$ ($m \in \mathbb{N}^\star$) family of states which has been the first to be theoretically described in 1983 by R. B. Laughlin [55] and which has then been coined the *Laughlin series*. The most emblematic and most experimentally convenient (i.e. having a large gap compared to $k_B T$ and requiring an accessible B) Laughlin state is $\nu = 1/3$.

2.2.1 Ground state: the Laughlin ansatz

The FQH state is a many-body problem involving N interacting particles. Let us define $z_j = x_j + iy_j$ the position of the j^{th} particle in the 2D plane (identified to the complex plane, i being the complex unity).

Starting from the wave-function of a single-electron subject to a magnetic field (see Eq. (2.3)), Laughlin proposed a N-quasiparticles wave-function Ψ_N through a generalizing ansatz of the

form:

$$\Psi^{(N)}(z_1, \cdots, z_N) = \prod_{k<l}^{N} f(z_k - z_l) \exp\left(-\frac{1}{4}\sum_{j}^{N} |z_j|^2\right). \tag{2.7}$$

This ansatz respects the spatial symmetries (angular momentum conservation and transnational invariance) of the problem.

Moreover, the function f has to be compatible with the physical constraints of the system. Firstly, as two particles cannot be at the same position, the argument $z_k - z_l$ has to be zero when $k = l$. Second, as it has been deduced from a polynomial function, $f(z)$ reads $f(z) = z^m$ with m an odd integer (to respect the antisymmetry imposed by the Fermi-Dirac statistics of the electrons). Therefore the Laughlin ansatz giving a wave-function which respects all these constraints is:

$$\Psi_{\nu}^{(N)}(z_1, \cdots, z_N) = \prod_{k<l}^{N} (z_k - z_l)^m \exp\left(-\frac{1}{4}\sum_{j}^{N} |z_j|^2\right) \tag{2.8}$$

Finally, the m odd integer is found to be the inverse of the filling factor: $m = 1/\nu$. Indeed, in Eq. (2.7), there are $N-1$ factors of the form $(z_k - z_l)^m$ (one for each of the $N-1$ remaining electrons) so the maximal power of the polynomial is $m(N-1)$, i.e. $\prod_{k<l}(z_k - z_l)^m \sim z_k^{m(N-1)}$ for any given k.

This maximal power is fixed by the number of states N_B in each LL so we get the linear relation (with δ a shift which disappears in the thermodynamic limit $N, N_B \to +\infty$):

$$mN - \delta = N_B \implies \nu \equiv \frac{N}{N_B} = \frac{1}{m} = \frac{1}{2s+1} \tag{2.9}$$

2.2.2 Fractional charge of excited state

So far, the description that we made of the Laughlin picture has focused on the ground state of the system. But the most striking prediction of Laughlin was the emergence of quasiparticle excitations carrying a fractional charge $e^* \equiv \nu e$.

Let us consider a Laughlin system in its ground state to which we adiabatically add a flux quantum h/e. As the wave function will then evolve adiabatically and as Coulomb interactions open a finite energy gap in the bulk of the system, the adiabatic theorem implies that the resulting state remains an eigenstate of the system : it is a *quasihole* (or alternatively a *quasiparticle* if one removes a quantum of flux instead of adding one). Such an adiabatic insertion (removal) of the quantum of flux at position z_0 corresponds mathematically to a multiplication of the ground state wave-function by $\prod_{i=1}^{N}(z_i - z_0)$ so that the quasihole (quasiparticle) wave-function is:

$$\begin{aligned}\Psi_{\text{qp}}(z_1, \cdots, z_N) &= \prod_{i=1}^{N}(z_i - z_0)\Psi_{\nu}^{(N)}(z_1, \cdots, z_N) \\ &= \prod_{i=1}^{N}(z_i - z_0)\prod_{k<l}^{N}(z_k - z_l)^{1/\nu} \exp\left(-\frac{1}{4}\sum_{j}^{N} |z_j|^2\right)\end{aligned} \tag{2.10}$$

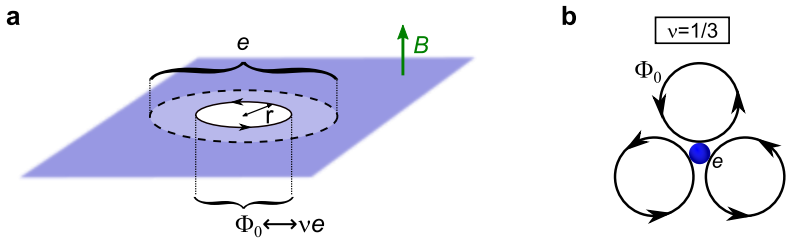

Figure 2.3: **Fractional charge.**
a Adding (removing) a flux quantum (pictured as an arrowed circle) creates a $-\nu e$ quasihole (νe quasiparticle) in the Laughlin fluid.
b At $\nu = 1/3$, there is one electron per three flux quanta, which can be seen as one charge $e^* = e/3$ per flux quantum

The charge of one of these elementary excitations of the fractional quantum Hall fluid can be deduced from electrostatic arguments. The supplementary flux quanta (varying adiabatically between 0 and $\Phi_0 = h/e$ in a delay dt) induces the electric field $\mathcal{E}_\Phi$ along the closed contour C of radius r:

$$\mathcal{E}_\Phi = -\frac{1}{2\pi r}\frac{d\Phi}{dt} \tag{2.11}$$

Knowing the conductance of the medium $\nu e^2/h$, the linear current density j_r associated with this electric field is then:

$$j_r = -\frac{1}{2\pi r}\frac{d\Phi}{dt}\frac{\nu e^2}{h} \tag{2.12}$$

and we can deduce the total charge Q along the closed curve of radius r associated with time dt:

$$Q = \int_t \oint_C j_r dt = -2\pi r \int_t \frac{1}{2\pi r}\frac{d\Phi}{dt}\frac{\nu e^2}{h} dt = -\nu e \int_t d\Phi \frac{e}{h}$$

$$\Longrightarrow \boxed{Q = -\nu e} \tag{2.13}$$

In other words, the adiabatically added quantum of flux h/e occupies the equivalent of ν of an electron (see Fig. 2.3). In the emblematic example of $\nu = 1/3$, there will then be one electron for three quanta of flux. In summary, the natural excitations of a Laughlin fluid are therefore quasiparticles (quasiholes) of charge $e^* = \nu e$.

2.2.3 Experimental evidence of the fractional charge

Experimental evidences of the fractional charge of these bulk low-excitation quasiparticles have been found soon after the predictions in various systems. It is by now firmly established.

It was first demonstrated in (Al)GaAs heterostructures through shot noise measurements described in the introductory section 1.4.1. Indeed, if one phenomenologically applies the expression of the excess shot noise induced by a QPC set in the WBS regime with transmission $\tau \to 1$ (see Eq. (1.20))

$$S_{ii} = 4k_{\mathrm{B}}T\nu G_{\mathrm{K}} + 2e^{*}\tau I_{\mathrm{back}}\left[\coth\frac{e^{*}V}{2k_{\mathrm{B}}T} - \frac{2k_{\mathrm{B}}T}{e^{*}V}\right] \tag{2.14}$$

(with $I_{\mathrm{back}} = \nu(1-\tau)G_{\mathrm{K}}V$ the back-scattered current, tunneling from one edge to the opposite one), it directly gives the charge $e^{*} = \nu e$ transmitted between the opposite edges of a QPC. In that case, the QPC has to be set in the WBS regime so the two opposite edges are separated by the $\nu = 1/3$ FQH state. Therefore, the tunneling quasiparticles are natural excitations of the bulk, i.e. Laughlin quasiparticles. This was the strategy used by two simultaneous and independent experiments [11, 10] which demonstrated the fractional charges of anyons in the $\nu = 1/3$ regime through auto-correlations and cross-correlations of currents induced by a voltage-biased QPC (see Fig. 2.4). These measurements in the WBS regime have then been extended to the SBS regime [56] and other fractions like $\nu = 2/5$ [41], $\nu = 2/3$ [57] and even the non-abelian case $\nu = 5/2$ [7]. These measurement techniques are now standard and will be used during this thesis (even though it remains phenomenological and recent investigation could refine this analysis, see Appendix C for details).

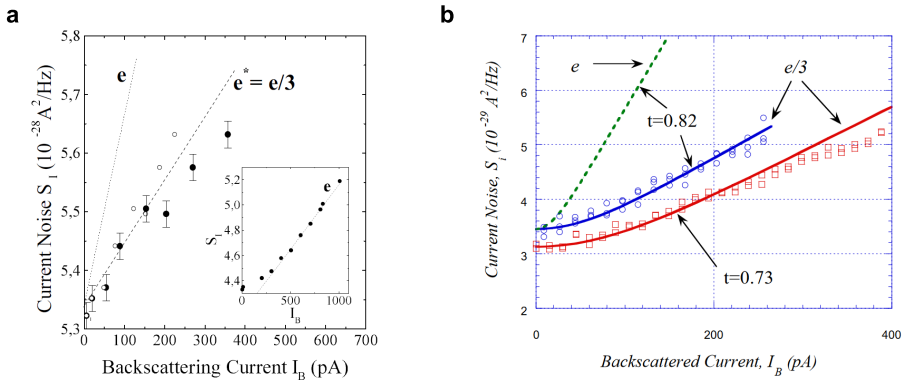

Figure 2.4: **Experimental evidence of fractional charge from Refs [10] and [11].** Shot noise experiment in the $\nu = 1/3$ FQHE performed in Refs. [10] (a) and [11] (b). The data are in agreement with the standard shot noise expression Eq. (2.14) phenomenologically applied for $e^{*} = e/3$ and $\tau = t$

While the DC shot noise is a powerful technique to demonstrate fractional charges of quasiparticles, note that these results have been confirmed by other techniques: measurements combining shot noise with microwave excitations [58, 59], interferometry signature [60, 61], or charging spectroscopy with antidots or single electron transistor [62, 63].

2.2.4 Fractional statistics

As mentioned in the introductory chapter, the quasiparticles hosted in the FQH Laughlin bulk are predicted to obey fractional braiding statistics when they are interchanged. "Braiding" refers to a mathematical operation corresponding to the interchange of the quasiparticles, or the winding of one around the other.

The mutual exchange phase θ between quasiparticles of respective charges q and q' is predicted to be given by (see e.g. [64, 65]):

$$\theta = \frac{\pi}{\nu}\frac{qq'}{e^{2}} \tag{2.15}$$

where ν is the filling factor [1]. In this simplest case of Laughlin quasiparticles ($e^* = \nu e = e/m$), it gives an exchange phase $\theta = \pi/m$. This statistics will be investigated in Chapter 4. Note that when q and q' are different, θ is called the "mutual exchange phase" while when they are identical it is simply named the "exchange phase".

2.2.5 A three-decades quest for experimental evidence of fractional statistics

While the fractional charge of Laughlin anyons has been experimentally proven soon after the prediction, unambiguous signatures of anyon fractional statistics have remained elusive for three decades.

Yet, proposals and experimental attempts for probing this non-trivial exchange phase have abounded in the 1990s.

Anyon exchange phase in Fabry-Perot interferometers

The first intuitive strategy proposed for accessing the anyonic exchange phase was based on interferometers [66, 67]. Indeed, let us consider the case of a Fabry-Perot geometry [2] made up of two QPCs enclosing an area A (see Fig. 2.5a). Under a magnetic field B, two carriers of charge e^* following different paths will acquire a phase difference due to the Aharonov-Bohm effect:

$$\Delta\phi = \frac{e^*}{\hbar} AB = 2\pi \frac{e^*}{e} \frac{BA}{\Phi_0} \tag{2.16}$$

with $\Phi_0 = h/e$ the flux quantum.

But in the specific case of Laughlin anyons ($\nu = 1/m$), inserting a quasiparticle in the loop adds a fractional term $2\pi/m$ to the phase. Then, adding N quasiparticles inside the enclosed path (which can be done thanks to a gate tuning the central region density) gives a total phase:

$$\Delta\phi = 2\pi \frac{e^*}{e} \frac{BA}{\Phi_0} + 2\theta N \tag{2.17}$$

The second term is then a direct consequence of the fractional exchange phase of anyons. Therefore, if one tunes the total phase thanks to a central gate depleting electrons, detecting $2\pi/m$ jumps in the resulting interference pattern would give direct evidence of the fractional exchange phase.

Many attempts using this strategy have been made [71, 72, 73, 74]. However, for a long time, the observation of anyonic phases through interferometry has been hampered by [75, 76, 67] charging energy effects (with an especially important impact in small systems). Indeed, in Coulomb-dominated cases, changes of charge in the bulk would impact the effective interferometer area A and blur the specific contribution of the exchange phase. It is only recently that, thanks to a device carefully compensating Coulomb interactions with screening gates, Nakamura *et al.* provided a clear signature of anyon statistics in such a Fabry-Perot interferometers [45] (see Fig. 2.5).

[1] more precisely, it is the filling factor of the channel of interest

[2] other geometries have been proposed such as Mach-Zehnder [68] and Hanbury-Brown-Twiss [69]

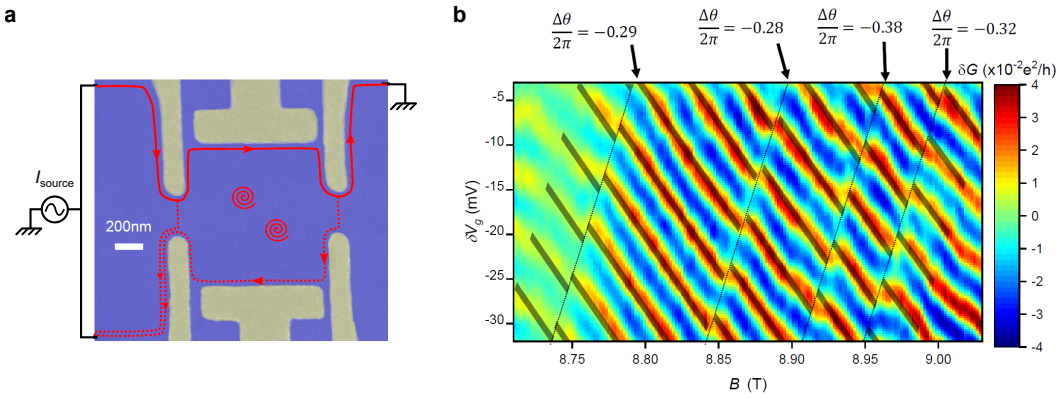

Figure 2.5: **Interference signature of fractional statistics from Refs. [45, 70].** **a** Experimental device used in Refs. [45, 70]. Two QPCs define a Fabry Perot interference cavity allowing edge anyons to encircle bulk anyons (spirals), making the interferometer sensitive to the fractional exchange phase θ. A plunger gate allows us to tune the effective surface of the cavity by applying negative DC gate voltage V_g. **b** Interference pattern obtained by changing the magnetic flux across the sample (thanks to V_g or B). The conductance change δG is plotted versus B and δV_g. The discrete phase jumps are attributed to the anyonic exchange phase θ.

Anyon exchange phase through the "source-analyzer" (or "collider") geometry

The second main strategy for probing anyon statistics is based on cross-correlation noise measurement in a Hong-Ou-Mandel-like geometry, combining several QPCs (sources and analyzer) and two opposite diluted beams of anyons. Following a proposal of Rosenow *et al.* [1], this strategy provided strong evidence of anyon statistics simultaneously to Ref. [45] with the pioneering results of Bartolomei *et al.* [2]. Since then, such versatile systems provided important new insights into the physics of anyons [48, 50, 49].

Probing signatures of unconventional exchange statistics with this method is one key result of this thesis. It will be extensively presented in Chapters 4 and 5.

2.3 Composite fermion picture in Jain series

Laughlin's theory successfully describes the states of filling factor $\nu = 1/m$ (with m an odd integer) but many other fractions have been experimentally observed [52, 41, 58] with the more general form $\nu = p/(2sp+1)$ (with $p, s \in \mathbb{N}$) such as $\nu = 2/5, 3/7, ...$ Note that in that case, the denominator is also an odd integer. Jain proposed a theory to generalize the Laughlin picture [77, 78] and this family of FQH states was coined the *Jain series*. Note that the Laughlin series is a specific case of the Jain series, with $p = 1$.

In Jain picture, each electron is bounded to $2s$ flux quantum, resulting in a composite particle, called *composite fermion* (CF) to stress their fermionic behavior because of the even number of flux quanta [3]. Figure 2.6 schematizes the physical picture developed by Jain. The number of remaining unbounded flux quanta determines the effective number of states per LL $N_B^* = N_B - 2sN_{el}$ and the resulting CFs are therefore subject to an effective magnetic field B^*:

[3] with an odd number, one would have composite bosons

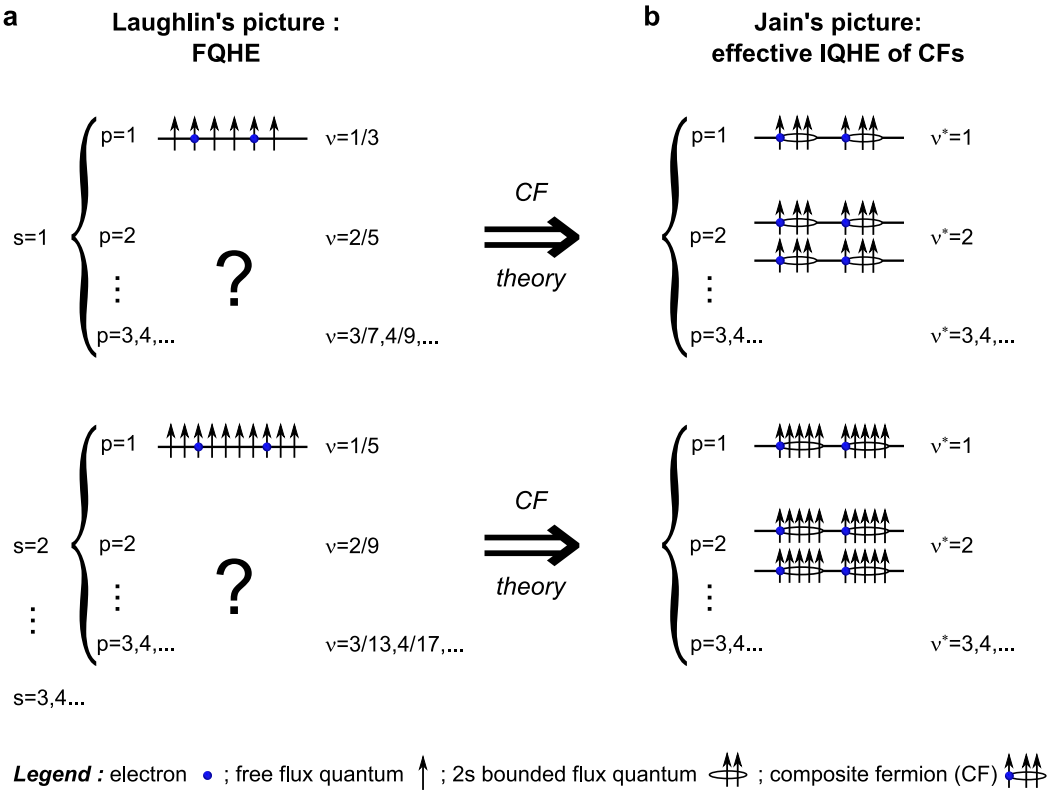

Figure 2.6: **Composite fermion picture.**
a Laughlin description of FQHE: in edge states, there are $2s+1$ flux quanta (arrows) per electron (blue point). This picture does not describe states other than $\nu = 1/(2s+1)$ as symbolized by question marks.
b Jain composite fermion (CF) generalized theory. $\nu = p/(2sp+1)$ FQH states can be seen as $\nu^* = p$ IQH states of composite fermions, made up of one electron and one $2s$ bounded flux quanta vortex (encircled arrows).

$$B^* = B - 2s\frac{h}{e}n_{2\mathrm{D}} \tag{2.18}$$

One can then define an effective filling factor ν^* as the ratio between the number of electrons and the effective number of flux quanta:

$$\nu^* = \frac{N_{el}}{N_B^*} \implies \nu^{*-1} = \nu^{-1} - 2s \tag{2.19}$$

which leads to $\nu = \nu^*/(2s\nu^*+1)$. For p completely filled LLs, one gets $\nu = p$ and we effectively get the relation defining the Jain series:

$$\nu^* = \frac{p}{2sp+1} \tag{2.20}$$

Remarkably, for integer values of s, the FQH state of quasiparticles with filling factor ν can be interpreted as an IQH state of composite fermions with filling factor ν^*. For instance, the $\nu = 2/5$ FQH state can be seen as the $\nu^* = 2$ IQH state of composite fermions made up of 1 electron and 2 flux quanta (see Fig. 2.6)[4].

[4] $\nu^* = 1$ corresponding to the $\nu = 1/3$ the Laughlin case

One can therefore directly deduce the charge of elementary excitations in this CF picture. In the case of IQHE, there is $1/s$ flux quantum per electron of charge e. Then, in the case of FQHE seen as IQHE of composite fermions, there are $(2sp+1)/s$ flux quanta per electrons which gives the charge e^* of the quasiparticles [79]:

$$e^* = \frac{e}{2sp+1} \tag{2.21}$$

The fractional statistics for such quasiparticles in the Jain series is predicted to be [80, 4]:

$$\theta = \pi \left[1 - \frac{2s}{2sp+1} \right] \tag{2.22}$$

Recently, the $\nu = 2/5$ state has been explored both in interferometers and in source analyzer systems but the quantitative agreement with prediction is less clear than in the simpler $\nu = 1/3$ case [45, 49, 48] (as will be largely discussed in the dedicated Chapter 5).

2.4 Edge physics of the quantum Hall effect

Up to now, we have described the low energy excitations within the bulk set in the FQH regime. But, as mentioned before, current in such a system is only carried along the edges of the sample. The nature of charges propagating along quantum Hall edges is indeed different from the bulk quasiparticles: while the lowest energy excitations have a fixed charge (e.g. e in the IQHE and νe in the WBS regime of the FQHE) with a given exchange phase, edge can carry any arbitrary charge [81] with a large variety of exchange phase.

This calls for a description of the physics at the QH edges. The following paragraph briefly gives some key elements, based on more detailed reviews [40, 82]. First, we synthesize the description of IQH edge channels taking into account inter-channel Coulomb interactions and then we describe the description of FQH edge channels.

2.4.1 A Tomonaga-Luttinger liquid theory to describe edge channels

In the quantum Hall effect, edge channels are one-dimensional chiral conductors. In this case, Coulomb interactions can play a major role and leads to the breakdown of the usual Fermi picture of the system. This breakdown applies for IQHE with interacting particles and in the FQHE. Instead, to describe the system, one should use the chiral *Tomonaga-Luttiger liquid* (TLL) model [83, 84] which is no longer based on free-fermionic quasiparticles but on collective bosonic excitations called plasmons. In other words, the chiral TLL framework maps the problem of 1D interacting electrons into a free boson system.

In this framework, as the energy excitation is much lower than the Fermi energy, the spectrum of the system can be linearized in the vicinity of the two Fermi wave vectors $\pm k_{\mathrm{F}}$, describing chiral edges with left-mover and right-mover particles (in the following, we focus of one chiral edge channel).

This low-energy effective theory of the edge channels allows us to take into account the effect of interactions in a straightforward way, using the so-called *bozonization* operation. It consist in expressing the fermionic field operators as *chiral* bosonic fields ϕ, which obey the commutation relation:

$$[\phi(x), \phi(x')] = i\text{sign}(x - x') \tag{2.23}$$

ϕ is linked to the charge density ρ at position x and the edge current I at time t by:

$$\rho(x,t) = \frac{e}{2\pi}\partial_x\phi(x,t) \tag{2.24}$$

$$I(x,t) = \frac{e}{2\pi}\partial_t\phi(x,t) \tag{2.25}$$

Using Eqs. (2.23) and (2.24) gives the following commutation relations for the charge density:

$$[\rho(x,t), \rho(x')] = \frac{e^2}{4\pi^2}\partial_x\partial_{x'}(i\pi\text{sign}(x - x')) \tag{2.26}$$

$$= -\frac{ie^2}{2\pi}\delta'(x - x')\mathbb{1} \tag{2.27}$$

In the following, we will express the physical quantities of the system in term of charge density ρ.

The general Hamiltonian describing the system is the sum of a kinetic term and an interacting term $\mathcal{H} = \mathcal{H}_0 + \mathcal{H}_{\text{int}}$. The repulsive electron-electron interactions responsible for the second term are characterized by the *Luttinger interaction parameter* K. In general, for free electrons (the non-interacting IQHE case) $K = 1$ while repulsive interactions imply $K < 1$.

Let us see how the chiral TLL model can be applied in the two particular cases studied in this thesis: interacting particles in the IQHE and FQH systems.

2.4.2 Edge magneto-plasmons in the IQHE

The presence and major role played by Coulomb interactions can generate fractional charges propagating along IQH edges. Several strategies have been proposed to obtain such fractional charges instead of usual electrons, including the use of a metallic island [64, 46], of an interface between an IQHE and a FQHE region [85, 86], of voltage pulses [87] or of inter-channel interplay between opposite [85, 88] or copropagating channels (see e.g. [89, 90] [5]). In the following, we focus on the latter strategy: taking advantage of the intrinsic inter-channel interactions between two IQH copropagating channels.

In the integer quantum Hall regime, at $\nu > 1$, we consider charges flowing in the multiple chiral co-propagating edge channels. In the absence of Coulomb interactions an injected electron in one channels remains a usual single electronic mode, with Fermi statistics and which propagate at a drift velocity v ($\sim 10^4$ to 10^5 m s^{-1}). However, in the presence of inter-channel Coulomb interactions, the nature of elementary excitations of the system drastically changes: electrons injected in one channel become collective modes called *edge magneto plasmons* (EMP).

Let us focus on the case $\nu = 2$, where the edge state is composed of two chiral co-propagating channels. This section gives a brief theoretical description of the emerging excitations in such a system.

[5] and [91] [92] for related theoretical works

Fields and Hamiltonian

We consider two such copropagating channels, labeled 'i' (for the inner one) and 'o' (for the outer one) which are assumed to be identical. One electronic charge is injected at time t and position x in the channel α ($\alpha = i, o$) and propagates along the edge path over a sufficiently long distance so the interactions have a significant impact (typically on a few microns). As mentioned in the previous section, following the chiral Tomonaga-Luttinger liquid (TLL) description of the quantum Hall edge [81], the charge density can be expressed in terms of bosonic fields $\phi_\alpha(t, x)$ [93, 94, 95].

The QH edge Hamiltonian $\mathcal{H}$ describing the system is $\mathcal{H} = \mathcal{H}_0 + \mathcal{H}_{\text{int}}$. It has a free-fermion kinetic contribution:

$$\mathcal{H}_0 = \frac{h}{2e^2} \sum_\alpha \int v_\alpha \rho_\alpha^2 dx \tag{2.28}$$

with v_α the velocity in channel $\alpha = i, o$. It also has a second term describing the interaction contribution. More precisely, the second term $\mathcal{H}_{\text{int}}$ models the Coulomb interactions:

$$\mathcal{H}_{\text{int}} = \frac{h}{2e^2} \sum_{\alpha,\beta} \int \int U_{\alpha,\beta} \rho_\alpha \rho_\beta dx dy \tag{2.29}$$

where $U_{\alpha,\beta}$ is the strength of interactions between channels α and β. Note that in our case, we neglect intra-channel interactions and we consider that the two channels act symmetrically. Moreover, as we assume that the Coulomb interactions are short-ranged, i.e. screened at a distance d much smaller than the propagation distance L, we may write $u(x - y) = u\delta(x - y)$ (with δ the Dirac distribution). This leads to:

$$\mathcal{H}_{\text{int}} = 2u \frac{h}{2e^2} \int \rho_i \rho_o dx \tag{2.30}$$

Finally, combining Eq. (2.28) and (2.30), one gets the total Hamiltonian of the system:

$$\boxed{\mathcal{H} = \frac{h}{2e^2} \int dx \left[v_i \rho_i^2 + v_o \rho_o^2 + 2u \rho_i \rho_o \right]} \tag{2.31}$$

Physically, this Hamiltonian corresponds to the charging energy for a local capacitive coupling between channels. Indeed, $e^2/(hv)$ is the quantum capacitance per unit length of a quantum Hall edge channel.

Fractionalization into two distinct eigenmodes

The Hamiltonian of Eq. (2.31) can be diagonalized and written in the following form :

$$\mathcal{H} = \frac{h}{2e^2} \int dx [v_+ \rho_+^2 + v_- \rho_-^2] \tag{2.32}$$

This is done using the rotation matrix $R(\varphi)$ [96, 90]:

$$\begin{pmatrix} \rho_+ \\ \rho_- \end{pmatrix} = R(\varphi) \begin{pmatrix} \rho_o \\ \rho_i \end{pmatrix} = \begin{pmatrix} \cos\varphi & \sin\varphi \\ -\sin\varphi & \cos\varphi \end{pmatrix} \begin{pmatrix} \rho_o \\ \rho_i \end{pmatrix} \tag{2.33}$$

where the so-called *mixing angle* φ, defined by $\tan 2\varphi = 2u/(v_o - v_i)$, is a key parameter of this system. It encodes the separation between the two collective modes resulting from interactions

and corresponding to the eigenmodes $\rho_\pm$ of the Hamiltonian with distinct velocities $v_\pm$. They are defined by:

$$\rho_+ = \cos(\varphi)\rho_o + \sin(\varphi)\rho_i \quad \text{with} \quad v_+ = \frac{v_o + v_i}{2} + \frac{u}{\sin 2\varphi} \tag{2.34a}$$

$$\rho_- = -\sin(\varphi)\rho_o + \cos(\varphi)\rho_i \quad \text{with} \quad v_- = \frac{v_o + v_i}{2} - \frac{u}{\sin 2\varphi} \tag{2.34b}$$

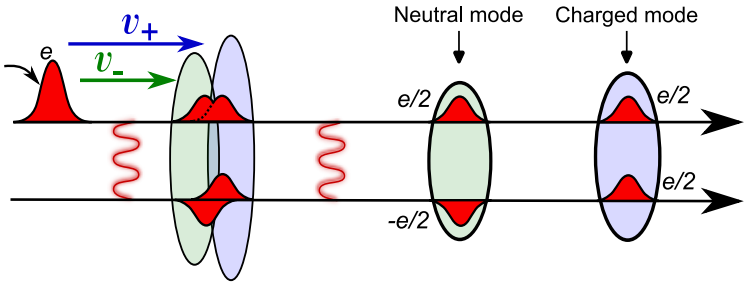

Figure 2.7: **Principle fractionalization induced by inter-channel interactions at $\varphi = \pi/4$.**
An electronic mode (red packet) splits into two collective modes made up of pairs of fractional charges distributed over the two copropagating chiral edge channels (black line with arrows). The "fast" charged mode (blue ellipse) and the "slow" neutral mode (green ellipse) propagate with respective velocities $v_\pm$

Thus, as the two velocities are different, the initial electronic mode is indeed fractionalized into these two distinct modes.

Let us now focus on the case where $\varphi = \pi/4$ and where an electron is injected on the outer channel, as illustrated in Figure 2.7. It corresponds to the regime of strong interactions. In that case, the two distinct modes are :

- one 'fast' mode of velocity v_+, that carries a total charge e distributed over the two channels. In the following, it will be referred to as "the charged mode" and the wave packets on each channel will be referred to as "fractional charges" or simply "wave packets".
- one 'slow' mode of velocity v_- that carries a zero total charge: two opposite charges are distributed over the two channels (see Fig. 2.7). In the following, it will be referred to as "the neutral mode" or "the spin mode".

In this limit of strong interactions, $\varphi = \pi/4$, the resulting collective modes are completely delocalized between the two original edge channels. The charged mode is made up of two charges $e/2$ (one on each channel), and the neutral mode is composed of one charge $e/2$ in the channel of injection and one charge $-e/2$ in the other channel.

In the opposite limit $\varphi = 0$, interactions are negligible and the two eigenmodes simply reduce to the initial edge states, i.e. one single electron on the outer channel.

For intermediate values of φ, the wave packets carry charges intermediate between $\pm e$ and $\pm e/2$. By computing the excess charge densities, i.e. the deviations of the expectation values

of particle density operators with respect to the equilibrium situation when no electron is injected, the charges carried by the fast and slow excitations in outer (o) and inner (i) channels are [97, 90] :

$$q_{o,+} = e\cos^2\varphi, \quad q_{o,-} = e\sin^2\varphi \tag{2.35}$$

$$q_{i,\pm} = \pm e\cos\varphi\sin\varphi \tag{2.36}$$

This intermediate case involves wave packets carrying different charges which complexifies the discussions. In the following chapters, we will focus on the simpler cases $\varphi = 0, \pi/4$.

2.4.3 Wen's hydrodynamical picture of FQHE

We now turn to the description of FQH edge states, focusing on Laughlin case $\nu = 1/m$. During the 1990s, X. G. Wen [81] used the following hydrodynamical picture to map them into a chiral TLL liquid, with the Luttinger parameter $K = 1/m$ in the Laughlin case. Let us give the key elements of this picture without diving into the details.

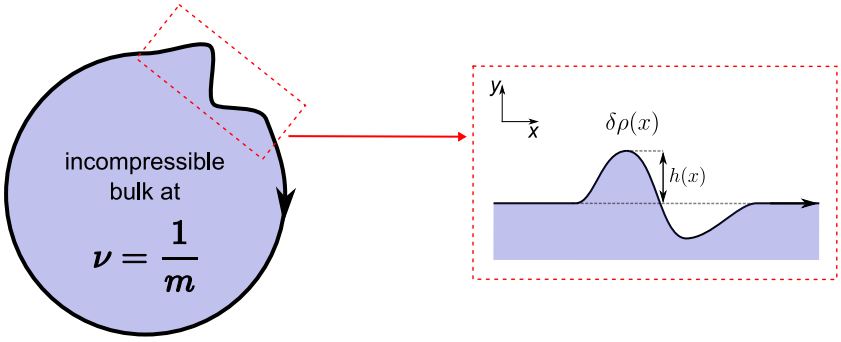

Figure 2.8: **Wen hydrodynamical picture.**
An incompressible bulk in the $\nu = 1/m$ FQHE forms a droplet with a chiral edge. Due to incompressibility, excitations must conserve the droplet area and are then a deformation of the edge (of height $h(x)$) of arbitrary charge $\delta\rho(x)$, propagating chirally along the droplet surface.

We consider an incompressible bulk, set at filling factor $\nu = 1/m$ and at fixed density n_{2D}. It then forms a two-dimensional "droplet" as pictured in Figure 2.8. As the bulk is incompressible, the only possible excitations must conserve the total area, which implies that they are small charge density fluctuations $\rho(x)$ per unit length deforming the droplet at the edge and chirally propagating along its surface. The propagation is described using the coordinates (x, y) with x the linear abscissa.

Such a fluctuation of the charge density at the edge can then be expressed in terms of a small displacement $h(x)$, orthogonal to the surface:

$$\rho(x) = \int_0^{h(x)} en_{2D}dy = en_{2D}h(x) \tag{2.37}$$

Note that these edge excitations may then carry an arbitrary charge.

In the presence of a confining potential $V(x)$ (V does not depend on y because the curvilinear abscissa follows the equipotential of V), the system is described by the electrostatic Hamiltonian:

$$\mathcal{H} = \frac{1}{2}\int_0^L V(x)\rho(x)dx \tag{2.38}$$

V can be expressed in term of the confining electric field $\mathbf{E} = -\nabla V = (\partial_y V)\mathbf{u}_y$:

$$V = Eh(x) = \frac{hn_{2D}v}{e\nu}h(x) \tag{2.39}$$

where we have used the drift velocity $v = E/B$ and the filling factor $\nu = hn_{2D}/(eB)$. Finally, combining Equations (2.37) and (2.39), we get :

$$\boxed{\mathcal{H} = \frac{hv}{2e^2\nu}\int dx(\rho(x))^2} \tag{2.40}$$

Note that this Hamiltonian has been obtained with classical arguments and that quantization is achieved by imposing the commutation relations between the canonical conjugate variables of the problem. Note also that the same result can be obtained by introducing the following Luttinger bosonic field ϕ whose derivative is proportional to the charge density (see Eq. (2.24), with a $\sqrt{\nu}$ factor):

$$\partial_x\phi = \frac{2\pi}{\sqrt{\nu}}\rho(x) \tag{2.41}$$

Physically, this Hamiltonian can be seen as the charging energy for a capacitance $C_\nu = \nu e^2/(hv)$, which is consistent with a redistribution of the electron density by ν in the Laughlin case. Finally, one can note that when such Hamiltonian is coupled to a potential $V(x,t)$, we can recover the fractional quantum Hall conductance. Indeed the total Hamiltonian is then:

$$\mathcal{H} = \frac{hv}{2\nu e^2}\int dx\rho(x,t)^2 + \int \rho(x,t)V(x,t)dx \tag{2.42}$$

$$= \frac{hv}{2\nu e^2}\int dx\left[\left(\rho(x,t) + \frac{\nu e^2}{hv}V(x,t)\right)^2 - \left(\frac{\nu e^2}{hv}\right)^2 V(x,t)^2\right] \tag{2.43}$$

Minimizing it gives the charge density $\rho = -(\nu e^2)/(hv)V(x,t)$ and, knowing the expression of the current density $j(x,t) = v\rho(x,t)$, we deduce the conductance G of the quantum Hall edge channel:

$$G = \frac{j(x,t)}{V(x,t)} = \nu\frac{e^2}{h} \tag{2.44}$$

Therefore, from the formal analogy between the FQH regime and a classical incompressible droplet with a surface wave, introduced by Wen [6], we recover the Hamiltonian of a chiral TLL. Then, this system maps with TLL theory, i.e. one can describe the FQH edges as a chiral Tomonaga-Luttinger liquid.

[6] with a different normalization choice but with the same expressions of the physical quantities as the one obtained here

2.4.4 Bulk-edge correspondence

At this point, we have to emphasize again that the charges contributing to the current are *edge* anyons, while the anyons of charge e/m and exchange phase π/m in the Laughlin series $\nu = 1/m$ (described in Sec. 2.2) are low-energy excitations in the *bulk*. Hence, these two kinds of quasiparticles are a priori different.

However, it is possible to access the properties of bulk quasiparticles through transport in the edges thanks to the so-called *bulk-edge correspondence*. The filling factor ν of the gapped bulk is a topological invariant of the system, meaning that it is necessary to close the bulk gap in order to change ν. The existence of gapless edge states is a consequence of the change of this topological invariant at the interface between the bulk and the vacuum outside the sample. The relation between the number of edge modes and the bulk topological invariant is the bulk-edge correspondence [98, 99]. Quasiparticles of the bulk can then flow along the gapless edges and one can get information about their nature through their transport properties.

Experimentally, we use QPCs to specifically create beams of edge anyons identical to the one in the bulk, taking advantage of the bulk-edge correspondence.

Indeed, in the WBS regime, two opposite edges are separated by a robust bulk at the Laughlin filling factor $\nu = 1/m$. Natural quasiparticles tunneling from one edge to the other and flowing along the downstream edge channel then correspond to the lowest energy excitations of the bulk, i.e. Laughlin anyons. In essence, QPC will then be used as a filter to specifically investigate edge anyons identical to bulk anyons.

In the SBS regime, opposite edges at a QPC are separated by vacuum and the natural quasiparticles tunneling from one edge to the other are e-charged quasiparticles. In this opposite regime, the QPC can be used as a filter of charge e.

2.4.5 Conductance and I-V characteristics

As the edges in the FQHE follow the TLL theory, the conductance of the channels is given by:

$$G = K\frac{e^2}{h} \tag{2.45}$$

where K is the so-called *Luttinger parameter* and is predicted to be precisely ν in the case of Laughlin fractions. When two edges are close enough (for instance at a QPC constriction), bulk-edge correspondence implies that edge quasiparticles can tunnel from one conducting channel to another above the incompressible bulk.

In the TLL framework, Kane and Fisher theoretically described the conductance and I-V characteristics across such a constriction [100, 101]. According to these predictions, the conductance varies with the temperature T following the power law:

$$G(T) \sim T^{2/K-2}, \tag{2.46}$$

and, similarly, the I-V characteristics are predicted to follow:

$$I(V)|_{T=0} \sim V^{2/K-1} \tag{2.47}$$

This is in marked contrast with the familiar Fermi liquid model. Indeed, for free fermions, the I-V characteristics is linear, and $G(T)$ is constant. Accordingly, measuring the I-V characteristics and $G(T)$ in one-dimensional FQH edge channels has been seen as a good way to probe the peculiar behavior of quasiparticles in such systems.

However, experimental investigations of these power-law relations led to an unexpected deviation from predictions (2.46) and (2.47), in particular at $\nu = 1/3$ where theory predicts $G \sim T^4$ (see e.g. [102, 103, 104] and [105] for a review). Although the obtained power law confirms a profoundly different underlying physics in the FQHE from IQHE (predicted to behave as a Fermi liquid), the experimental power law exponents are significantly different from those predicted by theory which is still not well understood. Note that such TLLs have been successfully emulated with circuits in the IQHE with the expected power law in AlGaAs [106] and graphene [107].

The discrepancy between experiment and theory could be linked to the so-called *edge reconstruction* [108, 109, 110]. Indeed, due to the long-range Coulomb interactions and the smoothness of the confinement potential along the edges, the edge state can reconstruct into several copropagating channels. Some of these channels can carry additional charged or neutral modes, complicating the description. For instance, in *hole-conjugate states* (i.e. the states symmetric to Laughlin states with respect to $\nu = 2$), counter-propagating modes are predicted [111, 65].

Then although power laws in $G(T)$ and $I - V$ characteristics of a FQHE constriction give results significantly different from the Fermi liquid description and although recent insights are very promising (see [107] in graphene), discrepancies are still puzzling and no consensus has emerged yet from studies attempting to explain them [112, 113]. This calls for alternative ways to probe the exotic physics of FQHE.

2.4.6 Scaling dimension

Up to now, we have seen that the main features that distinguish the exotic quasiparticles in FQHE from standard fermions are their fractional charge, fractional exchange statistics, and nonlinear power laws. But all these characteristic numbers can be linked to a more general parameter derived from a conformal field theory and called the *scaling dimension* Δ. The scaling dimension is characteristic of the edge channel and can be seen as the parameter controlling the decay of self-correlations with time. Note this parameter is sometimes defined up to a factor two in the literature (see e.g. [1]) and labeled $\delta = 2\Delta$. Although in the remainder of the manuscript, we will focus on the charge and the statistics of a quasiparticle without discussing in detail its scaling dimension, it can be interesting to give a few insights about this important parameter. The remainder of this section aims to do so, following the description given by Schiller *et al.* [65].

As previously mentioned, FQH edge states are described in the TLL framework by N edge modes (with bosonic operators) distributed over several channels. The mode l ($l \in [\![1, N]\!]$) has a chirality $\chi_l = \pm 1$ and can be charged or neutral. Its contribution to the total charge is encoded into a set of numbers $q_l \geq 0$ ($q_l = 0$ in the case of neutral mode). At fixed filling factor ν, the set (q_l) is constrained by the following relation [7]:

[7] because the current of the channel is then $I_l = \chi_l q_l \frac{e^2}{h} V$, and we know that the edge's conductance is $\nu \frac{e^2}{h}$

$$\sum_l \chi_l q_l^2 = \nu \tag{2.48}$$

A quasiparticle in the FQHE can be described by a second-quantized bosonic operator $\psi_{\mathrm{qp}}(x,t)$ (x being the position on the edge and t the time). In the general case, it can be decomposed over several edge modes. The distribution of a quasiparticle over the multiple modes is then encoded by a set of real numbers a_l.

The considered quasiparticle is characterized by two main quantum numbers: its charge Q and its scaling dimension Δ, respectively given by:

$$Q = e\sum_l \chi_l q_l a_l \tag{2.49}$$

$$\Delta = \frac{1}{2}\sum_l a_l^2 \tag{2.50}$$

While the charge has an intuitive physical meaning, the scaling dimension's significance is less transparent. As it is directly linked to the particle correlation function at the same position, it can be physically pictured as a parameter that controls the decay of self-correlations with time. If the edge structure has a single chirality (i.e. all the modes propagate in the same direction like at $\nu = 1/3$ and $\nu = 2/5$), Δ is also directly linked to the exchange statistics [65].

ν	N	χ_i	q_i	a_i	Δ_i	θ_i	δ_i
$1/3$	1	$+1$	$1/\sqrt{3}$	$1/\sqrt{3}$	$1/6$	$\pi/3$	$1/3$
$2/5$	2	$+1$	$1/\sqrt{15}$	$\sqrt{3/5}$	$3/10$	$3\pi/5$	$3/5$
		$+1$	$1/\sqrt{3}$	$1/\sqrt{3}$	$1/6$	$\pi/3$	$1/\sqrt{3}$

Table 2.1: Summary of parameters describing the edge state at filling factor $\nu = 1/3$ and $\nu = 2/5$. χ_i encodes the chirality of the edge state, q_i encodes the quasiparticle's charge, a_i its delocalization on the channels. Δ (or alternatively $\delta = 2\Delta$) is the scaling dimension controlling the dynamics of the edge (for instance the power-law of the I-V characteristics), and θ is the exchange phase

Recently, a proposal by Schiller *et al.* [65] suggested that Δ could be probed directly through the shot noise generated by a single QPC in the WBS regime. Indeed, by performing a complete quantum analysis, they derived an exact analytical expression in the FQHE (instead of the phenomenological expression of Eq. (2.14).

In the Laughlin case, Δ is linked to the filling factor ν, to the exchange statistics θ and to the Luttinger parameter K by the simple relations $\Delta = \nu/2 = \theta/(2\pi) = K/2$. Therefore, in principle, a simple shot noise measurement could give a strong signature of all these parameters governing the physics of edge quasiparticles in the FQHE [65]. Table 2.1 summarizes the parameters describing the edge modes for the fractional filling factors investigated in this thesis ($\nu = 1/3$ and $\nu = 2/5$).

Chapter 3

Observation of quasiparticle Andreev-like scattering in the fractional quantum Hall regime

In this chapter, we report an experimental observation of Andreev-like reflection of quasiparticles in the $\nu = 1/3$ fractional quantum Hall (FQH) regime. This represents one of the main results of this thesis, as it demonstrates a nontrivial transport process of fractional quasiparticles, predicted in 2003 by Kane and Fisher [42].

A conventional free electron impinging on a barrier can be either elastically transmitted or reflected with various probability amplitudes. In that case, the barrier can be described as a beam-splitter, analogous to the well-known optical component, playing a central role in *electron quantum optics*. However, theory predicts that this picture does not apply to the emblematic FQH anyons that impinge on a barrier favoring e-charges transfer. Instead of a conventional transmission/reflection, a fractional quasiparticle facing a high barrier can be converted into a transmitted quasi-electron together with a reflected fractional hole.

Direct signatures of such unconventional transport processes are reported in the present chapter. Section 3.1 gives a brief theoretical description of the considered system as well as Kane and Fisher's predictions. In section 3.2, we review the pioneering experiments in similar systems which gave mitigated results. The specificity of the Andreev-like scattering process is then discussed in section 3.3 by highlighting its analogies and differences with the standard Andreev reflection. Subsequently, the experimental results obtained in this thesis are presented. After a description of the sample in section 3.4, the core measurement is reported in sections 3.5, 3.6 and then confronted with results from other regimes and different settings in sections 3.7 and 3.8.

3.1 Theoretical prediction

3.1.1 Charge mismatch between an impinging quasiparticle and a tunnelling quasi-electron

In 2003, Kane and Fisher studied the process which involves an anyon quasiparticle of fractional charge e^* impinging on a barrier that favors the tunneling transmission of a quasi-electron of charge e [42] (note that in the following, "charge e" will stand for such quasielectrons).

In that case, when there is a mismatch between the incident quasiparticle and the charge naturally transmitted through the barrier, three possible processes could be considered (see Fig. 3.1):

(i) the impinging quasiparticle is transmitted through the barrier with a probability t (Fig. 3.1a) ;

(ii) the impinging quasiparticle is reflected by the barrier with a probability r (Fig. 3.1b) ;

(iii) the quasiparticle is *Andreev reflected* with probability a, i.e. one e-charged quasiparticle is transmitted while, due to charge conservation, a quasihole of charge $-(1-\nu)e$ is simultaneously reflected from the barrier. (Fig. 3.1c).

In the following, we suppose that these are the only allowed processes (i.e. $t + r + a = 1$).

The third process, coined *Andreev-like scattering* [42], is remarkably different from the beam-splitter picture of QPCs conventionally used in electron quantum optics. Indeed, with this nontrivial mechanism, the number and even the nature of quasiparticles change. Kane and Fisher predicted that this scenario (iii) applies to high barriers in the FQHE and proposed to test this picture by measuring the cross-correlations between reflected and transmitted current fluctuations.

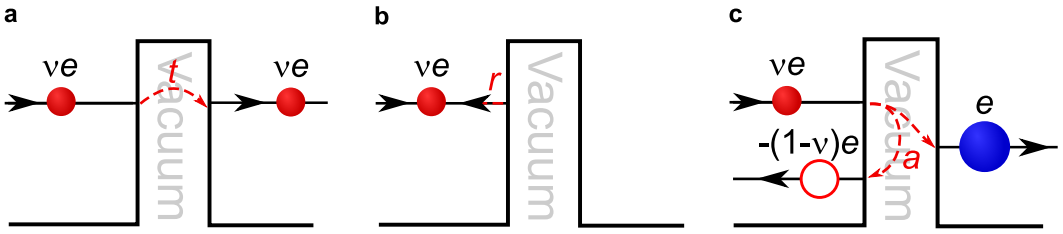

Figure 3.1: **Transfer processes on the barrier.**
a The impinging anyon is transmitted through the vacuum barrier with probability t.
b The impinging anyon is reflected upon the vacuum barrier with probability r.
c The impinging anyon is *Andreev-reflected* upon the barrier with probability a.

3.1.2 Implementation of Andreev-like scattering in the fractional quantum Hall regime

In a two-dimensional electron gas (2DEG) set at a Laughlin fractional filling factor $\nu = 1/m$, we consider two QPCs in series as presented in Fig. 3.2 [42].

The first upstream one, called the "*source*", is set in the weak backscattering (WBS) regime ($\tau_S \equiv 1 - I_S/I_{inj} \to 1$) and biased by a DC-voltage V_S^{qp}. The natural charges tunneling through this source QPC are anyons and tunneling processes are rare. Hence, the QPC creates a diluted beam of νe-charged quasiparticles.

The second downstream QPC, called the "*analyzer*", is set in the opposite strong backscattering (SBS) regime ($\tau_A \equiv I_T/I_S \to 0$), favoring the tunneling of charge e. Indeed, as the gas is essentially depleted between the two sides of the QPC, the only excitations tunneling above the vacuum will be e-charged quasiparticles [114, 115]. Therefore, this second QPC plays the role of the barrier upon which the transfer processes (i), (ii) and (iii) are considered.

In the limit of low temperature, numerical calculations performed in Ref. [42] at $\nu = 1/3$ (analytical expressions have only been derived for $\nu = 1/2$) showed that the transmission of

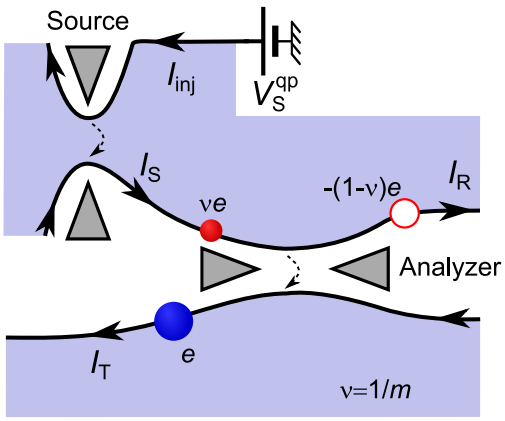

Figure 3.2: **Implementation of Andreev-like scattering with two QPCs in series in the FQH regime.**
For a Laughlin fraction $\nu = 1/m$, a diluted beam of anyons is created at the source QPC and impinges on a second downstream analyzer QPC which favors the tunneling of charge e. The dominant transport process is Andreev-like scattering i.e. the incident νe charge (red dot) will be converted into a transmitted charge e (blue dot) and a reflected quasihole of charge $-(1-\nu)e$ (open red dot)

νe-charged quasiparticles vanishes in the SBS regimes. Then, according to theory [42], the process (i) is suppressed ($t = 0$) and the only remaining allowed processes are (ii) and (iii).

Therefore, the dominant transfer mechanism through the barrier is Andreev-like scattering (with probability a), involving simultaneously a transmitted quasiparticle of charge e and a backscattered quasihole of charge $-(1-\nu)e$, illustrated in Fig. 3.1c.

3.1.3 Shot noise as the key signature of involved charges

It is important to note that the e transmission and $-(1-\nu)e$ backscattering occur simultaneously and that the two resulting current fluctuations are *correlated*. Then, measuring concomitantly the auto- and cross-correlations of current fluctuations will unambiguously give the involved charges:

- the noise created by the source QPC $S_\Sigma \equiv \langle \delta I_S^2 \rangle$ gives access to the impinging charges
- the excess auto-correlations of transmitted current $\Delta S_{TT} \equiv \langle \delta I_T^2 \rangle_{exc}$ are directly proportional to the transmitted charge across the analyzer.
- the cross-correlations between transmitted and reflected current $S_{RT} \equiv \langle \delta I_T \delta I_R \rangle$ follow, in this picture, the straightforward relation $\langle \delta I_T \delta I_R \rangle = -(1-\nu)\langle \delta I_T^2 \rangle_{exc}$, where the factor $-(1-\nu)$ directly corresponds to the ratio between the tunneling and reflected charges.

Those noise measurements are the key experimental result of this chapter.

3.2 Pioneering experiments

A pioneering experiment by Comforti *et al.*, performed before Kane and Fisher's predictions, was implemented in such a device composed of several QPCs in series [43]. In this geometry,

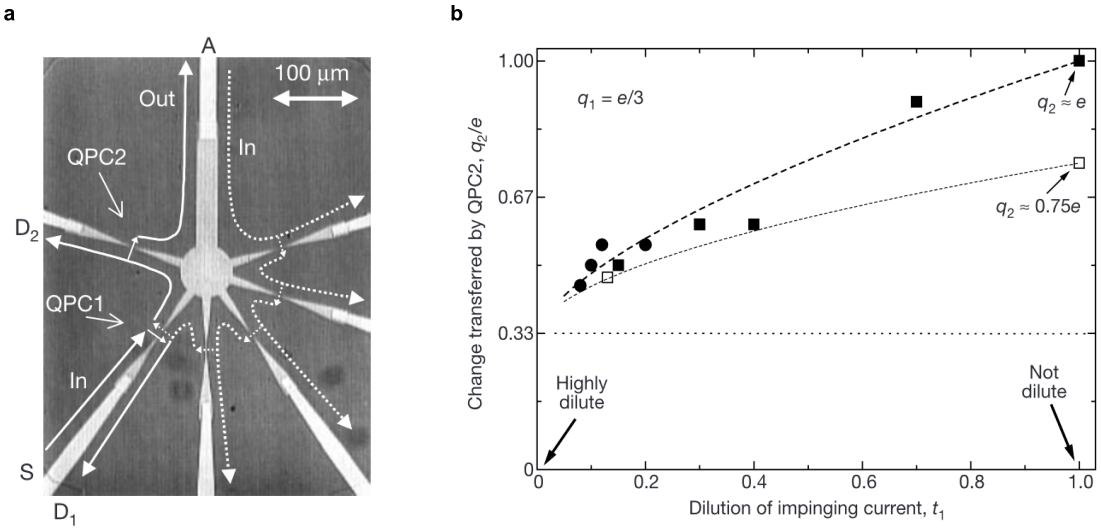

Figure 3.3: **Pioneering results from Comforti *et al.* [43].**
a SEM image of the device of Ref. [43]. The long distance between the two QPCs could explain the discrepancies with theory.
b Tunneling charge across the analyzer QPC as a function of the source transmission. The charge tends to $e/3$ for a highly diluted beam.

a source QPC in the WBS regime creates a diluted beam of $e/3$ charges that impinges on a second downstream analyzer QPC.

Nonetheless, the experimental results of this seminal work appeared to be in contradiction with the subsequent predictions of [42]. Indeed, the charges measured via auto-correlations of the current transmitted across the second downstream QPC approached $e/3$, in marked contrast with the charge e predicted by [42] see Fig. 3.3b.

To explain this unexpected behavior, Kane and Fisher argued that the observed $e/3$ transferred charge could be an effect of the finite operating temperature ($T = 65$ mK) whereas with a further decreases in temperature, the charge could potentially return to e, in agreement with the $T = 0$ K theory. Moreover, one could imagine that the very long propagation distance of ~ 100 µm between the two QPCs in these experiments could alter the $e/3$ quasiparticles and explain such deviations.

A following experiment [116] mitigated these results by studying the charge transmitted by the second QPC as a function of its transmission t_2 (the transmission of the first QPC being labeled by t_1). As the temperature is reduced, the result of this study showed a trend between charges $e/3$ in the WBS regime and charges e in the SBS regime (see Fig. 3.4).

Finally, these measurements only probed the charges transmitted through the second "analyzer" QPC by measuring the auto-correlations of the transmitted current. But, as emphasized by [42], a key feature of Andreev-like reflection processes is the fact that transmitted and reflected currents are correlated and that a signature of the simultaneously reflected quasihole can then be found in the cross-correlations between the two outgoing currents. Implementing this experiment in a setup which allows to measure cross-correlations would therefore shed new light on this apparent disagreement between the pioneering results and the follow-up theory and experiment.

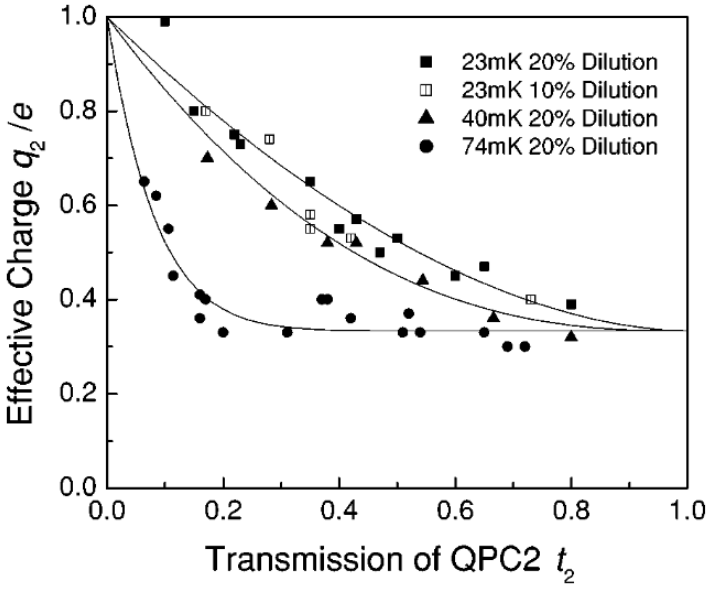

Figure 3.4: **Tunneling charge versus analyzer transmission from Chung *et al.* [116].**
For a highly diluted beam, one observes a cross-over between $e/3$ tunneling charge when the analyzer is in WBS to e tunneling charge when the analyzer is in SBS regime

3.3 Analogies and differences with standard Andreev reflection

The Andreev-like scattering process predicted in FQH regime [42] involves the transmission of a quasiparticle as well as the backscattering of a quasihole, which naturally leads to a direct analogy with the standard Andreev reflection (AR) [117]. However, important differences between AR and its quantum Hall analogs are stressed in this section.

3.3.1 Standard Andreev reflection

In the conventional Andreev reflection, predicted in 1964 [117, 118] and widely observed since then (see [119] for a review), a direct bias provides incident electrons of charge $Q_i = e$, momentum k_i and finite energy E_i, which flows within a normal-state metal (labeled N) and faces an interface with a s-wave superconducting region (labeled S). As the superconducting gap forbids the transmission of electrons through the interface, the impinging charge e is converted into a zero-energy Cooper pair (of charge $Q_t = 2e$) in the S region and into a simultaneously backscattered hole of charge $Q_r = -e$, momentum $k_r = -k_r$ and energy $E_r = E_i$ (see Fig. 3.5). Charge, momentum, and energy conservation are therefore ensured by this process, at Fermi energy E_F.

Moreover, the two electrons forming the spin-singlet Cooper-pair have opposite spins. Hence, spin conservation imposes that the incident electron with spin up (down) is converted into a reflected hole with spin down (up) and a Cooper-pair of spin up|down (down|up). This impor-

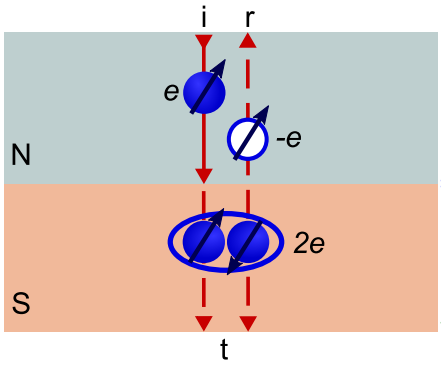

Figure 3.5: **Standard Andreev reflection principle.**
At an interface between a normal (N) and a superconducting (S) region, an electron (blue disc) from a non-diluted incident beam is converted into a Cooper pair (encircled pair of blue dots) in the S region and a backscattered hole (open blue dot) in the N region. The incident, transmitted, and reflected paths followed by excitations are represented by red lines with arrows and are respectively labeled as 'i', 't', and 'r'.

tant remark implies that Andreev reflection will be inhibited in a fully spin-polarized system because Cooper pairs cannot form in the S region. Note that the spin up (down) of a hole corresponds to a spin down (up) of an electron and both are displayed as up arrows in Fig 3.2.

3.3.2 Andreev-like reflection in a Quantum Hall interface

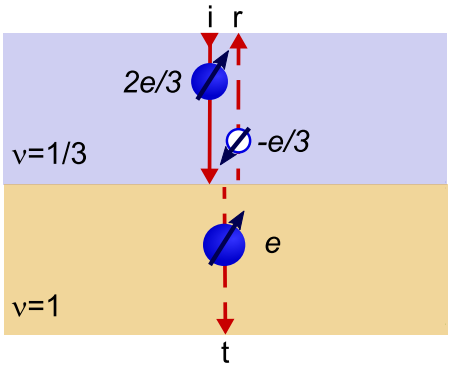

Figure 3.6: **Andreev-reflection process in the Quantum Hall regime.**
At an interface between a $\nu = 1/3$ and a $\nu = 1$ region, a pair of anyons from an incident non-diluted beam converts into a transmitted charge e and a backscattered quasihole $-e/3$. The incident, transmitted, and reflected paths followed by excitations are represented by red lines with arrows and are respectively labeled as 'i', 't', and 'r'.

Recently, an analog of the standard AR but different from the one predicted by [42] has been implemented in AlGaAs|GaAs [120] and graphene [107], following predictions of the 1990s [85, 121]. In that case, an interface between a $\nu = 1/3$ and a $\nu = 1$ region is formed by metallic gates locally controlling the gas density. A charge $Q_i = 2e/3$ from a full incident beam in the $\nu = 1/3$ region is converted into an electron transmitted in the $\nu = 1$ region and a backscattered quasihole of charge $Q_r = -e/3$ in the $\nu = 1/3$ region (see Fig. 3.6). In

such systems, the Andreev-like scattering manifests itself as excess conductance $G > \nu e^2/h$ [120, 107].

Importantly, in that case, the process involves quasiparticles of different nature and charges, and the energy E_i of the incident quasiparticles redistributes into the outgoing electron and quasihole of lower energies:

$$E_i > E_t, E_r \tag{3.1}$$
$$Q_i \neq Q_r, Q_t \tag{3.2}$$

Furthermore, due to the magnetic field necessary for the QHE, the system is fully spin-polarized (all excitation in the system will have the same spin).

3.3.3 Andreev-like scattering at a barrier in the FQHE

The process predicted by Kane and Fisher and described in the first section is different from these two previous processes. Indeed, Andreev-like scattering in that case does not involve an interface between two regions with different filling factors (see Fig. 3.7). Moreover, this process requires a *diluted* impinging beam in order to avoid several quasiparticles combining into a bigger charge. Finally like in the previous case, the involved excitations do not have the same nature, the same charge (in absolute value) nor the same energies but have the same spin (because the system is spin-polarized).

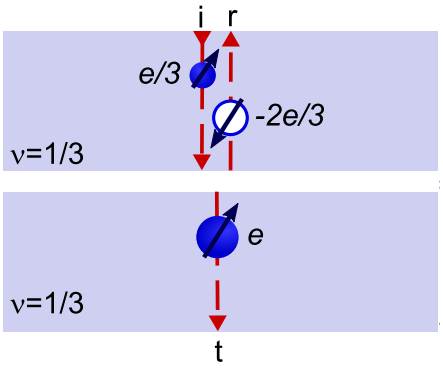

Figure 3.7: **Andreev-like scattering at a barrier in FQH regime.**
In a system set at $\nu = 1/3$ without interface, an $e/3$ charged anyon impinging on a barrier favoring the transmission of e-charged quasiparticles results into a transmitted quasi-electron of charge e and a backscattered quasi-hole of charge $-2e/3$. The incident, transmitted, and reflected paths followed by the excitations are represented by red dashed lines with arrows and are respectively labeled as 'i', 't', and 'r'.

Table **??** summarizes the analogies and differences between the three different processes.

3.4 Experimental device

3.4.1 Description of the sample

The sample to test *Andreev-like reflection* was patterned by e-beam lithography on a high-mobility AlGaAs|GaAs heterostructure, forming a two-dimensional electron gas (2DEG) of

Process	Standard AR	AR-like at an IQHE-FQHE interface	AR-like at a barrier in the FQHE
Beam	indifferent	indifferent	diluted
Charges	$Q_i = -Q_r, Q_t = 2e$	$Q_i \neq -Q_r, Q_t$	$Q_i \neq -Q_r, Q_t$
Energies	$E_i = E_r, E_t = 0$	$E_i > E_t, E_r$	$E_i > E_t, E_r$
Spin	two-spin system	one-spin system	one-spin system

Table 3.1: Summary of the analogies and differences between the three Andreev and Andreev-like processes

density $n = 1.2 \times 10^{11}$ cm^{-2} and mobility $\mu = 1.8 \times 10^{6}$ cm^2 V^{-1} s^{-1}, buried 140 nm below the surface. Details about the nanofabrication process are given in Appendix A. The device geometry is presented in Fig. 3.8 at large scale (optical image in panel (a)) and small scale (SEM picture in panel (b)).

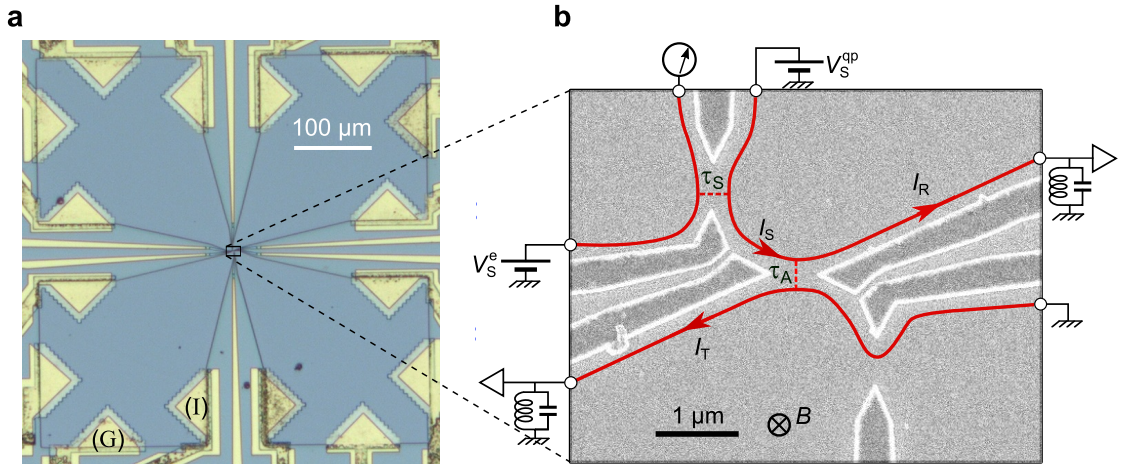

Figure 3.8: **Image of the sample.**
a Large-scale optical picture of the device. Au-Ge-Ni ohmic contacts appear as large triangles. The two contacts used for the Hall resistance measurement (see Fig. 3.9) are labeled (I) and (G). Split gates are shown as straight yellowish lines in the middle of each side of the picture.
b Scanning electron microscope (SEM) image of the measured Ga(Al)As sample. Aluminum gates (darker with bright edges) defining QPCs are tuned by field effect. The current flows along chiral edge channels displayed as red lines. The source is biased with V_S^{qp} at $V_S^e = 0$ and $1 - \tau_S \ll 1$ (V_S^e at $V_S^{qp} = 0$ and $\tau_S \ll 1$), producing a Poissonian beam of fractionally charged quasiparticles $I_S = (1 - \tau_S)V_S^{qp}/R_H$ (of quasi-electrons $I_S = \tau_S V_S^e/R_H$).

The device is cooled down to $T \simeq 35$ mK and immersed in a strong perpendicular magnetic field $B \simeq 13.5$ T. The quantum Hall resistance $R_H = 3h/e^2$ corresponds to the aimed Laughlin's fraction $\nu = 1/3$ (see Fig. 3.9).

At this fraction, the current flows chirally into a single edge channel displayed as red continuous lines in Fig. 3.8b. The edge biases are set and measured thanks to large ohmic contacts of negligible resistance, positioned $\simeq 150$ µm away from the central region and represented by black circles on Fig. 3.8b.

In the central region, the heart of the sample consists of three QPCs, made with pairs of aluminum gates deposited at the surface of the sample (darker areas with bright edges on Fig. 3.8b). Each gate acts on the gas by field effect with an applied DC-voltage V_g. The outer (top-left or alternatively bottom-right) QPCs are independently used as sources of diluted νe anyons, impinging on the downstream QPC, playing the role of the analyzer. For the observation of the *Andreev-like reflection* process, only one source is used at a time, the other allowing to check the reproducibility of the results.

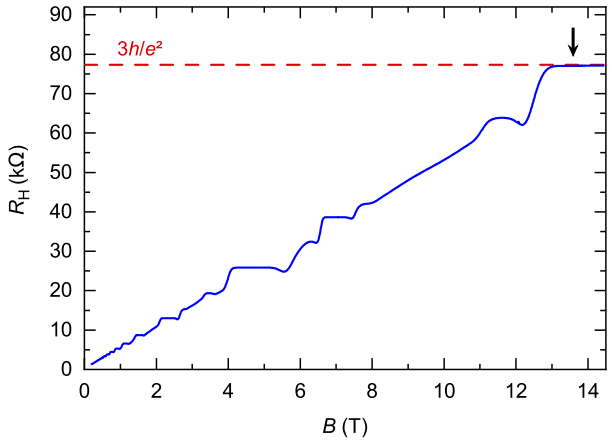

Figure 3.9: **Quantum Hall transverse resistance plateaus.**
Two-wire resistance between an ohmic contact and cold grounds (respectively labeled (I) and (G) on Fig. 3.8) measured as a function of the applied perpendicular magnetic field B at low temperature ($T \sim 100$ mK). All QPCs are fully pinched off during this B sweep. The red dashed line denotes the resistance of the used plateau and its value $R_H = 3h/e^2$ corresponds to the Laughlin fraction $\nu = 1/3$. The black arrow indicates the value of B chosen for the measurements.

3.4.2 QPC characterizations

Quantum point contact transmissions are set by applying a voltage on the gates, which depletes the buried gas by field effect. The complete crossover between fully closed and fully open QPCs can therefore be obtained by sweeping the gate voltage as presented in Fig. 3.10. This figure displays the current transmission ratio as a function of the gate voltage for the applied bias $V_{DC} = 0$ (black line) and $V_{DC} \simeq 40$ µV (red line). The SBS and WBS regimes are implemented in the vicinity of the black arrows.

Note that the actual settings of each QPC have an impact on the others. Due to this capacitive 'cross-talk' between gates (separately calibrated), the gate tuning procedure for the source QPCs and the analyzer central QPCs are chosen to be slightly different. Indeed, the central 'analyzer' profile (Fig. 3.10c) is obtained by sweeping simultaneously both gates of the QPC, in order to keep the left and right edges as identical as possible. By contrast, for the source top-left (bottom-right) QPC, only the upper (lower) gate is swept (Fig 3.10a and b respectively), in order to reduce the cross-talk to the central analyzer QPC.

As frequently observed for fractional filling factors [48, 58], the transmission profiles present resonances that make it challenging to maintain the QPCs stable, especially in the SBS regime

where the voltage dependence of the transmission is the most important [115, 114, 56]. Intriguingly, the gate voltage required to fully close the central QPC is significantly more negative than the two other source QPCs, in spite of a very similar geometry. This different behavior is systematically observed for other devices on the same chip. It could be due to the different orientation of the central QPC with respect to the underlying GaAs crystal, and to a mechanical strain caused by the metallic gates.

Moreover, we observe that the DC-voltage dependence changes its monotonicity at $\tau \sim 0.8$. Thus, in the WBS regime, τ monotonously decreases with the DC-bias $|V|$. This behavior at high transmission, though also observed in other labs [122], is not expected by theory [115, 100] and remains puzzling.

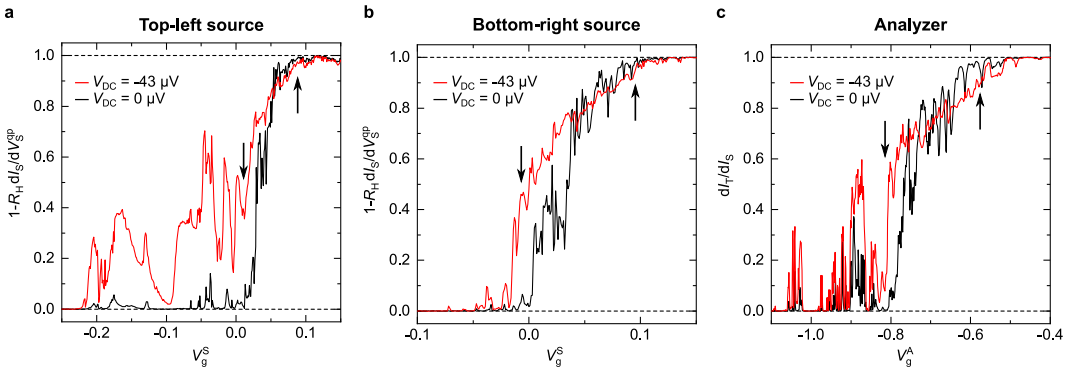

Figure 3.10: **Transmission profiles of the QPCs.**
a (**b**) Differential top-left (bottom-right) source transmission ratio $1 - R_{\mathrm{H}} \mathrm{d}I_{\mathrm{S}}/\mathrm{d}V_{\mathrm{S}}^{\mathrm{qp}}$ as a function of the voltage $V_{\mathrm{g}}^{\mathrm{S}}$ applied to the source QPC gate that is farthest from the analyzer QPC.
c Analyzer differential transmission ratio $\mathrm{d}I_{\mathrm{T}}/\mathrm{d}I_{\mathrm{S}}$ versus gate voltage $V_{\mathrm{g}}^{\mathrm{A}}$ symmetrically applied to both analyzer QPC gates. The black and red continuous lines correspond to measurements in the presence of a direct DC-voltage bias $V_{\mathrm{S}}^{\mathrm{qp}} = V_{\mathrm{S}}^{\mathrm{e}} = 0$ µV and -43 µV, respectively. The arrows indicate the approximate working points in the SBS (down arrows) and WBS (up arrow) regimes during measurements.

3.5 Charge transmitted across individual voltage-biased QPCs

Observing the Andreev-like scattering process at $\nu = 1/3$ requires first to ensure that the source and analyzer QPCs are actually set in the WBS and SBS regimes respectively, transmitting corresponding $e/3$ and e charges. This is done by standard shot noise measurements [10, 11], involving a direct DC-voltage bias of the considered QPC.

3.5.1 Analyzer QPC characterization

The analyzer QPC is set in the strong backscattering regime, i.e. at low transmission $\tau_{\mathrm{A}} \equiv I_{\mathrm{T}}/I_{\mathrm{S}} \ll 1$. To ensure that the tunneling charge across this barrier is e, as predicted by theory [114, 115], a specific measurement must be performed. Without changing any gate voltage that could impact the QPCs tuning, the same DC-voltage $V_{\mathrm{S}}^{\mathrm{e}} = V_{\mathrm{S}}^{\mathrm{qp}}$ is applied on both

sides of the source QPC (see Fig. 3.11a). By doing so, the source remains unbiased while the analyzer is put under the DC-voltage $V_S^e = V_S^{qp}$.

Figure 3.11c displays the noise measured in this configuration. Blue dots correspond to transmitted (full symbols) and reflected (open symbols) excess auto-correlation noises respectively defined as:

$$\Delta S_{TT} \equiv \langle \delta I_T^2 \rangle - \langle \delta I_T^2 \rangle (V_S^{qp} = V_S^e = 0) \tag{3.3}$$

$$\Delta S_{RR} \equiv \langle \delta I_R^2 \rangle - \langle \delta I_R^2 \rangle (V_S^{qp} = V_S^e = 0) \tag{3.4}$$

Green dots display the cross-correlation shot noise $S_{RT} \equiv \langle \delta I_T \delta I_R \rangle$ between the two outgoing leads. The sum $S_\Sigma \equiv \Delta S_{TT} + \Delta S_{RR} + 2S_{RT}$ is depicted as black triangles.

These noise signals are confronted with the standard phenomenological shot noise expression [123, 124]:

$$S_{sn} = 2e^* \frac{\tau(1-\tau)V}{R_H} \left[\coth \frac{e^*V}{2k_BT} - \frac{2k_BT}{e^*V} \right] \tag{3.5}$$

where τ is the ratio of transmitted over incident DC-current (in this case $\tau = \tau_A$) and $R_H = 3R_K$ is the Hall resistance at filling factor 1/3. This phenomenological equation is the most robust for $e^*V \ll k_BT$ in the Poissonian regime ($\tau \ll 1$ or $1-\tau \ll 1$) but also holds at intermediate transmissions [124]. The positive lines in Fig. 3.11c correspond to S_{sn} predicted by Eq. (3.5) for $e^* = e$ (blue) and $e^* = e/3$ (red), at $T = 35$ mK and using the simultaneously measured transmission τ_A (Fig. 3.11b). Similarly, the negative blue line depicts -S_{sn} for $e^* = e$.

As expected and usually observed in such systems [42, 115, 114, 56], τ_A markedly increases with voltage (see Fig. 3.11b) which can lead to a crossover between $e^* = e$ at low τ_A and $e^* = e/3$ at high τ_A [56]. Accordingly, we find good agreement with $e^* = e$ for bias lower than 35 µV, corresponding to $\tau_A \lesssim 0.3$. Note that during Andreev-like scattering measurements, the impinging beam on the analyzer is diluted so the analyzer is slightly biased and remains in the SBS regime ($\tau_A \lesssim 0.3$).

Note that an important experimental verification consists of checking that S_Σ does not depend on the bias and remains zero (which is equivalent to checking that the three noise signals are equal in absolute value). Indeed, some unexplained discrepancies have been observed in similar devices between auto- and cross-correlation signals in FQHE [125], which could weaken our conclusions. In our case, we find that ΔS_{TT}, ΔS_{RR} and S_{RT} match each other at our experimental gain calibration accuracy. The found $e^* = e$ charge is therefore corroborated by the three noise signals.

Thus, this separate characterization, performed without changing the tuning of the system, consistently shows that the excitations naturally transmitted through the voltage-biased analyzer QPC are e-charged quasiparticles.

3.5.2 Source QPC characterization

The charge emitted by the sources also has to be characterized to ensure that the beam impinging on the analyzer is indeed a diluted beam of $e/3$ quasiparticles.

This is done simultaneously with the main Andreev-like scattering measurement. Indeed, without changing any gate voltage nor the voltage applied on either lead, one can have access to the shot noise created by the source alone at all times thanks to the current conservation:

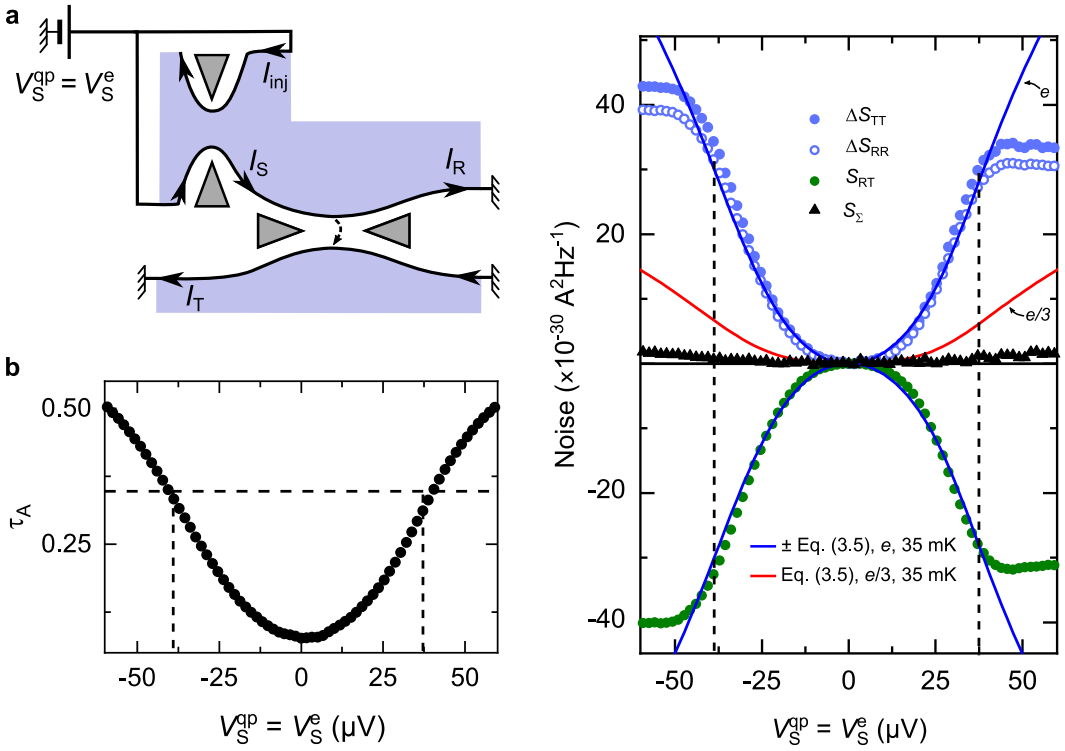

Figure 3.11: **Characterization of analyzer QPC, from transmission (b) and noise (c) vs direct voltage bias.**
a Specific configuration of the device for this characterization. The same voltage $V_S^{qp} = V_S^e$ is applied on both sides of the source QPC so that the analyzer is directly biased.
b Transmission ratio $\tau_A = I_T/I_S$. Dashed black lines indicate the current window (±36 pA) of SBS, for which $\tau_A \lesssim 0.3$ (before deviations away from the SBS regime).
c Auto- and cross-correlations of the transmitted (I_T) and reflected (I_R) currents. For small enough $\tau_A \lesssim 0.3$ (see dashed lines), the three noise signals match the expected tunneling charge e (blue lines) in marked contrast to $e/3$ (red line). The noise sum S_Σ, corresponding to the excess shot noise across the unbiased source, remains negligible.

$$I_S = I_T + I_R \tag{3.6}$$

Then, the shot noise created by the source QPC $\langle \delta I_S^2 \rangle$ is:

$$\langle \delta I_S^2 \rangle = \langle \delta I_T^2 \rangle_{exc} + \langle \delta I_R^2 \rangle_{exc} + 2\langle \delta I_T \delta I_R \rangle = S_\Sigma \tag{3.7}$$

Therefore, the previously defined S_Σ is exactly the shot noise across the voltage-biased source, which gives access to the charge emitted by the source through Eq. (3.5).

Figure 3.12 presents typical left and right source shot noise measurements. The individually considered source QPC is set in the WBS regime ($\tau_S \to 1$ see insets) and biased with the DC-voltage V_S^{qp} (while $V_S^e = 0$). The measured shot noise displayed in the main panels of Fig. 3.12 is compared with predictions of Eq. (3.5) depicted as continuous lines. At $T = 35$ mK, a good

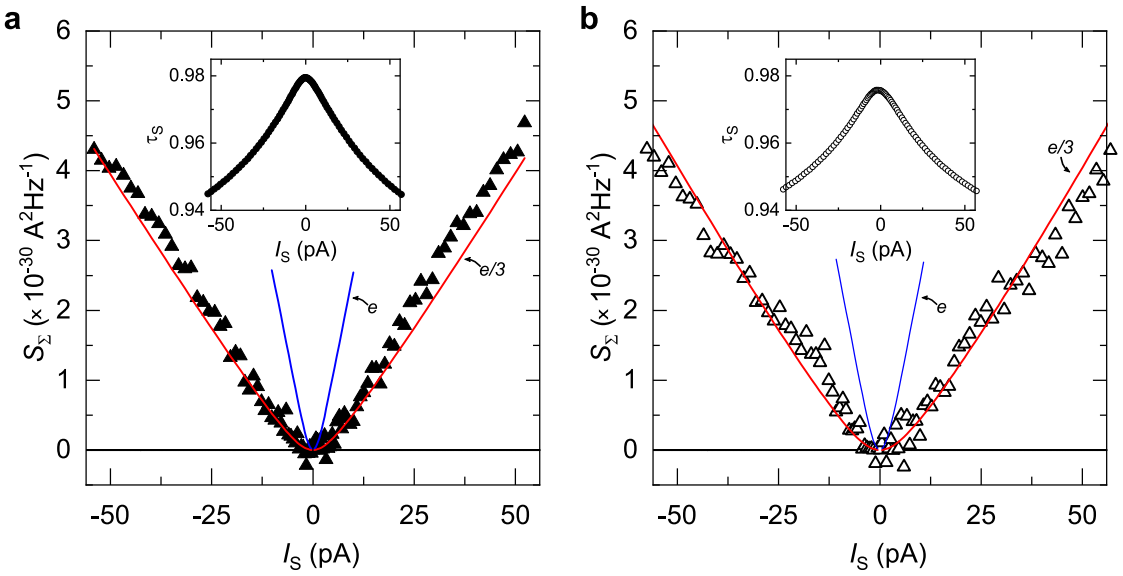

Figure 3.12: **Characterization of the charge emitted by the left (a) and the right (b) sources.**
a (b) Total noise signal S_Σ versus the current transmitted across the left (right) QPC source plotted as symbols. Continuous blue and red lines display the shot noise predictions of Eq. (3.5) for charge e and $e/3$ transfers respectively, using the measured transmission ratio τ_S across the considered source QPC (inset) and $T = 35$ mK.

agreement is found for $e^* = e/3$ (red line), while a strong discrepancy is observed for $e^* = e$ (blue line).

3.6 Observation of Andreev-like reflection of fractional quantum Hall quasiparticles

Let us turn to the investigation of the transport process of a diluted beam of $e/3$ quasiparticles across the downstream analyzer set in the SBS regime, favoring quasi-electron tunneling. In this section, the shown data correspond to the top-left source [1].

Figure 3.13 shows the noise signals as a function of the incident current I_S (panel (c)) and the simultaneously measured sum S_Σ (panel (b)) informing on the charge emitted by the source, as explained in the previous section. The operating configuration is schematized in the top panel (a). Note that the range of transmitted current I_T in Fig. 3.13b corresponds to that of impinging current I_S used in Fig. 3.13c ($I_T = \tau_A I_S$). The corresponding transmissions $\tau_S \to 1$ and $\tau_A \to 0$ of the source and analyzer QPCs during the measurements are respectively plotted in the insets of panels (b) and (c).

Symbols in Fig. 3.13 display noise data as well as the following phenomenological expectation in the dilute limit for charge e^* and temperature T represented by dashed lines:

$$S = 2e^* I_T \left[\coth \frac{e^*_S V^{qp}_S}{2k_B T} - \frac{2k_B T}{e^*_S V^{qp}_S} \right], \tag{3.8}$$

[1] consistent results have been obtained with the bottom-right source

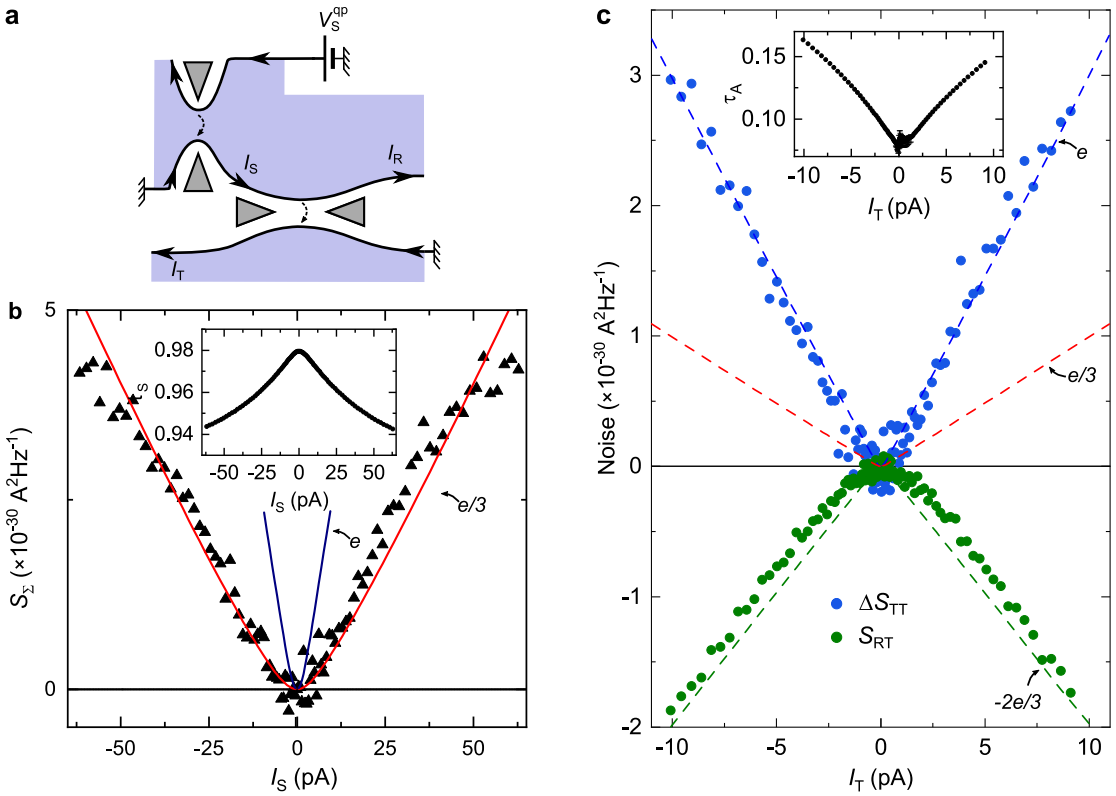

Figure 3.13: **Noise observation of the Andreev-like reflection.**
a Device configuration during the measurement.
b Simultaneous characterization of the charge emitted by the left source in the WBS regime (see Fig. 3.12).
c Transport process across the analyzer QPC with impinging $e/3$ quasiparticles. Blue and green dots display respectively the excess auto-correlations of the transmitted current and the cross-correlations between the transmitted and reflected currents. Dashed blue, red, and black lines show respectively $1e$, $e/3$, and $-(2/3) \times 1e$ shot noise predictions in the dilute incident beam limit. Inset displays the analyzer transmission τ_A with vertical error bars (when larger than the symbol size) corresponding to the standard error over the multiple sweeps.

Note that this formula corresponds to Eq (3.5) using $1-\tau = 1-\tau_A \simeq 1$, and $\tau\dfrac{V}{R_H} = \tau_A\dfrac{(1-\tau_S)V_S^{qp}}{R_H} = I_T$. The thermal rounding is associated with the source excitations of charge e_S^*.

Blue dots in Fig. 3.13c depict ΔS_{TT} the excess auto-correlations of the current transmitted across the analyzer, in good agreement with the $2e|I_T|$ slope (blue line) predicted for a Poissonian tunneling of charge e, different from the $e/3$ injected quasiparticles. This is in agreement with the prediction of the Andreev processes. By contrast, this result is markedly different from the $2e/3|I_T|$ slope (red line) denoting the Poissonian transfer of $e/3$ charges seen in the seminal work of Comforti *et al* [43].

Green dots display the simultaneously measured *negative* cross-correlations, closely following the slope of $-(2/3)2e|I_T|$. As stressed by [42], this provides an unambiguous signature of Andreev-like processes occurring on the analyzer QPC. Indeed the transmitted and reflected

currents resulting from the Andreev-like scattering are *correlated* because each transfer is directly related to a single simultaneously reflected $-2e/3$ quasihole. Therefore, one gets the straightforward connection

$$S_{\mathrm{RT}} = -(2/3)\Delta S_{\mathrm{TT}} \tag{3.9}$$

where the $-(2/3)$ prefactor is precisely the ratio between the transmitted and the backscattered charges.

To sum up, the predicted Andreev-like mechanism is directly and unambiguously confirmed by the auto-correlations of transmitted current denoting transfer of e-charges and by the simultaneously measured cross-correlations between reflected and transmitted currents denoting $-2(e/3)$ backscattered quasiholes.

3.7 Tuning the QPCs in other regimes

To underline the specificity of the Andreev signatures studied in the previous sections, it is instructive to tune the system into configurations where the source or analyzer QPCs are set to other regimes. The following sections present the results of these counterpoint measurements.

3.7.1 Incident e-charges upon a barrier in the SBS regime

First, we specifically change the regime of the source QPC. By tuning it to the SBS regime, the charge of incident quasiparticles will be e (see schematics in Fig. 3.14a), in contrast with the $e/3$ impinging quasiparticles of the previous section. In the Büttiker picture where the charge carriers are simple non-interacting electrons, let us determine the expected auto- and cross-correlations of currents in the leads outgoing from the analyzer QPC.

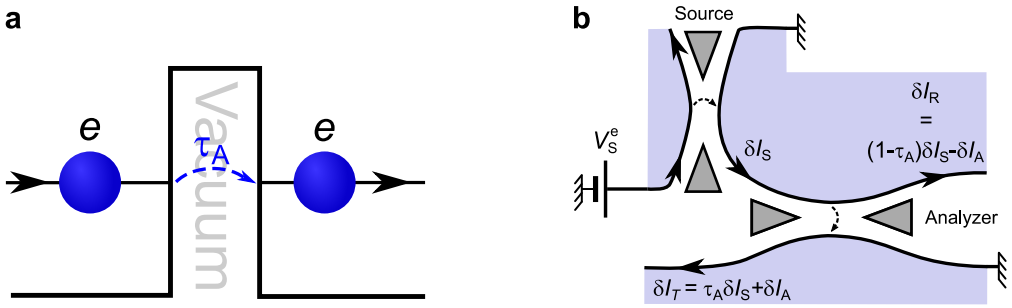

Figure 3.14: **Configuration with both QPCs in the SBS regime.**
a Principle: an incident beam of e-charged particles impinges on a barrier which favors the tunneling of e-charges.
b Schematics of the device in the SBS-SBS regime. For clarity, only fluctuations of current are indicated. The source QPC is biased by a DC-voltage V_{S}^{e}, creating downstream current fluctuations δI_{S}. The second analyzer QPC adds supplementary δI_{A} current fluctuations, resulting in $\delta I_{\mathrm{T}} = \tau_{\mathrm{A}}\delta I_{\mathrm{S}} + \delta I_{\mathrm{A}}$ and $\delta I_{\mathrm{R}} = (1-\tau_{\mathrm{A}})\delta I_{\mathrm{S}} - \delta I_{\mathrm{A}}$ fluctuations of transmitted and reflected currents respectively.

Theoretical prediction in the Büttiker picture for incident electrons

In the case of two QPCs in series set in the SBS regime as schematized in Fig. 3.14b, the upstream source QPC creates current fluctuations $\delta I_{\rm S}$ and the downstream analyzer QPC creates current fluctuations $\delta I_{\rm A}$. The total fluctuations of transmitted and reflected currents outgoing from the analyzer will therefore respectively be:

$$\delta I_{\rm T} = \tau_{\rm A}\delta I_{\rm S} + \delta I_{\rm A} \tag{3.10}$$
$$\delta I_{\rm R} = (1-\tau_{\rm A})\delta I_{\rm S} - \delta I_{\rm A} \tag{3.11}$$

with $\tau_{\rm S}$ the transmission of the source and $\tau_{\rm A}$ the transmission of the analyzer. One can deduce the cross-correlation of the reflected and transmitted currents $S_{\rm RT} \equiv \langle \delta I_{\rm R}\delta I_{\rm T}\rangle$:

$$S_{\rm RT} = \tau_{\rm A}(1-\tau_{\rm A})\langle \delta I_{\rm S}^2\rangle - \langle \delta I_{\rm A}^2\rangle \tag{3.12}$$

with the term proportional to $\langle \delta I_{\rm S}\delta I_{\rm A}\rangle$ being zero because the fluctuations $\delta I_{\rm S}$ and $\delta I_{\rm A}$ are uncorrelated. Let us derive these two terms.

As the noise $\langle \delta I_{\rm A}^2\rangle$ is the sum of the shot noise due to the effective transmission $\tau_{\rm A}\tau_{\rm S}$ of two QPCs in series and the (negative) redistribution of the source noise at the downstream QPC, we get:

$$\langle \delta I_{\rm A}^2\rangle = 2e(1-\tau_{\rm A}\tau_{\rm S})I_{\rm T}\left[\coth\frac{eV_{\rm S}^{\rm e}}{2k_{\rm B}T} - \frac{2k_{\rm B}T}{eV_{\rm S}^{\rm e}}\right] - \tau_{\rm A}^2\langle \delta I_{\rm S}^2\rangle \tag{3.13}$$

and therefore combining equations 3.12 and 3.13 gives:

$$S_{\rm RT} = \tau_{\rm A}\langle \delta I_{\rm S}^2\rangle - 2e(1-\tau_{\rm A}\tau_{\rm S})I_{\rm T}\left[\coth\frac{eV_{\rm S}^{\rm e}}{2k_{\rm B}T} - \frac{2k_{\rm B}T}{eV_{\rm S}^{\rm e}}\right] \tag{3.14}$$

Knowing the expression for $\tau_{\rm A}\langle \delta I_{\rm S}^2\rangle = 2e(1-\tau_{\rm S})I_{\rm T}\left[\coth\frac{eV_{\rm S}^{\rm e}}{2k_{\rm B}T} - \frac{2k_{\rm B}T}{eV_{\rm S}^{\rm e}}\right]$, we deduce from Eq. (3.12) and (3.13) the complete expression of the cross-correlations:

$$\boxed{S_{\rm RT} = -2eI_{\rm T}(1-\tau_{\rm A})\tau_{\rm S}\left[\coth\frac{eV_{\rm S}^{\rm e}}{2k_{\rm B}T} - \frac{2k_{\rm B}T}{eV_{\rm S}^{\rm e}}\right]} \tag{3.15}$$

Similarly the excess auto-correlations of the transmitted current $\Delta S_{\rm TT} \equiv \langle \delta I_{\rm T}^2\rangle$ are:

$$\Delta S_{\rm TT} = \tau_{\rm A}\langle \delta I_{\rm S}^2\rangle + \langle \delta I_{\rm A}^2\rangle \tag{3.16}$$

and using Eq. (3.14) and (3.13) leads to:

$$\boxed{\Delta S_{\rm TT} = 2eI_{\rm T}(1-\tau_{\rm A}\tau_{\rm S})\left[\coth\frac{eV_{\rm S}^{\rm e}}{2k_{\rm B}T} - \frac{2k_{\rm B}T}{eV_{\rm S}^{\rm e}}\right]} \tag{3.17}$$

In the Poissonian regime $\tau_{\rm A}, \tau_{\rm S} \ll 1$, we therefore expect vanishing cross-correlations: $S_{\rm RT} \to 0$, by contrast with the strong negative cross-correlations of the Andreev-reflection case.

Noise signal with incident e-charges

In the configuration with both QPCs in the SBS regime, the source is biased by V_S^e (while $V_S^{qp} = 0$) to create a diluted beam of e-charges. The source shot noise obtained from S_Σ is plotted in Fig. 3.15b as full (open) symbols for $\tau_S \leq 0.3$ ($\tau_S \geq 0.3$). For low enough transmissions $\tau_S \leq 0.3$ (see inset), it matches with the predictions of Eq. (3.5) for $e^* = e$ and $T = 35$ mK displayed as continuous blue line, whereas it is in marked contrast with $e^* = e/3$ (red line). Note that the analyzer was separately characterized like in section 3.5.1 and gave very similar results.

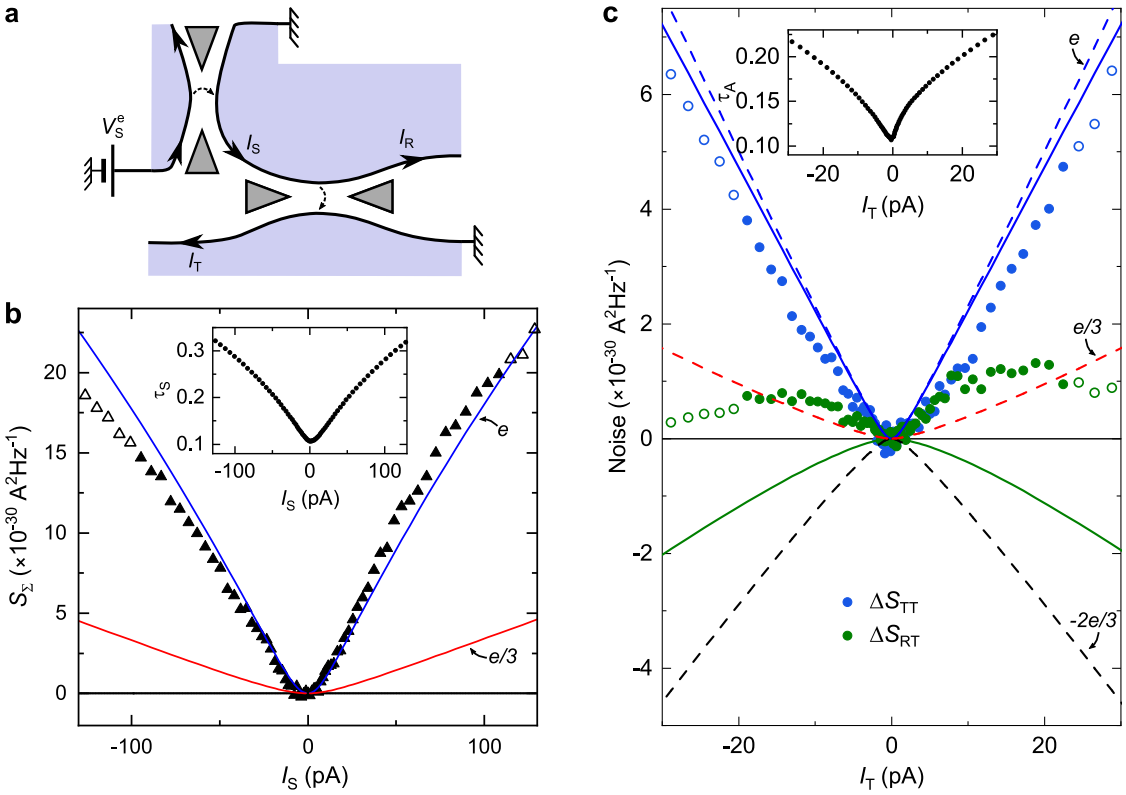

Figure 3.15: **Noise signal with incident e-charges.**
a Device configuration during the measurement.
b Simultaneous characterization of the charge emitted by the left source in the WBS regime, giving good agreement with e predictions
c Auto- (blue dots) and cross-correlations (green dots) noise signals. The blue, red, and black dashed lines display respectively shot noise with $1e$, $e/3$, and $-(2/3)e$ all in the Poissonian limit. Continuous lines display the free-electron predictions of ΔS_{TT} (Eq. (3.17), blue) and S_{RT} (Eq. (3.15), green)

Fig. 3.15 shows the simultaneously measured noise signal as full ($\tau_S \leq 0.3$) and open $\tau_S \geq 0.3$ dots. Auto-correlations of transmitted currents ΔS_{TT} displayed as blue dots reveal e-charges transmitted by the analyzer, which here trivially corresponds to the incident charges. Whereas this auto-correlation signal is similar to that of the previously discussed Andreev processes, the cross-correlations are markedly different. Indeed, S_{RT} is no longer strongly negative but positive and relatively small. For $T = 35$ mK, the non-interacting electron predictions of equations (3.15) and (3.17) are shown as continuous green and blue lines respectively. Note

that, due to the strongly increasing τ_S (inset of Fig. 3.15b), the predicted S_{RT} signal for free electrons is noticeably negative, and not zero as expected in the Poissonian limit. The observed small positive cross-correlations therefore suggest the important role of interactions in such systems (see Chapter 6 for a dedicated study of the role of interactions at $\nu = 2$ and Refs. [126, 127, 128] for predictions and pioneering experiments in IQHE regime). This makes the contrast with the strong negative Andreev signal even more remarkable.

Thus, by showing a cross-correlation signal strikingly different from that of the Andreev regime, the case of an incident beam of e-charges offers an interesting counterpoint clarifying the specificity of the Andreev-like reflections signatures.

3.7.2 Incident e-charges on a barrier in the WBS regime

One can also investigate the regime opposite to that of Andreev-like scattering, with an incident beam of electrons impinging on a barrier favoring the tunneling of $e/3$-quasiparticles. In this configuration, the source has to be set in the SBS regime and the analyzer in the WBS regime.

Naive picture of the expected transport mechanism across the analyzer

Although no specific theoretical predictions have been made in this particular configuration, a naive picture using charge conservation (similar to the Andreev-like scattering predictions of Kane and Fisher [42]) leads us to expect a similar transport process: the concomitant transfer of charge $e/3$ and backscattering of charge $+(2/3)e$ (see Fig. 3.16). Therefore, the shot noise signatures of such processes are:

- auto-correlations of transmitted current proportional to the charge $e/3$, i.e. $\Delta S_{TT} = 2(e/3)I_T \left[\coth \frac{eV_S^{qp}}{2k_BT} - \frac{2k_BT}{eV_S^{qp}}\right]$
- cross-correlations between the reflected and transmitted currents given by the ratio between the reflected and transmitted charges i.e. $S_{RT} = 2(2e)I_T \left[\coth \frac{eV_S^{qp}}{2k_BT} - \frac{2k_BT}{eV_S^{qp}}\right]$

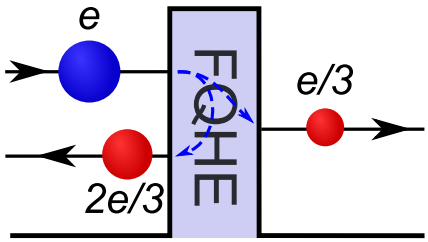

Figure 3.16: **Naively expected transport process across the analyzer QPC in the SBS-WBS regime.**
The charge $1e$ emitted by the source and impinging on a barrier favoring $e/3$ tunneling is converted into a transmitted charge $e/3$ and a simultaneously reflected quasiparticle of charge $+2e/3$.

Noise measurements in such source SBS - analyzer WBS regime

Figure 3.17 shows shot noise measurements in such a configuration. The charges emitted by the source (determined from S_Σ in panel (b)) are in good agreement with e-charge predictions (blue line), corroborating the picture of an impinging diluted beam of quasi-electrons.

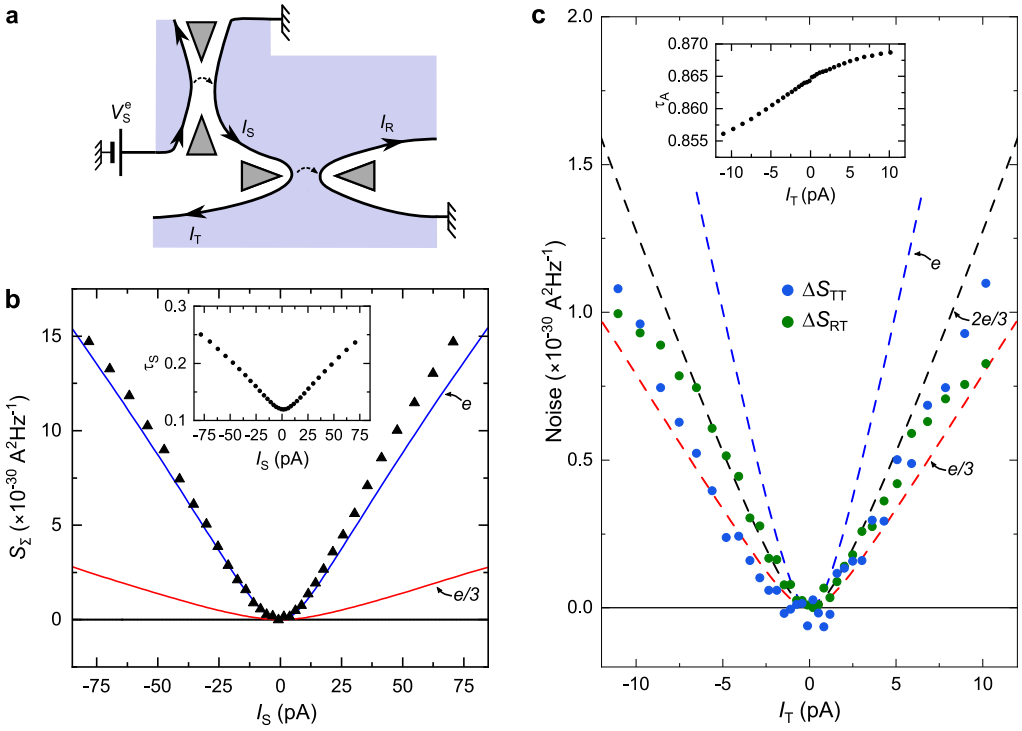

Figure 3.17: **Noise signal with incident e-charges on a barrier transmitting $e/3$-charges.**
a Device configuration during the measurement.
b Source charge characterization in the WBS regime via S_Σ (black triangles) in good agreement with e predictions (blue line) and in marked contrast with $e/3$ predictions (red line).
c Auto- (blue dots) and cross-correlation (green dots) noise signals. The blue, red, and black dashed lines display respectively shot noise with $1e$, $e/3$, and $-(2/3)e$ all in the Poissonian limit (Eq. (3.8)) Insets display the corresponding source (panel (b)) and analyzer (panel (c)) transmissions.

However, the auto- (blue dots) and cross-correlation (green dots) signals plotted in Fig. 3.17c present puzzling features.

Firstly, auto-correlations deviate from the $e/3$ prediction depicted as a red dashed line. Although these deviations do not prevent to discriminate between fractional charges and quasi-electrons, they drastically hamper a precise quantitative connection with the expected $e/3$ tunneling charges across the analyzer.

Similarly, in spite of their expected positive sign, cross-correlations between transmitted and reflected current do not match the $+2(e)$ slope that we would naively expect and seems instead close to a $+2/3(e)$ slope (dashed black line). The following paragraph brings precisions regarding the quantitative disagreement.

Discussion about the observed discrepancies

The observed discrepancies between data and naive expectations need to be discussed in light of experimental difficulties and previous results from other regimes.

Firstly, it is in practice very difficult to set the system in the specific configuration where the source QPC is in the SBS regime while the analyzer is in the WBS regime. Indeed, transmissions present strong voltage-dependence in the SBS regime as well as resonances leading to spurious additional noise. This makes it difficult to find operating points with stable transmissions and well-controlled impinging charges. Typically, such operating points were found for $\tau_{\mathrm{S}}(V_{\mathrm{S}}^{\mathrm{qp}} = 0) \simeq 0.1$ and $\tau_{\mathrm{A}}(V_{\mathrm{S}}^{\mathrm{qp}} = 0) \simeq 0.85$.

Secondly, the separate calibration of the central QPC (see section 3.5.1) presents deviations with respect to predictions as displayed in Fig. 3.18b. Thus, all three noise signals ΔS_{TT} (blue circles) ΔS_{RR} (blue discs) and ΔS_{RT} (green circles) present consistent deviations from the $e/3$ charge prediction (red line) and show instead an effective charge intermediate between $e/3$ and e. This result, although obtained in a different bias configuration, indicates that tunneling across the analyzer QPC involves a mixture of both e and $e/3$ charges, likely because the analyzer QPC is not fully in the WBS regime ($\tau_{\mathrm{A}} \simeq 0.86$). This could explain the quantitative mismatch observed in Fig. 3.17.

Finally and most importantly, the quantitative value of the positive cross-correlations has to be discussed in light of observations in other regimes.

The observed positive cross-correlations are markedly different from the signal measured in the Andreev regime which matches with the theory. However, the measured S_{RT} is comparable to that of the first source SBS - analyzer SBS counterpoint regime. To allow for a direct comparison, Fig. 3.18c,d shows the measurements of source noise (c) auto- and cross-correlations of currents (d) for the same operating point as in Fig. 3.17 but for a wider voltage range. The variations and quantitative values of the cross-correlation signal (up to 1×10^{-30} A^2 Hz^{-1}) appear to be very similar in Fig. 3.18d and Fig. 3.15c. Note that in both cases, the slope change from positive to negative at $I_{\mathrm{T}} \simeq 12$ pA can directly be linked to the change of the impinging charge seen in the S_{Σ} signal.

This quantitative correspondence between the two counterpoint configurations suggests that interactions between quasiparticles play an important role in both configurations. Although the measured signal in the source SBS - analyzer WBS regime has the same order of magnitude as that of the naive picture prediction, this match could be accidental and could instead be related to interactions along the source-analyzer path. Therefore, our data do not provide a definitive picture of the transport process across the analyzer QPC in this specific configuration.

To sum up, while the observed positive cross-correlation signal would be compatible with a mechanism involving simultaneously an $e/3$ transmitted charge and a $2e/3$ backscattered charge (naively deduced from the similar Andreev-like reflection process), experimental imperfections in the QPC tunings as well as similarity with the effect of interactions along the source-analyzer path prevent from reaching a definitive conclusion regarding the precise process in this configuration. This calls both for a specific theoretical study and for additional measurements clarifying the role of interactions (see Chapter 6).

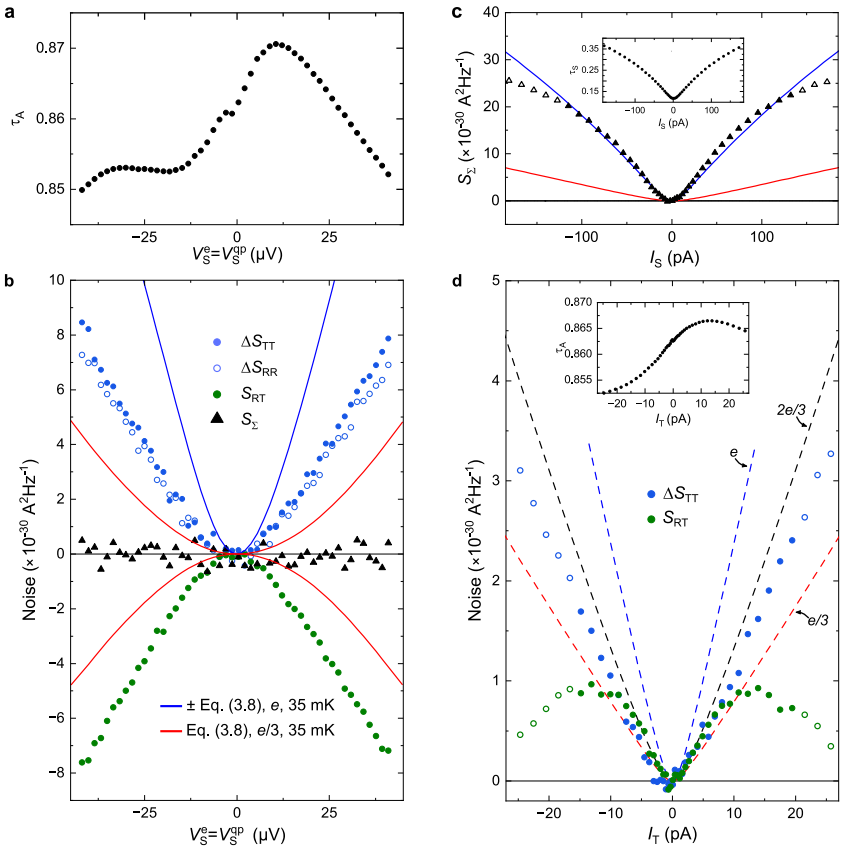

Figure 3.18: **Additional noise measurement in the source SBS - analyzer WBS regime.**
a,b Charge analyzer characterisation as presented in section 3.5.1. The Analyzer QPC is directly biased by applying DC-voltage $V_S^{qp} = V_S^e$. Panel (a) displays the measured transmission ratio $\tau_A = I_T/I_S$ in this specific configuration. Panel (b) shows noise signals ΔS_{RR} (blue disc) ΔS_{TT} (blue circles) and S_{RT} (green disc) which consistently indicate an effective tunneling charge between the predictions of Eq. (3.5) with $e^* = e$ (red line) and $e^* = e/3$ (blue line).
c,d Noise measurement in the source SBS - analyzer WBS regime on a wider current range than in Fig. 3.17. Panel (a) represents the source noise S_Σ (black triangles), predictions of Eq. (3.5) with $e^* = e$ (blue line) and $e^* = e/3$ (red line) as well as the source transmission τ_S (inset). Panel (b) displays the corresponding ΔS_{TT} (blue discs), ΔS_{RR} (blue circles) and S_{RT} (green discs) and τ_A (black dots in inset). Dashed blue, black and red lines represent shot noise predictions of Eq. (3.8) for $e^* = e$, $2e/3$, and $e/3$ respectively. Open symbols in panels (c) and (d) correspond to data with $\tau_S \leq 0.3$, for which the source notably deviates from the SBS regime.

3.8 Observations of Andreev scattering for different temperatures and tunings

As pointed out in [42], discrepancies between theoretical predictions (obtained for $T = 0$ K) and the pioneering experiment [43] could depend on temperature. Therefore, it is important to repeat the measurements at other temperatures and at other QPC operating points, to corroborate our observations.

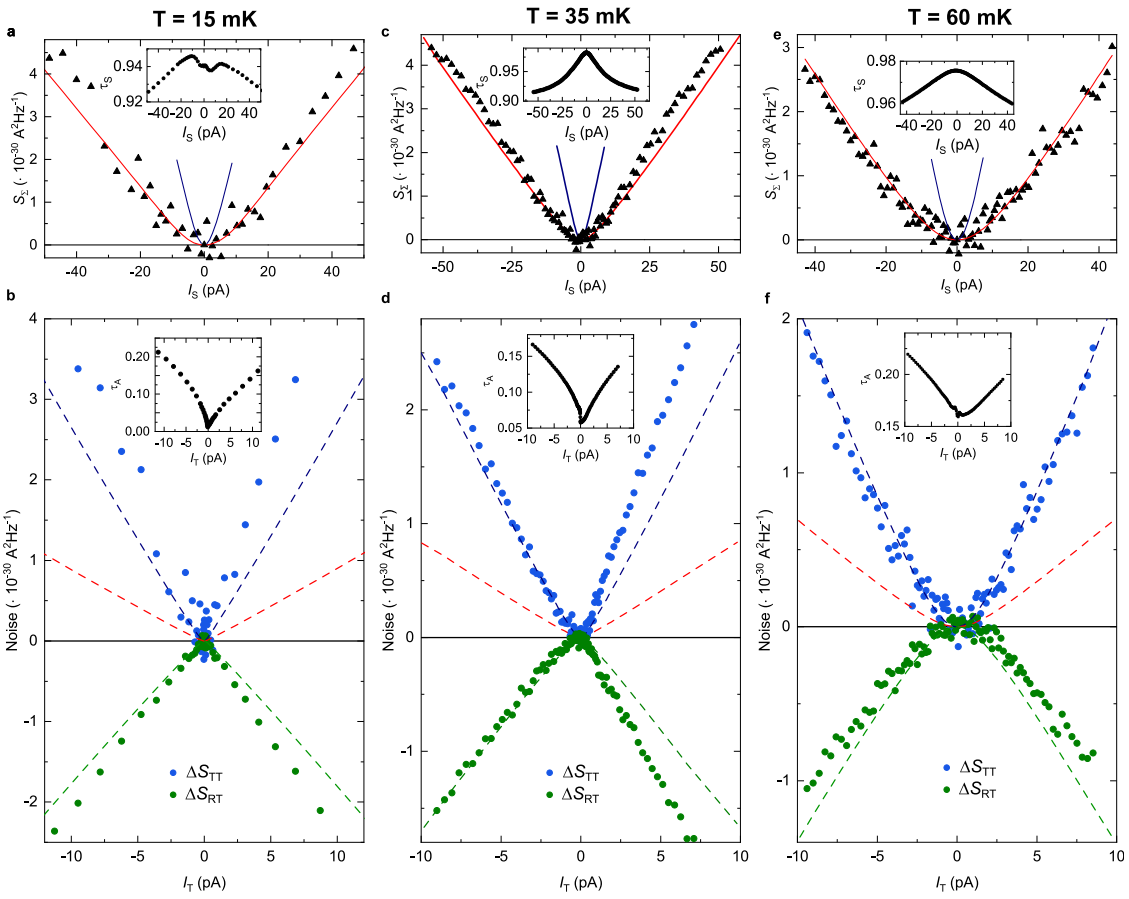

Figure 3.19: **Additional measurements at $T \simeq$ 15 (left) 35 (right) and 60 (right) mK in the source WBS - analyzer SBS regime.**
At 35 mK, the source QPC is the one located on the opposite side of the analyzer than for the data shown in Fig. 3.13. The data in (a) and (d), in (b) and (e), and in (c) and (f) were measured simultaneously. **a,b,c** The top panels display the sum noise S_Σ (black symbols) for the simultaneous characterization of the source tunneling charge, as in Fig. 3.13b but at different temperatures. The red (blue) lines correspond to the shot noise predictions of Eq. (3.5) for $e/3$ at the corresponding T. **d,e,f** The bottom panels represent the auto-correlations of the transmitted current (blue symbols) and the cross-correlations between transmitted and reflected current (green symbols), similarly to Fig. 3.13c. The dashed lines are the predictions of Eq. (3.8) at the corresponding T.

Fig. 3.19 shows such complementary measurements in the Andreev-like scattering regime where the source is in the WBS regime and the central in the opposite SBS regime. The source we used here is the bottom right QPC (see Fig. 3.8), different from the top-left of the previous results and the additional tested temperatures are $T \simeq 15\,\mathrm{mK}$ and $T \simeq 60\,\mathrm{mK}$. The reproducibility of these signatures is good overall. Indeed, we observe a similar signal as in Fig. 3.13, denoting Andreev-like scattering process signatures. However, in the specific point shown in panels (c,d) (corresponding to the same operating point as the one used in Fig. 3.13), but with the right source, a noticeable deviation from theory is observed in the positive voltage range.

Similarly, Fig. 3.20 shows additional measurements with both QPCs in the SBS regime at

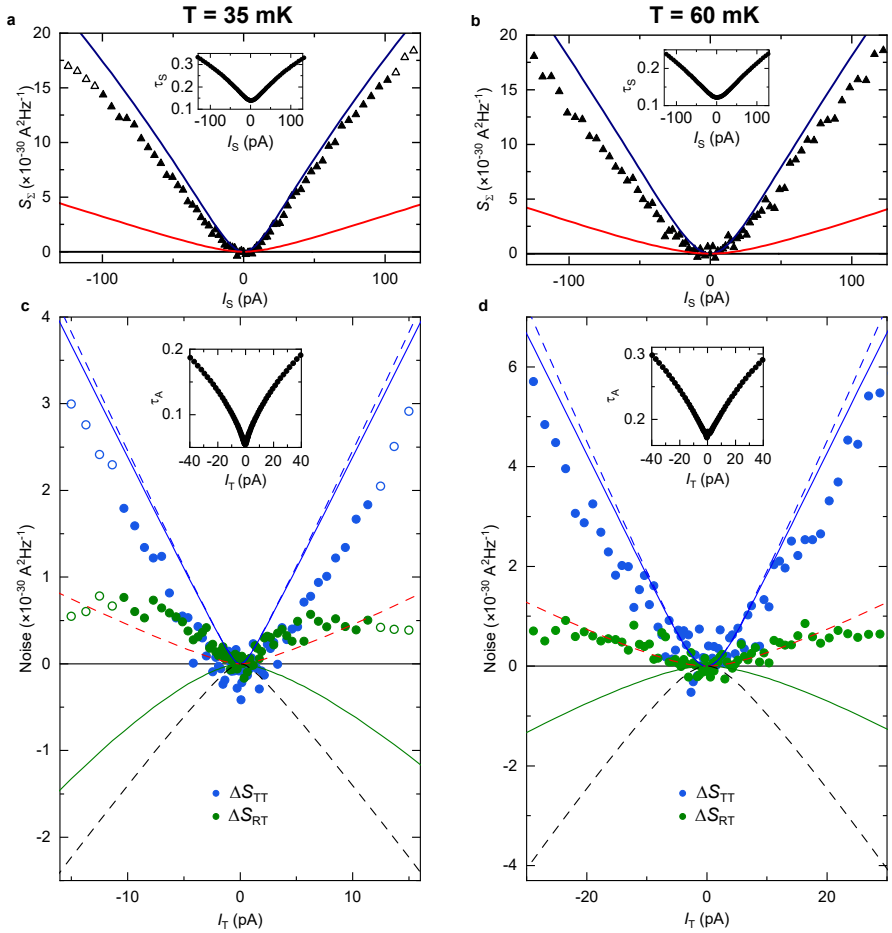

Figure 3.20: **Additional measurements at $T \simeq$ 35 mK and 60 mK in the source SBS - analyzer SBS regime.**
a,b,c,d The displayed data (symbols) confirm the observations shown in Fig. 3.15b,c. but for a distinct source QPC, and at a higher $T \approx 60$ mK (b,d) The data in (a) and (c), and in (b) and (d) were simultaneously measured.

$T \simeq 15$ mK and $T \simeq 60$ mK leading to the same conclusions as that of section 3.6.

3.9 Conclusion

In this chapter, we have studied the emergence of remarkably different transport processes of fractional quasiparticles. In the case of Andreev-like scattering at $\nu = 1/3$, one incident $e/3$ quasiparticle impinging on a QPC in the SBS regime is converted into both a transmitted quasi-electron and a backscattered hole with a charge of $-2e/3$, giving rise to negative cross-correlations. These signatures in the noise signal are robust over the temperature range from $T = 15$ mK to $T = 60$ mK and QPC operating points. The opposite positive cross-correlations measured when QPCs are set in different regimes underline the specificity of this nontrivial process, although the role of interactions remains to be clarified. Furthermore, as we will see in the next two chapters, the signature of Andreev-reflections can be discussed in light of another mechanism for which the device is set in the fourth configuration with both QPCs in the WBS regime.

The understanding of this process, which has triggered recent theoretical studies [129, 130], is important for the future exploration and manipulation of anyonic quasiparticles in quantum circuits. Indeed, remarkably, Andreev-reflection mechanisms do not conserve the number nor the nature of excitations, which is in marked contrast with the usual beam-splitter picture of QPCs, casting a new perspective on proposed anyonic analogs of quantum optics experiments. Considering the multiplicity of fractional charges accessible by tuning both the QPCs and the fractional filling factor, one could ask if analogous processes occur for other quasiparticles. For instance, at $\nu = 2/5$ could an incident $e/5$ quasiparticles transform into a backscattered $-2e/15$ hole and a transmitted $e/3$ quasiparticle? Thus, this observation could generalize into a larger family of Andreev-like processes, prompting further experimental and theoretical investigations.

Chapter 4

Signatures of anyon braiding in the $\nu = 1/3$ fractional quantum Hall regime

In this chapter, we address experimental signatures of unconventional exchange statistics in the $\nu = 1/3$ fractional quantum Hall regime. When their positions are swapped, two anyons are expected to accumulate an *exchange phase* $\theta \in [0, \pi]$ intermediate between those of bosons ($\theta = 0$) and of fermions ($\theta = 0$). While the quest for an unambiguous marker of anyon statistics has remained elusive for more than two decades, it is only recently, in 2020, that such first convincing signatures were detected using two complementary methods: through $2\pi/3$ phase jumps in a Fabry-Perot electronic interferometer [45] and through negative cross-correlations in a source-analyzer setup [131].

Specifically, the second method using one or two sources of quasiparticles impinging on a downstream "analyzer" promises to be adaptable to other platforms including fractional charges propagating along integer quantum Hall channels [46, 126] and has therefore triggered other experimental [48, 50, 49] and theoretical [47, 132, 129] studies.

This chapter presents one of the core experimental results of this thesis: the observation of non-trivial exchange statistics of quasiparticles at $\nu = 1/3$ via noise measurements. Three complementary markers of anyon statistics are investigated: strong negative cross-correlations when two balanced sources are used, a dependence of this signal upon source imbalance, and super-Poissonian auto-correlations when a single source is used. The contrast with the signal for conventional free fermions at $\nu = 2$, provinding vanishing cross-correlations, is demonstrated.

Moreover, this chapter aims to bring insight into the quantitative significance of such noise measurements by showing how the result relies on a specific normalization choice of the cross-correlations and how it can be distinguished from the Andreev-like scattering presented in the previous chapter.

Section 4.1 presents the physical picture of the underlying anyon exchange process. The noise predictions are recapitulated in sections 4.2 and 4.3. Then we turn to the experimental implementation in section 4.5 and to the main measurements for anyons at $\nu = 1/3$ (sections 4.6 to 4.10) and for fermions at $\nu = 2$ (section 4.11). Finally, additional tests investigating mechanisms that could hamper the conclusions are presented in section 4.12.

4.1 Probing anyon statistics through cross-correlations in source-analyzer setup

In this section, we present the physical process involving braiding of anyonic quasiparticles in the so-called "collider" geometry, using several QPCs in series. While the mechanism was initially seen as "collisions" of quasiparticles, it has been recently revised and is now interpreted as a *time-braiding* between impinging quasiparticles and a pair of quasiparticle-quasihole spontaneously generated on the "analyzer" QPC.

4.1.1 The "collider" geometry

The *source-analyzer* setup revealing the Andreev-like scattering of the previous chapter can be adapted to probe the unconventional exchange statistics of the quasiparticles in the FQH regime. With the inclusion of a second source on the other side of the analyzer, the system is composed of three QPCs, now all set in the weak-back scattering (WBS) regime (i.e. with a transmission ratio of current close to 1): two sources randomly emitting quasiparticles (respectively labeled $\mathrm{QPC_t}$ and $\mathrm{QPC_b}$) and a central "analyzer" constriction (labeled $\mathrm{QPC_c}$) on which the two incident beams "collide" (see the schematics in Fig. 4.1). The tuning of QPCs is characterized by their respective transmission ratios of current $\tau_\mathrm{t} \equiv 1 - I_\mathrm{t}/(V_\mathrm{t}/R_\mathrm{H})$, $\tau_\mathrm{b} \equiv 1 - I_\mathrm{b}/(V_\mathrm{b}/R_\mathrm{H})$ and $\tau_\mathrm{c} \equiv 1/2 \times [I_\mathrm{L}/I_\mathrm{t} + I_\mathrm{R}/I_\mathrm{b}]$.

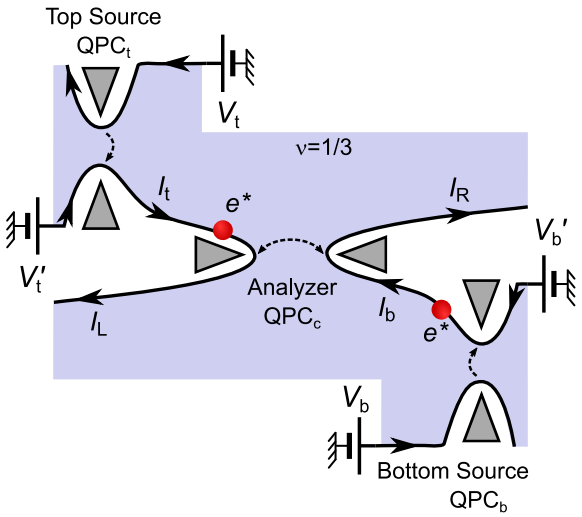

Figure 4.1: **Schematic of the setup.**
QPCs (pairs of facing triangles) at the top left ($\mathrm{QPC_t}$) and bottom right ($\mathrm{QPC_b}$) in the WBS regime form two sources of quasiparticles of fractional charge e^*. The emitted quasiparticles flow to the central analyzer QPC ($\mathrm{QPC_c}$) along the quantum Hall edge channels represented by arrowed lines. Cross-correlations $\langle \delta I_\mathrm{L} \delta I_\mathrm{R} \rangle$ provide information on the exchange statistics.

In this geometry, theory predicts negative cross-correlations between the two currents outgoing from $\mathrm{QPC_c}$, distinct from the previous Andreev-like scattering signature [1, 47, 46]. Instead, these negative cross-correlations are predicted to be a manifestation of the non-trivial exchange statistics of the involved quasiparticles. The remainder of this section clarifies the physical picture of the transport process across $\mathrm{QPC_c}$, as well as the connection between negative cross-correlations and anyon statistics.

4.1.2 Initial bunching/antibunching picture

As the considered system has the geometry of a Hong-Ou-Mandel (HOM) interferometer [133], the negative cross-correlations were initially interpreted as a signature of anyon statistics in terms of partial bunching (see Fig. 4.2) [1]. Indeed, this intuitive picture exhibits a marked difference between fermions and anyons in such a system. Two free fermions (e.g. electrons) arriving simultaneously at the central QPC are not able to come out in the same channel due to the Pauli principle, resulting in "antibunching" with only one electron per outgoing lead (Fig. 4.2a). On the contrary, two impinging bosons would bunch into the same outgoing lead (Fig. 4.2b). In the case of anyons, one would therefore expect partial bunching of the two colliding quasiparticles (Fig. 4.2c). A simple classical lattice model with a partial exclusion probability between quasiparticles has been proposed to illustrate the impact of anyon statistics on cross-correlations [1, 2].

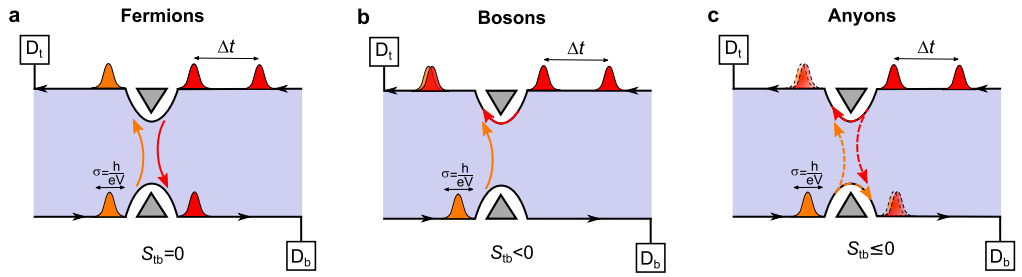

Figure 4.2: **Initial (anti)bunching 'collider' picture.**
a (b) Two opposite incident fermions (bosons), separated by a time $\Delta t > h/(eV)$ and depicted as orange and red packets, collide on the analyzer and antibunch (bunch) into the two outgoing leads. For a diluted beam of non-interacting fermions (bosons), theory predicts zero cross-correlations between detectors D_t and D_b.
c In the general case of two colliding anyons on QPC_c, an intermediate behaviour and negative cross-correlations are expected. However, due to the high dilution of the beams, actual 'collisions' are very rare and this process is not the dominant one.

However, further theoretical investigations revised this interpretation [46, 47]. Indeed, authors of these additional studies pointed out that actual "collisions" between two impinging quasiparticles have a contribution to cross-correlations that becomes negligible in the limit of highly diluted beams emitted by the Poissonian sources. In other words, quasiparticles of time width $\sigma = h/eV$ typically separated by a much higher time Δt are very unlikely to "collide" on QPC_c. Instead, another more subtle process is predicted to be dominant in such systems.

4.1.3 Time-braiding picture

This more subtle dominant process has been described in Refs. [47, 46]. The theoretical derivations of these later articles are the same as in Ref. [1] but the negative cross-correlations were instead attributed to a *time-braiding* mechanism due to an interference between the two sub-processes described in Figure 4.3.

In this description, the impinging anyons do not tunnel between the two edges. Instead, a quasiparticle-quasihole pair is excited on the central QPC_c i.e., due to quantum fluctuations, a quasiparticle spontaneously tunnels from one edge to the other, leaving a quasihole on the

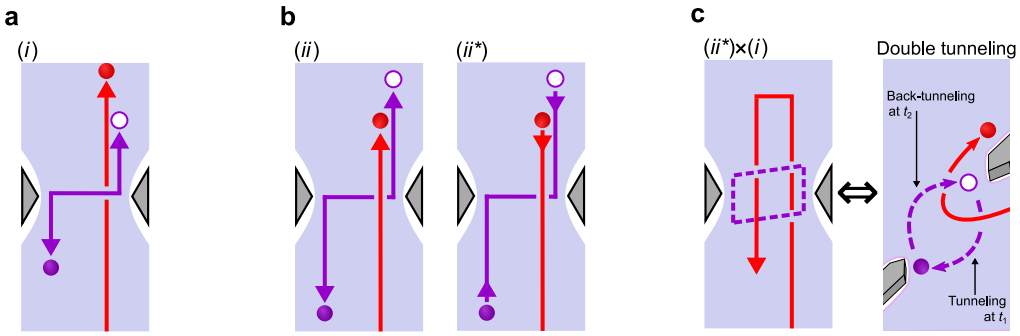

Figure 4.3: **Time-braiding process on QPC$_c$.**
a Sub-process (i): the incident anyon crosses QPC$_c$ *before* the quasiparticle-quasihole pair excitation.
b Sub-process (ii) and its conjugate (ii*): the incident anyon crosses QPC$_c$ *after* the quasiparticle-quasihole pair excitation.
c Interference between the two sub-processes (ii*) and (i). This interference mechanism maps onto a time-domain braiding: the quasiparticle-quasihole pair tunnels at time t_1 and annihilates at time t_2 by back-tunneling. It time-braids with the incident anyon that crosses QPC$_c$ during the interval $t_2 - t_1$.

other edge. For clarity, let us consider a single incident anyon (the process generalizes for an arbitrary number of impinging quasiparticles). Two sub-processes should be considered:

- (i) the quasiparticle-quasihole pair is excited at time t_1 *after* the passage of the impinging anyon through the QPC (see Fig. 4.3a);
- (ii) the quasiparticle-quasihole pair is excited at time t_2 *before* the passage of the impinging anyon through the QPC (see Fig. 4.3b).

The interference between processes (ii*) and (i) - here the exponent star $*$ stands for the conjugate - corresponds to a braiding in the time-domain between the impinging quasiparticle and the excited quasiparticle-quasihole pair.

Another equivalent representation, which may be more intuitive (see Fig. 4.3c), involves a quasiparticle which tunnels between the edges and leaves a hole behind at time t_1, and then tunnels back and recombines (or "pair-annihilates") with the hole at time t_2. The incident quasiparticle across the QPC between these two times is therefore effectively encircled. This description is valid as long as $(t_2 - t_1) \leq \hbar/(k_B T)$. Note that this picture has recently been extended to non-abelian anyons[1] [47].

The quasiparticle and the quasihole forming this pair are *correlated* and therefore directly result in negative cross-correlations between currents of the two outgoing leads. Note that these negative cross-correlations have a *strong* amplitude [2]. As previously mentioned, this process generalizes in the case of two opposite sources, i.e. one source on each side of QPC$_c$. In that case, during $t_2 - t_1$, the quasiparticle-quasihole pair can encircle several quasiparticles coming from opposite beams. For two sources emitting balanced beams of $e/3$-quasiparticles, the mere

[1] with a more general relevant parameter describing the braiding called the monodromy factor M ($M = e^{-2i\theta}$ for abelian anyons and $M = 1$ for free fermions), see Ref. [47]

[2] e.g. compared to another less important signal predicted in the IQHE and resulting from inter-channel Coulomb interactions, largely discussed in Chap. 6

presence of strong negative cross-correlations constitutes a first marker of non-trivial anyon statistics.

Moreover, these negative cross-correlations are predicted to depend on the balance between the two incoming currents. Indeed, impinging anyons from opposite sources are related to braiding with inverse winding directions. Hence, their contributions add with opposite signs and the fully-balanced-sources configuration induces less negative cross-correlations than the fully-imbalanced one. This dependence on the symmetry between the two incident beams constitutes a second marker of the non-trivial anyons statistics.

When combined together, these two complementary markers in the cross-correlations offer a strong qualitative signature of the underlying unconventional anyon statistics.

4.2 Theoretical predictions of anyon braiding signatures in cross-correlations

After having described the physical picture of the process, we now turn to outlining the theoretical predictions for cross-correlations as signatures of quasiparticle statistics in such a source-analyzer setup with all QPCs in the WBS regime. First, we derive the predictions for noninteracting electrons [123] and then we synthesize the predictions for Laughlin anyons [1, 47, 134, 46].

4.2.1 Generalized Fano factor

The statistics of the impinging quasiparticles is specifically examined through the *generalized Fano factor*:

$$\boxed{P_{\text{thy}} \equiv \frac{\langle \delta I_{\text{L}} \delta I_{\text{R}} \rangle}{S_\Sigma \tau_{\text{c}}(1-\tau_{\text{c}})}} \tag{4.1}$$

with $S_\Sigma \equiv \langle \delta I_{\text{L}}^2 \rangle + \langle \delta I_{\text{R}}^2 \rangle + 2\langle \delta I_{\text{L}} \delta I_{\text{R}} \rangle$ the total noise generated by both sources, as defined in section 3.5.1 (with $S_\Sigma \approx 2e^*(I_{\text{L}} + I_{\text{R}})$ at large bias).

Using this Fano factor allows us to minimize the voltage-dependant contribution of the shot noise of the sources and to specifically focus on the signal of interest generated by the analyzer QPC_{c}.

Note that the expression of Eq. (4.1) is slightly different and generalizes the original definition of P introduced in [1] [3]:

$$P_{\text{thy}}^{\text{bis}} = \frac{\langle \delta I_{\text{L}} \delta I_{\text{R}} \rangle}{2e^* I_+ \frac{\partial \langle I_{\text{T}} \rangle}{\partial I_-}\Big|_{I_-=0}} = \frac{\langle \delta I_{\text{L}} \delta I_{\text{R}} \rangle}{2e^* I_+ (1-\tau_{\text{c}}^{\text{bis}})}, \tag{4.2}$$

where I_{T} is the net current tunneling between the two edges, $I_+ = I_{\text{t}} + I_{\text{b}}$, $I_- = I_{\text{t}} - I_{\text{b}}$ and $\tau_{\text{c}}^{\text{bis}} = \tau_{\text{c}}(I_- = 0, I_+)$. Indeed, with the additional renormalization factor τ_{c}, Eq. (4.1) generalizes Eq. (4.2) and remains usable beyond the WBS limit $1 - \tau_{\text{t,b,c}} \ll 1$, in the same spirit as in the pioneering experiment of Bartolomei *et al.* [2]. Moreover, the choice of definition for the transmission ratio (τ_{c} or $\tau_{\text{c}}^{\text{bis}}$) has quantitative consequences that will be further discussed in

[3] Note that we use here the definition with symmetrized noise so with the corresponding factor 2

section 4.2.4. Finally, dividing by S_Σ instead of $2e^*I_+$ in our experimental definition allows us to take into account finite temperature effects.

4.2.2 Predictions for free fermions

In the case of noninteracting electrons, one can apply the Landauer-Büttiker-Martin formalism [123]. The top (t) and bottom (b) incident beams impinge on $\mathrm{QPC_c}$ (see Fig. 4.1) with respective electron energy distribution functions f_t and f_b. These distribution functions result from the source QPCs. Hence, $f_{\mathrm{t(b)}}$ have the following double-step distribution form:

$$f_{\mathrm{t(b)}}(\epsilon) = \tau_{\mathrm{t(b)}}\mathcal{F}(\epsilon, 0, T) + (1-\tau_{\mathrm{t(b)}})\mathcal{F}(\epsilon, V_{\mathrm{t(b)}}, T) \tag{4.3}$$

with $\mathcal{F}$ the Fermi-Dirac distribution function $\mathcal{F}(\epsilon, V, T) = \dfrac{1}{1+\exp\left(\frac{\epsilon - eV}{k_\mathrm{B}T}\right)}$.

In the Landauer-Büttiker-Martin scattering formalism introduced in section 1.3.2, the cross-correlations $S_\mathrm{LR} \equiv \langle \delta I_\mathrm{L} \delta I_\mathrm{R} \rangle$ between the fluctuations of the left and right outgoing currents are therefore given by:

$$S_\mathrm{LR} \equiv \langle \delta I_\mathrm{L} \delta I_\mathrm{R} \rangle = \frac{2e^2}{h}\tau_\mathrm{c}(1-\tau_\mathrm{c}) \int d\epsilon \left[f_\mathrm{t}(1-f_\mathrm{t}) + f_\mathrm{b}(1-f_\mathrm{b}) - f_\mathrm{t}(1-f_\mathrm{b}) - f_\mathrm{b}(1-f_\mathrm{t}) \right], \tag{4.4}$$

leading to:

$$\boxed{S_\mathrm{LR} = \frac{2e^2}{h}\tau_\mathrm{c}(1-\tau_\mathrm{c}) \int d\epsilon \left[f_\mathrm{t}(\epsilon) - f_\mathrm{b}(\epsilon) \right]^2} \tag{4.5}$$

In the case of perfectly symmetric identical sources, one has $f_\mathrm{t} = f_\mathrm{b}$ and consequently, we deduce from Eq. (4.5) that the cross-correlations S_LR vanish. Therefore, the generalized Fano factor remains zero in the free-fermion case: $P_\mathrm{thy} = 0$. Note that this result is valid for free fermions at arbitrary $\tau_{\mathrm{t,b,c}}$.

Furthermore, while the sources are set in the dilute limit $1-\tau_{\mathrm{t,b}} \ll 1$, we get $(1-\tau_{\mathrm{t,b}})V_{\mathrm{t,b}} \ll 1$ and $|f_\mathrm{t} - f_\mathrm{b}| \ll 1$ even in the asymmetric case ($\tau_\mathrm{t} \neq \mathrm{b}$ or $V_\mathrm{t} \neq V_\mathrm{b}$). Therefore, for free fermions in the WBS limit, the cross-correlations and Fano factor remain asymptotically zero even when sources are not symmetric.

Thus, in the case of noninteracting fermions, theory predicts *vanishing cross-correlations* and $P_\mathrm{thy} = 0$ both in the symmetric case (at any $\tau_\mathrm{t} = \tau_\mathrm{b}$) and in the asymptotic case of asymmetric sources set in the dilute limit ($(1-\tau_\mathrm{t}), (1-\tau_\mathrm{b}) \ll 1$). The qualitative difference with the predictions of strong negative cross-correlations in the case of Laughlin anyons is therefore striking.

4.2.3 Predictions for Laughlin anyons

Let us switch to the more general case of anyon quasiparticles and let us derive the analytical predictions for cross-correlations and for the Fano factor P, following the computations of [1] confirmed by [46]. In the following, we consider a Laughlin fraction $\nu = 1/m$.

The physics at the edge of a FQH fluid is described by the chiral Tomonaga-Luttinger liquid (TLL) formalism. In such a framework, the low energy one-dimensional quasiparticle propagation can be described with bosonic fields $\phi_{\mathrm{t,b}}$ (where the indexes t,b refer to the arm

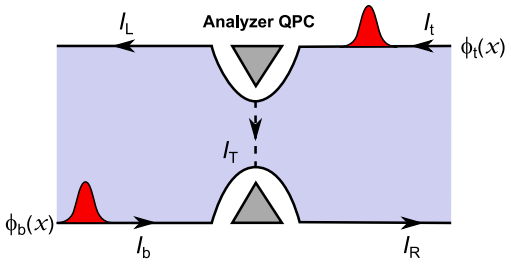

Figure 4.4: **Configuration at QPC$_c$.**
The top (t) and bottom (b) edges, described by bosonic fields $\phi_{t,b}(x)$ are pinched off at the analyzer QPC$_c$, which induces a tunnel current I_T. The left and right outgoing currents are labeled I_L and I_R respectively.

going into QPC$_c$), associated to charge densities $\rho_{t,b} = \partial_x \phi_{t,b}/2\pi$ and currents $I_{t,b} = e\partial_t \phi_{t,b}/2\pi$ (see Fig. 4.4). At equal times and different positions, they satisfy the following commutation relation:

$$[\phi_t(x), \phi_b(y)] = i\nu\pi\delta_{t,b}\text{sign}(x-y) \tag{4.6}$$

and, similarly, at different times and equal positions we have:

$$[\phi_t(t_1), \phi_b(t_2)] = i2\Delta\pi\delta_{t,b}\text{sign}(t_1-t_2) \tag{4.7}$$

where Δ is the scaling dimension characteristic of the edge, related to the exchange phase by $\theta = 2\pi\Delta$ and given by $\Delta = \nu/2 = 1/(2m)$ in the case of Laughlin fractions [4]. Note that these relations are obtained assuming no edge reconstruction [1], as expected at $\nu = 1/3$ and checked in section 4.12.1.

Average value and fluctuations of the tunneling current

The tunneling of fractionally charged quasiparticles between the two edges at the central QPC$_c$ is described by the tunneling operator $\hat{T}$:

$$\hat{T}(t) = \zeta\psi_b(0,t)^\dagger\psi_t(0,t) = \zeta e^{i(\phi_t(0,t)-\phi_b(0,t))} \tag{4.8}$$

where ζ is the tunneling amplitude and $\psi^\dagger_{t(b)}(0,t)$ is the fermionic creation operator of a quasiparticle in the top (bottom) incoming arm, at position 0 and time t. The tunneling current operator from one edge to the other at QPC$_c$ is therefore:

$$\hat{I}_T = ie^*(\hat{T}^\dagger - \hat{T}) \tag{4.9}$$

One can then determine the average value and the fluctuations of the tunneling current:

$$I_T = \langle\hat{I}_T\rangle = e^*\int_{-\infty}^{+\infty} dt\langle[\hat{T}^\dagger(0), \hat{T}(0)]\rangle \tag{4.10}$$

$$\langle(\delta\hat{I}_T)^2\rangle = (e^*)^2\int_{-\infty}^{+\infty} dt\langle\left\{\hat{T}^\dagger(0), \hat{T}(0)\right\}\rangle \tag{4.11}$$

[4] this identity does not necessarily hold for more complex fractions

In the Laughlin case, the bosonic fields are decomposed into an equilibrium term and a nonequilibrium term associated to the Poissonian fluctuations:

$$\phi_{\mathrm{t(b)}} = \phi^{\mathrm{eq}}_{\mathrm{t(b)}} + 2\pi N_{\mathrm{t(b)}}/m \tag{4.12}$$

where the expectation value of the nonequilibrium component is $\langle \partial_t \hat{N}_{\mathrm{t(b)}} \rangle = \langle \hat{I}_{\mathrm{t(b)}} \rangle / e^*$. $\hat{I}_{\mathrm{t(b)}}$ corresponds to the incident current in edge t (b).

The correlator $[\cdot,\cdot]$ and anti-correlator $\{\cdot,\cdot\}$ can now be determined from the correlation function of the tunneling operator [1, 50, 46]:

$$\langle \hat{T}(t)\hat{T}^\dagger(0)\rangle = \langle \hat{T}(t)\hat{T}^\dagger(0)\rangle_{\mathrm{eq}} \exp\left[-\frac{\langle \hat{I}_{\mathrm{t}}\rangle}{e^*}(1-e^{-2i\pi/m})t\right] \exp\left[-\frac{\langle \hat{I}_{\mathrm{b}}\rangle}{e^*}(1-e^{+2i\pi/m})t\right] \tag{4.13}$$

with $\langle \hat{T}(t)\hat{T}^\dagger(0)\rangle_{\mathrm{eq}} = |\zeta|^2 e^{2i\pi\Delta \mathrm{sign}(t)} \dfrac{t_{\mathrm{cut}}^{\Delta}}{|t|^{\Delta}}$ the correlation function at equilibrium and t_{cut} is a short time cut-off.

The value of the mean tunneling current and of the tunneling current fluctuations can then be calculated at leading order of t_{cut} and T:

$$\boxed{\begin{aligned} I_{\mathrm{T}} &= C\sin(2\pi\Delta)\mathrm{Im}\left(I_+ + \frac{iI_-}{\tan(2\pi\Delta)}\right)^{\Delta-1} && \text{(4.14a)} \\ \langle (\delta \hat{I}_{\mathrm{T}})^2\rangle &= e^* C\cos(2\pi\Delta)\mathrm{Re}\left(I_+ + \frac{iI_-}{\tan(2\pi\Delta)}\right)^{\Delta-1} && \text{(4.14b)} \end{aligned}}$$

with $I_+ = I_{\mathrm{t}} + I_{\mathrm{b}}$, $I_- = |I_{\mathrm{t}} - I_{\mathrm{b}}|$ and $C = 4\nu|\zeta|^2 t_{\mathrm{cut}}^{\Delta}\Gamma(1-\Delta)[\pi(1-\cos\pi\Delta)/e^*)]^{\Delta-1}$. Γ is Euler's gamma function.

Cross-correlations and Fano factor

By relating the output currents I_{L} and I_{R} to the input and tunneling currents thanks to the charge conservation (assuming no charge accumulations) $I_{\mathrm{L}} = I_{\mathrm{t}} - I_{\mathrm{T}}$, $I_{\mathrm{R}} = I_{\mathrm{b}} + I_{\mathrm{T}}$, we deduce the cross-correlations between I_{L} and I_{R} :

$$\begin{aligned} \langle \delta I_{\mathrm{L}} \delta I_{\mathrm{R}}\rangle &= -\langle (\delta \hat{I}_{\mathrm{T}})^2\rangle + \langle \delta I_{\mathrm{t}} \delta I_{\mathrm{T}}\rangle - \langle \delta I_{\mathrm{b}} \delta I_{\mathrm{T}}\rangle \\ &= -\langle (\delta \hat{I}_{\mathrm{T}})^2\rangle + e^*\left(I_{\mathrm{t}}\frac{\partial\langle I_{\mathrm{T}}\rangle}{\partial I_{\mathrm{t}}} - I_{\mathrm{b}}\frac{\partial\langle I_{\mathrm{T}}\rangle}{\partial I_{\mathrm{b}}}\right) \end{aligned} \tag{4.15}$$

In this expression, the first term corresponds to the noise generated at $\mathrm{QPC_c}$ while the second is associated with the redistribution of current fluctuations in the incoming beams.

Combining equations (4.15) and (4.14a,b), we deduce the complete analytical expression of the generalized Fano factor P_{thy} defined in Eq. (4.1) [1]:

$$\boxed{\begin{aligned} P_{\mathrm{thy}}(I_-/I_+) = &-\frac{4\Delta}{1-4\Delta} + |I_-/I_+|\left\{\left(\tan 2\pi\Delta + \frac{(1-4\Delta)^{-1}}{\tan 2\pi\Delta}\right)\right. \\ &\left.\times \tan\left[(4\Delta-2)\arctan\frac{|I_-/I_+|}{\tan 2\pi\Delta}\right]\right\} \end{aligned}} \tag{4.16}$$

Note that this expression is only valid for $\nu \geq 1/5$, otherwise the argument $(4\Delta - 2)\arctan\frac{|I_-/I_+|}{\tan 2\pi\Delta}$ reaches $-\pi/4$ in the range $|I_-/I_+| \in [0,1]$, leading to a divergence of $P_{\rm thy}$.

Dependence of P upon input beam imbalance

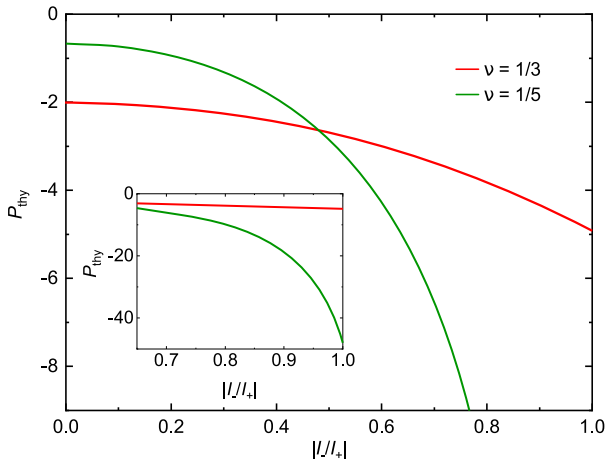

Figure 4.5: **Fano factor versus source imbalance at $\nu = 1/3$ and $\nu = 1/5$.** The predictions of Eq. (4.16) are displayed as a function of imbalance $|I_-/I_+|$ for $\nu = 1/3$ (red) and $\nu = 1/5$ (green). Inset shows the same predictions in the range $|I_-/I_+| \in [0.6; 1]$ on a larger vertical scale.

The previous equation (4.16) depends on the imbalance between currents from the two incoming arms, parameterized by $|I_-/I_+|$.

In the fully balanced case ($I_- = 0$) of two identical sources biased with $V_{\rm t} = V_{\rm b}$, this equation reduces to:

$$\boxed{P(0) = \frac{-4\Delta}{1-4\Delta} = -2}, \tag{4.17}$$

and it becomes progressively less negative for lower ν in the Laughlin series (see Fig . 4.5).

In the general case, the cross-correlation signal is predicted to noticeably increase with imbalance $|I_-/I_+|$ and, accordingly, the Fano factor becomes higher in absolute value. Fig. 4.5 shows variations of P with imbalance for the two Laughlin fractions $\nu = 1/3$ and $1/5$.

As discussed in section 4.1.3, this remarkable dependence with source asymmetry is due to the opposite winding directions for the braiding of impinging anyons from opposite sources, leading to two contributions adding with opposite signs.

As we will see in section 4.10, the variations of P with imbalance is a key feature to distinguish the signature of anyon statistics obtained in this regime from the different Andreev-like scattering studied in the previous chapter and which does not depend on $|I_-/I_+|$.

4.2.4 Alternative generalized Fano factors

In this section, we show that the quantitative prediction for P strongly depends on the definition used for the transmission ratio $\tau_{\rm c}$. Analytical expressions valid when all QPCs are set in the WBS regime and for large source voltages with respect to $k_{\rm B}T/e^*$ are provided for the two other normalization choices made in literature [1], [47].

Normalization with $\tau_c^{bis} = \tau_c(I_- = 0, I_+)$

In the definition of the Fano factor Eq. (4.16), τ_c used in the denominator is the differential transmission probability across QPC_c:

$$\tau_c = \frac{1}{2}\left(\frac{\partial V_L/\partial V_t}{1-\tau_t} + \frac{\partial V_R/\partial V_b}{1-\tau_b}\right), \tag{4.18}$$

which is measured simultaneously with the noise at all values of I_- and therefore directly accessible experimentally. However, this definition is different from the original definition of the Fano factor P_{thy}^{bis} proposed by Rosenow *et al.* [1]:

$$P_{thy}^{bis} = \frac{\langle \delta I_L \delta I_R \rangle}{e^* I_+ \frac{\partial \langle I_T \rangle}{\partial I_-}\Big|_{I_-=0}} = \frac{\langle \delta I_L \delta I_R \rangle}{e^* I_+ (1-\tau_c^{bis})} \tag{4.19}$$

with $\tau_c^{bis} = \tau_c(I_- = 0, I_+)$. At $I_- \neq 0$, this definition differs from τ_c and is not simultaneously measured with the noise signal.

Following this second definition and using Eqs. (4.15) and (4.14a,b), one gets [1]:

$$\begin{aligned} P_{thy}^{bis} = &-\frac{4\Delta}{1-4\Delta}\mathrm{Re}\left[X^{4\Delta-2}\right] \\ &+ \left|\frac{I_-}{I_+}\right|\left[\tan(2\pi\Delta) + \frac{\tan^{-1}(2\pi\Delta)}{(1-4\Delta)}\right]\mathrm{Im}\left[X^{4\Delta-2}\right], \end{aligned} \tag{4.20}$$

with $X \equiv 1 + i(|I_-/I_+|)\tan^{-1}(2\pi\Delta)$.

Note that this expression reduces to Eq. (4.1) at $I_- = 0$ because $\tau_c^{bis} = \tau_c$ in that case. Figure 4.6a, displays the variations of P_{thy}^{bis} for filling factors $\nu = 1/3, 1/5$ and $1/7$. This alternative definition of the generalized Fano factor induces substantial quantitative differences: while at $\nu = 1/3$ the limit $|I_-/I_+|$ gives $P(0) = -2$ in both cases, the opposite limit of full imbalance $|I_-/I_+| = 1$ leads to $P_{thy}^{bis} \simeq -3.1$ in contrast with $P_{thy} \simeq -4.9$ (see Table 4.1 for a summary).

Normalization with $\tau_c^{ter} = \tau_t^{-1}\partial V_L/\partial V_t'$

Another alternative definition of the transmission ratio τ_c^{ter} at QPC_c leads to a third expression of the Fano factor P_{thy}^{ter}. By defining τ_c^{ter} as the transmission ratio for thermal excitations with the sources in the WBS limit, $\tau_c^{ter} \equiv \tau_t^{-1}\partial V_L/\partial V_t'$, the corresponding Fano factor reads:

$$P_{thy}^{ter} = P_{thy}^{bis}(I_-/I_+)\frac{\sin(4\pi\Delta)}{4\pi\Delta}. \tag{4.21}$$

This is the normalization choice made in Ref. [47] where the reduction factor between P_{thy}^{bis} and P_{thy}^{ter} is $\sin(4\pi\Delta)/(4\pi\Delta) \simeq 0.41$. Accordingly, the quantitative value of P is notably reduced, with in particular: $P_{thy}^{ter}(0) \simeq -0.83$ and $P_{thy}^{ter}(|I_-/I_+| = 1) \simeq -1.28$. The variations of P_{thy}^{ter} with imbalance are displayed in Fig. 4.6b.

Table 4.1 summarizes the quantitative values of P_{thy}, P_{thy}^{bis} and P_{thy}^{ter} in both $|I_-/I_+| = 0$ and $|I_-/I_+| = 1$ limits.

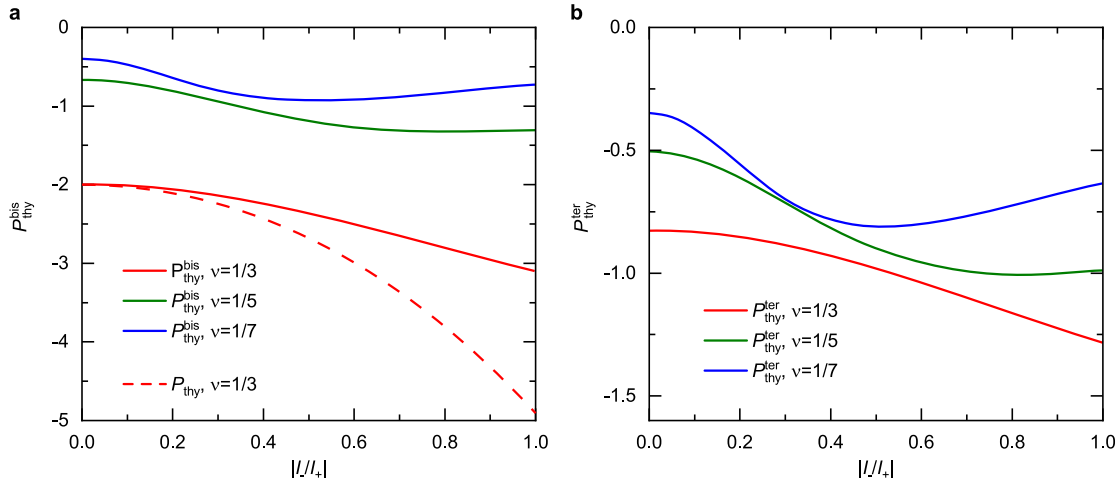

Figure 4.6: **Alternative P versus source imbalance.**
a (b) Alternative effective Fano factor $P^{\rm bis}_{\rm thy}$ ($P^{\rm ter}_{\rm thy}$) is plotted as a function of the relative difference in incident current $|I_-/I_+|$ for Laughlin's filling factors $\nu = 1/3$ (red), $\nu = 1/5$ (green) and $\nu = 1/7$ (blue). The dashed line indicates $P_{\rm thy}$ for comparison.

$\tau_{\rm c}$ variants	P variants at $(\lvert I_-/I_+\rvert = 0)$	P variants at $(\lvert I_-/I_+\rvert = 1)$
$\tau_c(I_-, I_+)$ from Eq. (4.18)	$P_{\rm thy} = -2$	$P_{\rm thy} \simeq -4.9$
$\tau_{\rm c}^{\rm bis} \equiv \tau_c(I_- = 0, I_+)$ [1]	$P^{\rm bis}_{\rm thy} = -2$	$P^{\rm bis}_{\rm thy} \simeq -3.1$
$\tau_{\rm c}^{\rm ter} \equiv \tau_t^{-1}\partial V_{\rm L}/\partial V_{\rm t}'$ [47]	$P^{\rm ter}_{\rm thy} \simeq -0.8$	$P^{\rm ter}_{\rm thy} \simeq -1.3$

Table 4.1: Predicted $P^{\rm WBS}_{\rm thy}$ at $\nu = 1/3$ for the three definitions of $\tau_{\rm c}$ and different sources imbalance (symmetric when $|I_-/I_+| = 0$ or fully asymmetric when $|I_-/I_+| = 0$, with $I_\pm \equiv I_{\rm t} \pm I_{\rm b}$). $\tau_{\rm c}$ is the transmission ratio of incident quasiparticles, $\tau_{\rm c}^{\rm bis}$ the same transmission ratio evaluated at $I_- = 0$, and $\tau_{\rm c}^{\rm ter}$ the transmission ratio of thermal excitations. The corresponding values of $P_{\rm thy}$ are respectively derived from Eq. (4.18), and Eqs. (4.20), (4.21).

Thus, the precise definition of $\tau_{\rm c}$ has an important impact on the quantitative value of P. It is important to carefully note the substantial differences induced by the choice of normalization for the Fano factor, as it conditions the quantitative conclusions that can be drawn from the experimental results.

4.3 Theoretical predictions of anyon braiding signature in auto-correlations

So far, all the predictions of anyon statistics focused on the cross-correlation signal. However, recent studies pointed out that in a system with only two QPCs in series, the auto-correlations of current across the downstream analyzer QPC also encapsulate the signatures of anyon statistics [47, 50].

Let us consider two QPCs in series (an upstream top source $\rm QPC_t$ and a downstream

analyzer $\mathrm{QPC_c}$) both set in the WBS regime ($(1-\tau_{\mathrm{t,c}}) \ll 1$).

This situation is a special case of the previously discussed configuration with one of the two sources inactivated. In other words, the present case maps onto the two-source configuration in the fully imbalanced limit $|I_-/I_+| = 1$. Consequently, the previous equations (4.14a,b) respectively give the transmitted current across QPC and its fluctuations for $I_- = I_+ = I_{\mathrm{t}}$ and replacing $\hat{I}_{\mathrm{T}}$ by $\hat{I}_{\mathrm{R}}$.

Hence, in this limit of WBS for sources, one can define a second Fano factor F concerning the auto-correlations of the transmitted current:

$$F_{\mathrm{thy}} \equiv \frac{\langle(\delta\hat{I}_{\mathrm{R}})^2\rangle}{2e^*\tau_{\mathrm{c}}I_{\mathrm{R}}} = \frac{\Delta S_{\mathrm{RR}}}{2e^*\tau_{\mathrm{c}}(1-\tau_{\mathrm{c}})I_{\mathrm{t}}} \tag{4.22}$$

valid beyond the WBS regime for $\mathrm{QPC_c}$ thanks to the τ_{c} factor. For Laughlin's fractions and if $(1-\tau_{\mathrm{c}}) \ll 1$, this equation reduces to [50]:

$$\boxed{F_{\mathrm{thy}} = -\coth(2\pi\Delta)\coth\left[(\frac{\pi}{2}-2\Delta)(4\Delta-1)\right]} \tag{4.23}$$

At $\nu = 1/3$, we therefore expect $F_{\mathrm{thy}} \approx 3.27$. Importantly, note that the current auto-correlation noise of the transmitted current is *super-Poissonian*, i.e. much higher than the $2e^*I_{\mathrm{t}}$ dependence expected in the naive 'beam-splitter' picture of $\mathrm{QPC_c}$ (either transmitting or reflecting the impinging quasiparticle): $\langle(\delta\hat{I}_{\mathrm{T}})^2\rangle = F_{\mathrm{thy}} \times 2e^*I_{\mathrm{R}} \gg 2e^*I_{\mathrm{R}}$.

4.4 Summary of noise predictions

To conclude on the theoretical predictions, let us give the following summary. The unconventional braiding between impinging anyons and quasiparticle-quasihole pairs spontaneously generated at $\mathrm{QPC_c}$ is predicted to give three complementary noise signatures in the source-analyzer setup:

- First, strong negative cross-correlations, in striking contrast with the vanishing cross-correlations expected in the free fermions case.
- Second, a marked dependence of these negative cross-correlations with impinging current imbalance.
- Finally, super-Poissonian auto-correlations of the current transmitted across $\mathrm{QPC_c}$,

The source-analyzer device therefore appears to be a powerful platform for probing non-trivial anyon braiding.

4.5 Experimental implementation

After this theoretical overview, let us turn toward the experimental implementation and signature of anyon statistics in such a source-analyzer setup.

4.5.1 Description of the sample

The device used to probe the signatures of anyon statistics in a source-analyzer setup is shown in Fig. 4.7. It is the same sample as the one used to reveal Andreev-like processes discussed in chapter 3 (see section 3.4.1 for further characteristics). Note that the 2DEG was grown in the same MBE chamber as the one used in the pioneering "collider" experiment by Bartolomei *et al.* [2] but in a different batch. Like in the study of the previous chapter, it is cooled down to $T = 35$ mK (unless specified otherwise) and immersed in a strong perpendicular magnetic field $B \simeq 13.5$ T, corresponding to the center of the quantum Hall plateau at $\nu = 1/3$ (see figure 3.9).

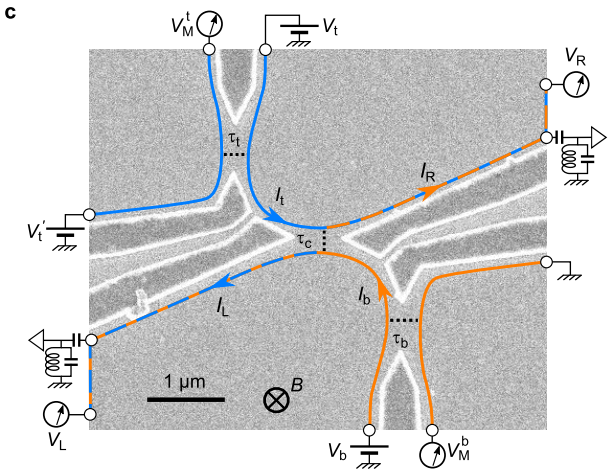

Figure 4.7: **SEM photograph of the sample.**
Aluminum gates on the surface of an AlGaAs|GaAs heterojunction appear darker with bright edges. Top-left (QPC_t) and bottom right (QPC_b) source QPCs are set to equal transmission ratios $\tau_t \approx \tau_b$ of the $\nu = 1/3$ FQH edge channel. The impinging beam imbalance $I_- \equiv |I_t - I_b|$ is tuned with DC-voltages $V_t - V_b$. V_t' is maintained at 0 except for the separate shot noise characterization of the central analyzer QPC_c, which is performed with a direct voltage bias ($V_t = V_t'$ and $V_b = 0$).

The core of the device is composed of three QPC constrictions in series separated by approximately 1.5 µm: two external sources (QPC_t and QPC_b) and a central analyzer (QPC_c). The corresponding differential transmissions $\tau_{t,b,c}$ are defined by

$$\tau_{t(b)} \equiv \frac{\partial V_M^{t(b)}}{\partial V_{t(b)}}, \tag{4.24}$$

$$\tau_c \equiv \left(\frac{\partial V_R / \partial V_b}{2(1-\tau_b)} + \frac{\partial V_L / \partial V_t}{2(1-\tau_t)} \right), \tag{4.25}$$

(with the partial derivative realized by lock-in measurements) and are tuned by field effect using aluminum split gates (darker with bright edges on Fig. 4.7). Note that here we define the differential transmissions of sources (unlike in the Andreev-like scattering study of the previous chapter). Representative transmission profiles of the considered QPCs have been discussed in the previous chapter and shown in Fig. 3.10.

Therefore, this sample directly realizes the proposal of [1] schematized in Fig. 4.1.

4.5.2 Separate characterization of QPC charges

Probing information on the statistics of the involved quasiparticles requires first to ensure that each QPC is set in the WBS regime, transmitting charges $e/3$. In the same spirit as the characterization of charges performed in section 3.5, this is achieved thanks to standard shot noise measurements [10, 11], by applying a direct DC-voltage V on the examined QPC and by using the conventional shot noise expression [123, 124]:

$$S_{\rm sn} = 2e^* \frac{\tau^{\rm DC}(1-\tau^{\rm DC})V}{R_{\rm H}} \left[\coth \frac{e^*V}{2k_{\rm B}T} - \frac{2k_{\rm B}T}{e^*V} \right] \tag{4.26}$$

where $\tau^{\rm DC}$ is the "DC-transmission", i.e. the ratio between the transmitted and the impinging DC-current on QPC. We simply obtain this value by integration of the differential transmissions $\tau_{\rm t,b,c}$ over the bias voltage.

To access the tunneling charge across each QPC separately, three distinct measurements are performed: one for the analyzer $\rm QPC_c$ and one for each source QPC. Moreover, the charge emitted by the source during the main measurement of the Fano factor P can also be determined via the total source noise S_Σ thanks to charge conservation, like in section 3.5.2 (see section 4.6 for the corresponding experimental data).

Characterization of the source QPCs tunneling charge

First, the charges of individual source $\rm QPC_{t(b)}$ are characterized by applying a finite voltage $V_{\rm t(b)}$ while $V_{\rm b(t)} = 0$. This situation corresponds to the fully imbalanced case $|I_-/I_+| = 1$ with only one source used at a time. As presented in section 3.5.2, the charge of the source can be inferred by current conservation through the sum signal $S_\Sigma = \Delta S_{\rm LL} + \Delta S_{\rm RR} + 2S_{\rm LR}$.

Black triangles in Fig. 4.8a(b) display S_Σ measured in such a configuration where the top-left $\rm QPC_t$ (bottom-right $\rm QPC_b$) source is individually biased by the DC-voltage $V_{\rm t}$ ($V_{\rm b}$). Continuous lines show the predictions of Eq. (4.26) with $e^* = e/3$ (red) and $e^* = e$ (blue), showing a good agreement between data and $e/3$-charged quasiparticles. The simultaneously measured transmission ratios $\tau_{\rm t}$ ($\tau_{\rm b}$) are presented in insets.

This agreement with $e/3$ predictions indicates that each source set in the WBS regime emits diluted beams of $e/3$-charged quasiparticles.

Analyzer QPC charge characterization

Second, the central QPC is set in the WBS regime $\tau_{\rm c} \ll 1$, and its tunneling charge is inferred from a separate noise measurement (previously discussed in section 3.5.1). Without changing any gate voltage susceptible to alter the tuning of QPCs, the same bias is swept on both sides of one source QPC: $V_{\rm t} = V'_{\rm t}$ while $V_{\rm b} = 0$ (or alternatively $V_{\rm b} = V'_{\rm b}$ while $V_{\rm t} = 0$), which is equivalent to applying a direct finite voltage $V_{\rm t} = V'_{\rm t}$ on $\rm QPC_c$. In practice, this characterization is performed just before the main noise measurement, and the tunneling charge across $\rm QPC_c$ is inferred thanks to linear fits at voltages above the thermal rounding ($e_{\rm c}V > 3k_{\rm B}T$).

Fig. 4.8c presents one such noise measurement (main panel) and the corresponding transmission ratio $\tau_{\rm c}$ (inset). The schematic indicates the device configuration. Excess auto-correlations $\Delta S_{\rm LL} \equiv \langle \delta I_{\rm L}^2 \rangle - \langle \delta I_{\rm L}^2 \rangle (V=0)$ (blue discs) $\Delta S_{\rm RR} \equiv \langle \delta I_{\rm R}^2 \rangle - \langle \delta I_{\rm R}^2 \rangle (V=0)$ (blue circles) and cross-correlations $S_{\rm LR}$ (green discs) are plotted in panel (c). Due to current conservation, these

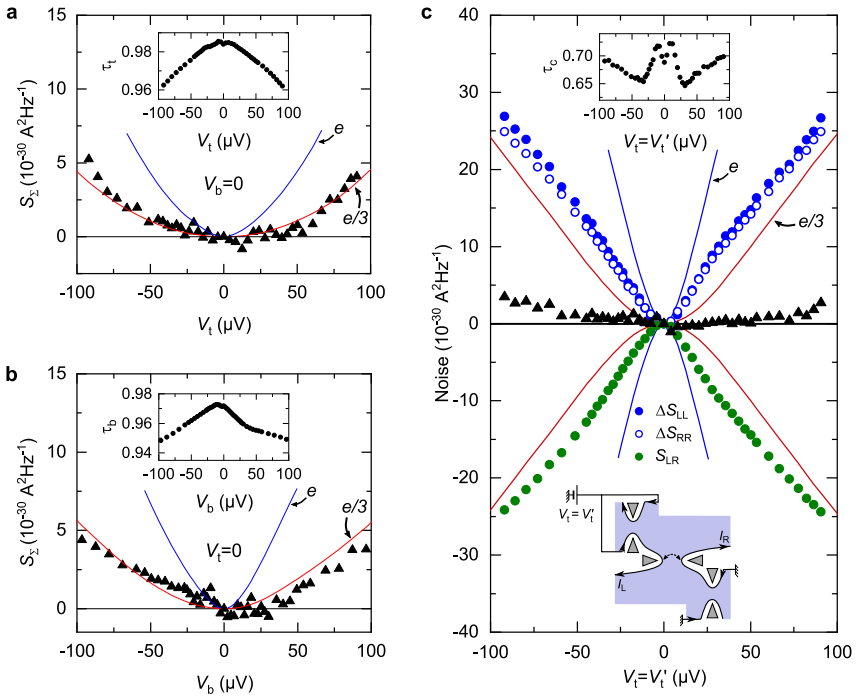

Figure 4.8: **Charge characterizations of individual QPCs**, all set in the WBS limit $\tau_{t,b} \simeq 0.95$, $\tau_c \simeq 0.89$ (see insets).
a (b) Shot noise characterization of the charge of the quasiparticles emitted by the source $\mathrm{QPC_t}$ ($\mathrm{QPC_b}$) via the sum signal S_Σ when the considered QPC is individually biased with $V_{t(b)}$ (while $V_{b(t)} = 0$).
c Auto- (blue symbols) and cross-correlations (green symbols) of current versus the DC-voltage $V_t = V_t'$, implementing a direct bias of $\mathrm{QPC_c}$. The data are confronted with predictions of Eq. (4.26) for charge $e/3$ (red line) and e (blue line).

three signals are expected to match each other (up to the sign for cross-correlations) and the corresponding sum S_Σ (black triangles) is predicted to be zero.

The data are confronted with the standard shot noise expression Eq. (4.26) with $e^* = e/3$ (red line) and $e^* = e$ (blue line). All noise signals are consistent with quasiparticles of charge $e/3$ and in marked contrast with charge e, confirming that the central analyzer QPC indeed transmits $e/3$-charged anyons.

The small but discernible deviation from $S_\Sigma = 0$ that develops at high voltage is attributed to a nonlocal heating of the source QPC, which induces a noise increase such as delta-T noise (see section 4.12.2 for a dedicated investigation). Note that such discrepancies between auto- and cross-correlations have been observed in other labs (see [125] for instance), although without an upstream QPC, and their origin remains unclear.

Note also that an intriguing change of slope for the central $\mathrm{QPC_c}$ appears at low voltage, which shows up as an arbitrary lower temperature in Eq. (4.26). This feature indicates that the phenomenological prediction of Eq. (4.26) could be refined: indeed a recent theoretical study of Schiller *et al.* predicts such a behavior and makes a link with the scaling dimension Δ [65] (see Appendix B for a further investigation).

In spite of these small discrepancies, the agreement with charge $e/3$ and the marked contrast with charge e in the robust cross-correlation signal indicate that the charges tunneling across the analyzer $\mathrm{QPC_c}$ are $e/3$-quasiparticles.

Thus, all three QPCs set in the WBS regime transmit the expected quasiparticles of fractional charge $e/3$. The investigation of anyon statistics through non-trivial braiding can now be performed by using both sources simultaneously.

4.6 Representative anyon signature with symmetric sources

We can now delve into the specific measurement of cross-correlations with symmetric sources and discuss how they inform on the anyon statistics of quasiparticles.

At $T \simeq 35$ mK, all three QPCs are set in the WBS regime ($\tau_{t,b} > 0.9$, $\tau_c \simeq 0.7$ as shown in the inset of Fig. 4.9c) and the same voltage is applied on both sources $V_t = V_b$ in order to induce two diluted beams of $e/3$-charged quasiparticles (see schematics of the device configuration in Fig. 4.9a).

In addition to the separate individual characterization of source charges (see the previous section 4.5.2), we can have access to the mean charges emitted from both sources simultaneously with the principal cross-correlation measurement. Indeed, as previously developed in section 3.5.2, the incident charges can be inferred through the noise sum S_Σ, which precisely corresponds to the shot noise across both voltage-biased sources:

$$S_\Sigma = 2e^* \left[\tau_t I_t \left(\coth \frac{e^* V_t}{2k_B T} - \frac{2k_B T}{e^* V_t} \right) + \tau_b I_b \left(\coth \frac{e^* V_b}{2k_B T} - \frac{2k_B T}{e^* V_b} \right) \right] \tag{4.27}$$

Note that this equation is the generalized form of Eq. (4.26) with two distinct sources. In the ideal case of fully symmetric bias in the Poissonian limit (i.e. $1 - \tau_t, 1 - \tau_b \ll 1$ and $V_t = V_b = V$), this equation reduces to:

$$S_\Sigma = 2e^* I_+ \left[\coth \frac{e^* V}{2k_B T} - \frac{2k_B T}{e^* V} \right] \tag{4.28}$$

Fig. 4.9b displays such S_Σ data (black triangles) in close agreement with predictions of Eq. (4.27) (red line). This quantitative matching attests that the same impinging quasiparticles that induce the cross-correlations of interest have indeed a charge $e/3$.

The main cross-correlation signal S_{LR} in the presence of two symmetric beams of incident quasiparticles is normalized by $\tau_c(1 - \tau_c)$ and plotted as a function of the noise sum S_Σ in Fig. 4.9c. Following the definition of Eq. (4.1), the experimental value of the generalized Fano factor P_{exp} is therefore straightforwardly obtained from a linear fit of the data (red dashed line). In the representative example of Fig. 4.9, the corresponding value of the generalized Fano factor (slope of the dashed line) is $P_{exp} \simeq 1.9$. This result, in remarkable quantitative agreement with the prediction $P_{thy}(0) = -2$, corroborates the pioneering observation of Ref. [2].

However, this striking agreement with theory is hampered by a weak dependence of P_{exp} upon the chosen definition of the QPC_c transmission ratio. Indeed, while P_{thy} is predicted to strongly depend on the specific definition of τ_c (see Table 4.1 in section 4.2.4), the observed value of P_{exp} is essentially unchanged due to $\tau_c \sim \tau_c^{bis} \sim \tau_c^{ter}$ (with changes lower than 10%, of the order of experimental accuracy). This difference between observations and predictions can be linked to the voltage-dependence of τ_c which drastically differs from the theoretically expected power-law $1 - \tau_c \propto V^{2\nu-2}$ [100] (see section 4.12.3 for further discussions).

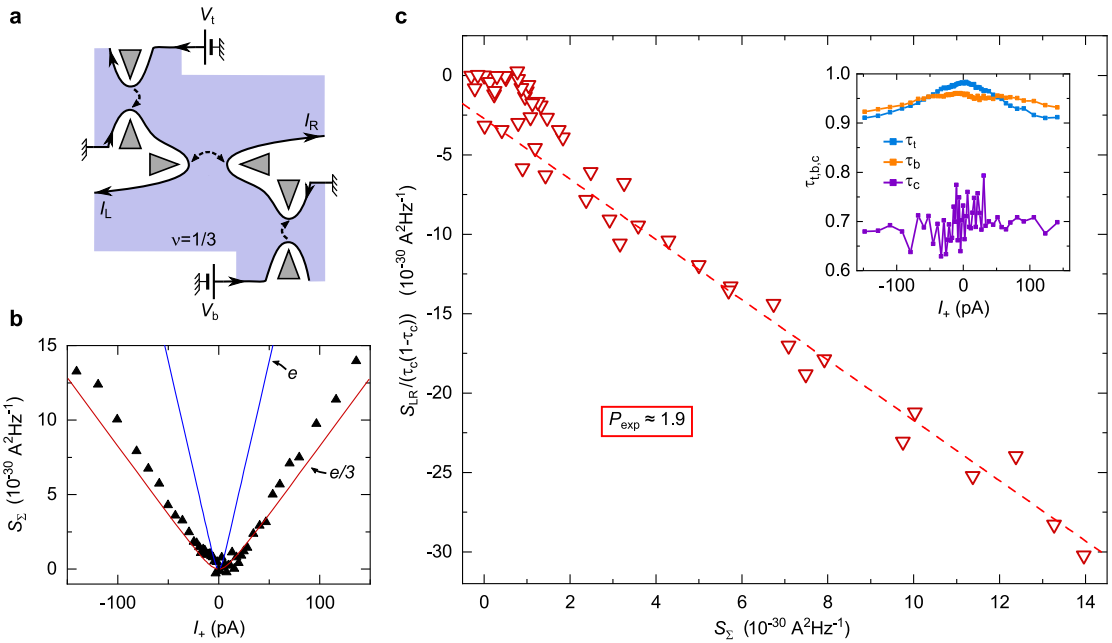

Figure 4.9: **Cross-correlation signature of anyons at $\nu = 1/3$ with balanced sources.** All QPCs are tuned in the WBS limit $\tau_{t,b} \simeq 0.96$, $\tau_c \simeq 0.7$ (see inset).
a Device configuration during the main cross-correlation measurement.
b Simultaneous determination of the incident charges via the sum noise S_Σ (black triangles) when sources are symmetrically voltage-biased. The red (blue) line corresponds to Eq. (4.27) predictions with $e^* = e/3$ ($e^* = e$).
c Normalized cross-correlations (red symbols) versus sum noise with symmetric sources. The generalized Fano factor $P_{\rm exp}$ (here $P_{\rm exp} = -1.9$) corresponds to the slope of a linear fit (red dashed line).

In spite of these quantitative reservations, the presence of a *strong negative cross-correlation* signal is itself a first key marker of unconventional exchange statistics of the involved quasiparticles. Exploring its dependence upon the incident current imbalance can provide a second complementary marker.

4.7 Dependence of P on the impinging current imbalance

As derived in section 4.2.3, the generalized Fano factor is predicted to strongly depend on the imbalance of impinging currents, which constitutes another signature of anyon statistics. Then, let us confront the measured $P_{\rm exp}$ dependence upon $|I_-/I_+|$ with the Eq. (4.16), (4.20) and (4.21), as shown in Fig. 4.10.

The experimental values of $P_{\rm exp}$ (open circles) are obtained for $\mathrm{QPC_c}$ set at $\tau_c \simeq 0.7$, with a tunneling charge across the central QPC $e_c \simeq 0.3e$. Each tested $|I_-/I_+|$ is tuned by keeping the ratio V_t/V_b constant while sweeping V_t, V_b. The horizontal error bars encapsulate the uncertainty resulting from the unequal variation of $\tau_t(V_t)$ and $\tau_b(V_b)$, while the vertical error bars represent the difference between the values of $P_{\rm exp}$ extracted at negative and positive voltage. The continuous red line displays the prediction of equation (4.16) with τ_c that is

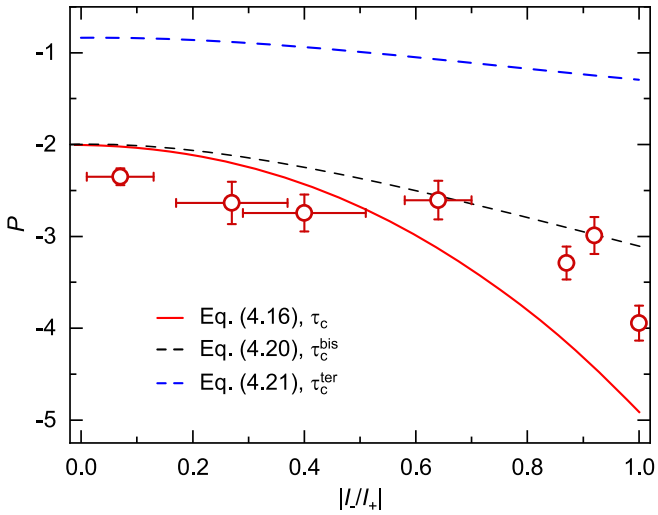

Figure 4.10: $P_{\rm exp}$ **versus incident current imbalance at** $\nu = 1/3$**.**
Red circles display the generalized Fano factor $P_{\rm exp}$ plotted versus the relative difference in incident currents $|I_-/I_+|$ for a given device tuning (all QPCs set in the WBS regime). Horizontal error bars represent variations in $|I_-/I_+|$ over the range of applied voltage. Vertical error bars correspond to the difference between values of $P_{\rm exp}$ separately extracted at negative and positive voltages. Lines display the predictions of Eq. (4.16) (red), (4.20) (dashed black) and (4.21) (dashed blue) respectively, corresponding to the different choice of $\tau_{\rm c}$ for normalization.

relevant for the quantitative comparison. Dashed black and blue lines represent equations (4.20) and (4.21) respectively (corresponding to $\tau_{\rm c}^{\rm bis}$ and $\tau_{\rm c}^{\rm ter}$).

The slight variation of $P_{\rm exp}$ at low asymmetry becoming progressively stronger with increasing $|I_-/I_+|$ is consistent with theory. Quantitatively, a reasonable agreement is found: ratios $P_{\rm exp}(1)/P_{\rm exp}(0) \simeq 1.5$ (confirming Ref. [2] for which $P_{\rm exp,[2]}(1)/P_{\rm exp,[2]}(0) \simeq 1.6$) and $P_{\rm thy}(0)/P_{\rm thy}(1) \simeq 2.5$ have indeed the same order of magnitude.

This expected significant *dependence of the generalized Fano factor on impinging current imbalance* offers a second strong and complementary marker of the quasiparticle fractional exchange phase.

4.8 Anyon signature in auto-correlations

As mentioned in section 4.3, when only one source is activated (which is equivalent to the fully imbalanced configuration $|I_-/I_+| = 0$), the autocorrelations of current transmitted across the QPC $\Delta S_{\rm RR}$ are predicted to manifest signatures of the unconventional braiding statistics of Laughlin anyons [50, 47, 134].

In that case, the signal of interest $\Delta S_{\rm RR}$ is investigated through the Fano factor F defined in Eqs. (4.22), (4.23) and predicted to give $F_{\rm thy} \approx 3.27$ at $\nu = 1/3$. Using the Fano factor F allows us to specifically investigate the braiding contribution of $\rm QPC_c$ to the auto-correlations and to get rid of the redistribution of the impinging source noise $2e^*I_{\rm t}(1-\tau_{\rm c}) = S_\Sigma(1-\tau_{\rm c})$.

In the same spirit as in section 4.2.1, the Fano factor can be generalized beyond the WBS regime via the following definition:

$$F_{\rm thy} \equiv \frac{\Delta S_{\rm RR}}{S_\Sigma \tau_{\rm c}(1-\tau_{\rm c})} \tag{4.29}$$

where S_Σ is the total noise signal which corresponds straightforwardly to the source noise.

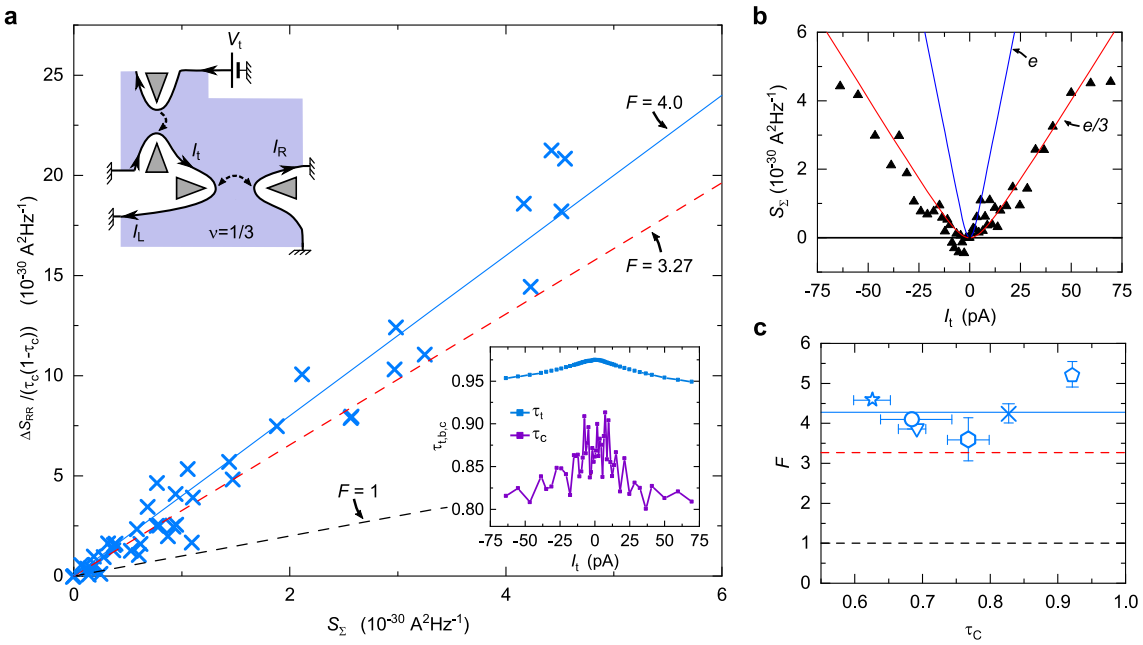

Figure 4.11: **Auto-correlations anyon signature with a single source at $\nu = 1/3$.** All QPCs are tuned in the WBS limit $\tau_{\rm t,b} \simeq 0.96$, $\tau_{\rm c} \simeq 0.85$ (see inset).
a Illustrative anyon signature in auto-correlations $\Delta S_{\rm RR}/(\tau_{\rm c}(1-\tau_{\rm c}))$ plotted versus the source noise S_Σ. The blue continuous line corresponds to a linear fit giving $F_{\rm exp} \simeq 4.0$ which can be compared to the prediction $F_{\rm thy} \approx 3.27$ (red dashed line) and the expectation in the naive beam-splitter picture $F_{\rm BS} = 1$ (black dashed line). The device configuration is schematized in the inset.
b Simultaneous characterization of the incident quasiparticle charges via the sum noise S_Σ (black triangles). The red (blue) line corresponds to the Eq. (4.27) prediction with $\tau_{\rm b} = 0$ and $e^* = e/3$ ($e^* = e$).
c Measured Fano factor $F_{\rm exp}$ for all operating points with QPC$_{\rm c}$ in the WBS regime ($\tau_{\rm c} > 0.6$) plotted as a function of the analyzer transmission ratio $\tau_{\rm c}$. The horizontal error bars encompass the variation of $\tau_{\rm c}$ over the fit range and the vertical error bars indicate the difference between the fits on positive and negative voltages. The continuous blue line corresponds to the mean value $\langle F_{\rm exp}\rangle$. The dashed line indicates the prediction $F_{\rm thy} \approx 3.27$ [50] (red) and the expectation in the naive beam-splitter picture $F_{\rm BS} = 1$ (black).

Figure 4.11 shows the results of a representative operating point at $\tau_{\rm t} \simeq 0.96$ and $\tau_{\rm c} \simeq 0.85$ (see inset in 4.11a). In panel (b), the impinging quasiparticle charge is ensured by comparing the source noise to the shot noise prediction of Eq. (4.26), which shows good agreement with charge $e^* = e/3$ (red line) in contrast with $e^* = e$ (blue line).

The main current auto-correlation signal $\Delta S_{\rm RR}$ is normalized by $\tau_{\rm c}(1-\tau_{\rm c})$ and plotted as a function of the source noise S_Σ. As for the cross-correlation signal, following the definition of Eq. (4.29), the generalized Fano factor $F_{\rm exp}$ is directly obtained from a linear fit of the data (blue continuous line), corresponding to $F_{\rm exp} \simeq 4.0$ for this illustrative example. This is in marked

contrast with the result expected in the naive 'beam-splitter' picture ($F_{\mathrm{BS}} = 1$ see black dashed line). Instead, we get a *super-Poissonian* noise which reveals the underlying anyon braiding process.

Qualitatively, the clear super-Poissonian auto-correlation signal is a signature of anyon statistics. This has been corroborated by a simultaneous independent experiment of the Weizmann Institute [50]. Quantitatively, the measured Fano factor is systematically higher than the predictions. Figure 4.11c displays the obtained F_{exp} for operating points with $\tau_{\mathrm{c}} > 0.6$ (the symbols match the ones of Fig. 4.9 and 4.13). Indeed, while theory predicts $F = 3.27$ (red dashed lines in panels (a) and (c)), the mean value of the Fano factor over all the explored points is $\langle F_{\mathrm{exp}} \rangle = 4.28$ (blue line). But, this stronger-than-expected signal makes the qualitative contrast with the naive 'beam-splitter' approach even more striking.

Therefore, the clear super-Poissonian auto-correlations of current obtained in the single source configuration constitute a third and complementary qualitative marker of the underlying anyon braiding process.

4.9 Robustness of anyon signature versus temperature

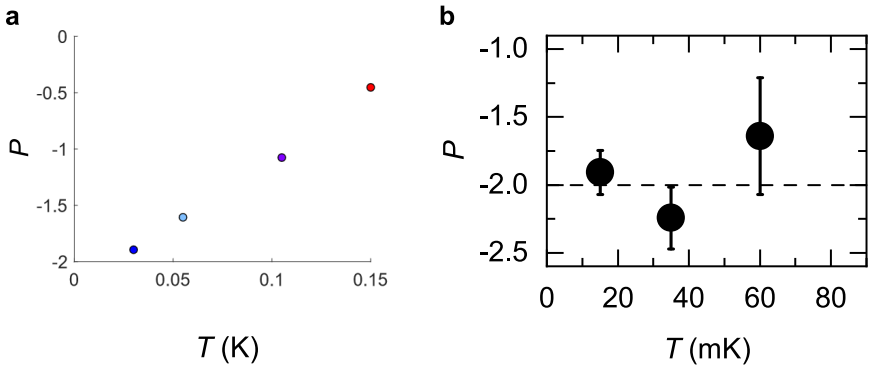

Figure 4.12: **Mean value $\langle P_{\mathrm{exp}} \rangle$ versus temperature at $\nu = 1/3$.**
a Evolution of P with temperature in the Bartolomei *et al.* experiment (adapted from [131])
b $\langle P_{\mathrm{exp}} \rangle$ measured at $T = 15$, 35 and 60 mK. The horizontal dashed line indicates the predicted value $P_{\mathrm{thy}} = -2$. Vertical error bars encompass the standard deviation between values of P over the considered analyzer settings.

The experiment by Bartolomei *et al.* demonstrated that the cross-correlation signal is reduced at higher temperatures (see Supplementary Information of [2] and Fig. 4.12a from [131]). Therefore, the important variation of P with temperature calls for additional measurement at lower T, to confirm that the Fano factor saturates at $P_{\mathrm{exp}} = -2$ for lower temperature and that the quantitative agreement of P_{exp} with the $T = 0$ K prediction $P_{\mathrm{thy}} = -2$ is not fortuitous.

To this aim, the measurements are reproduced at $T \simeq 60$ and $T \simeq 15$ mK and they confirm the observations at $T = 35$ mK. Figure 4.12 synthesizes the values of the Fano factor obtained at different temperatures from [131] (panel (a)) and in the present thesis work (panel (b)). The vertical bars in (b) display the standard deviation between values of P over all the considered analyzer operating points.

Our measurements show that the mean value $\langle P_{\rm exp}\rangle$ saturates at the predicted -2 value for temperatures lower than 50 mK. The small tendency observed with a slightly higher value of $\langle P_{\rm exp}\rangle$ at 60 mK (panel (b)), is consistent with the observations of Bartolomei *et al* (panel (a)).

The quantitative agreement of the generalized Fano factor with the theoretical prediction is therefore corroborated by these additional measurements at lower temperatures.

4.10 Discriminating between Andreev-like reflection and braiding process

4.10.1 Fano factor prediction in Andreev-like scattering regime

In the case of the Andreev-like scattering process discussed in the previous chapter, the negative cross-correlations can also be used to define an effective Fano factor $P_{\rm A}$, similarly to Eq. (4.1).

In this source WBS - analyzer SBS configuration, unconventional anyon braiding does not contribute to the negative cross-correlation signal. Indeed, as the analyzer is set in the SBS, the impinging anyon of field operator $\psi_q(x)$ and charge $q = e/3$ would braid with quasiparticles of field operator $\psi_{q'}(x')$ and charge $q' = e$ (x and x' being the positions of the involved quasiparticles). The commutation of $\psi_q(x)\psi_{q'}(x')$ into $\psi_q(x')\psi_{q'}(x)$ leads to a phase term $e^{i(\pi/\nu)(qq'/e^2){\rm sign}(x-x')} = e^{i\pi{\rm sign}(x-x')}$:

$$\psi_q(x)\psi_{q'}(x') = e^{i\frac{\pi}{\nu}\frac{q}{e}\frac{q'}{e}{\rm sign}(x-x')}\psi_q(x')\psi_{q'}(x) \tag{4.30}$$

and the braiding phase $\theta = \pi\dfrac{qq'}{\nu e^2}{\rm sign}(x-x')$ is therefore trivial if $q = e$ and $q' = e/3$. This trivial braiding in the sources WBS-analyzer SBS regime is irrelevant to explain the negative cross-correlations.

Instead, they are completely due to the Andreev-like scattering. At filling factor ν, as the transport process involves simultaneously a transmitted charge e and a back-scattered hole $-(1-\nu)e$, the cross-correlations are straightforwardly given by $-(1-\nu)$ times the shot noise of the tunneling current $2eI_+\tau_{\rm c}$, i.e.:

$$\boxed{\begin{aligned} P_{\rm A} = \frac{S_{\rm LR}}{2\nu e I_+\tau_{\rm c}} &= \frac{-(1-\nu)2eI_+\tau_{\rm c}}{2\nu eI_+\tau_{\rm c}} \\ P_{\rm A} &= \frac{-(1-\nu)}{\nu} \end{aligned}} \tag{4.31}$$

Importantly, note that $P_{\rm A}$ is independent of the relative asymmetry factor $|I_-/I_+|$. At the specific $\nu = 1/3$ filling factor, $P_{\rm A} = -2$. This quantitatively corresponds to the predictions of the braiding regime! Note that this quantitative match between $P_{\rm A}$ and $P_{\rm thy}$ is not valid for other ν in general.

Nevertheless, the quantitatively identical value of P for two distinct mechanisms (with only one related to the unconventional exchange phase of quasiparticles) makes it highly desirable to find a direct marker that discriminates between braiding and Andreev processes.

4.10.2 Robustness of $P(I_- \simeq 0)$ versus $\mathrm{QPC_c}$ transmission ratio

While the values of P_A and P_thy are predicted to be asymptotically equal for both the WBS and SBS regime, a difference could emerge in the intermediate regime $\tau_\mathrm{c} \sim 0.5$. To explore the cross-over between Andreev and braiding regimes, the value of P_exp is extracted while broadly changing the transmission ratio τ_c, as summarized in Fig. 4.13.

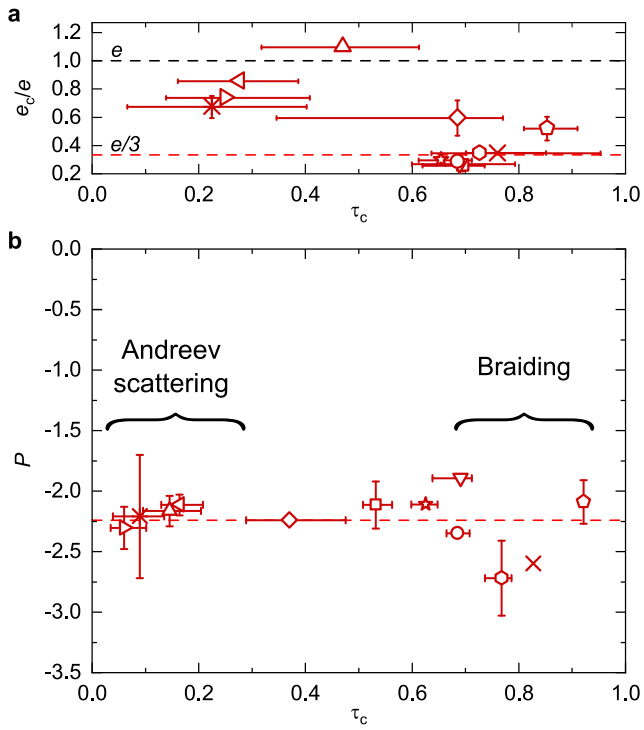

Figure 4.13: $P_\mathrm{exp}(I_- \simeq 0)$ **versus analyzer tuning.** Identical symbols correspond to a same device tuning (τ_c differs in (a) and (b) due to different voltage-bias configurations). Error bars are shown if larger than symbols. The horizontal error bars display the variation of τ_c in the bias range where e_c (a) or P_exp (b) are extracted. The vertical error bars encompass the difference between measurements at negative and positive voltages.
a. Analyzer charge cross-over from $e_\mathrm{c} \simeq e/3$ to e.
b. Absence of cross-over in $P_\mathrm{exp}(I_- \simeq 0, \tau_\mathrm{c})$. The horizontal dashed line indicates the mean value $\langle P_\mathrm{exp} \rangle = -2.2$. The expected dominant transport process is indicated by horizontal brackets.

The upper panel (a) displays the tunneling charge e_c across the central QPC for each of the operating points of the lower panel (b) (with matching symbols). The cross-over between $e_\mathrm{c} = e/3$ and e [114, 115, 56] is established. Note that the values of τ_c (x-axis) in panels (a) and (b) differ due to the different voltage-bias configurations. The horizontal error bars correspond to the variation of τ_c in the bias range, while vertical error bars encompass the difference between measurements at positive and negative voltages.

Panel (b) represents the measured Fano factor P_exp, plotted versus τ_c. A striking robustness of P_exp is observed as τ_c varies, blurring the cross-over between braiding and Andreev mechanisms.

The absence of distinguishable cross-over between the two processes calls even more strongly for a direct signature allowing to differentiate the braiding and Andreev mechanisms.

4.10.3 Using imbalance to distinguish between the two processes

Importantly, Andreev-like scattering and braiding processes have different behaviors when the impinging beams are imbalanced. In the case of Andreev reflection, each process is independent, which implies that the noise signal obtained in the fully symmetric ($|I_-/I_+| = 0$) and fully asymmetric ($|I_-/I_+| = 1$) configuration is expected to be the same. By contrast, as discussed in section 4.7, the cross-correlations induced by nontrivial anyon braiding significantly depend on the relative asymmetry $|I_-/I_+|$.

This feature provides a straightforward test to differentiate between the two processes, as displayed in Fig. 4.14. As illustrated in the schematics, we compare the two asymptotic situations $|I_-/I_+| = 1$ (green) and $|I_-/I_+| = 0$ (black) in both Andreev (panel (a)) and braiding (panel (b)) cases.

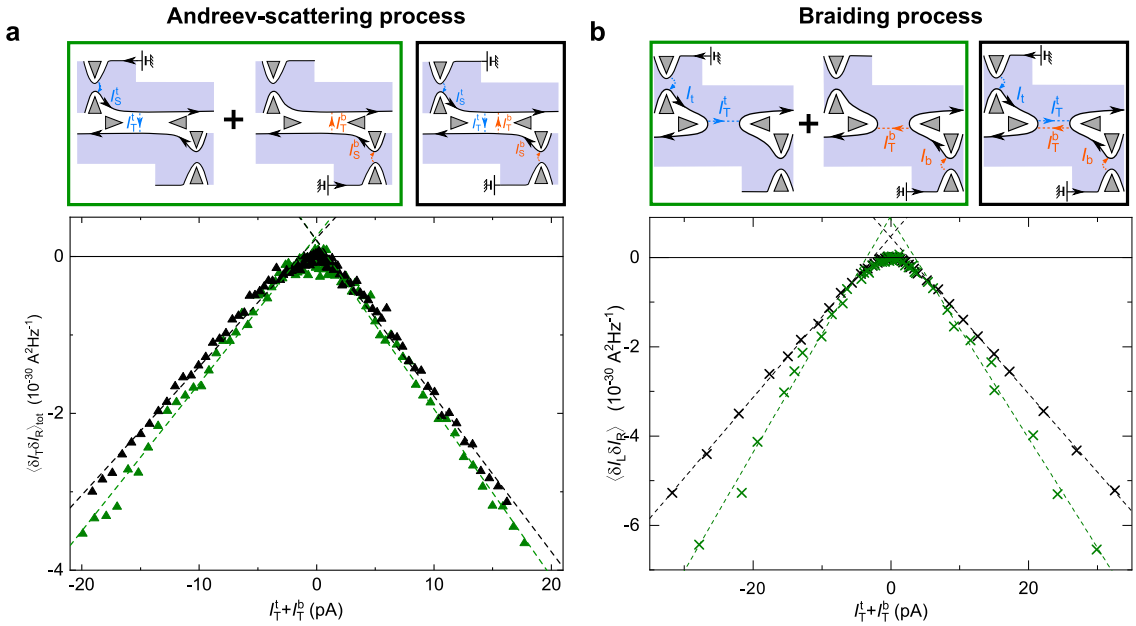

Figure 4.14: **Differentiating anyons braiding from Andreev mechanisms.**
a Cross-correlations with QPC$_c$ tuned such that $e_c \simeq e$ while $e_{t,b} \simeq e/3$. The displayed cross-correlation signal was obtained from two configurations: first as the sum of the noise measured alternatively with a single active source (green symbols and schematics) and second with two symmetrically biased sources (black symbols and schematics).
b cross-correlation measured thanks to the same procedure but in the braiding regime with QPC$_c$ tuned such as $e_c \simeq e_{t,b} \simeq e/3$

On the one hand, we measure the cross-correlation signal obtained with one active source at a time: first $V_t \neq 0$ and $V_b = 0$, second $V_b \neq 0$ and $V_t = 0$ (green boxed schematics). The sum of these two independently measured signals is then plotted versus the total transmitted current $I_T^t + I_T^b$ in the main panel of Fig. 4.14a,b (green symbols).

On the other hand, we measure the cross-correlation signal obtained in the balanced configuration where the sources of equal transmissions are simultaneously biased with symmetric voltages: $V_t = V_b$ (black boxed schematics). The measured S_{LR} is then plotted in the main panel of Fig. 4.14a,b (with dashed line corresponding to linear fits).

Hence, the main panels of (a) and (b) (which display the results of the illustrative oper-

ating point respectively displayed as triangles and crosses in Fig. 4.14) give a straightforward comparison, which confirms this discriminating property. While the Andreev-like mechanism (a) presents no difference between symmetric and asymmetric measurements, the configuration probing nontrivial braiding processes displays a marked dependence on imbalance (b).

Fig. 4.14 synthesizes a systematic comparison between balanced and imbalanced situations for all operating points along the cross-over between braiding and Andreev processes. It is quantified by the "Asymmetric to Symmetric" ratio AS/S between fitted linear slopes (dashed lines) and it is plotted versus normalized tunneling charge across $\mathrm{QPC_c}$ e_c/e, which controls the cross-over. When $e_\mathrm{c} \approx e/3$ (vertical dashed line), we systematically observe notably larger cross-correlations in the imbalanced configuration, whereas for larger values of e_c the asymmetric to symmetric configurations ratio approaches 1 (horizontal line). This reveals a change of the dominant transport mechanism as e_c increases and experimentally supports the expected crossover from unconventional exchange to the Andreev processes.

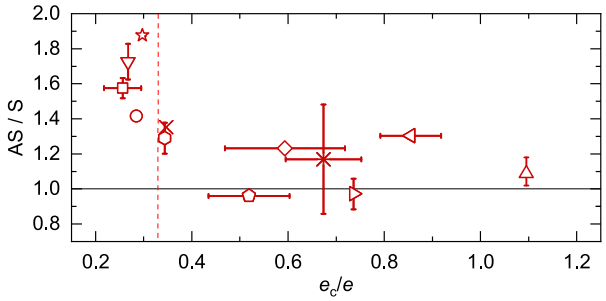

Figure 4.15: **Systematic comparison between the balanced and the imbalanced cases.**
Symbols (matching with the one of Fig. 4.13) correspond to the ratio (AS/S) of slopes $S_\mathrm{LR}/(I_\mathrm{T}^\mathrm{t} + I_\mathrm{T}^\mathrm{b})$ between asymmetric (one activated source at a time) and symmetric (both sources symmetrically biased) impinging beams of quasiparticles. Vertical error bars encompass the difference between slopes obtained at negative and positive voltages. (AS/S) is plotted versus the tunneling charge across $\mathrm{QPC_c}$ characterized previously. Horizontal error bars correspond to the variation of τ_c over the fitting range.

Therefore, this comparison constitutes a direct method to distinguish Andreev and braiding processes. In addition to being a marker of anyonic statistics, the dependence of noise signal with asymmetry sharpens the difference between these two distinct mechanisms.

4.11 Cross-correlations at $\nu = 2$

As a counterpoint to the strong negative cross-correlations informing on anyon statistics, the data are compared to the signal measured at $\nu = 2$ ($B = 2.4$ T). At this filling factor, the device is in the integer quantum Hall (IQH) regime, with two identical propagating channels referred to as "inner" and "outer", as illustrated in Fig. 4.16. The data shown in the following are measured with excitations on the outer channel while the inner one is fully reflected by QPCs. Fig. 4.16 shows the typical transmission profile of a QPC (here $\mathrm{QPC_t}$) in the $\nu = 2$ IQH regime, validating the sequential opening of two identical copropagating channels. Note that the considered transmission concerned only the active outer channel.

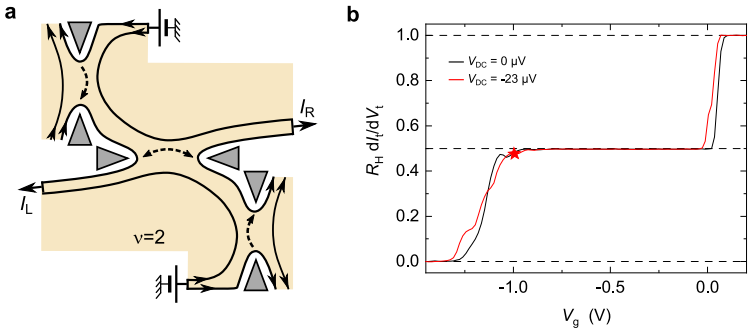

Figure 4.16: **Device configuration at $\nu = 2$.**
a The system is set to filling factor $\nu = 2$ (the 2DEG is illustrated by a yellowish region), corresponding to two co-propagating edge channels (black lines with arrows). Here, the excitations are carried by the 'outer' channel (furthest from the bulk).
b Typical transmission ratio $R_{\mathrm{H}} dI_{\mathrm{t}}/dV_{\mathrm{t}}$ of a $\mathrm{QPC_t}$ (the other two have very similar shapes) in the $\nu = 2$ IQH regime at bias voltage 0 and -23 μV. The operating point is indicated by the red star.

Transport in such an IQH system involves electrons with Fermi statistics. As discussed in section 4.2.2, in the limit of diluted beams of free fermions, the cross-correlations are therefore expected to be zero.

Importantly, note that the prediction of vanishing cross-correlations in the IQH regime is only valid in the non-interacting fermions picture. Indeed, interactions between two copropagating edge channels are expected to induce a cross-over from Fermi quasiparticles to bosonic *edge magneto-plasmon* (EMP) charge density waves [126, 97]. Such transition driven by interactions will be specifically studied in Chapter 6, with another dedicated device.

But for the sample discussed in the present chapter, the inter-channel interactions are negligible due to the short source-analyzer propagation distance and due to the small accessible voltage range ($|V| \lesssim 30$ μV). Hence, the discussion of this section remains in the free-fermion framework.

Figure 4.17 displays typical cross-correlation measurements performed at $\nu = 2$ with the same procedure as in the FQH regime (see section 4.6). All three QPCs are tuned to partially transmit the outer channel at transparencies comparable to the $\nu = 1/3$ case. Hence, the sources are tuned to emit balanced diluted beams of electrons $\tau_{\mathrm{t,b}} \simeq 0.95$ and $\mathrm{QPC_c}$ is set to $\tau_{\mathrm{c}} \simeq 0.8$. The side panels (a) and (b) respectively present the charge characterization of sources (measured simultaneously to the main panel results) and of the analyzer (measured slightly before in the specific direct bias configuration). Both the source and analyzer noise signals are found to match with charge e, following the prediction of Eq. (4.27) and Eq. (4.26) respectively. For the highest voltages $|V| > 50$ pA, note that an additional noise develops (indicated by open symbols), deviating from theoretical expectations and reducing the investigated range. This supplementary noise could be linked to inter-channel interactions driving the system beyond the considered free-fermion picture of this chapter.

The main panel Fig. 4.17c displays the renormalized cross-correlations $S_{\mathrm{LR}}/(\tau_{\mathrm{c}}(1-\tau_{\mathrm{c}}))$ as a function of the source shot noise S_Σ, in the same spirit as in Fig. 4.9c. In the investigated voltage range where all tunneling charges are e (full symbols), the cross-correlation signal is found to be slightly positive with a corresponding $P_{\mathrm{exp}} \simeq +0.2$ (obtained with a linear fit indicated by a black dashed line), different from the $\nu = 1/3$ FQHE case ($P \simeq -2$, red dashed line).

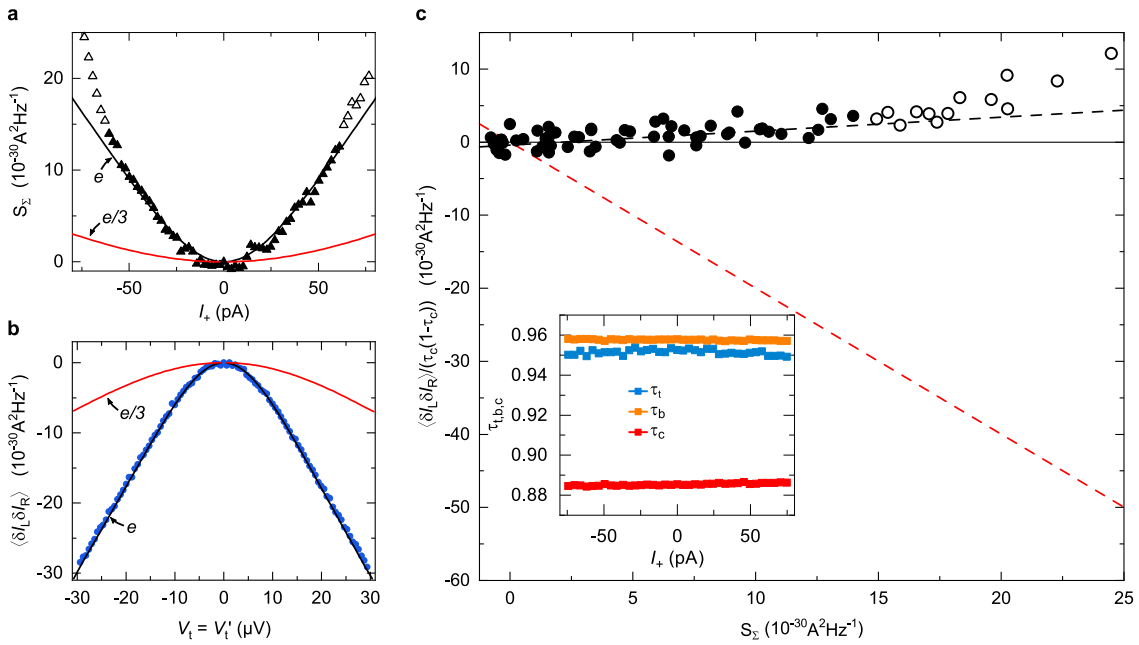

Figure 4.17: **Cross-correlations at $\nu = 2$ with balanced sources.** Similarly to Fig. 4.9, all QPCs are set in the WBS regime ($\tau_{t,b} \simeq 0.95$ and $\tau_c \simeq 0.5$ see inset of (c)) with $V_t = V_b$ and $V_t' = 0$, except for the analyzer characterization in (b) for which $V_t = V_t'$ and $V_b = 0$.
a,b Shot noise characterization of the tunneling charges $e_{t,b}$ (a) and e_c (b). Symbols correspond to the noise data, matching with the prediction for a tunneling charge e (black lines) at $S_\Sigma \lesssim 15 \times 10^{-30}$ A^2 Hz^{-1} (full symbols).
c Normalized cross-correlation measured in the balanced sources-analyzer configuration (symbols) are plotted vs source shot noise S_Σ. A linear fit at $S_\Sigma < 15 \times 10^{-30}$ A^2 Hz^{-1} (black dashed line) gives $P_{exp} \simeq +0.2$. The red dashed line corresponds to the Fano factor obtained at $\nu = 1/3$.

Even though this cross-correlation signal S_{LR} is not perfectly zero, possibly due to residual inter-channel interactions, it is in marked contrast with the strong negative S_{LR} found in the $\nu = 1/3$ regime.

Thus, these small and positive signal obtained in the fermion case of $\nu = 2$ corroborates that strong negative cross-correlations constitute a marker of unconventional anyon statistics in the Laughlin fraction $\nu = 1/3$.

4.12 Additional tests

The experimental results presented in this chapter provide strong signatures of anyonic unconventional braiding statistics, in agreement with predictions and measurements of other labs [2, 48, 50]. However, several experimental artifacts such as edge reconstruction and nonlocal heating could have an undesired impact on the noise signal and therefore may hamper our conclusions. The following sections investigate specifically those possible artifacts.

4.12.1 Absence of channel substructure along the $\nu = 1/3$ edge

In the $\nu = 1/3$ fractional quantum Hall regime, the edge is predicted to be composed of a single channel [55]. The predictions of Ref. [1, 135, 47, 46] have been obtained in this picture. But the integer filling factor $\nu = 1$, which is expected to present the same single channel structure can experimentally display additional substructures attributed to the smooth confinement potential combined with Coulomb interactions [136]. Such artifact is therefore associated with the microscopic details of the considered sample, hence calling for a specific investigation in our sample.

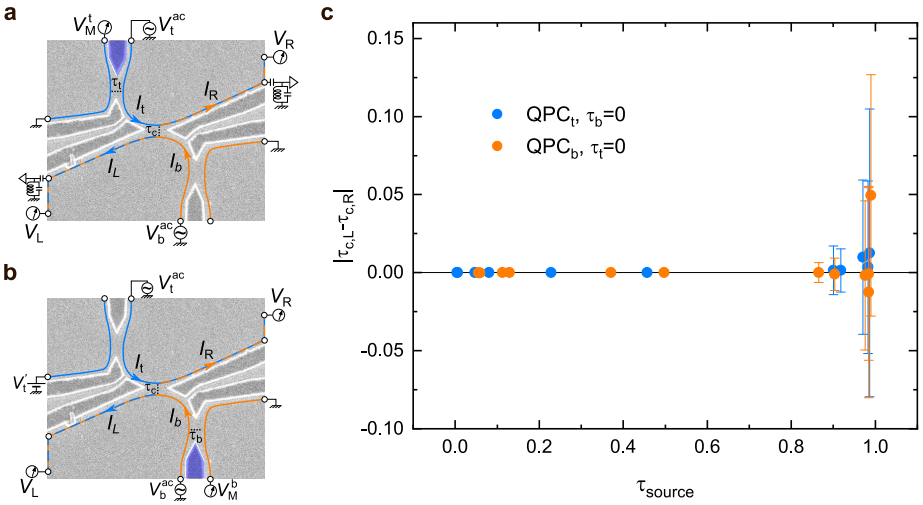

Figure 4.18: **Testing the absence of edge channel substructure at $\nu = 1/3$.**
a (b) Sample configuration for this measurement. The central transmission is obtained simultaneously in two ways. First, it is obtained with closed QPC$_b$ (QPC$_t$), from a small ac signal V_b^{ac} (V_t^{ac}) directly applied on QPC$_c$, giving $\tau_{c,L}$ ($\tau_{c,R}$). Second, it is deduced from a small ac signal V_t^{ac} (V_b^{ac}) applied on the partially open source QPC$_t$ (QPC$_b$) of transmission $\tau_{t(b)}$. The measurement is performed over the range $\tau_c \in [0, 1]$ at 10 different values of τ_c (tuned using only the gate furthest from QPC$_c$ colored in blue).
c The difference between the two simultaneously measured QPC$_c$ transmissions is plotted as a function of the source transmission $\tau_{t(b)}$ for both configurations of the (a) panel (light blue) and (b) panel (orange). The vertical error bars encompass the statistical error.

To check that such additional substructures do not emerge in our $\nu = 1/3$ case, we compare the transmissions across QPC$_c$ in the two following cases (see Fig. 4.18a and b):

- when a full beam directly impinges on QPC$_c$,
- when the current impinging on QPC$_c$ is first diluted by a source QPC at intermediate transmission.

If there is a robust edge substructure along the 1.5 µm path between the source and the analyzer QPCs, a current imbalance between the first case and the second case would result in a difference between the two corresponding transmissions. By contrast, if there is no such edge

reconstruction, the transmissions in both cases must be identical whatever the tunings of the QPCs.

In practice, we set the device in the configuration where the bottom-right (or alternatively top-left) source is fully closed while the top-left (bottom-right) one is partially open (see Figure 4.18a,b). In that way, we can compare the transmission of QPC_c obtained from the closed source side ($\tau_{c,R(L)}$, corresponding to the first direct bias case) and the simultaneously measured one obtained from the other side ($\tau_{c,L(R)}$corresponding to the second case). The measurement is performed for a complete sweep of τ_c transmission at 6 different values of the open source transmissions. Note that the tuning of the source is set using the split gate furthest from QPC_c (colored in blue on Fig. 4.18a,b) to limit the impact on the analyzer.

Figure 4.18c displays the difference between the two simultaneously measured transmissions $|\tau_{c,L} - \tau_{c,R}|$ plotted as a function of the 6 explored source transmissions. The vertical error bars indicate the statistical error. Note that this error increases when the source transmissions approach 1, due to a much lower resolution on the impinging current. Orange and light blue dots correspond to the two tested configurations: top-left source is partially open while the bottom-right is closed (light blue) and bottom-right source is partially open while the top-right is closed (orange).

At our experimental accuracy, the two transmission signals are therefore found to be identical in both source configurations.

Therefore the absence of channel substructure at $\nu = 1/3$ is validated by this measurement, corroborating the model in which the noise constitutes a signature of anyon statistics.

4.12.2 Non-local heating

In the canonical picture of the $\nu = 1/3$ FQH state, the two sources are supposed to be fully disconnected from one another and to be unaffected by QPC_c due to chirality. While the electrical current systematically follows chirality, we nevertheless observed that a small fraction of heat current deviates from this predicted behavior, as mentioned in section 4.5.2 through the deviation of S_Σ from 0. Such *non-local heating* signature is essentially negligible in the WBS and SBS regimes but remains detectable. This section provides a brief study of this effect.

When some power is locally injected with a voltage bias at one source QPC set at intermediate transmission, a small noise is found to be generated at the other QPC, violating chirality. A similar signature could appear due to counter-propagating neutral modes (observed in other fractions such as 2/3 [137]) flowing upstream along the edges or within the bulk [138, 139]. But in our case, this effect even persists when QPC_c is closed ($\tau_c = 0$) and therefore cannot be attributed to such neutral modes. Instead, we explain it as a non-local heat transfer due to long-range Coulomb interactions [136, 140].

For the characterization of this non-local heating, τ_c is set at 0 or 1. Thus, the measured current auto-correlations ΔS_{LL} and ΔS_{RR} can be fully attributed to the upstream powered source QPC. One of the source QPCs, denoted here as the *generator*, is directly voltage-biased. The other source QPC, denoted as the *detector*, remains unbiased and is connected to the amplification line where the increase of the noise signal of interest ΔS_{det} (ΔS_{LL} or ΔS_{RR}) is measured.

In the simple case where one of these sources is set at perfect transmission or reflection, no additional noise is observed. If the generator is tuned at $\tau_{gen} = 0$ or 1, there is no power locally

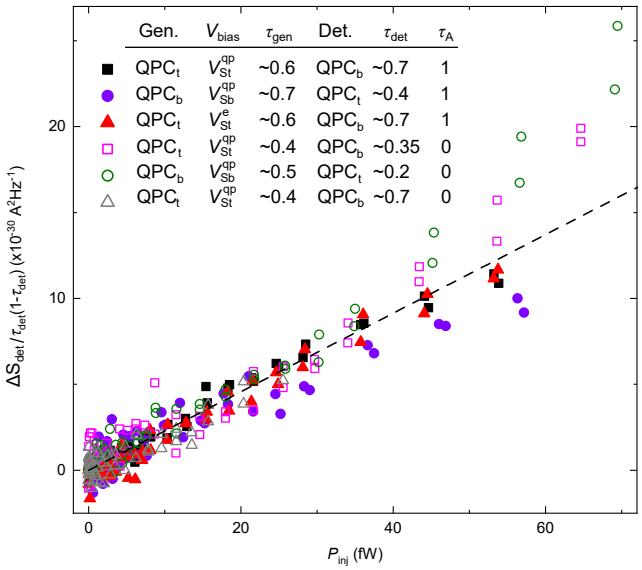

Figure 4.19: **Non-local heating.**
The normalized noise increase $\Delta S_{\rm det}/(\tau_{\rm det}(1-\tau_{\rm det}))$ generated from an unbiased 'detector' source QPC$_{\rm t(b)}$ of transmission $\tau_{\rm det}$ is displayed as a function of the power $P_{\rm inj}$ injected at a second 'generator' source QPC$_{\rm b(t)}$ of transmission $\tau_{\rm gen}$. The detector and generator are electrically separated by chirality, and by a gapped FQH state ($\tau_{\rm c} = 1$) or a depleted 2DEG ($\tau_{\rm c} = 0$). Here, measurements are performed at $T \simeq 35\,$mK, with $P_{\rm inj} = 2V^2_{\rm bias}\tau_{\rm gen}(1-\tau_{\rm gen})e^2/(3h)$. The voltage bias $V_{\rm bias}$ is indexed by 'St' or 'Sb' depending on whether it is applied on QPC$_{\rm t}$ or QPC$_{\rm b}$. The dashed line corresponds to a linear fit $\Delta S_{\rm det}/(\tau_{\rm c}(1-\tau_{\rm c})) = 2.3\,10^{-16}P_{\rm inj}$.

injected in the downstream channel ($P_{\rm inj} = 0$), which remains cold up to the detector location (because such power is proportional to $\tau_{\rm gen}(1-\tau_{\rm gen})$ [141]). Hence, the detector is not 'heated up' (i.e. with the same voltage, temperature, and therefore distribution function on both sides) which does not induce an excess electrical noise. If instead the detector is set at $\tau_{\rm det} = 0$ or 1, the partition noise (such as the delta-T noise) $\propto \tau_{\rm det}(1-\tau_{\rm det})$ vanishes [142, 143, 144].

In the general case of intermediate transmissions, we expect the non-local heating to depend on $P_{\rm inj} \equiv 2V^2_{\rm bias}\tau_{\rm gen}(1-\tau_{\rm gen})e^2/(3h)$ (the power locally injected on the edge channel at the generator location) and to scale as $\tau_{\rm det}(1-\tau_{\rm det})$ (the sensitivity of the noise detector). Figure 4.19 shows the noise signal of interest $\Delta S_{\rm det}$ normalized by $\tau_{\rm det}(1-\tau_{\rm det})$ plotted as a function of $P_{\rm inj}$ for various device tuning. All the shown data are measured at $T = 35$ mK.

In that representation, all the data fall on each other, corroborating the picture of such a non-local heating effect. Thanks to this measurement, one can estimate the excess noise due to such an artifact with a linear fit (black dashed lines) : $\sim\ P_{\rm inj}\tau_{\rm det}(1-\tau_{\rm det}) \times 2.3 \times 10^{-16}$ A^2 Hz^{-1}. Note that such an effect also takes place between the source and the central QPC, which is consistent with the small increase of S_Σ observed in Fig. 4.8.

Therefore, this specific study of the upstream heat flow consistently explains the unexpected excess noise observed in S_Σ at high voltage. Importantly, note that in the main configuration, the source transmissions are set near 0 or 1, making this effect negligible.

4.12.3 Bias dependence of the QPC transmissions

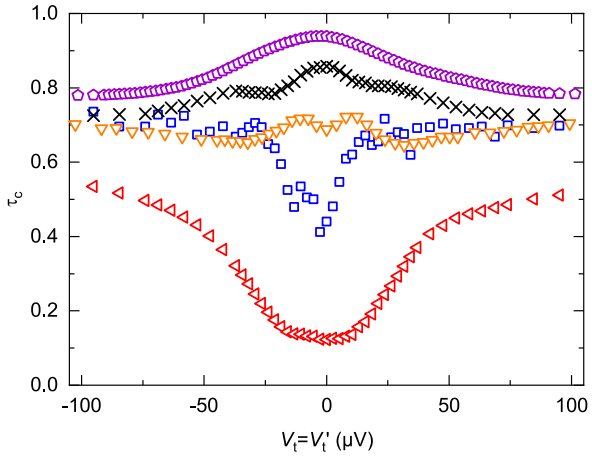

Figure 4.20: **QPC_c transmission versus direct voltage bias at $\nu = 1/3$.** The QPC_c current transmission ratio is plotted versus direct voltage bias $V_t = V_t'$. The different symbols, corresponding to different tunings of QPC_c, are chosen to match with the ones of Fig. 4.13.

In Laughlin fractional quantum Hall regime, the current transmission ratio across a QPC is expected to depend on the applied DC bias voltage [115, 100]. However, the experimental QPC transmissions often have a voltage bias dependence different from the predictions (see for instance Ref. [2] and Refs. [105, 122] for a detailed review). This is also the case in the sample used in this thesis.

Figure 4.20 shows τ_c, the transmission of QPC_c as a function of the direct voltage bias at $\nu = 1/3$ for a large range of tunings. In the WBS regime ($(1-\tau_c) \ll 1$), one observes a reduction of τ_c when the bias increases, in contrast with predictions of a transmission approaching 1 when the bias increases [115, 100].

Intriguingly, while τ_c has a significant impact on the quantitative value of the Fano factor, $P_{exp}(I_- = 0)$ was found to be in agreement with predictions in spite of the unexpected τ_c voltage-dependence. Hence, while the strong negative cross-correlations and their dependence on imbalance constitute an important marker of anyon statistics, these unexplained τ_c variations with bias suggest staying cautious with quantitative conclusions.

4.13 Conclusion

In this chapter, we presented noise observations of exotic anyon braiding statistics in the $\nu = 1/3$ fractional quantum Hall state. The braiding of a quasiparticle-quasihole pair generated at QPC_c with the impinging anyons shows up as three complementary markers in the noise signal.

First, the presence of important negative cross-correlations is itself a strong qualitative evidence of anyon braiding, in marked contrast with the slightly positive signal observed for fermions at $\nu = 2$. Although a good quantitative agreement with theory is found in the balanced source-analyzer configuration the importance of the normalization choice on the precise expected value suggests to remain cautious.

Second, the dependence of cross-correlations on the source imbalance constitutes another evidence of unconventional exchange statistics and allows us to discriminate this mechanism from the distinct Andreev-like scattering process.

Finally, the *super-Poissonian* autocorrelations, much higher than the signal expected in a trivial 'beam-splitter' partition picture also highlight the anyon unconventional braiding process.

These signatures call for measurements beyond the Laughlin fractions, with more complex edge structures involving several copropagating channels. For instance, in the $\nu = 2/5$ Jain state $e/5$ charge in the inner channel could reveal anyon statistics through a similar signal. This is the topic of the following chapter.

Moreover, it has recently been predicted that small positive or negative cross-correlation signals could appear for interacting fermions [126] and that anyon braiding could be emulated in the IQH regime [46]. Therefore, a specific measurement to clarify the role of interactions in such systems will be presented in Chapter 6.

Chapter 5

Cross-correlation investigation of anyon statistics at $\nu = 2/5$

The previous chapter provided several complementary signatures of anyon statistics in the emblematic $\nu = 1/3$ case. A natural extension of this study is to investigate the more complex Jain $\nu = 2/5$ regime, composed of two copropagating edge channels. In particular, the same source-analyzer setup allows us to explore a different kind of anyon quasiparticle: $e/5$ charges propagating along the inner channel of conductance $e^2/(15h)$. Are cross-correlations also non-zero in that case, pointing to a non-trivial braiding process involving $e/5$ quasiparticles? This is the topic of the present chapter, which investigates the same source-analyzer device as previously.

First, we present the hierarchical Jain 2/5 state in Section 5.1. Then, after describing the characterization of an unwanted inter-channel tunneling artifact in Section 5.2, the main measurements in the inner channel are reported and discussed in Section 5.3. Finally, a complementary measurement in the outer channel is briefly presented in Section 5.4.

5.1 Description of the Jain $\nu = 2/5$ state

As mentioned in Section 2.3, the $\nu = 2/5$ fraction is described by Jain's theory [77, 78] involving several copropagating edge channels and a description of anyons in terms of composite fermions.

In this section, we present the edge structure of the $\nu = 2/5$ fractional quantum Hall (FQH) state and provide the expected value of the generalized Fano factor P_{thy} if one naively applies the predictions of the previous chapter (see Eq. (4.16) to that case, even though the theory has been specifically developed for Laughlin fractions.

5.1.1 Edge structure of the $\nu = 2/5$ FQH state

The edge structure of the $\nu = 2/5$ fractional quantum Hall state is more complex than the Laughlin $\nu = 1/3$ fraction. Indeed, for such a Jain state, theory predicts two adjacent edge channels propagating in the same direction along each edge [81] (see Fig. 5.1a). In the simplest picture of weak tunneling and weak Coulomb blocking between these edge channels, they are expected to have different conductances and to carry two distinct varieties of anyons emitted by a source QPC set in the weak back-scattering (WBS) regime.

Indeed, the outer channel (i.e. closest to the sample edge, illustrated by a red line in Fig. 5.1a) is predicted to have a conductance $G_{\rm out} = \nu_{\rm out} e^2/h$ with $\nu_{\rm out} = 1/3$. The conductance of the inner channel (black line), on the other hand, is predicted to be $G_{\rm in} = \nu_{\rm in} e^2/h$ with $\nu_{\rm in} = 1/15$ [81].

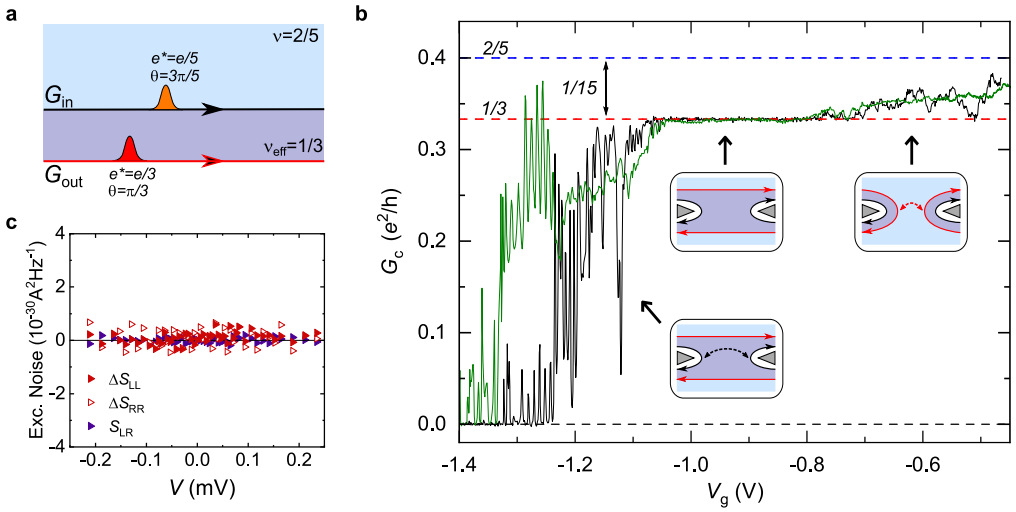

Figure 5.1: **Edge structure of the $\nu = 2/5$ FQH state.**
a Two adjacent channels (continuous lines with arrow) propagate along the edge of the sample in the $\nu = 2/5$ FQHE (light blue region). Weak back-scattering in the inner channel (black line) can excite quasiparticles of charge $e^* = e/5$ and exchange phase $\theta = 3\pi/5$, whereas the outer one (red line) excite quasiparticles of charge $e^* = e/3$ and exchange phase $\theta = \pi/3$. The region between the two edge channels (colored in darker blue) is, locally, in the $\nu_{\rm out} = 1/3$ FQH state. Note that this description ignores inter-channel coupling (tunneling and Coulomb interactions).
b Transmission profile of $\rm QPC_c$ at $V_{\rm DC} = 0$ (black line) and $V_{\rm DC} = 90$ µV as a function of the split gate voltage $V_{\rm g}$. The two steps separated by a robust plateau validate the picture of a sequential opening of the channels (see schematics in the inset). The first step at $V_{\rm g} \in [-1.3\ {\rm V}, -1\ {\rm V}]$ corresponds to the opening of the outer channel, while the second one at $V_{\rm g} > -0.8$ V corresponds to the opening of the inner channel. The horizontal dashed lines indicate the conductances $e^2/(3h)$ (red) and $2e^2/(5h)$ (blue). Inset: Schematics of the different configurations.
c Auto and cross correlations noise measured when $\rm QPC_c$ is set on the $e^2/(3h)$ plateau and submitted to a direct DC-bias voltage V.

This edge structure picture of two separated copropagating edge channels can first be attested by the dependence of the total differential conductance $G_{\rm c}$ across the central $\rm QPC_c$ with the voltage $V_{\rm g}$ applied on the two central metallic split gates. Such $G_{\rm c}(V_{\rm g})$ profile is presented in Figure 5.1b at zero (black line) and 90 µV (green line) DC-bias voltage.

This profile presents two clearly distinct steps, corresponding to the sequential partitioning of the two channels. The first step $0 < G_{\rm c} < e^2/3h$, in the range $V_{\rm g} \in [-1.3\ {\rm V}, -1\ {\rm V}]$, corresponds to the opening of the outer channel. The second step $e^2/3h < G_{\rm c} < 2e^2/5h$, in the range $V_{\rm g} \in [-0.8\ {\rm V}, -0.5\ {\rm V}]$, manifests the (imperfect) opening of the inner channel. Finally, the robust intermediate plateau at $G_{\rm c} = e^2/3h$ corresponds to the full transmission of the outer channel and the full reflection of the inner channel, which is confirmed by the absence of shot

noise when a DC-bias is applied to QPC_c (see Fig. 5.1c). Schematics of Fig. 5.1b illustrate these three configurations.

Within this two-copropagating edge channels picture, QPC_c is characterized by the current ratio τ_{out} and τ_{in} along the outer and inner edge channels respectively. They can be expressed by:

$$\tau_{out} = \frac{G_c}{e^2/3h} \tag{5.1a}$$

$$\tau_{in} = \frac{G_c - e^2/3h}{e^2/15h} \tag{5.1b}$$

These formulas lead us to adopt the following definition of the differential transmission of QPC_c in the presence of two upstream sources of respective transparencies τ_t and τ_b:

$$\tau_c \equiv \frac{\nu}{\nu_{eff}} \times \frac{1}{2}\left(\frac{\partial V_L/\partial V_t}{1-\tau_t} + \frac{\partial V_R/\partial V_b}{1-\tau_b}\right) \tag{5.2}$$

with ν_{eff} the effective filling factor associated with the conductance of the active channel: $\nu_{eff} = 1/15$ for the inner channel and $\nu_{eff} = 1/3$ for the outer channel. $V_{L,R,b,t}$ are defined in Fig. 5.2a (they are the same as in Chap. 4).

For all QPCs, note that G_c does not attain the maximum value of $(2/5)e^2/h$ (horizontal blue dashed line in Fig. 5.1b) indicating that it is not possible to fully open the inner channel. The maximum inner channel transmission achieved is $\tau_c \approx 0.9$ (as presented in the inset of Fig. 5.4b).

5.1.2 Quasiparticles in the $\nu = 2/5$ FQH state

The two channels of the $\nu = 2/5$ FQH state are predicted to carry different species of quasiparticles when excited with a QPC in the WBS regime. As developed in Section 2.4.6, the main parameter describing the anyon properties is the so-called *scaling dimension*, linked to both the conductance power-law dependence with the voltage bias and the exchange statistics of the quasiparticle [65, 145, 146]. Let us summarize the properties of the two topologically-protected varieties of quasiparticles in the $\nu = 2/5$ state.

On the one hand, the outer channel of conductance G_{out} is predicted to carry quasiparticles of scaling dimension $\Delta = 1/6$, charge $e/3$ and exchange phase $\theta = \pi/3$ [65]. Although the filling factor is different from 1/3, these quasiparticles are predicted to be identical to the ones of Laughlin fraction $\nu = 1/3$. Noise measurements of the outer channel are therefore predicted to corroborate the results of the previous chapter.

On the other hand, quasiparticles of charge $e/5$ have been observed [41, 56, 58] in the inner channel, with a scaling dimension expected to be $\Delta = 3/10$ and a corresponding fractional exchange statistics $\theta = 3\pi/5$ (see e.g. [65]).

This situation does not directly match a Laughlin fraction and is therefore the most interesting one. The remainder of this chapter mainly focuses on results in the inner channel.

5.1.3 Naive prediction of the generalized Fano factor P

Like in the case of the $\nu = 1/3$ fraction, the statistics of quasiparticles are investigated through the generalized Fano factor defined as

$$P_{\text{thy}} \equiv \frac{\langle \delta I_{\text{L}} \delta I_{\text{R}} \rangle}{S_\Sigma \tau_{\text{c}}(1-\tau_{\text{c}})}, \tag{5.3}$$

in order to minimize the impact of the trivial source shot noise contribution S_Σ and to specifically focus on the contribution of QPC_{c}. For Laughlin anyons, Refs. [1, 47, 46] showed that this quantity is connected to the scaling-dimension Δ and therefore to the exchange phase $\theta = 2\pi\Delta$, with

$$\boxed{P_{\text{thy}} = \frac{-4\Delta}{1-4\Delta}}, \tag{5.4}$$

for perfectly symmetric incoming beams.

At this point, we stress that the theoretical predictions connecting cross-correlations in a source-analyzer setup with fractional anyon statistics have only been developed for the Laughlin fractions [1] and have recently been extended to non-Abelian anyons [47]. However, these do not yet specifically address the hierarchical Jain states involving several copropagating edge channels.

Nonetheless, by naively assuming that the outer channel can be ignored, one might apply the prediction of Eq. (5.4) with the scaling dimension of the $e/5$ quasiparticles of the inner channel (see e.g. [65]):

$$\Delta = \left(\frac{e^*}{e}\right)^2 \frac{1}{2\nu_{\text{in}}} = \frac{3}{10} \tag{5.5}$$

The exchange phase, in that case, is $\theta = 3\pi/5$ and ν_{in} refers to the effective filling factor of the inner channel i.e. $\nu_{\text{in}} = 2/5 - 1/3 = 1/15$

Therefore, with the corresponding $\Delta = 0.3$, one gets $P = +6$ which is markedly different from the $P = -2$ prediction of $\nu = 1/3$. In particular, it is intriguingly *positive*. This is not due to the cross-correlations which remain negative, but to the differential transmission τ_{c} becoming negative for dilute beams [1]. According to B. Rosenow (private communication), this signals a breakdown of predictions at $\Delta > 1/4$.

Hence, even though one can naively apply the theory developed for Laughlin fractions in this case it does not bring quantitative predictions.

5.1.4 Experimental implementation of source-analyzer setup at $\nu = 2/5$

The sample investigated at the Jain $\nu = 2/5$ fraction is the same as the one used at $\nu = 1/3$ in the Andreev-like scattering and anyon braiding studies of the previous chapters. It is made from a two-dimensional electron gas ($n = 1.2 \times 10^{11}$ cm^{-2} and $\mu = 1.8 \times 10^6$ cm^2 V^{-1} s^{-1}) buried within a AlGaAs|GaAs heterostructure ~ 100 nm below the surface. This 2DEG is immersed in a strong perpendicular magnetic field B and set in the vicinity of the $\nu = 2/5$ FQH plateau center, at $B \approx 11.5$ T (see Fig. 5.2b).

Figure 5.2a schematizes the considered device. Like in the previous chapters, two top (t) and bottom (b) upstream QPCs are used as sources of quasiparticles in the investigated channel (colored lines with arrows on Fig. 5.2). By applying DC-voltage $V_{\mathrm{t(b)}}$, one obtains two diluted beams of quasiparticles that flow to a central 'analyzer' QPC where a braiding mechanism is susceptible to emerge and to be detected in the outgoing current cross-correlation signal $S_{\mathrm{LR}} = \langle \delta I_{\mathrm{L}} \delta I_{\mathrm{R}} \rangle$.

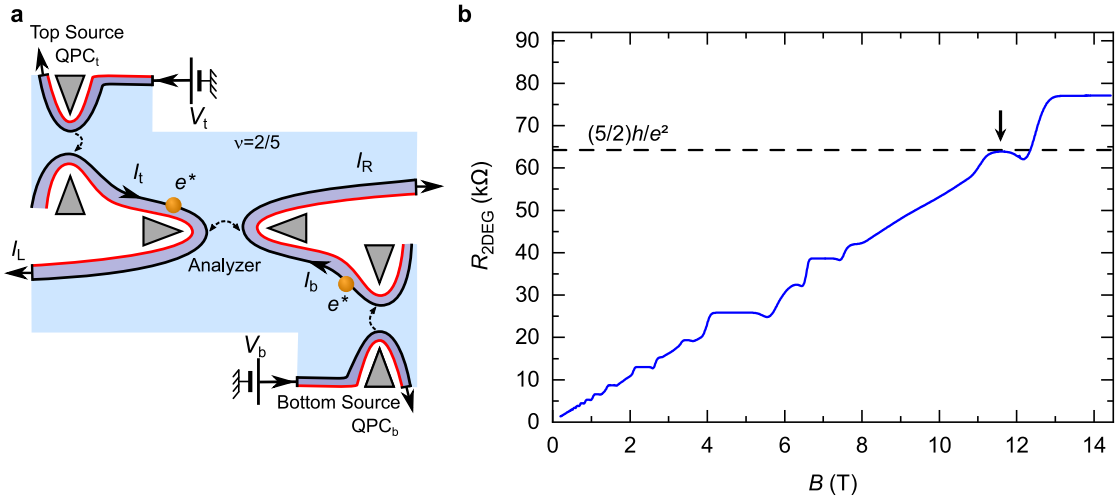

Figure 5.2: **Source-analyzer setup implementation at $\nu = 2/5$.**
a Schematics of the setup at $\nu = 2/5$. Like in the previous $\nu = 1/3$ case, two sources QPC$\mathrm{t,b}$ are tuned to partition the considered channel (here the inner one). By applying a DC-voltage bias $V_{\mathrm{t,b}}$, the sources create beams of anyons (orange dots) impinging on a downstream central "analyzer" QPC$_{\mathrm{c}}$, set to a partial transmission of the same channel. The inner (outer) channel is displayed as a black (red) line with arrows. The region between channels is colored with darker blue to illustrate the local $\nu_{\mathrm{out}} = 1/3$ FQH state.
b Two-wire resistance between an ohmic contact and a cold ground versus the perpendicular magnetic field B (at $T \sim 100$ mK). All QPCs are fully pinched off during this B sweep. The arrow shows the chosen value of B and the dashed line indicates the plateau $R_{\mathrm{H}} = (5/2)h/e^2$ corresponding to the Jain fraction $\nu = 2/5$.

Let us now turn to the noise measurement with symmetric sources in the inner channel of the $\nu = 2/5$ FQH state.

5.2 Characterization of inter-channel tunneling

For an edge structure involving several copropagating channels, a transfer of charge from one channel to the other can occur along the propagation path. For instance, such inter-channel tunneling processes have been detected at $\nu = 2$ for propagation distances of tens of microns [147, 148, 149].

At $\nu = 2/5$ such tunneling events between the two copropagating channels could also happen and result in a negative additional contribution to cross-correlations, different from the contribution due to the braiding mechanism. Hence, inter-channel charge transfer would impact the value of P. To ensure that the measured signal can indeed be attributed to braiding, a careful calibration of these processes is necessary. This is the object of this section.

5.2.1 Physical picture and prediction for inter-channel tunneling contribution to negative cross-correlations

Along the path of the impinging beam of anyons (i.e. between $\mathrm{QPC_{t,b}}$ and $\mathrm{QPC_c}$) an inter-channel tunneling process consists in the tunneling of a quasiparticle from the inner edge channel to the outer one (see the illustrative schematics in Fig. 5.3a).

This results in a pair of two correlated excitations: a quasiparticle in one channel and a quasihole in the other. These two *correlated* excitations have opposite charges. Consequently, they result in an additional *negative* cross-correlation contribution, distinct from the braiding signal of interest.

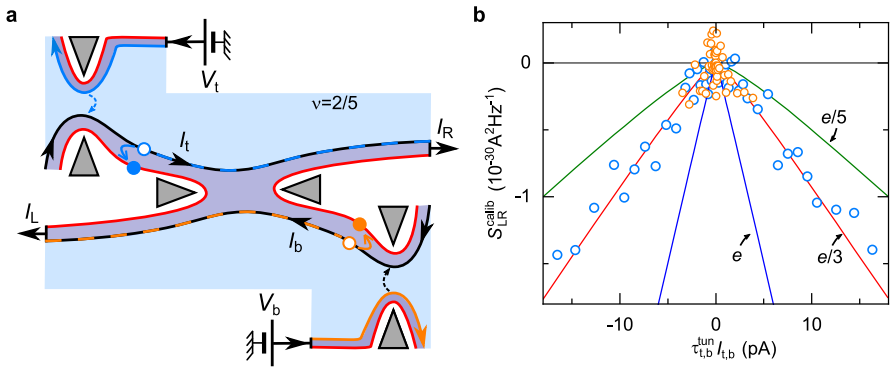

Figure 5.3: **Inter-channel tunneling picture.**
a Inter-channel tunneling picture: a quasiparticle from the inner channel tunnels to the outer one, leaving a quasihole behind. Setting the central QPC on the noiseless $e^2/(3h)$ plateau allows us to specifically calibrate the cross-correlation signal induced by this process.
b Cross-correlations measured with $\mathrm{QPC_c}$ on the intermediate transmission plateau are completely attributable to inter-channel tunneling. The signal is plotted as a function of the corresponding tunneling current $\tau_{\mathrm{t,b}}^{\mathrm{tunn}} I_{\mathrm{t,b}}$ and compared to shot noise predictions (Eq. (5.7)) with charge e (blue line) $e/3$ (red line) and $e/5$ (green line). Blue (orange) symbols correspond to the injection from $\mathrm{QPC_{t(b)}}$.

More quantitatively, a tunneling event between channels creates a current fluctuation δI in the outer channel directly correlated to an opposite fluctuation $-\delta I$ in the inner channel. If the downstream analyzer $\mathrm{QPC_c}$ is set at the full transmission of the outer channel and intermediate transmission τ_c of the inner channel, the resulting total (i.e. summed over both channels) fluctuations of current in the transmitted and reflected paths are respectively $\delta I - \delta I \tau_c$ and $-\delta I(1-\tau_c)$.

This results in a contribution to the main cross-correlation signal given by:

$$S_{\mathrm{LR}}^{\mathrm{tun}} = -\delta I^2 (1-\tau_c)^2 \tag{5.6}$$

where one can directly note that in the simple case $\tau_c = 0$, as the analyzer is noiseless, the measured cross-correlations can be fully attributed to the inter-channel tunneling.

Importantly, note that the tunneling-induced current fluctuation δI depends on the charge transferred between the two channels. Indeed, as the inter-channel region is an incompressible strip of local filling factor $\nu_{\mathrm{eff}} = 1/3$ [81], the tunneling events are expected to involve $e^*_{\mathrm{tun}} = e/3$ charges and generate cross-correlations that follow the phenomenological shot noise formula:

$$S_{\mathrm{LR}} = 2e^*_{\mathrm{tun}} \frac{\tau(1-\tau)V}{R_{\mathrm{H}}} \left[\coth \frac{e^*_{\mathrm{tun}} V}{2k_{\mathrm{B}}T} - \frac{2k_{\mathrm{B}}T}{e^*_{\mathrm{tun}} V} \right] \tag{5.7}$$

Are the tunneling charges in our case the expected $e/3$ quasiparticles? Figure 5.3b displays such cross-correlations for individually biased top and bottom source QPC, plotted versus the inter-channel tunneling current $I^{\mathrm{tun}}_{\mathrm{t(b)}}$ (i.e. the fraction of current that effectively tunnels from one channel to the other). This is done in the simple case where $\tau_{\mathrm{c}} = 0$, so that all the noise signal is due to tunneling. While the noise signal from $\mathrm{QPC_b}$ (orange dot) is essentially negligible due to very low tunneling transmission, the cross-correlations due to $\mathrm{QPC_c}$ (blue dots) are compatible with predictions of Eq. (5.7) for $e^* = e/3$ (red line), in contrast with $e^* = e/5$ (green line) and $e^* = e$ (blue line).

This corroborates the picture of $e/3$-charged quasiparticles tunneling from the inner to the outer channel along the path between the sources and the central QPC.

Let us now describe the experimental procedure to calibrate the inter-channel tunneling. The characterization is done in two steps: one calibration step using the noiseless $\mathrm{QPC_c}$ plateau and then the estimation of the tunneling contribution to the total signal.

5.2.2 Calibration procedure of inter-channel tunneling

First, we detune the central $\mathrm{QPC_c}$ from the inner channel operating point (at intermediate transmission $\tau_{\mathrm{c}} > 0$) and we set it to the $e^2/3h$ plateau (at zero inner channel transmission $\tau_{\mathrm{c}} = 0$), as presented in the schematics of Figure 5.4a. In order to minimize the impact on other QPCs due to split gate cross-talk, we only change the voltage applied to the gate of the analyzer QPC that is not located along the considered path.

At this plateau tuning of the central QPC, non-zero current in the left (right) lead measured at the frequency of injection from the top (bottom) path (see Fig. 5.4a) constitutes a direct measurement of inter-channel tunneling current.

Quantitatively, at $\tau_{\mathrm{c}} = 0$, one can define the differential inter-channel tunneling transmission $\tau^{\mathrm{tun}}_{\mathrm{t(b)}}$ as the ratio between the current tunneling from the inner to the outer edge and the total injected current:

$$\tau^{\mathrm{tun}}_{\mathrm{t(b)}} \equiv \frac{\partial I_{\mathrm{L(R)}}/\partial V_{\mathrm{t(b)}}}{\partial (I_{\mathrm{L}} + I_{\mathrm{R}})/\partial V_{\mathrm{t(b)}}} \tag{5.8}$$

In practice, the tunneling of the top path is found to be much higher than the one of the bottom path, as illustrated in the inset of Fig. 5.4a. Indeed, while $\tau^{\mathrm{tun}}_{\mathrm{b}}$ (orange symbols) is always lower than 5%, $\tau^{\mathrm{tun}}_{\mathrm{b}}$ can approach 20% (blue symbols) in the presented example, corresponding to the worst case among all investigated configurations.

All the cross-correlation noise signal $S^{\mathrm{calib}}_{\mathrm{LR}}$ obtained in this $\tau_{\mathrm{c}} = 0$ calibration configuration is therefore completely due to the inter-channel tunneling processes. The main panel of Fig. 5.4a presents such a calibrated noise signal plotted as a function of the individual bias $V_{\mathrm{t,b}}$. While the signal coming from the bottom path (orange dots) is very small, the substantial cross-correlations due to inter-channel tunneling along the top path (blue dots) justify this calibration.

These unwanted negative cross-correlations, distinct from the braiding signal of interest, have now to be distinguished from the main measurement results.

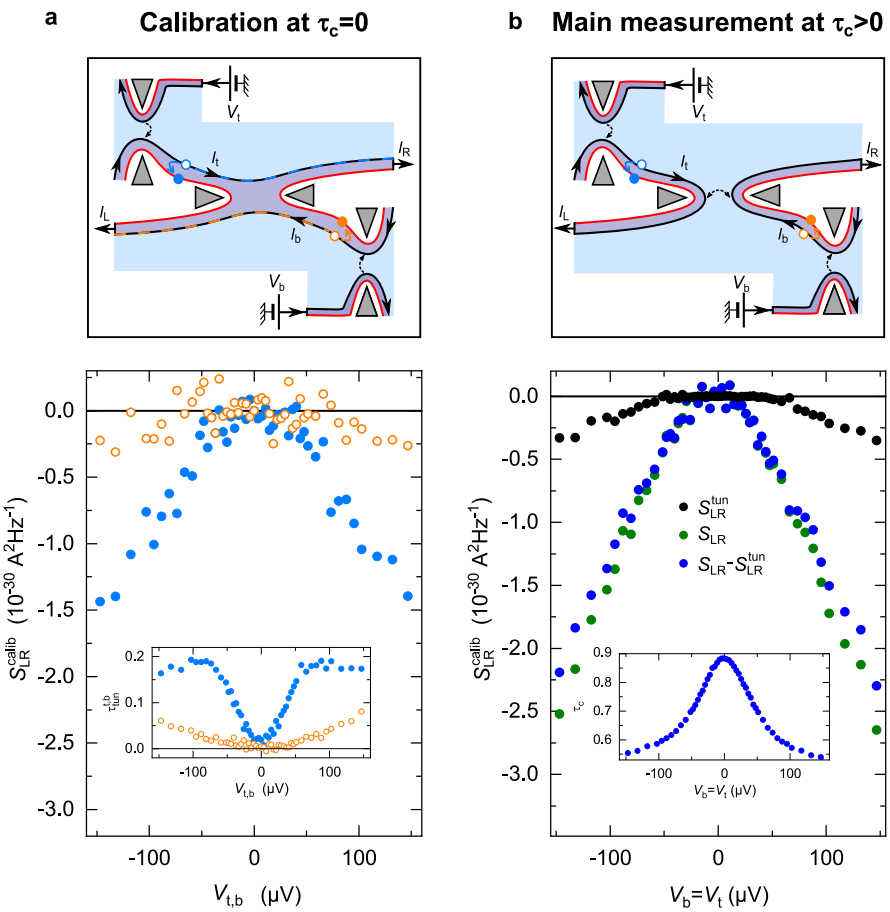

Figure 5.4: **Inter-channel tunneling calibration procedure.**
a QPC_c is first set at $\tau_c = 0$ (schematics) to calibrate the contribution of inter-channel tunneling processes to cross-correlations. The main panel displays the measured cross-correlations S_{LR}^{calib} separately obtained for tunneling along the top (blue) and bottom (orange) paths, and plotted versus the DC-bias voltage of the corresponding source V_t (with $V_b = 0$) and V_t (with $V_b = 0$). In this configuration, S_{LR}^{calib}, can be fully attributed to inter-channels tunneling processes. The corresponding tunneling fractions are presented in the inset and correspond to the highest value (up to 20%) obtained among all operating points.
b QPC_c is then set back to the main measurement configuration: at $\tau_c > 0$ (see inset) and with both sources symmetrically biased ($V_t = V_b$). Green dots display the raw measured cross-correlation signal S_{LR}. Black dots indicate the estimated contribution of inter-channel tunneling ($(1-\tau_c)^2$ times the sum of data from panel (a)). Finally, the "corrected" data difference $S_{LR} - S_{LR}^{calib}$ is plotted as blue dots. The discrepancies between the blue and green symbols allow one to appreciate the impact of inter-channel tunneling on the signal of interest.

5.2.3 Contribution of inter-channel tunneling to cross-correlations

Once this tunneling fraction is calibrated, one can indeed estimate its unwanted contribution to the negative cross-correlation signal when QPC_c is set back to the main operating point (with intermediate transmission $\tau_c > 0$) and fed by two symmetric beams of quasiparticles generated at the source QPCs now simultaneously biased at the same $V_t = V_b$ (see schematics of Fig. 5.4b).

As explained in Section 5.2.1, the additional inter-channel tunneling signal S_{LR}^{calib} redis-

tributes on QPC_c. Hence, if QPCs are set to partition the inner channel, the negative cross-correlation contribution due to tunneling S_{LR}^{tun} is simply obtained by applying the reduction factor $(1-\tau_c)^2$ to the calibrated cross-correlation signal S_{LR}^{calib} [1]:

$$S_{LR}^{tun} = (1-\tau_c)^2 S_{LR}^{calib} \tag{5.9}$$

Figure 5.4b presents the tunneling contribution to cross-correlations for the same operating point as Fig. 5.4a, but in the configuration $\tau_c > 0$, as illustrated by the upper schematics. Inset in the main panel displays the corresponding τ_c measured simultaneously with the noise, approximately equal to 0.9 at zero bias in this case. In the main panel, green symbols display the raw directly measured cross-correlations, including the contribution attributed to tunneling in the presence of two symmetric diluted beams of quasiparticles. Black symbols correspond to the estimated tunneling-induced cross-correlations S_{LR}^{calib}, i.e. the sum of the signals obtained in the calibrated configuration of the panel (a) S_{LR}^{calib} times the reduction factor $(1-\tau_c)^2$. Blue symbols display the difference $S_{LR} - S_{LR}^{calib}$, i.e. the contribution of negative cross-correlations not attributed to inter-channel tunneling.

This procedure allows us to estimate the unwanted inter-channel tunneling contribution to negative cross-correlations and to make sure that it remains small compared to the signal of interest attributed to a nontrivial braiding of quasiparticles. In the following, the quantitative value of the generalized Fano factor P_{exp} will be extracted from both the raw measured cross-correlations ignoring inter-channel tunneling (green symbols in Fig. 5.4) and from the signal with removed inter-channel tunneling contribution (blue symbols in Fig. 5.4).

Confronting the two obtained values allows a direct appreciation of the small influence of inter-channel tunneling artifacts.

5.2.4 Characterization of current chirality

In addition to the inter-channel tunneling, a small but discernible fraction of current violating chirality is another experimental artifact that has to be carefully characterized at $\nu = 2/5$. Indeed, while the quantum Hall chirality of the electrical current is systematically obeyed at the level of large ohmic contacts, a small deviation can develop in the device center for the $\nu = 2/5$ filling fraction which is less robust than at $\nu = 1/3$ and $\nu = 2$.

The chirality is controlled by making sure that the signals $\partial V_M^t/\partial V_b$ and $\partial V_M^b/\partial V_t$ remain zero at any device tuning (see Fig. 5.5a). While this is systematically the case at our experimental accuracy for $\nu = 1/3$ and $\nu = 2$, we found a small unexpected signal as displayed in Fig. 5.5b. Note that if we assume that the non-chiral signal is only due to the inner channel current, the relevant non-chiral fraction is enhanced by a factor of 6 (i.e. $(2/5)/(1/15)$), up to 2.5% in the illustrative example of Fig. 5.5 and at the most 3% in the worst case investigated.

The obtained value introduces uncertainty on QPC transmission but does not impact qualitative conclusions deduced from the noise signal.

[1] Note that if one set the QPCs to excite the outer channel, this reduction factor becomes τ_{out}^2 (with τ_{out} the differential transmission of the outer channel)

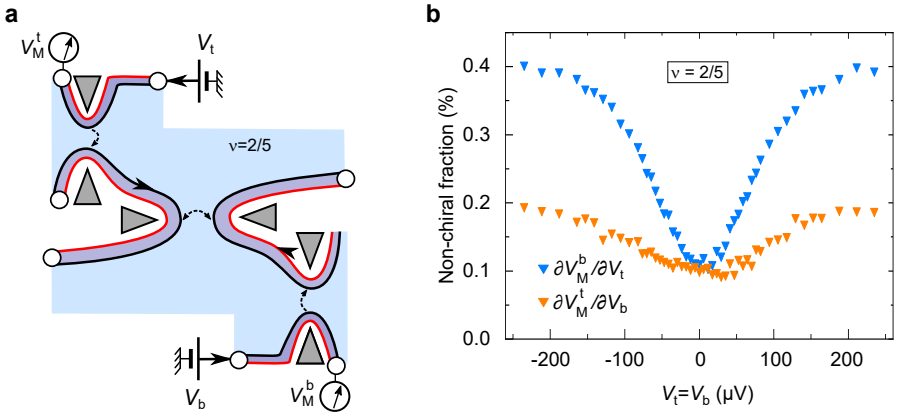

Figure 5.5: **Current chirality characterization.**
a Device schematics at $\nu = 2/5$. To ensure chirality, the signals $\partial V_{\mathrm{M}}^{\mathrm{t}}/\partial V_{\mathrm{b}}$ and $\partial V_{\mathrm{M}}^{\mathrm{b}}/\partial V_{\mathrm{t}}$ have to be zero.
b Differential emitted/detected current (voltage) ratios $\partial V_{\mathrm{M}}^{\mathrm{t(b)}}/\partial V_{\mathrm{b(t)}}$ indicating fraction of current violating chirality.

5.3 Noise signature of exotic quasiparticles in the inner channel at $\nu = 2/5$

We can now turn to the specific investigation of cross-correlation anyon signature in the $\nu = 2/5$ Jain FQH regime. Apart from the inter-channel tunneling calibration described in the previous section, the QPC characterization, cross-correlation measurements, and P extraction procedure are the same as the one at $\nu = 1/3$ discussed in the previous chapter: the charge tunneling at the sources $\mathrm{QPC_{t,b}}$ and then at the central $\mathrm{QPC_c}$ are first separately characterized. Then, the main noise measurement with symmetrically biased sources is performed with a simultaneous characterization of the impinging quasiparticles.

Let us first briefly describe the characterization of QPCs in the specific case of the $\nu = 2/5$ inner channel.

5.3.1 Separate characterization of the QPC tunneling charges

Like in the previous chapter the separate characterization of charges tunneling across individual QPCs is achieved by applying a direct DC-voltage V on the QPC of interest [10, 11] and by comparing the measured shot noise to the conventional phenomenological shot noise expression [123, 124]:

$$S_{\mathrm{sn}} = 2e^* \frac{\tau(1-\tau)V}{R_{\mathrm{H}}} \left[\coth \frac{e^*V}{2k_{\mathrm{B}}T} - \frac{2k_{\mathrm{B}}T}{e^*V} \right] \tag{5.10}$$

Unless specified, the temperature in the following is $T = 35$ mK.

Figure 5.6 synthesizes such separate QPC charge characterizations via shot noise.

Individual source QPC characterization

For the characterization of source charges, DC-voltage bias $V_{\mathrm{t(b)}}$ is individually applied to QPCt(b) and the induced source shot noise is accessed thanks to the total noise $S_\Sigma \equiv$

$\Delta S_{\rm LL} + \Delta S_{\rm RR} + 2S_{\rm LR}$ by current conservation (see Section 3.5 for more details). Note that S_Σ is not impacted by the inter-channel tunneling artifacts because these processes conserve the overall downstream current.

The obtained signal S_Σ, corresponding to $\mathrm{QPC}_{\rm t(b)}$ source noise, is plotted versus the applied DC-voltage $V_{\rm t(b)}$ in Fig. 5.6a(b) as black triangles. For both top and bottom sources, the data match with the prediction of Eq. (5.10) for $T = 35$ mK $e^* = e/5$ (green line), in contrast with $e^* = e/3$ (red line), and a fortiori with $e^* = e$. This agreement between data and prediction validates the picture of two diluted beams of $e/5$-charged quasiparticles impinging on $\mathrm{QPC}_{\rm c}$.

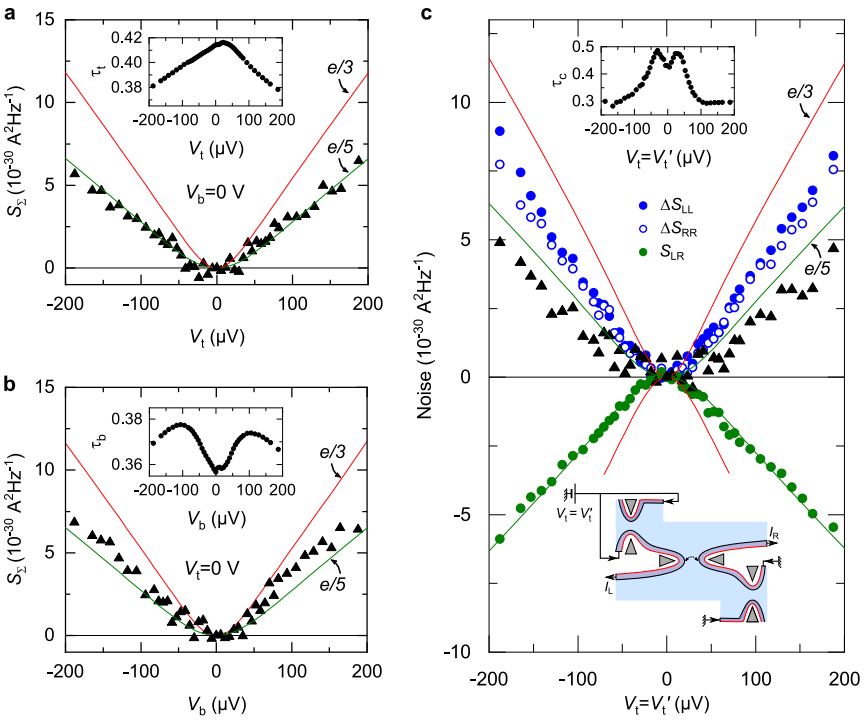

Figure 5.6: **Individual QPC tunneling charge characterization in the inner channel of the $\nu = 2/5$ state.**
a (b) Shot noise characterization of the charge emitted by the source $\mathrm{QPC}_{\rm t}$ ($\mathrm{QPC}_{\rm b}$) through the measured noise sum signal S_Σ versus source voltage $V_{\rm t(b)}$ (while $V_{\rm b(t)} = 0$).
c Auto- (blue symbols) and cross-correlation (green symbols) signals as a function of the DC-voltage $V_{\rm t} = V_{\rm t}'$, implementing a direct bias of $\mathrm{QPC}_{\rm c}$ (see schematics in set). The data are confronted to the Eq. (5.10) predictions with charge $e/3$ (red line) and $e/5$ (green line) at $T = 35$ mK.

Separate central QPC characterization

The charge $e_{\rm c}$ tunneling across $\mathrm{QPC}_{\rm c}$ is also characterized with the same procedure as in the previous chapters. The same DC-bias voltage is applied on both sides of a source QPC which imposes a direct bias $V_{\rm t} = V_{\rm t}'$ on $\mathrm{QPC}_{\rm c}$. The charge $e_{\rm c}$, is again inferred by comparing the noise auto- and cross-correlation signals to predictions of Eq. (5.10) (continuous lines), as presented in Fig. 5.6c.

The robust cross-correlations $S_{\rm LR}$ are in remarkable agreement with $e^* = e/5$ (green line, displaying $-1\times$ Eq. (5.10)) which indicate that quasiparticles across $\mathrm{QPC}_{\rm c}$ are $e^* = e/5$ and

not $e^* = e/3$ (red line). Note that the transmission ratio of the three QPCs remains in the range $[0.25, 0.5]$ (see insets in Fig. 5.6), far from the dilute quasiparticle source limit that is experimentally inaccessible.

However, the auto-correlation signals ΔS_{LL} (blue discs) and ΔS_{RR} (blue circles) present an intermediate slope between the predictions with $e^* = e/3$ and $e^* = e/5$. As a consequence, the total noise signal S_Σ, predicted to be zero in that specific case is unexpectedly far from negligible. This surprisingly strong deviation of S_Σ from zero might be related to the non-local heating observed at $\nu = 1/3$ and specifically investigated in Section 4.12.2.

Discussion about the unexpected increase of S_Σ

How this non-zero S_Σ signal observed during the distinct $\mathrm{QPC_c}$ characterization could impact our conclusions about the possible non-trivial braiding of quasiparticles? Three arguments lead us to answer that this impact is likely moderate.

First, as previously mentioned in Section 4.5.2, the cross-correlations (which match very well with charge $e_\mathrm{c} = e/5$) were previously established to give more robust information than auto-correlations [125].

Second and most importantly, the unexpected increase of S_Σ is obtained with DC-voltage bias settings different from the main source-analyzer configuration ($V_\mathrm{t} = V_\mathrm{b}$ with $V_\mathrm{t}' = 0$ instead of $V_\mathrm{t} = V_\mathrm{b}$ with $V_\mathrm{t}' = 0$). In the main DC-bias configuration, as a direct voltage is applied to both sources, the effect of local heating on S_Σ is expected to be suppressed (the shot noise at high bias does not depend on T). But even if such an unexpected increase of S_Σ also appeared in the main configuration, it would reduce the absolute value of P without suppressing it, and therefore, it would not impact our qualitative conclusions (see equation (5.3)).

Now that the charges naturally tunneling across each QPC are characterized, let us focus on the noise signal in the main source-analyzer configuration.

5.3.2 Representative cross-correlation signature of exotic quasiparticle signature in the $\nu = 2/5$ inner channel

In the same spirit as in the previous chapter, the negative cross-correlations are specifically investigated through the experimental generalized Fano factor P_{exp}

$$P_{\mathrm{exp}} = \frac{S_{\mathrm{LR}}}{S_\Sigma \tau_\mathrm{c}(1-\tau_\mathrm{c})} \tag{5.11}$$

where the denominator is chosen to minimize the direct, voltage-dependent contribution of the shot noise from the sources S_Σ, thus focusing on the signal of interest generated at the analyzer.

Figure 5.7 displays such a cross-correlation signal in the inner edge channel of the $\nu = 2/5$ FQH state. The two sources are symmetrically voltage biased at $V_\mathrm{t} = V_\mathrm{b}$ (with $V_\mathrm{t}' = 0$) as illustrated in the schematics (a).

The simultaneously measured total noise signal S_Σ, corresponding to the total source noise, is presented in Fig. 5.7b. When plotted versus the total incoming current $I_+ = I_\mathrm{t} + I_\mathrm{b}$ and compared with the following phenomenological predictions (valid beyond the Poissonian regime)

$$S_\Sigma = 2e^* \left[\tau_\mathrm{t} I_\mathrm{t} \left(\coth \frac{e^* V_\mathrm{t}}{2k_\mathrm{B}T} - \frac{2k_\mathrm{B}T}{e^* V_\mathrm{t}} \right) + \tau_\mathrm{b} I_\mathrm{b} \left(\coth \frac{e^* V_\mathrm{b}}{2k_\mathrm{B}T} - \frac{2k_\mathrm{B}T}{e^* V_\mathrm{b}} \right) \right] \tag{5.12}$$

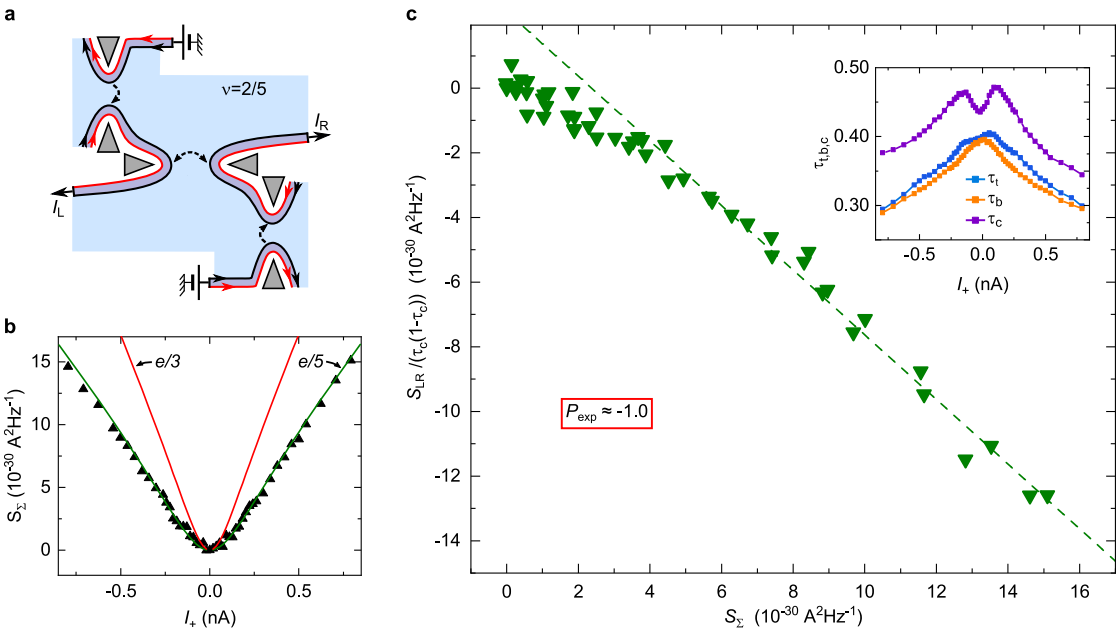

Figure 5.7: **Cross-correlation signature of exotic quasiparticles in the inner edge channel at $\nu = 2/5$.**
a Device configuration in the main cross-correlation measurement: with all QPCs tuned to partition the inner channel of the $\nu = 2/5$ state, the sources are symmetrically biased so that beams of quasiparticle impinge on $\mathrm{QPC_c}$.
b Simultaneous characterization of the impinging charges through the noise S_Σ (black triangles) induced by the symmetrically biased sources. The green (red) line displays Eq. (5.12) with $e^* = e/5$ ($e^* = e/3$).
c With symmetric sources, normalized cross-correlations (green symbols) corrected with the estimated inter-channel tunneling contribution and plotted versus the same source noise S_Σ also shown in (a). The generalized Fano factor P_{exp} (in this illustrative example $P_{\mathrm{exp}} \simeq -1.0$) is extracted from a linear fit of the data (green dashed lines). The simultaneously measured QPC transmission ratios $\tau_{\mathrm{t,b,c}}$ are shown in the inset.

for $T = 35$ mK $e^* = e/3$ (red line) and $e^* = e/5$ (green line), it directly informs on the average impinging charge during the measurement. The good agreement between data and the green line confirms that the impinging quasiparticles have indeed the expected charge $e/5$.

The main panel Fig. 5.7c, presents the normalized cross-correlations $S_{\mathrm{LR}}/(\tau_{\mathrm{c}}(1-\tau_{\mathrm{c}}))$ corrected by the inter-channel tunneling contribution and plotted versus the source noise S_Σ. Following Eq. (5.11), the value of P_{exp} can be straightforwardly extracted from a linear fit (dashed green line). The value obtained in this representative example is $P \simeq -1$ (we get $P \simeq -1.07$ from the raw data including the inter-channel tunneling contribution).

Qualitatively, the obtained clearly negative value of P_{exp}, in contrast with the free fermions predictions ($P = 0$), could indicate that the underlying process involves an unconventional exchange phase, like in the $\nu = 1/3$ regime. Quantitatively, the extracted value of P_{exp} is much weaker than the one at $\nu = 1/3$.

However, the marked difference and the opposite sign of P_{exp} with respect to the naive prediction $P_{\mathrm{thy}} = +6$ (see Section 5.1.3), indicate that the theory developed for Laughlin fractions does not directly apply in this Jain case (the theory breaks down for $\Delta > 1/4$ which is

the case here). The presence of several copropagating channels is also likely to play an important role [2] and impedes a direct connection between the measured signal and the braiding phase of a free $e/5$-charge quasiparticle. Section 5.3.4 will summarize our current understanding of the meaning of such negative cross-correlations in the inner channel of the $\nu = 2/5$ Jain's state.

5.3.3 Robustness of P_{exp} versus $\mathrm{QPC_c}$ tuning τ_{c}

This section recapitulates the experimental generalized Fano factor extracted for the $e/5$ quasiparticle of the inner channel over five different device settings.

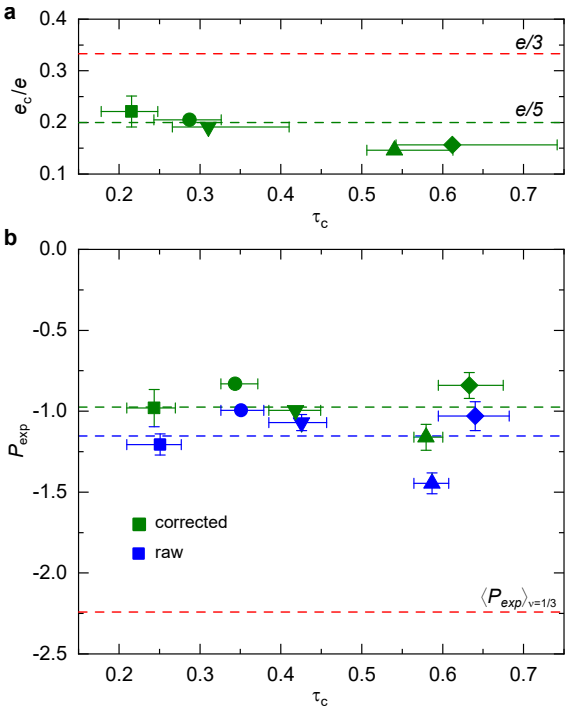

Figure 5.8: **Effective Fano factor for $e = e/5$ quasiparticles at $\nu = 2/5$.**
a Separately characterized $\mathrm{QPC_c}$ tunneling charge e_{c} versus τ_{c}.
b Observed value of P_{exp} with (green symbols) and without the correction for inter-channel tunneling. The same symbol as in (a) corresponds to an identical device tuning (τ_{c} changes due to a different biasing). The horizontal dashed lines display the corresponding mean values $\langle P \rangle \simeq -0.97$ (green) and $\langle P \rangle \simeq -1.15$ (blue), together with the previous $\nu = 1/3$ observation ($P_{\mathrm{exp},1/3} = -2.24$, red). When larger than the symbols, horizontal and vertical error bars respectively display the variation of τ_{c} during the measurement and the difference between the values obtained separately for negative and positive DC-voltages.

Figure 5.8 synthesizes this overview. For each configuration, the characteristic charge $e_{\mathrm{c}} \simeq e/5$ is extracted from linear fits of S_{LR} plotted versus $V_{\mathrm{t}} = V_{\mathrm{t}'}$ (while $V_{\mathrm{b}} = 0$, like in Fig. 5.6c) beyond the thermal rounding ($V > k_{\mathrm{B}}T/e^*$).

The extracted charges are plotted versus the corresponding τ_{c} in Fig. 5.8a and present a good agreement with $e/5$, stable over the whole rather broad explored range $\tau_{\mathrm{c}} \in [0.2, 0.8]$. Quasiparticles of charge $e/3$ naively expected in the SBS regime of the inner channel were

[2] they can have negative cross-correlations even in the IQH regime [126], as discussed in the following chapter

not observed at these explored transmissions[3]. Resonances and the strong voltage dependence of τ_c in the SBS regime prevented us from exploring lower τ_c tunings. Horizontal error bars encompass the variation of τ_c over a given device configuration and the vertical error bars indicate the difference between fits over positive and negative voltages.

Note that for all those operating points, the source charges are also in good agreement with $e/5$ (see Eq. (5.12)) in spite of the transmissions being far from the diluted regime ($\tau_{t,b} \in [0.25, 0.5]$ typically), which was not accessible experimentally.

The extracted values of P_{exp} are summarized in Fig. 5.8b with symbols matching those of Fig. 5.8a for identical operating points (the different τ_c are due to a different bias configuration). The green symbols correspond to the "corrected" values of P_{exp}, i.e. extracted after removing the additional inter-channel tunneling contribution (see Section 5.2 for the detailed calibration procedure). The averaged value over all the operating points $\langle P_{exp} \rangle = -0.97$ is indicated by the horizontal dashed line.

The blue symbols display the "raw" values of P_{exp}, including the inter-channel tunneling signal, and give an average value $\langle P_{exp}^{raw} \rangle = -1.15$ (dashed blue line). The difference between blue and green data sets is relatively small with respect to the overall value of P_{exp} ($\simeq 20\%$) without presenting any noticeable trend, which indicates that the inter-channel tunneling does not impact the qualitative conclusions.

Like in the $\nu = 1/3$ FQH regime, P_{exp} is remarkably stable with τ_c. However, as there is no mismatch between source and central QPC charges, no cross-over to a distinct Andreev-like scattering mechanism (see Chapter 3) can develop.

5.3.4 Can we connect the observed negative cross-correlations to a nontrivial anyonic exchange phase?

This section aims to briefly clarify the meaning that, at this stage of our understanding, one can give to the observed negative cross-correlations in the case of the inner channel at $\nu = 2/5$.

Qualitatively, the obtained clearly negative value of $\langle P_{exp} \rangle \simeq -1$ is in striking contrast with the predictions for free fermions ($P = 0$). Like in the previous $\nu = 1/3$ investigated fraction, this qualitative feature indicates that the underlying process could involve an unconventional exchange phase. Moreover, as there is no charge mismatch between the sources and QPC_c, no distinct Andreev-like scattering could develop in this case and blur the physical origin of such negative cross-correlations. Note that the influence of source asymmetry was impeded in our case due to the inaccessible WBS regime for sources (here $1 - \tau_{t,b} \gtrsim 0.5$). Here, an asymmetry corresponds to a complex combination of direct voltage bias and incident fractional quasiparticles.

Quantitatively, the value of P_{exp} is much smaller than the observed $P \simeq -2$ at $\nu = 1/3$ and far from the naive prediction $P = +6$. Then, the connection between this negative signal and the anyon braiding statistics is not as straightforward as the simpler Laughlin case. Indeed, for an edge structure involving several copropagating channels, interactions between the channels can induce small negative cross-correlations in the WBS regime, even in the IQHE [126, 128]. This will be largely developed in the following chapter with a specific investigation of the role of interactions in such systems. Furthermore, the theory developed for Laughlin fractions [1],

[3] τ_c in our case was maybe too high to remain in the SBS regime

and recently extended to a non-Abelian channel [47], does not yet encompass hierarchical states such as $\nu = 2/5$. Quantitative conclusions are therefore impeded by these two challenges.

Thus, even though the observed negative cross-correlations constitute a clear marker of exotic excitations (in contrast with the free-fermions case) and could be linked to an unconventional braiding process, an unambiguous connection with the fractional statistics would require both a complete theoretical description of this system for Jain's states and further experimental investigations. In particular, the role of inter-channel Coulomb interactions needs to be clarified.

5.4 Noise signature of exotic quasiparticles in the outer channel

5.4.1 The outer channel of the $\nu = 2/5$ state

At $\nu = 2/5$, theory predicts that the bulk region between the two edge channels (illustrated by darker blue in all the schematics of this chapter) is locally in the effective filling factor $\nu_{\text{eff}} = 1/3$ [81, 125] and, consequently, that the tunneling charge across a QPC partitioning this outer channel are $e/3$-charged anyons. Such $e/3$-quasiparticles in the outer channel at $\nu = 2/5$ have largely been observed in the past 20 years (see e.g. [56, 58]). But to go further, one could naturally ask if they present the same noise signature of anyonic statistics as the quasiparticles of the pure $\nu = 1/3$ state discussed in Chapter 4.

In order to perform such a comparison between quasiparticles at $\nu_{\text{eff}} = 1/3$ and at pure $\nu = 1/3$ regime, similar noise measurements can therefore be reproduced in the outer channel of the same $\nu = 2/5$ regime. However, in the investigated sample, many experimental artifacts in the outer channel made it difficult to extract a cross-correlation signal resulting only and unambiguously from a braiding process on QPC_c. Indeed on the outer channel, we had to deal with inter-channel tunneling (like in the inner one see Section 5.2) but also with channel mixing (meaning that both channels are simultaneously partitioned by the QPC instead of being well separated), with a significant fraction of current flowing in the bulk (which violates chirality), and with important QPC resonances adding spurious noise to the signal.

Considering all these artifacts, we only managed to obtain one single operating point. This point is discussed in the remainder of this section but we stress that it will only provide qualitative information due to the lack of reproducibility that we had to face.

5.4.2 Individual QPC characterization

The standard characterization of the charges tunneling across QPCs partitioning the outer channel is presented in Figure 5.9. Like in the inner channel or the pure $\nu = 1/3$ case, these measurements are performed just before the main measurement and without changing any split gate voltage.

Both source shot noise characterizations (Fig. 5.9a and b) are compared with Eq. (5.10) and present tunneling charges in reasonable agreement with $e/3$ (red line) and in marked contrast with $e/5$ (green line).

The characterization of QPC_c is performed by applying $V_\text{t} = V_\text{t}'$ while $V_\text{b} = 0$ (which implements a direct voltage bias on the analyzer QPC) and the measured noise signals are plotted in Fig. 5.9c. Like in the inner channel case, the auto-correlation signals ΔS_{LL} and

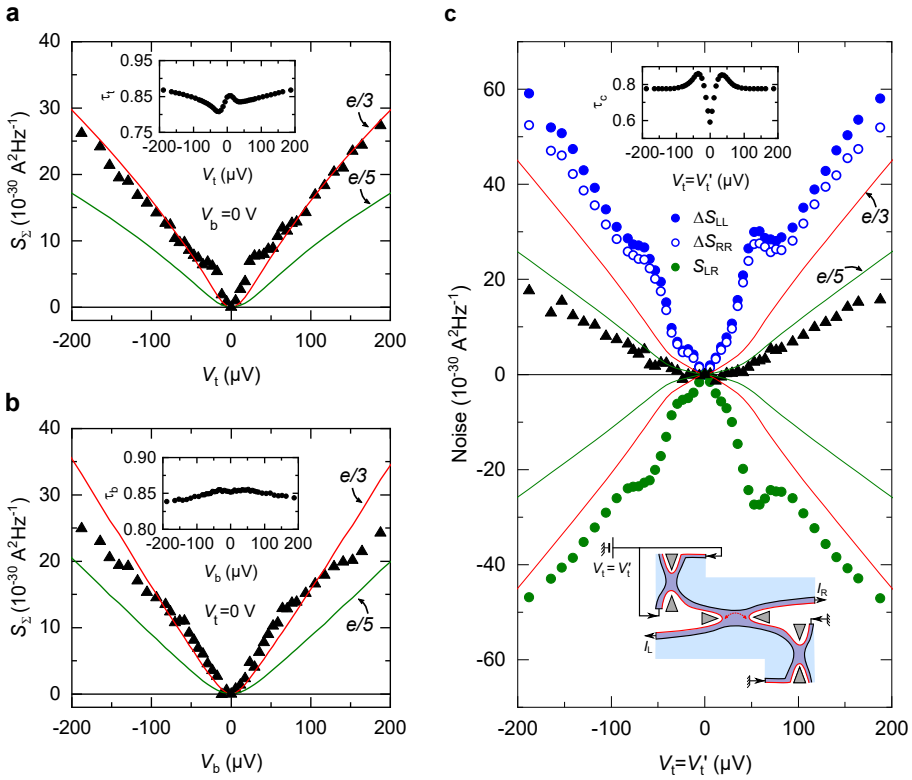

Figure 5.9: **Individual charge characterization in the $\nu = 2/5$ outer channel.**
a (b) Shot noise charge characterization of the top left QPC_c (bottom-right QPC_b) source via the sum signal S_Σ. The measurement are displayed versus $V_{t(b)}$ (while $V_{b(t)} = 0$).
c Auto- (blue symbols) and cross-correlation (green symbols) signals versus the DC-voltage $V_t = V_t'$, realizing a direct bias of QPC_c (see schematics in inset). The data are confronted to Eq. (5.10) predictions with $e/3$ (red line) and $e/5$ (green line) at $T = 24$ mK.

ΔS_{RR} (blue dots) are significantly higher than the more robust cross-correlations (green dots) which induce a nonzero sum signal S_Σ (black triangles). But despite this unexplained feature and in spite of a peak indicating a resonance at intermediate voltage, signals at low and high voltage are reasonably compatible with charges $e/3$ (red line) and clearly not with charge $e/5$ (green line).

With these individual characterizations being performed, let us measure the cross-correlations noise signal in the configuration with balanced sources.

5.4.3 Cross-correlation signal with balanced sources

Figure 5.10 presents the main cross-correlation measurement performed with all QPCs set on the outer channel and in the case of balanced sources (see the schematics of panel (a)). The simultaneously measured source noise signal S_Σ is displayed in Fig. 5.10b (black triangle) and indicates $e/3$ incoming charges (the data match with the red line and not with the green line).

Like in the previous cases, the signature of anyon statistics is investigated in panel (c) by plotting the renormalized cross-correlations $S_{LR}/(\tau_c(1-\tau_c))$ as a function of the source noise S_Σ. For the displayed data, the inter-channel contribution (of the same order of magnitude as

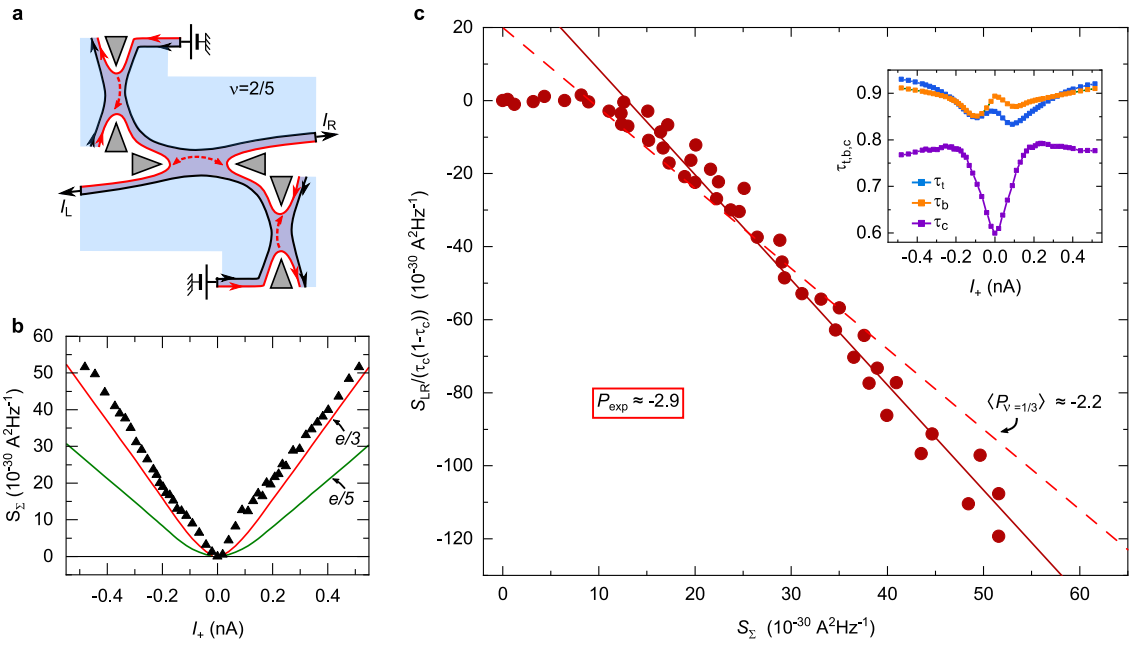

Figure 5.10: **Cross-correlations with symmetric sources on the $\nu = 2/5$ outer channel for the investigated operating point.**
a Device configuration: with all QPCs set to partition the outer channel (red line with arrow), the source QPCs are symmetrically DC-voltage biased.
b Shot noise characterization of the source charge, measured simultaneously with data of (c). The red and green lines indicate predictions with fractional charges $e^* = e/3$ and $e/5$ respectively.
c Cross-correlations with removed tunneling contribution in the symmetric source-analyzer configuration are plotted versus the source noise S_Σ. The generalized Fano factor $P_{\text{exp}} = -2.9$ is obtained from a linear fit of the data as displayed by the dark red plain line. The red dashed line indicates the slope obtained in the $\nu = 1/3$ case (see Chapter 4). Inset: QPCs transmissions

the inner channel case) is removed. The generalized Fano factor extracted from a linear fit on the negative data gives $P_{\text{exp}} = -2.9$ which remains in the same order of magnitude as the pure $\nu = 1/3$ Fano factor $\langle P_{\nu=1/3} \rangle = -2.2$ (see Sec. 4.6).

Thus, while the lack of reproducibility prevents to make quantitative conclusions, the presence of a negative signal of the same order of magnitude as the one obtained in the $\nu = 1/3$ regime suggests comparable anyon statistics and a similar underlying braiding process. Note that an independent experimental investigation in the LPENS lab gave consistent results [48].

5.5 Conclusion

In this chapter, we reported qualitative signatures of anyon statistics in the hierarchical $\nu = 2/5$ fraction, with a negative cross-correlation signal measured in a balanced source-analyzer set-up.

In the inner channel of this $\nu = 2/5$ Jain fraction, a non-zero generalized Fano factor P_{exp} indicates the presence of an underlying braiding process involving anyons different from the pure $\nu = 1/3$ Laughlin anyons discussed in the previous chapters. This negative signal

obtained with symmetric sources is indeed in striking contrast with the free-fermion prediction of vanishing cross-correlations. However, the quantitative value of P_{exp} is far from the $P = +6$ that one expects by naively using predictions of Refs. [1, 134, 47, 46] derived in the case of non-interacting Laughlin anyons. This suggests that the hierarchical Jain fractions might present additional features that the theory does not fully describe yet.

In the outer channel, the explored operating point that was not hampered by experimental artifacts also provided negative cross-correlations consistent with the results of the $\nu = 1/3$ fraction indicating that the involved anyons have similar anyon statistics.

Besides, note that these measurements obtained beyond the simple Laughlin fraction involved several edge channels that are expected to interact. Recently, due to such inter-channel Coulomb interactions, non-zero cross-correlations have been predicted [126, 46, 150] even at the integer fraction $\nu = 2$. Negative cross-correlations could therefore provide a signature of interaction-driven anyon quasiparticles propagating along integer quantum Hall edge channels. The following chapter aims to implement and clarify the role of inter-channel interactions in a source-analyzer setup in the $\nu = 2$ integer quantum Hall regime.

Chapter 6

Signature of anyonic statistics of fractional charges in the integer quantum Hall regime

In the integer quantum Hall (IQH) regime, Coulomb interactions can turn injected electrons into more complex collective excitations. In particular, at filling factor $\nu = 2$, interactions between the two copropagating channels lead injected electrons to split into the so-called *edge magneto-plasmons* (EMP), which are charge density modes delocalized over the two IQH edge channels and propagating at distinct velocities.

Following seminal work focusing on inter-channel interactions and energy relaxation at $\nu = 2$, an intense study of edge magneto-plasmons has developed in the past decade both theoretically (e.g. [151], [89], [96], [152], [153], [154]) and experimentally. The picture of EMP, which is composed of one neutral and one charged mode in our case, has for instance been evidenced through interferences of density waves [155], shot noise generation [97], charge-density correlation in Hang-Ou-Mandel geometry [156] or even more direct time-resolved charge waveform measurements [157]. Hence, this picture is by now firmly established.

In this final experimental chapter, we study the nature of IQH edge fractional charges resulting from EMP propagation in a balanced source-analyzer geometry, set up at $\nu = 2$. We report the observation of non-zero cross-correlations between the current fluctuations at the outputs of the analyzer, matching with the EMP theory. We also establish the connection of this signal with the anyon braid phase of the fractional charges emerging along the IQH edge channel. In particular, the negative signal detected in the dilute regime is interpreted as a signature of an anyon exchange phase, which opens the way to study anyons in the IQH regime, which can be used as a simpler platform than the FQHE.

Section 6.1 presents the principle of the source-analyzer experiment in IQHE and the theoretical predictions for EMP in this geometry. After describing the experimental device in Section 6.2, experimental results are presented first with the evidence of EMP generation in our system (Section 6.3). Then, we report the observation of a non-zero cross-correlation signal in the case of two balanced impinging beams, and we establish its link to the fractional exchange phase in the specific diluted regime (Section 6.4). Finally, additional experimental tests corroborating the main results are presented in Section 6.5.

6.1 Fractional charges in a source-analyzer set-up: principle and predictions

In Chapter 2, we have seen that inter-channel Coulomb interactions can induce fractional charges in the Integer Quantum Hall effect (see Sec. 2.4.2). The strength of interactions is encoded in the *mixing angle* $\varphi \in [0, \pi/4]$. $\varphi = 0$ corresponds to the non-interacting limit. In the case $\nu = 2$, at $\varphi = \pi/4$ and after a long enough interaction time, an initial electronic excitation injected into one channel splits into two excitations delocalized over both channels:

- a *neutral excitation*, made of one wave packet carrying a charge $+e/2$ on one channel and one wave packet carrying a charge $-e/2$ in the other channel. It propagates at velocity v_-
- a *charged excitation*, made of one $+e/2$-charged wave packet in each channel. It propagates at velocity v_+

As these two excitations have different velocities (see Fig. 2.7), they can split for a long enough propagation. In the following, we will specifically investigate the wave packets in one channel and we will call them "fractional charges".

Is the exchange statistics of these resulting fractional charges anyonic? Using a source-analyzer setup with diluted beams of edge magneto-plasmons could bring strong insights to answer this question.

6.1.1 Principle of the measurement

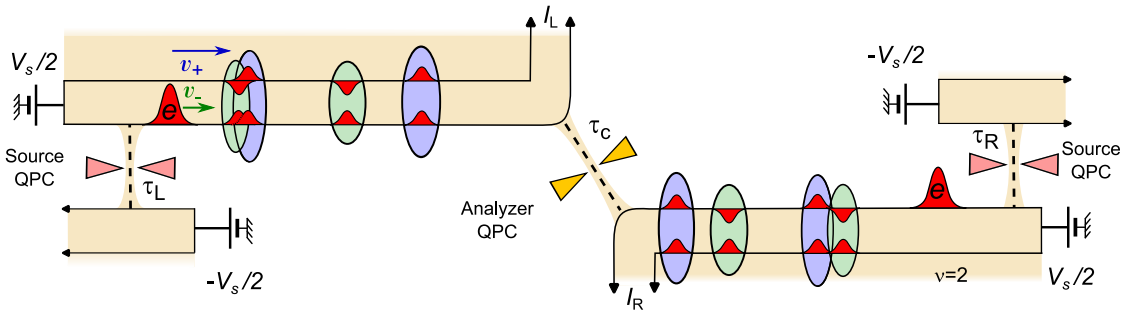

Figure 6.1: **IQH edge fractional charges in a source-analyzer set-up at $\varphi = \pi/4$.** Two source QPCs (pink triangles), identically biased by $\pm V_S/2$, create electron excitations (red wave packet facing up) in one edge channel at $\nu = 2$. Due to interactions, electronic excitations split (encircled pairs of red wave packets) and the two resulting beams of fractional charges impinge upon the opposite sides of a central "analyzer" QPC (yellow triangles). The cross-correlations fluctuations between outgoing currents $\langle \delta I_L \delta I_R \rangle$ are investigated.

The experiment implemented in this chapter aims to explore the nature of fractional charges along an IQH edge via the noise signal obtained from a source-analyzer setup. The principle is similar to the one used in Chapters 4 and 5 in the fractional quantum Hall regime, and is illustrated in Fig. 6.1. At $\nu = 2$, two balanced opposite source QPCs (pink triangles), with essentially identical transmissions τ_S) inject electrons (red wave packets facing up, near

the sources) into the outer edge channel. Due to Coulomb interactions between the two copropagating channels (black lines with arrows), the electron wave packets split into a charged and a neutral excitation (pairs of smaller wave packets encircled by blue and green ellipses respectively) delocalized between the two copropagating channels. The width $h/(eV_S)$ of the wave packets at a given distance is controlled thanks to the voltage $\pm V_S/2$ symmetrically applied on sources, allowing to tune the separation.

The fractional charges localized in the outer edge channel ($e/2$ at $\varphi = \pi/4$ and long distance) impinge on the central QPC, which creates current shot noise. The cross-correlations of currents between the two outgoing beams are then measured to detect the signatures of their unconventional properties. Let us now present the predictions of EMP theory.

6.1.2 Predictions in the edge magneto-plasmon framework

As seen in the previous chapters, in the source-analyzer geometry, cross-correlations $S_{LR} \equiv \langle \delta I_L \delta I_R \rangle$ constitute a powerful tool to detect signatures of exotic excitations. Indeed, for conventional *non-interacting* fermions, a simple Büttiker treatment gives the cross-correlations:

$$S_{LR} = \frac{2e^2}{h}\tau_c(1-\tau_c)\int d\epsilon \left[f_L(\epsilon) - f_R(\epsilon)\right]^2 \tag{6.1}$$

with $f_{L,R}$ the respective Fermi distributions of the left and right incoming beams. Remarkably, S_{LR} vanish in the balanced case $\tau_L = \tau_R$ (i.e. $f_L = f_R$).

Let us determine how this observable behaves in a balanced source-analyzer setup for the $\nu = 2$ case with short-range Coulomb *interacting* fermions, resulting in edge magneto-plasmons.

Cross-correlations:

Recently, several theoretical studies have provided predictions for the cross-correlation shot noise resulting from two beams of EMP propagating along IQH edge channels in a source-analyzer setup. In particular, Idrisov *et al.* [126] and D. Kovrizhin [150] gave quantitative predictions. In the following, we present the expectations derived by D. Kovrizhin in private communications [150]. They are based on a formalism previously developed in Ref. [96, 158, 159] which uses bosonization and refermionization techniques allowing to transform the Hamiltonian for interacting electrons into a free bosons one. Under this treatment, supposing $\varphi = \pi/4$ and that the sources have equal transmissions ($\tau_L = \tau_R = \tau_S$), the total cross-correlation noise can be expressed at $T = 0$ K as:

$$S_{LR} = 4\frac{e^2}{h}\tau_c(1-\tau_c)\tau_S(1-\tau_S)|eV_S| + 4\frac{e^2}{h}\tau_c(1-\tau_c)\frac{\hbar}{2\pi}\int_{-\infty}^{\infty}\left(|\langle e^{-i\pi\mathcal{N}_+}\rangle + \langle e^{-i\pi\mathcal{N}_-}\rangle|^2 - 1\right)\frac{dt}{t^2} \tag{6.2}$$

where $\mathcal{N}_\pm$ is the operator counting the excitations of respective velocities $v_\pm$, within the spatial interval $v_\pm t$ [96, 159] [1].

The first term on the right-hand side of Eq. (6.2) corresponds to the direct redistribution of the low-frequency source noise $\tau_c(1-\tau_c)S_\Sigma$. S_Σ is the total noise from both sources that we access by current conservation: $S_\Sigma \equiv \Delta S_{LL} + \Delta S_{RR} + 2S_{LR}$ (see Sec. 3.5 for details). As

[1] Note that this equation has been numerically extended to finite temperature by D. Kovrizhin and we will use such predictions at $T = 11$ mK for comparison with experimental data

the low-frequency edge current propagates unchanged, assuming that inter-channel tunneling is negligible, this first term is robustly independent of Coulomb interactions.

The second term is the noise specifically generated at the analyzer $\mathrm{QPC_c}$. It is the signal of interest, which carries information about the nature of the fractional charges involved. In general, it has to be evaluated numerically but one can derive analytical expressions in two specific cases.

First, in the special case $\tau_\mathrm{S} = 0.5$, the integral can be approximated at $T = 0$ mK by the expression $-\frac{|eV_\mathrm{S}|}{2\pi}\sqrt{\pi/2}$, giving a complete analytical formula for S_LR:

$$\boxed{\begin{aligned} S_\mathrm{LR}(V, \tau_\mathrm{S} = 0.5) &= \frac{e^2}{h}\tau_\mathrm{c}(1-\tau_\mathrm{c})|eV_\mathrm{S}|\left(1-\sqrt{\frac{2}{\pi}}\right) \\ &= \tau_\mathrm{c}(1-\tau_\mathrm{c})S_\Sigma\left(1-\sqrt{\frac{2}{\pi}}\right) \end{aligned}} \tag{6.3}$$

Note that in this case S_LR is clearly positive.

Second, in the asymptotic case $\tau_\mathrm{S} \to 0$, Eq. (6.2) can be expanded and leads to the following expressions:

$$\boxed{\begin{aligned} & S_\mathrm{LR} \sim 4\frac{e^2}{h}\tau_\mathrm{c}(1-\tau_\mathrm{c})\tau_\mathrm{S}(1-\tau_\mathrm{S})|eV_\mathrm{S}|\left[\frac{4}{\pi^2}\ln(\tau_\mathrm{S}) + \frac{4}{\pi^2}\tau_\mathrm{S}\ln(\tau_\mathrm{S}) - 0.30\tau_\mathrm{S} + 0.94\right] \\ \text{i.e.}\quad & S_\mathrm{LR} \sim \tau_\mathrm{c}(1-\tau_\mathrm{c})S_\Sigma\left[\frac{4}{\pi^2}\ln(\tau_\mathrm{S}) + \frac{4}{\pi^2}\tau_\mathrm{S}\ln(\tau_\mathrm{S}) - 0.30\tau_\mathrm{S} + 0.94\right] \end{aligned}} \tag{6.4}$$

Note that in that case, the signal is negative, due to the term in $\ln(\tau_\mathrm{S})$ which dominates in the low source transmission limit. A similar expression has been derived in Ref. [126].

Therefore, in the EMP framework, the renormalized cross-correlations $S_\mathrm{LR}/(\tau_\mathrm{c}(1-\tau_\mathrm{c}))$ are predicted to be independent of the transmission of $\mathrm{QPC_c}$ and most remarkably, to present a cross-over from a negative signal in the regime $\tau_\mathrm{S} \to 0$ to a positive signal in the regime $\tau_\mathrm{S} \sim 0.5$. This feature is shown in Fig. 6.2 by plotting the renormalized $S_\mathrm{LR}/(\tau_\mathrm{c}(1-\tau_\mathrm{c}))$ as a function of τ_S.

Importantly, the cross-correlation signal is therefore in remarkable contrast with the free fermion prediction of Eq. (6.1) for which we expect vanishing cross-correlations at $\tau_\mathrm{L} = \tau_\mathrm{R} = \tau_\mathrm{S}$.

Generalized Fano factor:

Like in the previous chapters, in order to minimize the voltage-dependent contribution of the source noise (first term) and to specifically focus on the analyzer contribution (second term), the relevant parameter to investigate the signal is the *generalized Fano factor* P_EMP, defined by:

$$P_\mathrm{EMP} \equiv \frac{S_\mathrm{LR}}{\tau_\mathrm{c}(1-\tau_\mathrm{c})S_\Sigma} \tag{6.5}$$

Using Equations. (6.3) and (6.4) of respective regimes $\tau_\mathrm{S} \sim 0.5$ and $\tau_\mathrm{S} \to 0$, we deduce the expressions of P_EMP for these two regimes (see inset in Fig. 6.2) in the limit $eV \gg k_\mathrm{B}T$:

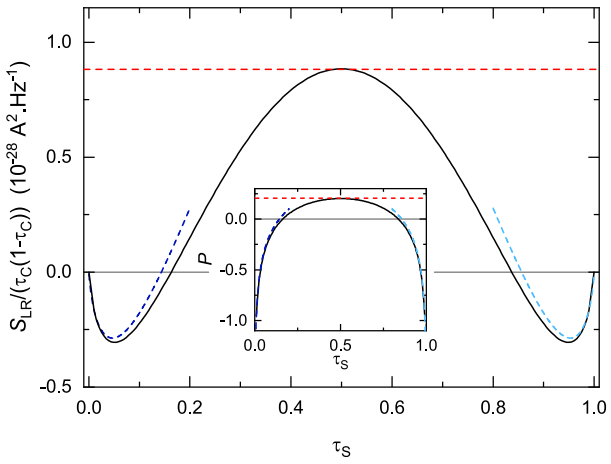

Figure 6.2: **Cross-correlations cross-over prediction in the EMP theory.** Renormalized cross-correlations plotted versus the source transmission τ_S. Black line displays numerical calculations at $T = 0$ K and $\tau_c = 0.5$. The horizontal red dashed line indicates Eq. (6.3). Blue dashed line corresponds to the asymptotic predictions of Eq. (6.4) (light blue line is the same using the substitution $\tau_S \to (1 - \tau_S)$) Inset: corresponding predictions for $P_{\rm EMP}$ from Eqs. (6.5) and (6.7)

$$\boxed{P_{\rm EMP}(\tau_S = 0.5) = \left(1 - \sqrt{\frac{2}{\pi}}\right) \simeq +0.20} \tag{6.6}$$

$$\boxed{P_{\rm EMP}(\tau_S \to 0) = \left[\frac{4}{\pi^2}\ln(\tau_S) + \frac{4}{\pi^2}\tau_S \ln(\tau_S) - 0.30\tau_S + 0.94\right] \underset{\tau_S=0.05}{\simeq} -0.35} \tag{6.7}$$

Therefore, this non-zero $S_{\rm LR}$ signal (and P value) is in marked contrast with the free fermion predictions. In particular, in the dilute regime $\tau_S \to 0$ a negative signal is predicted.

6.1.3 A signature of anyonic statistics in the dilute beam limit

Can the negative signal predicted in the $\tau_S \to 0$ limit for EMP at $\nu = 2$ be related to an anyonic exchange phase? Indeed, as we saw in Chapter 4, negative cross-correlations constitute a marker of anyon statistics for balanced diluted beams in Laughlin's $\nu = 1/3$ case. Fractional charges propagating along IQH edges have also been predicted to have a fractional mutual exchange statistics [64, 46] when braided with an electron-hole pair. It is then natural to wonder if the expected signal can be linked to an anyonic exchange statistics of the fractional $e/2$ charges. Note that in the $\nu = 2$ case, the signal is predicted to depend on τ_S which is different from the $\nu = 1/3$ case (which only requires the WBS regime [2]. One can also ask whether a time-braiding process happens, similar to the one occurring for quasiparticles in the FQH regime discussed in Chap. 4 and 5.

These questions have been tackled by Morel *et al.* [46], who consider a source-analyzer setup that mixes two beams of fractional charges in the IQH regime. In this proposal, wave packets of fractional charges e/N are generated due to the Coulomb interactions within a metallic island

[2]at $\nu = 1/3$, as soon as the sources are set up in the WBS regime, the signal is not expected to depend on τ_S

connected to N IQH edges (see Fig. 6.3a). But the arising "quasiparticles" are predicted to have the same nature as fractional charges resulting from inter-channel interactions or generated by pulses [64]. In the following, we consider such fractional charges $e/2$. Note that, as mentioned in Chapter 2, other strategies have been proposed generate fractional charges along IQH channels thanks to an interface between an IQHE and a FQHE region [85, 86], ot with voltage pulses [87].

In their work, Morel *et al.* predicted that an incident $e/2$ charge performs a time braiding with a spontaneously created electron-hole pair. This process appears similar to the one described in the previous chapters but an important difference has to be stressed. Here, the spontaneously excited pair at the central QPC is made of an electron and a hole, with a different nature from those of the incident charges $e/2$. The present experiment then probes the *mutual* braiding statistics between electron and fractional charges.

The process is illustrated in Fig. 6.3b and may be seen as follows: the electron-hole pair is excited at time t_1, then the incident $e/2$ charge passes across the QPC, and finally the electron-hole pair tunnels back (annihilates) at time t_2. This process holds as long as $t_2 - t_1 < \hbar/(k_B T)$ (for details, see Sec. 4.1.3). This time braiding is equivalent to a double exchange, corresponding to the fractional mutual exchange phase:

$$\theta_{q,q'} = \frac{\pi}{\nu_{\text{eff}}} \frac{qq'}{e^2} \tag{6.8}$$

where ν_{eff} is the effective filling factor of the channel (here $\nu_{\text{eff}} = 1$) and q, q' are the fractions of charge involved in the process. Importantly, in the present case, they are different $q = e/2$ and $q' = e$, leading to $\theta_{e,e/2} = \pi/2$. Note that this is in contrast with the case discussed in Chapter 3 where the involved e and $e/3$ quasiparticles led to the trivial phase π and did not contribute to the negative cross-correlations.

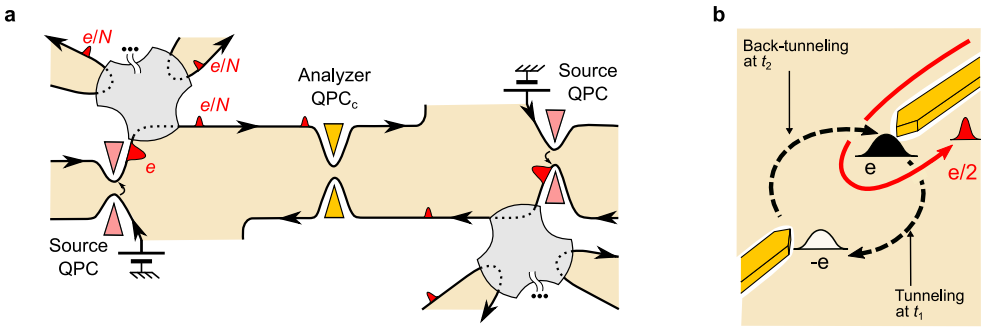

Figure 6.3: **Braiding of fractional charges.**
a Set-up proposed in Ref. [46] where the fractional charges along IQH edge channels (red wave packets) are produced thanks to a metallic island (grey regions). Only one IQH edge channel is represented (black line with arrows)
b Schematics of the process: in the $\nu = 2$ IQH state, an incident fractional quasiparticle of charge $e/2$ (red wave packet) braids with a quasiparticle-quasihole (black full and open wave packets) at the analyzer QPC (pair of yellow triangles). The time braiding can be seen as follows: a quasiparticle-quasihole is spontaneously excited at time t_1, the incident $e/2$ charge passes across the QPC, and finally the quasiparticle-quasihole tunnels back at time t_2.

In the dilute regime, Morel *et al.* predicted that this fractional mutual exchange phase man-

ifests itself as *negative* cross-correlations in the case of a balanced source-analyzer configuration [46]. These predictions were made in the IQH regime but with a similar derivation as the one of Rosenow *et al.* made for Laughlin fractions [1].

The leading term in cross-correlations found by the authors of Ref. [46] in the dilute regime is predicted to be

$$S_{\rm LR} \simeq \tau_{\rm c}(1-\tau_{\rm c})S_\Sigma\left[1+\frac{\sin\left(\theta_{q,q'}\right)^2}{\theta_{q,q'}^2}\ln\tau_{\rm S}\right], \quad \text{i.e.} \quad P = 1+\frac{\sin\left(\theta_{q,q'}\right)^2}{\theta_{q,q'}^2}\ln\tau_{\rm S}, \tag{6.9}$$

The term $\dfrac{\sin\left(\theta_{e,e/2}\right)^2}{\theta_{e,e/2}^2}\ln\tau_{\rm S}$ corresponds to the contribution of the central QPC and is related to the mutual braiding statistics. In the investigated case $\theta_{e,e/2} = \pi/2$, one gets :

$$S_{\rm LR} \simeq \tau_{\rm c}(1-\tau_{\rm c})S_\Sigma\left[1+\frac{4}{\pi^2}\ln\tau_{\rm S}\right], \quad \text{i.e.} \quad P = 1+\frac{4}{\pi^2}\ln\tau_{\rm S}, \tag{6.10}$$

Interestingly, the term linked to the mutual exchange phase $4/(\pi^2)\ln\tau_{\rm S}$ corresponds to the first term of the asymptotic Eq. (6.7) derived with the EMP approach. Note that P depends on $\tau_{\rm S}$, in contrast with the Laughlin case discussed in Chapter 4, for which P has a fixed value in the dilute regime.

Therefore, the EMP approach matches with the predictions of anyonic exchange phase derived in the dilute regime. The negative cross-correlations in this limit can be linked to the anyonic mutual exchange phase of the fractional charge $e/2$ with e charges.

6.1.4 An alternative picture in the Büttiker description?

One might wonder what would be the expected cross-correlations considering a more simple phenomenological description of the channels involving only fermions in interactions. Indeed, this system can naively be pictured as two channels with a double-step initial energy distribution (resulting from two Fermi distributions) and with inter-channel energy transfer. In this naive description, the inter-channel interactions result in the same relaxed *Fermi* distribution of effective temperature T^* in the two channels.

This kind of phenomenological description has previously been used for explaining previous experimental results (see e.g. [128] at $\nu = 1$ and [141, 160, 93] at $\nu = 2$). The cross-correlations in that picture have the form:

$$S_{\rm LR} = \tau_{\rm c}(1-\tau_{\rm c})S_\Sigma - 2\frac{e^2}{h}\tau_{\rm c}(1-\tau_{\rm c})\int_{-\infty}^{\infty}\left[f_{\rm L}(1-f_{\rm R})+f_{\rm L}(1-f_{\rm R})\right]d\epsilon \tag{6.11}$$

with L (R) denoting the left (right) distribution in the outer channel and with S_Σ the total noise incoming from both sources which is equal to $2\times 2\frac{e^2}{h}\tau_{\rm S}(1-\tau_{\rm S})eV_{\rm S}(\coth\frac{eV_{\rm S}}{2k_{\rm B}T}-\frac{2k_{\rm B}T}{eV_{\rm S}})$ in the balanced case. This formula reduces to the free-electron prediction (6.1) if $f_{\rm L,R}$ are double-steps. Again, the first term of Eq. (6.11) is the trivial redistribution of this total source noise while the second term is the specific contribution of the analyzer $\rm QPC_c$. In the considered case of balanced sources, the integral in the second term reduces to the thermal contribution $2k_{\rm B}T^*$, as it is assumed that the double-step distribution relaxes into a hot Fermi distribution at T^*. In the case of two channels[3] we have [160, 93]:

[3]the relation generalizes to n channels by replacing the factor $3/2$ by $3/n$

$$T^* = \sqrt{T^2 + \frac{3}{2}\tau_S(1-\tau_S)\left(\frac{eV}{\pi k_B}\right)^2} \tag{6.12}$$

Using Eq. (6.11) and (6.12), we deduce the cross-correlations expected in this naive fermionic case:

$$S_{LR} = \tau_c(1-\tau_c)S_\Sigma - 4\frac{e^2}{h}\tau_c(1-\tau_c)k_B T^*, \tag{6.13}$$

and in the limit $T = 0$ K, it reduces to:

$$S_{LR} = \tau_c(1-\tau_c)4\frac{e^2}{h}\tau_S(1-\tau_S)eV_S - 4\frac{e^2}{h}\tau_c(1-\tau_c)k_B\sqrt{\frac{3}{2}\tau_S(1-\tau_S)\left(\frac{eV}{\pi k_B}\right)^2} \tag{6.14}$$

The corresponding expected Fano factor is then:

$$\boxed{P_{\text{Fermions}} = 1 - \frac{\sqrt{3}}{\pi\sqrt{2\tau_S(1-\tau_S)}}} \tag{6.15}$$

Fig. 6.4 shows the evolution of the renormalized cross-correlations with τ_S.

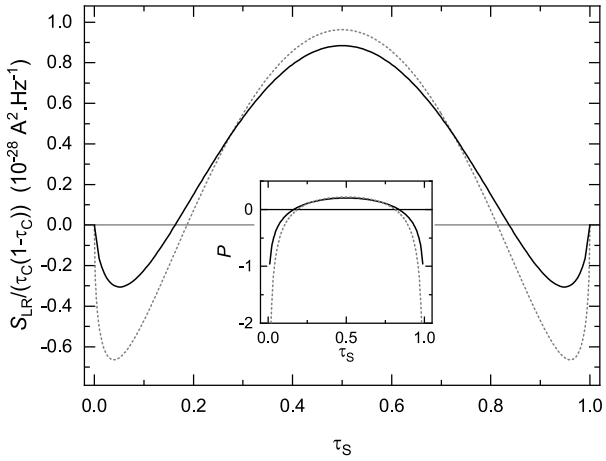

Figure 6.4: **Comparison between the Büttiker and the EMP approaches.** Renormalized cross-correlations are displayed versus the source transmission τ_S at $T = 0$ K and $\tau_c = 0.5$. The black line displays numerical EMP predictions of Eq. (6.2). The grey dotted line corresponds to the predictions in the Büttiker framework Eq. (6.14).
Inset: corresponding predictions for P from Eqs. (6.5) and (6.15)

Therefore, this alternative description of the system with interacting fermions can also lead to non-zero cross-correlations with the same change of sign between the dilute regime and the $\tau_S \sim 0.5$ regime, due to the relative importance of the source noise redistribution (positive) and the specific contribution of QPC_c (negative). Moreover, as seen in Fig. 6.4, the shape of the prediction for both models is similar, although the quantitative values are different. The mere presence of negative cross-correlations cannot be directly attributed to anyon exchange

phase because a simple fermion model also predicts this qualitative signal. Then, attributing this signal to a fractionalization of the injected electron and establishing a connection with the fractional statistics of the involved charges first requires validating the EMP picture by complementary measurements.

6.1.5 Equivalence length-voltage to tune from the free electron regime to the interacting regime

The effect of interactions develops along the source-analyzer path, as the injected electron wave packet fractionalizes. It can be adjusted in two ways. Either it is tuned by increasing the propagation distance so the modes have more time to split due to the velocity difference; or it is adjusted by increasing the energy injected in the partitioned channel with the DC-voltage bias V_S, in which case the injected electron is narrower and thus splits at a shorter distance. It is therefore natural to define a dimensionless parameter encoding the intensity of interactions:

$$\lambda = d_0 \frac{eV_S}{hv} \tag{6.16}$$

where d_0 is the actual physical distance travelled by charges between the source and QPC_c and v is the drift velocity. In our sample, d_0 and v are not precisely known but only one fitting parameter is used to compare the data with the EMP predictions: δt. Physically, it corresponds to the *time delay* between the arrival of fractionalized $e/2$ charges at the analyzer QPC.

If one defines the characteristic time of the wave packets $\Delta t_{WP} = h/(eV_S)$, two regimes of interest appears :

- if $\Delta t_{WP} \ll \delta t$, we get $\lambda \gg 1$, corresponding to important interaction effects
- if $\Delta t_{WP} \gg \delta t$, we get $\lambda \ll 1$, corresponding to negligible interaction effects

In the following, we choose to fix the source QPC that we use and thus the actual propagating distance. The effect of interactions is tuned by adjusting V_S [4].

6.2 Experimental device

We now turn to the experimental implementation of such a source-analyzer noise investigation of fractional charges properties.

6.2.1 Sample description

The experimental device we used is presented in Fig. 6.5. It is patterned in an AlGaAs|GaAs heterostructure forming a two-dimensional electron gas buried 95 nm below the surface, with mobility 2.5×10^6 cm^2 V^{-1} s^{-1} and density 2.5×10^{11} cm^{-2} (see Appendix B for nanofabrication details). The sample is cooled-down to $T = 11$ mK (additional measurements done at 22 mK are reported in Sec. 6.5.1). It is immersed into a $B = 5.2$ T perpendicular magnetic field, near the center of the $R_H = h/(2e^2)$ Hall plateau, at $\nu = 2$ (see Fig. 6.6).

[4]Note that changing V_S slightly changes the position of the channels and can have an impact on d but we neglect this impact in our analysis.

In such IQH regime, the bulk is incompressible and the electrical current flows chirally along two copropagating edge channels (black lines with arrows in Fig. 6.5). These edge channels are voltage-biased and measured through large ohmic contacts of negligible resistance located ~ 150 µm away from the displayed central region (illustrated by white circles in Fig. 6.5).

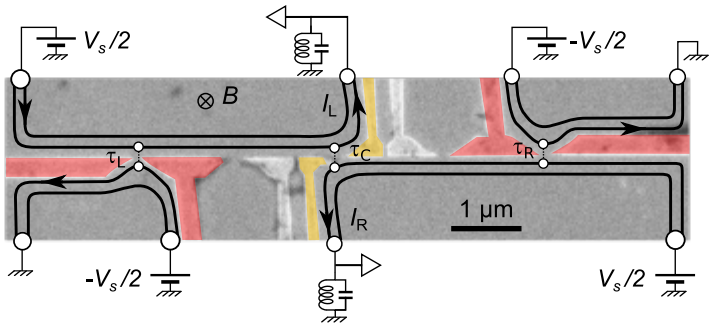

Figure 6.5: **Image of the sample.**
False colored scanning electron microscopic (SEM) image of the AlGaAs|GaAs sample. Aluminum gates defining two sources (red) and one analyzer (yellow) QPCs are tuned by field effect. Two other patterned gates (uncolored) are set at a constant negative voltage (-1.2 V) so that the corresponding QPCs remain fully closed. The current chirally flows along two copropagating edge channels (black arrowed lines). Sources are biased by $\pm V_S/2$ DC-voltage.

The central part constitutes the heart of the sample. It is made up of three active QPCs, out of five nanofabricated ones. Each QPC is separately tuned by field effect with a pair of aluminum split gates (the colored area in Fig. 6.5 corresponds to the used gates). The external left and right QPCs, respectively labeled $\mathrm{QPC_L}$ and $\mathrm{QPC_R}$ (defined by red gates in Fig. 6.5), are 3 µm away from the downstream central "analyzer" QPC labeled $\mathrm{QPC_c}$ (yellow gates). Note that two other source QPCs have been designed closer to $\mathrm{QPC_c}$ (1.5 µm) but were not used during the measurements and remained fully closed.

The cross-correlations between the outgoing currents I_L and I_R constitute the main observable of our measurement. They are measured with home-made cryogenic amplifiers [26] in the bandwidth of [0.78,0.92] MHz containing the resonant frequency (~ 0.86 MHz) of two identical tank circuits along the two amplification chains [27] (see Appendix A for technical details).

6.2.2 Sample characterization

Figure 6.6a displays a transverse Hall resistance measurement, showing an about 1 T wide quantum Hall plateau at $R_\mathrm{H} = h/(2e^2)$, corresponding to the $\nu = 2$ state. The vertical arrow indicates the chosen magnetic field for the measurements $B = 5.2$ T.

The QPCs are characterized by sweeping the split gate voltage V_g. A typical measured profile of transmission is plotted in Figure 6.6b. This figure displays the current transmission ratio τ across the central QPC for two values of DC-voltage bias: $V_\mathrm{DC} = 0$ (black line) and -117 µV (red line).

Like in the $\nu = 2/5$ case (see Chap. 5), the two-step shape of the curve validates the picture of two copropagating channels, sequentially opening and well separated. Here they are identical, as confirmed by the noiseless intermediate plateau at $\tau = 0.5$. While the inner channel transmission ($V_\mathrm{g} \in [-0.5, -0.2]$V) exhibits resonances and is significantly impacted by V_DC, the

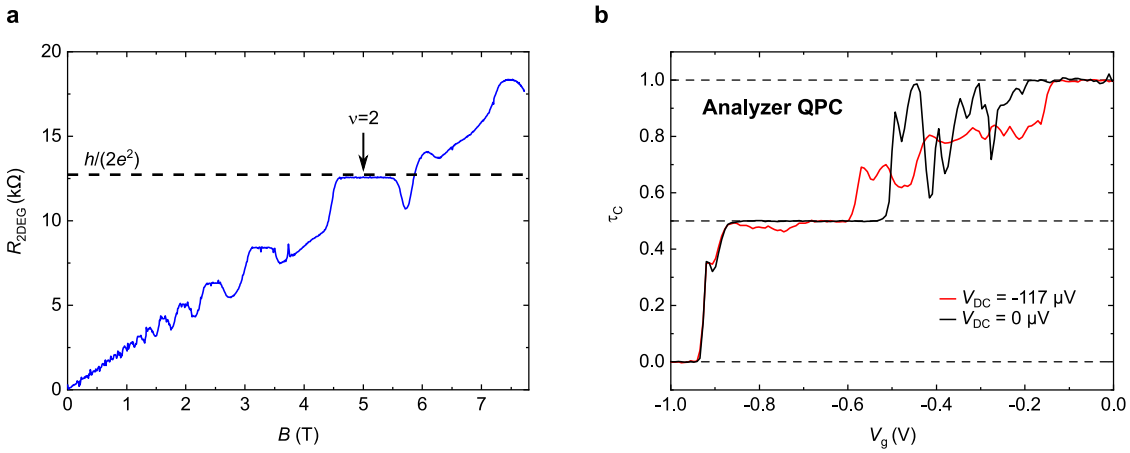

Figure 6.6: **Sample characterization.**
a Transverse Hall resistance R_{H} measured as a function of the applied perpendicular magnetic field B at low temperature ($T \sim 100$ mK). All QPCs are fully pinched off during this B sweep. The black arrow indicates the chosen value of B. Dashed line indicate $R_{\mathrm{H}} = h/(2e^2)$.
b Analyzer differential transmission ratio τ versus the voltage V_{g} symmetrically applied to both $\mathrm{QPC_c}$ split gates. The black and red continuous lines correspond to the measurements in the presence of a direct DC-voltage bias $V_{\mathrm{DC}} = 0$ μV and -117 μV, respectively.

outer edge channel transmission ($V_{\mathrm{g}} \in [-0.95, 0.85]$V) is much smoother and essentially not impacted by the bias. Hence we shall perform the majority of our measurements using the outer channels.

We can now turn to the investigation of fractional charges along the IQHE edge in this source-analyzer setup.

6.3 Evidence of EMP and charge fractionalization

Before investigating the properties of fractional charges along the IQH edge, we first validate the relevance of the EMP model, and determine at which V_{S} the injected electrons effectively fractionalize along the source-analyzer path. In this section, we experimentally establish the fractionalization by measuring the incoming distribution function at the central QPC with noise spectroscopy, for various values of bias.

6.3.1 Energy distribution function spectroscopy through shot noise

In the Landauer-Büttiker framework [25], the current cross-correlations between two beams outgoing from a biased QPC of transmission τ_{S} are given by Equation (6.11).

Therefore, measuring the cross-correlation shot noise between leads L and P allows us to probe one incoming energy distribution function at $\mathrm{QPC_c}$ if the other is known. This is done in a measurement based on three key elements illustrated in Fig. 6.7:

- First, we create an out-of equilibrium situation at one of the source QPCs set at an intermediate transmission probability τ_{S} by applying a constant DC-voltage V_{S}. On the

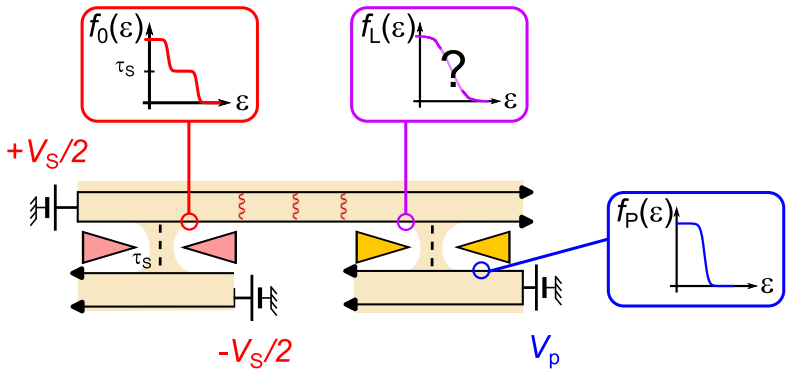

Figure 6.7: **Distribution function spectroscopy principle.**
The source QPC with transmission ratio τ_S is set out of equilibrium at fixed bias $\pm V_S/2$, creating a double-step distribution function (red inset). Along the source-analyzer path, interactions induce relaxation. The resulting relaxed distribution function (purple inset) is probed at QPC_c which is biased on the opposite side by a varying DC-voltage V_p. The Fermi distribution (blue inset) on this opposite side of QPC_c allows us to scan the unknown distribution through the induced cross-correlations between outgoing currents.

partially transmitted edge channel, this induces a double-step distribution at the source QPC, very different from a relaxed thermal distribution (red inset in Fig. 6.7).

- Second, along the source-analyzer path, interactions induce a relaxation of the distribution. At very short time delay compared to $h/(eV_S)$ (i.e. $\lambda \ll 1$), interactions have a negligible impact and the resulting incoming distribution function at QPC_c is unchanged. At a very long time delay, interactions make the distribution relax into a broad single-step distribution (but different from a Fermi distribution). The cross-over between these two regimes can be probed by tuning in situ V_S.

- Finally, the resulting incoming distribution function is scanned by sweeping a voltage V_p on the opposite side of the downstream QPC. In practice, this is done by applying the same voltage V_p on both sides of the opposite unused source QPC, which is equivalent to applying a direct bias on QPC_c. Sweeping V_p induces cross-correlation shot noise S_{LR} following Eq. (6.11). Assuming that f_P is a Fermi distribution at $T = 0$ K, the unknown distribution function f_L at QPC_c can be simply deduced by deriving these cross-correlations, which gives:

$$f_L = \frac{1}{2}\left(1 + \frac{h}{e^2\tau_c(1-\tau_c)}\frac{\partial S_{LR}(\varepsilon)}{\partial \varepsilon}\right). \tag{6.17}$$

Note that the temperature induces a rounding of the functions. For convenience, f_L defined in Eq. (6.17) will be called "distribution function" in the following, even at finite temperature.

Thus, by probing the distribution function at a given applied source voltage bias, one can deduce whether the system is in a regime with a strong or weak effect of interactions, i.e. if at the level of the analyzer the injected electrons are fractionalized or not.

6.3.2 Energy distribution in the outer channel

Spectroscopy at τ_S= 0.5

We first set $\tau_S = 0.5$ so the two steps of the initial energy distribution have the same height, allowing us to clearly see a change of its shape.

The measured distribution functions in this device configuration are shown in Fig. 6.8 for $V_S = 23$ µV (panel (a)) and 70 µV (panel (b)). The measurements were performed by using the sources independently (circles for the left and triangles for the right), which gave essentially identical results. In practice, we measure the excess current cross-correlations $\langle \delta I_L \delta I_R \rangle - \langle \delta I_L \delta I_R \rangle (V_P - V_S = 0)$ [5] between the two leads outgoing from QPC_c (insets) and we derive the data following Eq. (6.17).

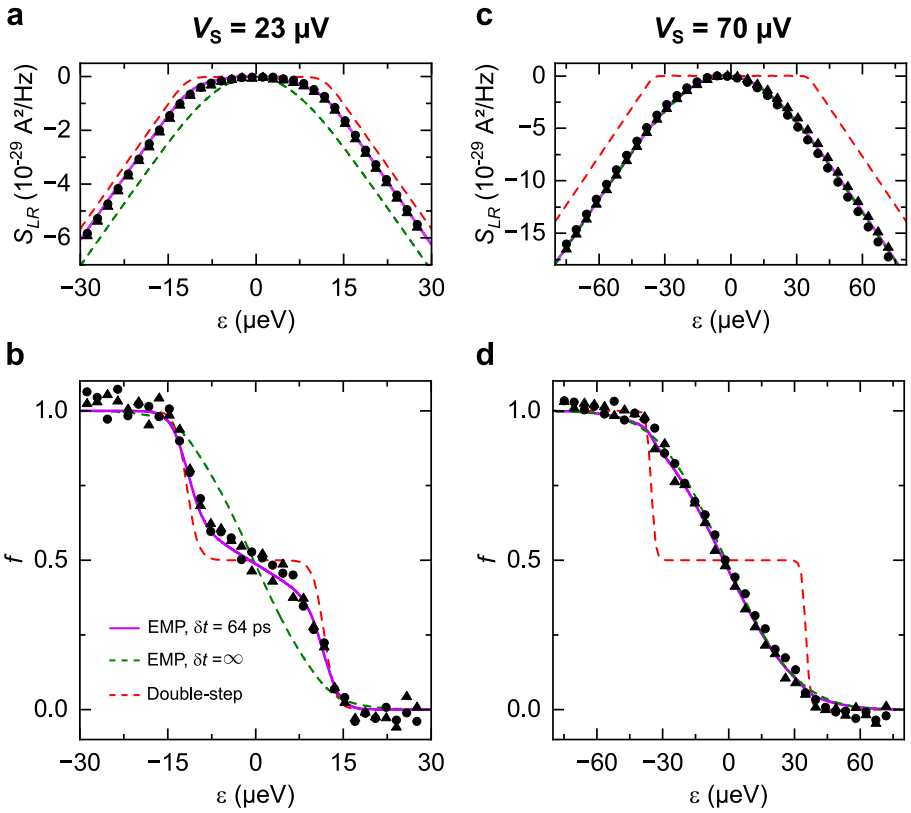

Figure 6.8: **Distribution function spectroscopy at $\tau_S \sim 0.5$.**
a (c) Measured cross-correlation signal at $V_S = 23$ µV ($V_S = 70$ µV) using left source (circles) and right source (triangles) plotted versus the energy $\epsilon = eV_p$.
b (d) Distribution function obtained by derivation of the upper panels' data (see Eq. (6.17)). The data are compared to the initial double-step Fermi distribution (red dashed line) and the predictions of the EMP theory $\delta t = \infty$ (green dashed line). A fit of the EMP theory (purple line) gives an time delay of $\delta t = 64$ ps (corresponding to $v = 2.6 \times 10^4$ m s^{-1} if $d_0 = 3.1$ µm is the straight distance between QPCs).

The data are then compared to the initial double-step distribution function at $T = 11$ mK (red dashed line) and to the numerical predictions (green dashed line) computed in the edge

[5] We had to use the excess current cross-correlations due to small experimental offset at $V = 0$, drifting with time.

magneto-plasmon framework [150] at $T = 11$ mK and infinite time delay ($\delta t = \infty$, corresponding to a full fractionalization at $\varphi = \pi/4$).

At $V_S = 23$ µV, displayed in Fig. 6.8a, the system is in the low bias regime with a small effect of interactions. The measured distribution function is then closer to the initial double-step distribution than to the prediction at $\delta t = \infty$. This indicates a partial separation of the excitations at this voltage.

In contrast, in the high voltage regime (strong effect of interactions) $V_S = 70$ µV, the data displayed in Fig. 6.8b are in good agreement with the numerical predictions at infinite time delay. This denotes the complete equilibration between the two channels and supports the presence of edge magneto-plasmons described by a mixing angle $\varphi = \pi/4$.

Assuming that it does not change with V_S, one can deduce the time delay δt in our sample by comparing the data with the EMP numerical predictions.

It corresponds to time delay between the arrival of successive fractionalized $e/2$ charges at the analyzer QPC. For all the tested bias voltages $V_S = 12$, 23, 35, 47, 59, 70 and 82 µV, displayed in Fig. 6.9, we fit t and find 64 ps as the best fit value. The corresponding fits are displayed as purple lines in Figs. 6.8 and 6.9.

Is this value realistic? Assuming that d_0 is the straight distance between the centers of the QPCs [6] (3.1 µm) the drift velocity deduced from these fits is $d_0/\delta t$ 5×10^4 m s^{-1} which corresponds in order of magnitude to the usual values measured in similar 2DEG (see e.g. [155] measuring $v \sim 4.6 \times 10^4$ m s^{-1} in a 2DEG grown in the same chamber than ours).

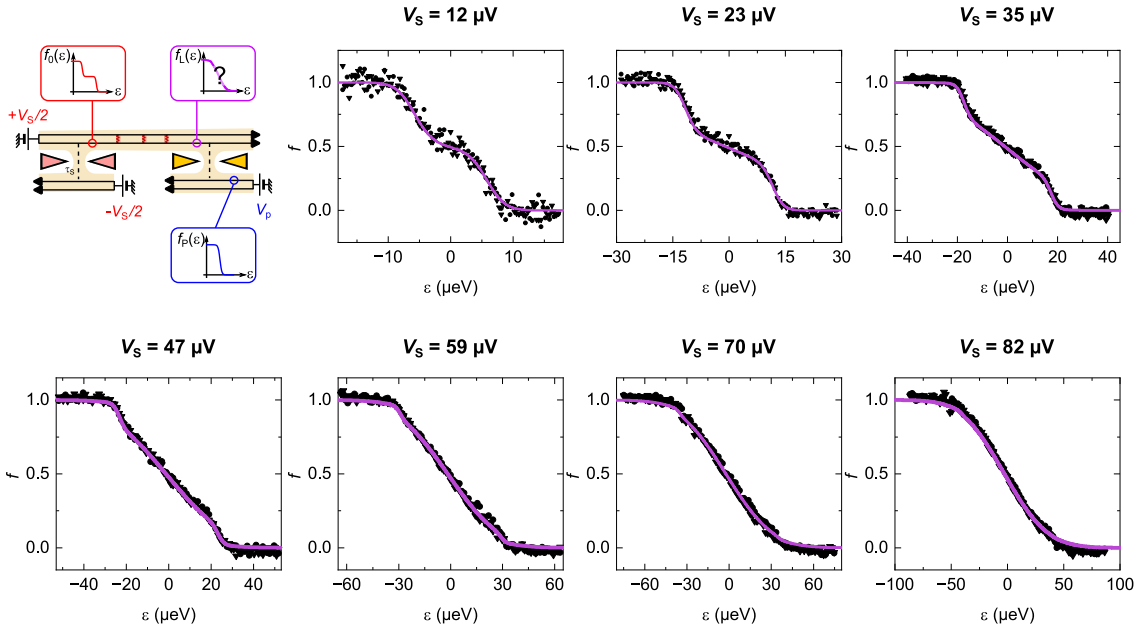

Figure 6.9: **Distribution functions at all tested V_S.**
a Configuration of the measurement. $T = 11$ mK
b to h Distribution functions obtained for DC bias voltage $V_S = 12$, 23, 35, 47, 59, 70 and 82 µV. Circles and triangles respectively display the data obtained from left and right sources. The purple lines display the fits with EMP theory at $T = 11$ mK using the single fit parameter $\delta t = 64$ ps for all V_S.

Fig. 6.9, which presents all the measured distribution functions, illustrates the cross-over

[6] although in practice it is a little bit different

from a double-step-like shape at $V_S = 12$ µV to a relaxed distribution at $V_S = 70$ µV and 82 µV. The remarkable fit quality with $\delta t = 64$ ps for all the intermediate voltage values strongly supports the EMP picture.

Moreover, from this complete cross-over, we observe that the shape of the data and the one of the fits do not evolve for voltages higher than 70 µV. Therefore, the regime of strong effect of interactions and good separation of the wave packets is reached at $V_S = 70$ µV.

This will be the reference DC bias voltage used in the following sections.[7]

Spectroscopy at $\tau_S \sim 0.05$ and 0.95

The same measurement is reproduced at $V_S = 70$ µV but in the Poissonian regime, at $\tau_S \simeq 0.05$ and $\tau_S \simeq 0.95$ to specifically investigate the regime where anyon signatures may appear. The results are shown in Figure 6.10. In both cases, for $\tau_S \simeq 0.05$ (a) and $\tau_S \simeq 0.95$ (b), the agreement with the predictions of the EMP theory is remarkable and full relaxation is obtained at this voltage. This second measurement in a different regime constitutes another strong hint corroborating the picture of EMP.

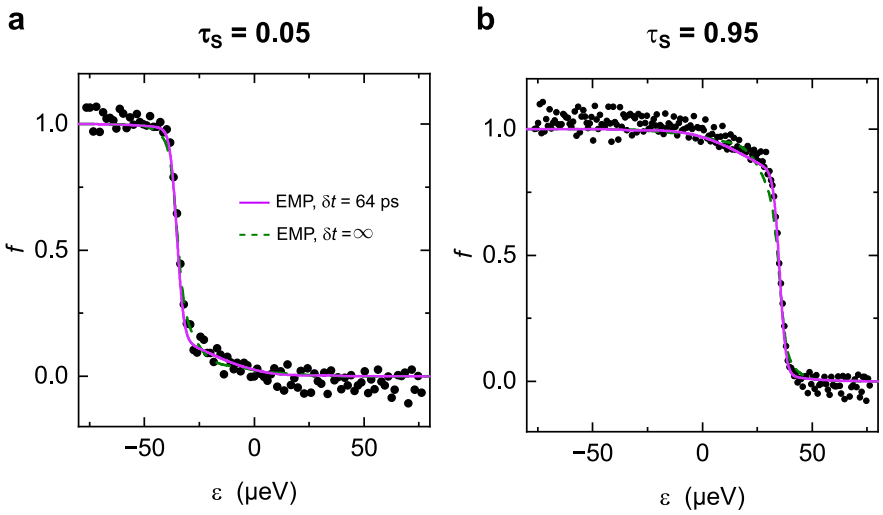

Figure 6.10: **Distribution function spectroscopy in the dilute regime.**
a (b) Distribution function obtained at $\tau_S = 0.05$ (0.95) using left source (black circles) plotted versus the energy $\epsilon = eV_p$. The data are in good agreement with the EMP theory (purple line) at previously found time delay $\delta t = 64$ ps. The green dashed line indicates predictions of the EMP theory at $\delta t = \infty$.

Therefore, these spectroscopic measurements with the source and the central QPCs partially transmitting the outer channel, and their good matching with the EMP theory validate the description of edge-magneto plasmons. Inter-channel Coulomb interactions split an initial electron into two pairs of wave packets (a slow and a fast one), with fractional charges, delocalized over the two channels. As theory has been derived at $T = 11$ mK and $\varphi = \pi/4$, these results point to a mixing angle of $\pi/4$ in our sample, with both channels carrying the same kind of fractional charges. The regime of full separation between the charged and neutral modes is reached at $V_S = 70$ µV, with $e/2$ fractional charges impinging on QPC_c.

[7] We did not use higher voltages due to the emergence of an inter-channel tunneling artifact, see Sec. 6.5.4.

6.3.3 Complementary measurements by probing the inner channel

To consolidate the picture of EMP, one can reproduce this spectroscopic measurement by setting the source QPC and the probe QPC_c to transmit different channels. Indeed, in the ideal picture of EMP, at $\delta t = \infty$ and $\varphi = \pi/4$, the channel which is not partitioned by the source QPC is predicted to exhibit the same energy distribution at the level of QPC_c as the one measured in the previous section at $V_S = 70$ µV.

In our case, due to the resonances of the inner channel of QPC_c, we choose to inject electrons in the inner channel (i.e. the source QPC partitions the inner channel) and by probing the energy distribution with QPC_c by setting it to the outer channel, (see schematics in Fig. 6.11a).

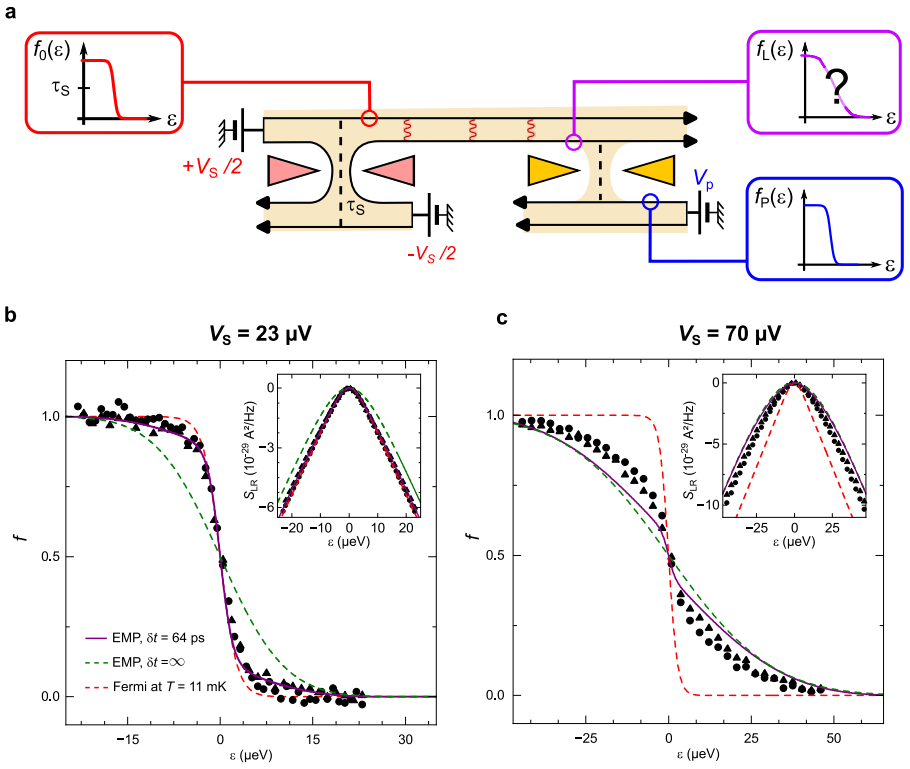

Figure 6.11: **Spectroscopy with source and analyzer set on different channels.**
a Spectroscopy configuration with injection on inner channel with source QPC while the central QPC probes the outer channel
b, c Circles and triangles respectively display the results with left and right sources. Distribution functions (obtained by deriving the cross-correlation signal in insets) obtained at $V_S = 23$ (b) and 70 µV (c). The data are compared to a Fermi distribution (red dashed line) and to the numerical predictions in the EMP framework at 64 ps (purple line) and infinite (green dashed line) time delay.

Fig. 6.11 displays the corresponding measurement. At low bias ($V_S = 23$ µV, panel (b)), the data are close to a simple Fermi distribution at $T = 11$ mK, as expected in the regime of low interactions (red dashed line). By contrast, they are clearly different from the expectations numerically derived in the EMP framework at $\delta t = \infty$ (green dashed line). Note that this numerical prediction is the same as the outer channel one because, at $\delta t = \infty$ and $\varphi = \pi/4$, both channels are expected to carry the same amount of energy and are supposed to follow the same distribution. The predictions at $\delta t = 64$ ps are in good agreement with the data.

At higher voltage (V_S = 70 µV, panel (c)) the shape of the distribution changes and approaches the continuous purple (δt = 64 ps) and green dashed ($\delta t = \infty$) lines. However, the quantitative matching with the prediction is far from being as clear as the one found when both QPCs transmitted the outer channel. This discrepancy with theory may be linked to the resonances of the inner channel transmission across the source QPC (the transmission profile of the outer one was much more canonical) and to relaxation towards other degrees of freedom at the level of the source. Thus, although the distribution deformation tendency is in qualitative agreement with expectations, this complementary measurement impedes quantitative conclusions in the case of a source partitioning the inner channel. Note that further measurements with symmetric sources on the outer channel and QPC_c on the inner one will be able to confirm convincingly $\varphi = \pi/4$.

6.4 Non-zero cross-correlations in the symmetric source-analyzer configuration

We can now turn to the main cross-correlation measurement in the symmetric source-analyzer (i.e. "collider") configuration with two balanced sources ($\tau_L \simeq \tau_R$). In this configuration, the same voltage is applied on both sources and sweet on a typical range of ± 80 µV to investigate the cross-correlations between the outgoing beams.

6.4.1 Poissonian regime

First, we focus on the Poissonian regime of low source transmission, where the cross-correlations are predicted to exhibit signatures of anyon statistics. Indeed, in this regime, the trivial source shot noise contribution to the resulting cross-correlations is dominated by the contribution of QPC_c involving a non-trivial braiding.

Accordingly, the two sources are tuned to the same transmission $\tau_S \simeq 0.05 \ll 1$ in order to create symmetric Poissonian beams of electrons. Note that due to electron-hole symmetry, when $(1 - \tau_S) \simeq 0.05 \ll 1$, the same result is predicted and measurements are also performed in this configuration. The differential transmission of QPC_c is set at $\tau_c \simeq 0.5$ to maximize the signal. The transmissions $\tau_{L,R,c}$ obtained during the measurement at plotted in Fig. 6.12b.

We then symmetrically sweep the voltage $\pm V_S/2$ on both sides of the two sources so that they are subjected to a sweeping V_S bias, and we measure the cross-correlations between the two outgoing currents S_{LR}.

The signal is specifically analyzed through the generalized Fano factor P_{exp} defined in Eq. (6.5), in the same spirit as in the previous chapters.

In Figure 6.12 we show this measurement at $\tau_S = 0.05$ (full symbols) and $\tau_S = 0.95$ (open symbols). The data presented in the three panels are measured simultaneously. The panel (b) shows the total noise generated by both sources $S_\Sigma \equiv \Delta S_{LL} + \Delta S_{RR} + 2S_{LR}$, obtained by current conservation (see Sec. 3.5.2). This source noise is confronted with the standard shot noise formula (black line)

$$S_{sn} = 2e\frac{\tau^{DC}(1-\tau^{DC})V}{R_H}\left[\coth\frac{eV}{2k_BT} - \frac{2k_BT}{eV}\right] \tag{6.18}$$

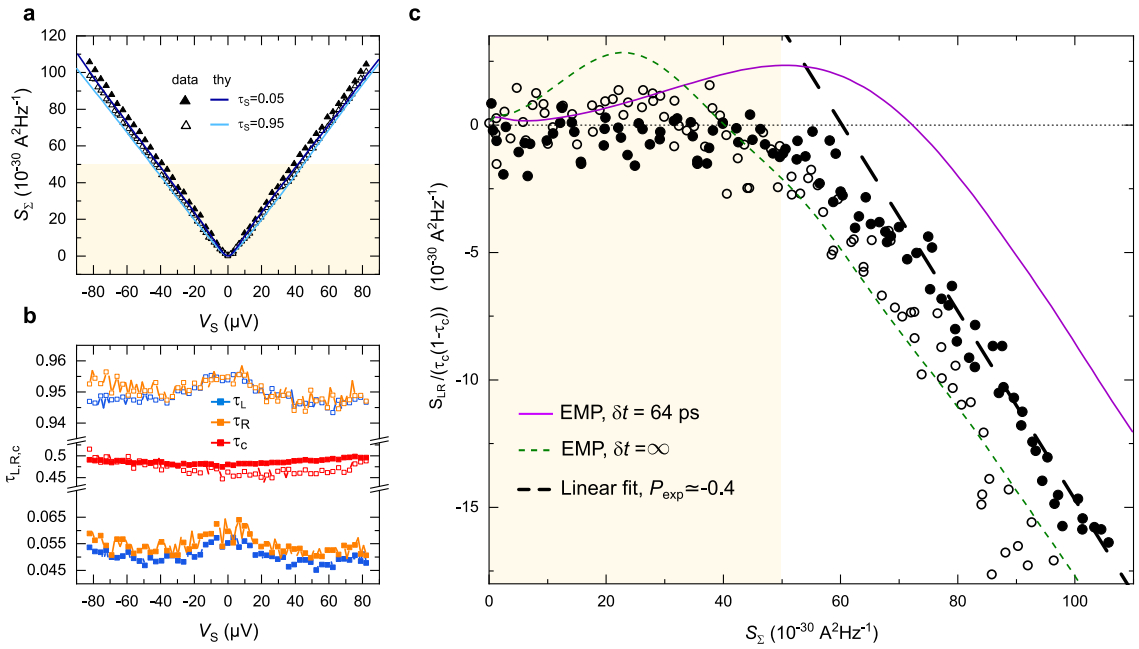

Figure 6.12: **Cross-correlations with balanced sources in the dilute regime.** Data at $\tau_S \simeq 0.05$ ($\tau_S \simeq 0.95$) are displayed as full (open) symbols. V_S is swept between $\pm$ 80 μV typically.
a Source noise S_Σ at both $\tau_S \simeq 0.05$ and $\tau_S \simeq 0.95$, in good agreement with Eq. (6.18) (continuous lines).
b Simultaneously measured transmissions $\tau_{L,R,c}$ (respectively blue, orange and red) at $\tau_S \simeq 0.05$ and $\tau_S \simeq 0.95$.
c Renormalized cross-correlations plotted versus the source noise of panel (a). The colored area highlights the two regimes. In the range $V_S > 70$ μV, a linear fit (black dashed line) gives $P_{exp} \simeq -0.37$. Continuous purple and dashed green lines display the EMP theory at respective effective time delays $\delta t = 64$ ps and $\delta t = \infty$.

and is in very good agreement with this prediction, validating the picture of electrons tunneling through the source QPCs.

The Figure 6.12c displays the central result. The cross-correlations S_{LR} are renormalized by $\tau_c(1-\tau_c)$ and plotted versus the source noise S_Σ. One can clearly see two distinct regimes:

- At low bias $V_S \lesssim 50$ μV, the cross-correlation signal is essentially zero which corresponds to the free fermion prediction Eq. (6.1) and is consistent with the not fully relaxed distribution function presented in the previous section.

- Instead, at high bias $V_S \gtrsim 50$ μV, the signal becomes negative, consistent with non-trivial braiding.

This signal is interpreted as a qualitative signature of the anyonic exchange phase of the fractional charges along IQH edge channels.

To go further, we can extract the value of the generalized Fano factor from a linear fit in the range $V_S > 70$ μV (black dashed line in Fig. 6.12c), where the mode separation is complete. We get $P_{exp} \simeq -0.37$, very close to the asymptotic value predicted by the EMP theory at $T = 0$ and $\tau_S \to 0$: $P_{EMP}(T = 0, \tau_S \to 0) \simeq -0.35$.

However, the comparison of the data with the complete EMP numerical calculations mitigates the overall quantitative agreement. The full purple line and the dashed green line respectively display the numerical predictions at time delay $\delta t = 64$ ps (obtained from the fit of the previous spectroscopy measurement) and $\delta t = \infty$. While the predicted slope at high voltage is compatible with the experimental data in both cases, the agreement in the low-bias region is less good. Notable differences between theory and experiment can be highlighted. Indeed, theory supposes:

- identical and energy independent sources transmissions $\tau_{\rm L} = \tau_{\rm R}$ (supposed equal to 0.05)
- identical effective time delays for both left and right paths
- an absence of energy relaxation with other degrees of freedom.

In the experiments, these conditions are not perfectly satisfied: $\tau_{\rm S}$ varies from ~ 0.05 to $\sim$0.06, we notice $\sim 10\%$ differences between left and right time delays t. These differences could impact the data-theory comparison on the cross-correlation signal with dilute symmetric beams.

6.4.2 Beyond the Poissonian regime

One can wonder how this signal changes beyond the Poissonian regime. The total cross-correlation signal is the sum of a *positive* source contribution $S_\Sigma \geq 0$ and a *negative* contribution due to process occurring on the analyzer $\mathrm{QPC_c}$ $S_{\rm c} \leq 0$: $S_{\rm LR} = S_\Sigma + S_{\rm c}$. When the sources are set to intermediate transmission, beyond the Poissonian regime, the contribution of the sources becomes dominant and we expect positive cross-correlations.

Let us explore this regime by measuring the cross-correlation signal in the case of balanced sources both set to $\tau_{\rm S} \sim 0.5$, with a symmetric voltage $V_{\rm S}$ varying between typically $\pm$ 80 µV. Figure 6.13 presents the results obtained in that case. Like in the previous section, panels (a) and (b) display respectively the source noise S_Σ and the transmissions, measured simultaneously with the main $S_{\rm LR}$ signal. In Figure 6.13c, we plot the renormalized cross-correlation signal versus S_Σ. Like in the Poissonian regime, we see two regimes:

- one regime where the signal is null at $V_{\rm S} \lesssim 25$ µV, which corresponds to the free fermion expectation
- one regime with *positive* cross-correlations ($V_{\rm S} \gtrsim 25$ µV).

In the high-bias region, we can again extract the generalized Fano factor $P_{\rm exp} \simeq 0.25$ from a linear fit for $V_{\rm S} > 70$ µV (black dashed lines) and confront it to the EMP numerical predictions $P_{\rm EMP}(T = 0, \tau_{\rm c} \to 0) \simeq 0.2$. The continuous purple line and the green dashed line display the EMP predictions at this $\tau_{\rm S}$ over the whole $V_{\rm S}$ range for $\delta t = 64$ ps and $\delta t = \infty$ respectively. Intriguingly, oscillations appears in the $\delta t = 64$ ps predictions and vanish at $\delta t = \infty$. These oscillations are not seen in the experimental data for the explored voltage range which remains unexplained yet.

Apart from this intriguing feature, the evolution of the observed noise is compatible with the predictions: the experimental slope $P_{\rm exp} \simeq 0.25$ is reasonably close to the $\delta t = \infty$ prediction $P_{\rm thy}(\tau_{\rm S} = 0.5) = +0.2$.

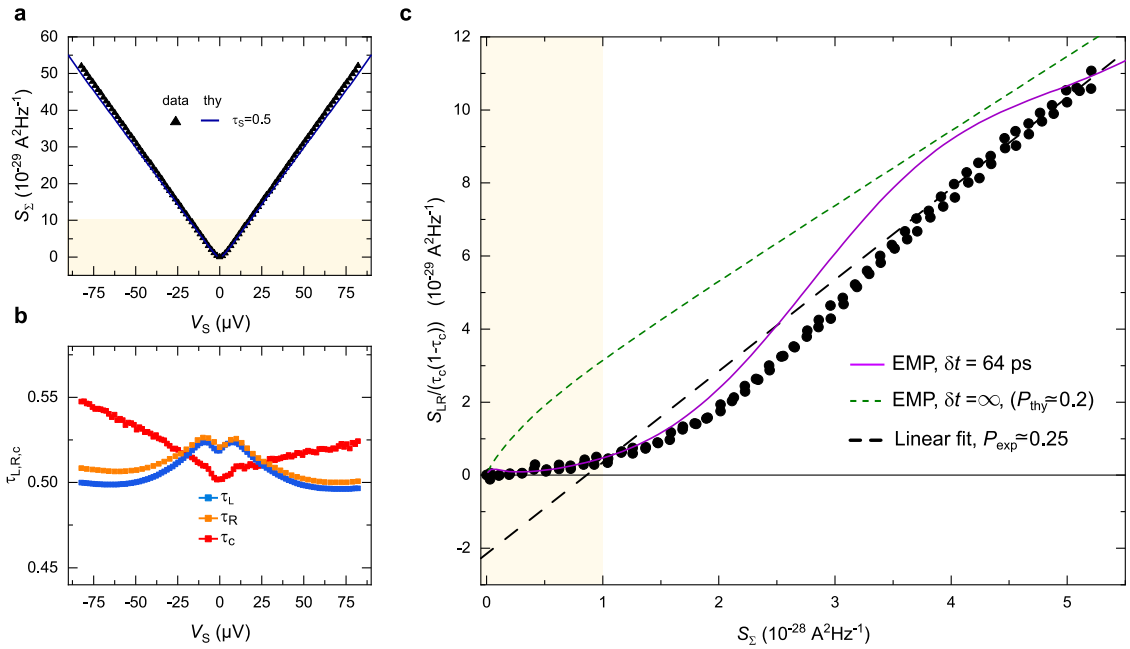

Figure 6.13: **Cross-correlations with balanced sources at $\tau_S \simeq 0.5$ when V_S is swept between $\sim \pm$ 80 μV.**
a Simultaneously measured source noise S_Σ, in good agreement with Eq. (6.18) (dark blue line).
b Transmissions $\tau_{L,R,c}$ (respectively blue, orange, and red) during the measurement.
c Renormalized cross-correlations plotted versus the source noise of panel (a). The colored area highlights the change of regime: zero to positive S_{LR}. In the positive signal region, a linear fit (black dashed line) gives $P_{exp} \simeq 0.25$. Continuous purple and dashed green lines display the EMP theory at respective time delays $\delta t = 64$ ps and $\delta t = \infty$.

6.4.3 Complementary measurements with QPC_c probing the inner channel

Tuning the central QPC to a partial transmission of the inner channel when sources inject energy into the outer one can bring important additional information.

Indeed, as previously mentioned, when all the QPCs probe the same channel, the total cross-correlation signal has two contributions :

- the trivial redistribution of the source noise $\tau_c(1-\tau_c)S_\Sigma$
- the contribution of the central QPC S_c linked to the charge fractionalization. This second contribution is the signal of interest.

The source noise contribution is only present when the sources and QPC_c partially transmit the same channel. Then, we can get rid of this trivial term by setting QPC_c to partially transmit a different channel than the sources. Due to the resonances and important energy dependence of the inner channel transmissions, we choose to inject energy at the sources into the outer channel and to set the central QPC partially transmitting the inner one[8]. To maximize the

[8]Indeed, QPC_c is essentially unbiased in the balanced "collider" configuration and the inner channel is usable in that case.

signal, we set τ_c as close to 0.5 as possible (in spite of substantial variations).

The corresponding measurement is presented in Fig. 6.14.

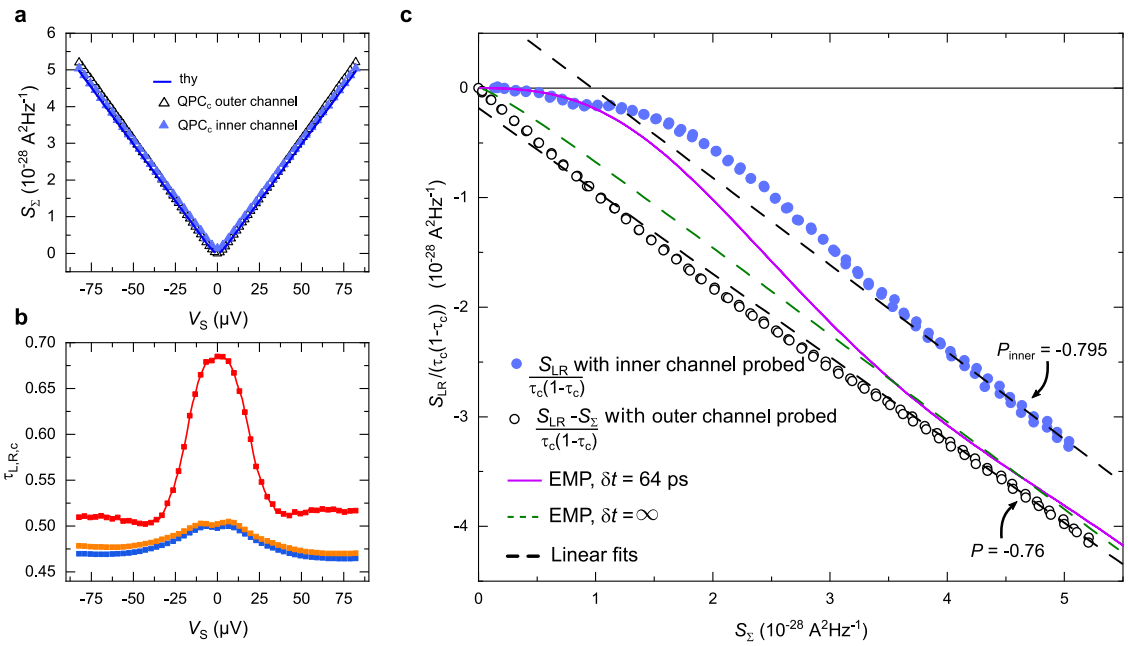

Figure 6.14: **Cross-correlations with balanced sources with QPC$_c$ probing inner channel when V_S is swept between ± 80 μV.**
a Simultaneously measured source noise S_Σ at both τ_S, in good agreement with data of Fig. 6.13 (open symbols) and with Eq. (6.18) (blue line).
b Transmissions of the outer channel for sources $\tau_{L,R}$ and of the inner channel for QPC$_c$ (respectively blue, orange and red).
c Renormalized cross-correlations plotted versus the source noise of panel (a). Blue dots correspond to the measurement when QPC$_c$ probes the inner channel. Open black dots indicate the measurement when QPC$_c$ probes the outer channel (Fig. 6.13b) minus the source noise. Continuous purple and dashed green lines display the EMP theory at respective time delays $\delta t = 64$ ps and $\delta t = \infty$. Fits of the data in the region $V_S > 70$ μV (black dashed line) give the Fano factors of 0.795 (inner channel) and 0.757 (outer channel)

Panel (a) displays the sources noise $S_\Sigma = \Delta S_{RR} + \Delta S_{LL} + 2S_{LR}$ (blue triangles) measured simultaneously with the main cross-correlations data. They match with the standard shot noise predictions Eq. (6.18) and are essentially identical to the one measured in the previous section when all QPCs probed the outer channel (open black triangles, same data as in Fig. 6.13a)

Panel (b) indicates the corresponding transmissions of the source QPCs (blue and orange symbols, essentially identical) and the central QPC (red symbols, presenting noticeable variations, as expected for the inner channel).

In Fig. 6.14c, the main cross-correlation signal renormalized by $\tau_c(1-\tau_c)$ is plotted versus S_Σ and displayed as blue dots. The signal is *negative*, like the specific QPC$_c$ contribution expected by the EMP theory. At high bias (i.e. in the regime of complete fractionalization $V_S > 70$ μV), a linear fit gives $P_{inner} = -0.795$, close to the prediction $P^{thy}_{inner} = P^{thy}_{outer} - 1 = 0.2 - 1 = 0.8$. The dashed green and full purple continuous lines display the EMP predictions with $\delta t = 64$ ps and $\delta t = \infty$ respectively, with compatible slopes at high voltages.

Moreover, the data are compared to those obtained previously when all the QPCs partially transmitted the outer channel. The open black dots display this previous measurement (see Fig. 6.13) with the trivial contribution of the sources removed: $S_{\mathrm{LR}}^{\mathrm{outer}} - S_{\Sigma}$. At high voltage, a linear fit gives a Fano factor equal to 0.757. The good matching between the two configurations corroborates the picture of EMP with $\varphi = \pi/4$.

6.4.4 Evolution of cross-correlation signal versus the source transmission τ_{S}

We saw that the cross-correlation signal drastically depends on the source regime (τ_{S} extreme or close to 0.5) and even changes sign due to the relative importance of the *positive* trivial contribution of the sources and the negative contribution of $\mathrm{QPC_c}$. Let us deepen this investigation by measuring S_{LR} over the whole range of τ_{S}.

Cross-correlations versus τ_{S}

Figure 6.15 displays the renormalized cross-correlation signal versus the transmission of the source with $\mathrm{QPC_c}$ probing the outer (panel (a)) and the inner (panel (b)) channels. We make sure that the transmissions of both sources are equal thanks to a calibration step performed beforehand. Moreover, the measurement is again done at $\tau_{\mathrm{c}} = 0.5$ to maximize the signal and at $V_{\mathrm{S}} = 70$ µV, ensuring that the fractional charges have developed.

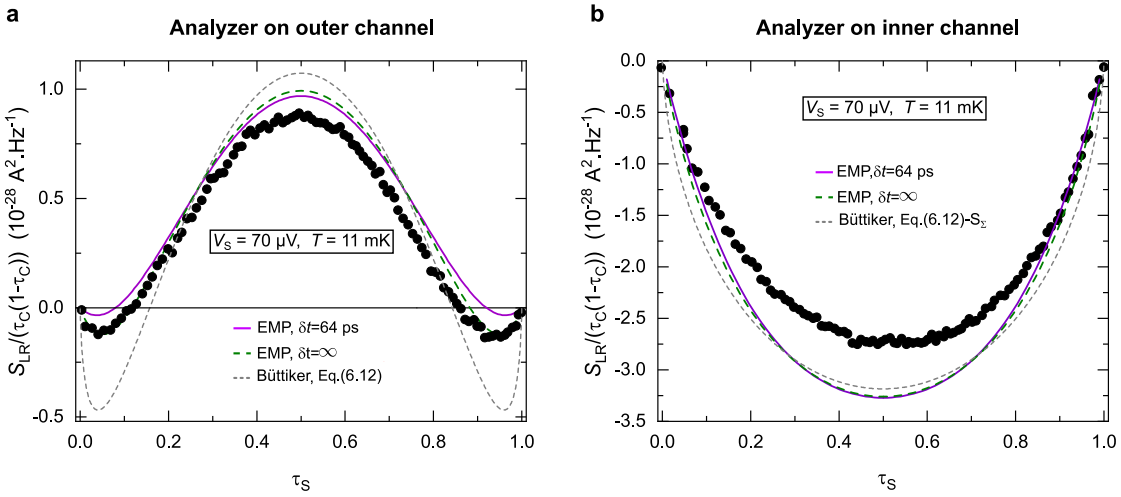

Figure 6.15: **Full crossover of S_{LR} versus τ_{S} at $T = 11$ mK.**
a Cross-correlation signal plotted versus τ_{S} at $V_{\mathrm{S}} = 70$ µV and $\tau_{\mathrm{c}} = 0.5$. The purple and dashed green lines respectively indicate EMP predictions for $\delta t = 64$ ps and $\delta t = \infty$. The grey dotted line displays the expectation for inter-channel exchange of energy in the Büttiker framework at $T = 11$ mK, see Eq. (6.11).
b Same measurement with $\mathrm{QPC_c}$ probing the inner channel.

In Fig. 6.15a, the first striking feature is the symmetry around the vertical $\tau_{\mathrm{S}} = 0.5$ line which reflects the electron-hole symmetry (whereby at $\tau_{\mathrm{S}} = 0.95$ we have negative cross-correlations due to an impinging beam of hole-like fractional charges). As the total signal has two contributions of opposite signs (positive for the sources and negative for the central QPC), their relative importance clearly appears through the change of sign of the signal: the contribution

of the central QPC_c is dominant if $\tau_S, (1-\tau_S) \lesssim 0.15$ and the contribution of the source noise dominates if $\tau_S \in [0.15, 0.85]$.

We can now compare the experimental data with the predictions of EMP theory at $\varphi = \pi/4$, respectively displayed as a continuous purple line for $\delta t = 64$ ps (time obtained from the fits of Sec. 6.3.2) and a green dashed line for $\delta t = \infty$. We note that at low and high transmission, the infinite length EMP prediction better captures the data than the expectation at $\delta t = 64$ ps, in contrast with the regime at $\tau_c \sim 0.5$. This small quantitative disagreement remains unexplained and might be attributed to features not captured by theory, such as an energy relaxation into other degrees of freedom or it could be due to high energy excitations hidden in the experimental noise. However, in spite of these small discrepancies, the matching with the EMP theory is good overall. Quantitatively this matching seems better than the one with the phenomenological alternative predictions derived in the Landauer-Büttiker framework at $T = 11$ mK and $\delta t = \infty$ (see Sec. 6.1.4) and plotted as grey dotted lines.

In particular, the agreement in the diluted beam limit together with the previous energy distribution fits that establish the EMP framework give a solid basis to interpret the signal as a signature of anyonic mutual exchange statistics.

Interestingly, the contribution of QPC_c can be specifically investigated by reproducing this measurement with electrons injected into the outer channel and the cross-correlation signal probed in the inner channel (in the same spirit as in Sec. 6.3.3). Thus, as the probed inner channels have seen no direct injection of charge, the trivial shot noise contribution of the source is suppressed and the whole cross-correlation signal should only result from the fractionalization mechanism. The signal in that case is expected to be negative in the whole τ_S range.

The result of such a measurement is plotted in Fig. 6.15b. The numerical predictions are plotted as green and purple lines for respective time delays $\delta t = \infty$ and $\delta t = 64$ ps. The sign and the shape of the signal are qualitatively consistent with the expectations, but deviations are observed between data and theory, especially in the regime $\tau_S \simeq 0.5$.

Fano factor versus τ_S

These sweeps have been reproduced at other DC bias values (V_S = 12, 23, 35, 47, 59 and 82 µV), allowing to extract an effective Fano factor P_{exp}. As energy distribution spectroscopy showed that the separation of the modes and the equal distribution of charge over the two channels is complete for bias V_S, P_{exp} is extracted from the two highest voltages 70 and 82 µV.

When electrons are injected in the outer channel, in the same spirit as in Fig. 6.15, we can separate the trivial contribution of the sources $\tau_c(1-\tau_c)S_\Sigma$ and the specific contribution of the central QPC S_c by comparing the configurations where QPC_c is tuned to transmit the outer and the inner channel. For clarity, let us define the corresponding experimental values of $P_{outer,inner}$ by :

$$P_{outer} = 1 - \frac{S_c}{\tau_c(1-\tau_c)S_\Sigma} \tag{6.19}$$

$$P_{inner} = -\frac{S_c}{\tau_c(1-\tau_c)S_\Sigma} \tag{6.20}$$

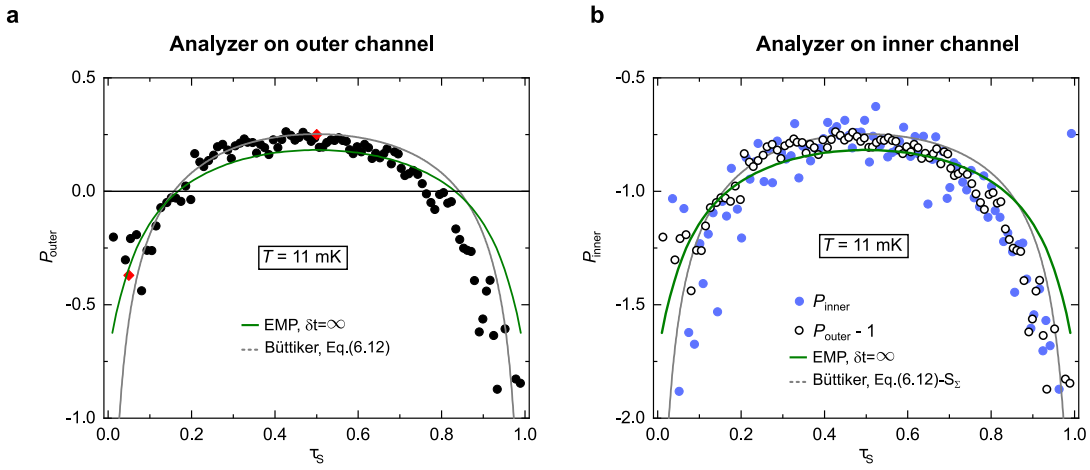

Figure 6.16: **Fano factor P versus τ_S at $T = 11$ mK.**
a Fano factor P_{outer} in the configuration where QPC_c probes the outer channel extracted from the two highest voltages (70 and 82 μV) and plotted versus τ_S at $\tau_c = 0.5$. The grey and green lines respectively indicate Büttiker and EMP predictions for $\delta t = \infty$ and $T = 11$ mK.
b Blue dots corresponds to P_{inner}, i.e. the same measurement with QPC_c probing the inner channel. Open data corresponds to data of panel (a) minus 1, i.e. the specific contribution of QPC_c to the value of P_{outer}.

Fig. 6.16 displays the obtained values of $P_{outer,inner}$ plotted versus τ_S. In both cases, the theoretical predictions for P are plotted as green (EMP at $\delta t = \infty$) and grey (Büttiker framework) lines. The prediction at $\delta t = 64$ ps cannot be extracted with only these two values of V_S due to the oscillations predicted in the theory but not observed experimentally.

In Fig.6.16a, we observe a change of sign of P_{outer} from negative to positive with a maximum around 0.3 at $\tau_S = 0.5$. This is in agreement with the change of the slope sign observed between Fig. 6.12 and Fig. 6.13. Moreover, the quantitative values extracted here are consistent with the ones at $\tau_S \simeq 0.05$ and 0.5 (red rhombuses) extracted in these previous figures.

When we compare data with theoretical predictions, we observe that the expected shape is reproduced. However, we cannot distinguish between the two predictions at our experimental accuracy. The resolution is indeed hampered by the only two values of voltages from which the fits are obtained and by the drastically reduced signal at very high and very low τ_S.

The results when QPC_c partially transmits the inner channel, are plotted as blue dots in Fig. 6.16b. Like in panel (a), both predictions capture the global shape of the data at our experimental accuracy.

Moreover, in that second case, as we specifically investigate the contribution of the central QPC S_c related to the EMP propagation, we can directly compare P_{outer} and P_{inner} which are related by $P_{inner} = P_{outer} - 1$. Accordingly, open black circles in Fig. 6.16b display $P_{outer} - 1$ which match with P_{inner} at our experimental accuracy.

This confirms:

1. the description of cross-correlations as the sum of a trivial source term and of a specific contribution of QPC_c linked to the fractionalization process

2. the measurements previously obtained with the outer channels

3. the value of the mixing angle $\varphi = \pi/4$ in our sample.

Therefore, at high voltage, when the splitting of the mode is complete, the same fractional charges propagate in both channels. At very low and very high source transmission, the obtained signal can be linked to the fractional mutual statistics predicted for those $e/2$-charged quasiparticle braiding with an electron-hole pair.

6.5 Additional tests

To consolidate the results obtained in the previous sections, we performed several complementary measurements reported in this section.

6.5.1 Other temperature

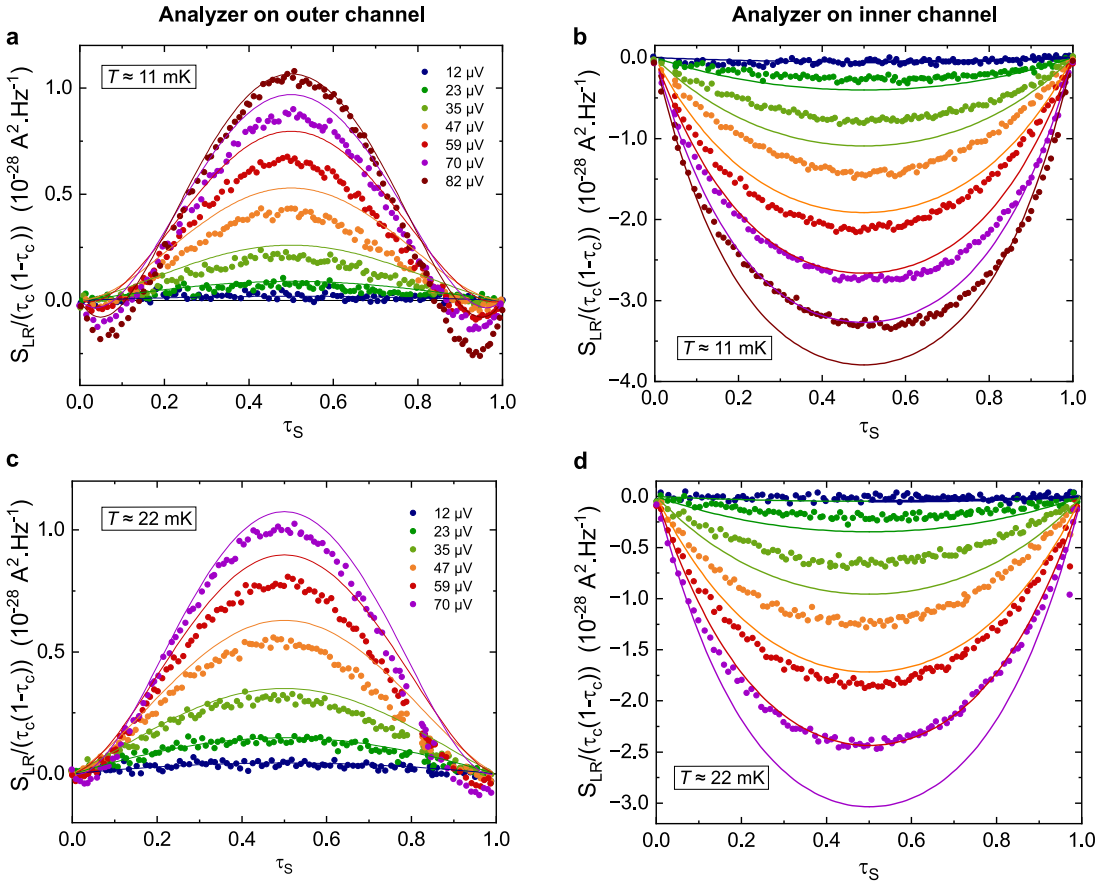

Figure 6.17: **cross-correlation signals at $T = 11$ and 22 mK.**
At $\tau_c = 0.5$, renormalized cross-correlations are plotted versus τ_S for $T = 11$ (a,b) and 22 mK (c,d), with QPC_c set on outer (a,c) and inner (b,d) channel. The continuous lines display predictions of the EMP theory for $\delta t = 64$ ps. Colors indicate the various tested DC bias voltage V_S.

First, the spectroscopy and the main cross-correlation observation in the balanced source-analyzer configuration have been reproduced at higher temperature $T = 22$ mK. Figure 6.17 summarizes the obtained renormalized cross-correlations for both temperatures at all

tested DC-voltages. In the same spirit as in Fig. 6.15, the relative importance of source and analyzer contributions are compared: the left (right) panel displays the results with QPC_c probing the outer (inner) channel.

Note that the thermal effects are important here, as seen in Fig. 6.17c where the negative signal contribution vanishes for $T = 22$ mK.

In spite of moderate discrepancies (both the negative signal at extreme transmission and the positive signal in the middle are over-estimated), we obtain a qualitative agreement with the theory, whereby the expected trend is clearly reproduced.

6.5.2 Energy relaxation

The inter-channel coupling can be seen in terms of the total electronic energy by plotting the heat flow $J_{\rm meas}$ probed at QPC_c as a function of $P_{\rm inj}$, i.e. the injected power at the source in the outer channel. The injected power is given by:

$$P_{\rm inj} = \frac{1}{R_K}\left[\int_{-\infty}^{\mu}(\mu-\epsilon)(1-f_{\rm inj}(\epsilon))d\epsilon + \int_{\mu}^{+\infty}(\epsilon-\mu)f_{\rm inj}(\epsilon)d\epsilon\right] \tag{6.21}$$

where $f_{\rm inj}$ is the double-step distribution function at the position of the source QPC and μ is the electrochemical potential[9]. The first term is the power due to quasiholes and the second one is due to quasiparticles. Similarly, the heat flow $J_{\rm meas}$ is obtained with the same formula by using the data from the energy distribution functions (see Figs. 6.8 and 6.11) instead of the double-step distribution.

Fig. 6.18 shows the corresponding results using the simultaneously measured transmission $\tau_S(V_S)$ (which depends on V_S). Full symbols display the measurements done by injecting power in the outer channel while open symbols correspond to the injection into the inner channel. In the low-interactions regime, all the injected energy remains in the channel of injection, following the red line $J_{\rm meas} = P_{\rm inj}$ if we inject energy in the outer channel and the black line $J_{\rm meas} = 0$ if we inject energy in the inner one. At high bias, i.e. in the strong interaction regime, as we expect the energy to be fully and evenly distributed in both channels, the data should saturate to the green line $J_{\rm meas} = P_{\rm inj}/2$.

When power is injected in the outer channel (full symbols) we do observe the expected cross-over from no relaxation to full relaxation, as expected. However, an apparent energy loss is observed ($\simeq 20\%$) with data of the biggest injected power being below the green dashed line. When power is injected into the inner channel, the data do not saturate towards the full relaxation green line, suggesting a significant loss of energy. Such missing energy has been observed in other experiments [141, 160, 93]. It may result from high energy excitations hidden in the experimental noise, from a coupling to other degrees of freedom not identified yet, or, in the case of inner channel injections, to the resonances in the transmission across the source QPC.

The purple and orange lines display the theoretical energy relaxation with injection into the outer and inner channels respectively within the EMP description. They are calculated from theoretical distribution functions at $\delta t = 64$ ps. For the outer channel, the agreement with data is good: it shows a clear cross-over from the regime with one channel carrying all the energy to the regime with energy equitably distributed in both channels. However, data from the inner channel (open symbol) do not coincide with the theory (orange line). As previously mentioned,

[9] $\mu = \int_{-\infty}^{+\infty}\epsilon f_{\rm inj}(\epsilon)d\epsilon$

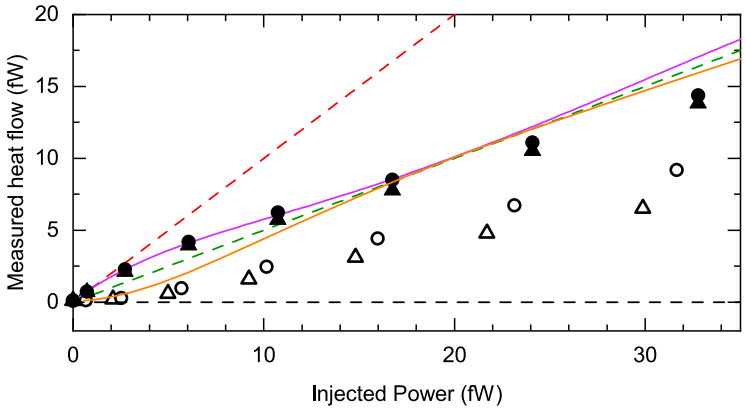

Figure 6.18: **Energy relaxation.**
Measured power at the probe QPC_c (transmitting the outer channel) plotted versus the power injected at the source. The red and black dashed lines respectively display $J_{meas} = P_{inj}$ and $J_{meas} = 0$ corresponding to the expectations for the outer and inner channels if the inter-channel interactions are fully suppressed. The blue dashed line indicates $P_{inj}/2$, corresponding to full relaxation (i.e. $\delta t = \infty$). The purple continuous line indicates the numerical prediction of the EMP theory with time delay $\delta t = 64$ ps. Circles and triangles respectively display results with left and right sources. Full (open) symbols correspond to injection into the outer (inner) channel.

the inner channels exhibit much more artifacts and do not provide quantitative conclusions. We can only observe an increasing tendency of J_{meas} from 0 (all the energy in the unprobed inner channel) to $J_{meas} > 0$ (part of the energy is transferred into the probed outer channel).

6.5.3 Independence with τ_c

Moreover, one remarkable feature of the theory is the independence of the renormalized cross-correlations with the analyzer QPC_c transmission. To check that our experimental results corroborate this prediction, we compared the signal on the whole τ_S range at two significantly different values of analyzer transmission: $\tau_c \simeq 0.5$ and $\tau_c \simeq 0.2$. The obtained results, displayed in Fig. 6.19, show identical results (at our experimental accuracy) for both values of τ_c, which validates the EMP predictions.

6.5.4 Inter-channel tunneling

Like in the $\nu = 2/5$ case, the presence of two copropagating edge channels at $\nu = 2$ can induce inter-channel tunneling (see Sec. 5.2). Although, at $\nu = 2$ it is usually negligible for small paths, at a long effective propagating distance such tunneling events can develop and alter our cross-correlation signal. Indeed, a carrier hopping from the outer channel to the inner one results in a spurious δI current fluctuation within the inner channel correlated to a $-\delta I$ in the outer one. Therefore, such artifacts would create an unwanted additional cross-correlations noise $(1 - \tau_c^2)\delta I^2$ on the measured cross-correlations.

To check that this artifact does not impact the measured signal, we calibrate the tunneling signal by injecting energy into the outer channel while the central QPC is set on the e^2/h plateau. Therefore, measuring non-zero current $I_{R(L)}$ coming from the injection pad set at

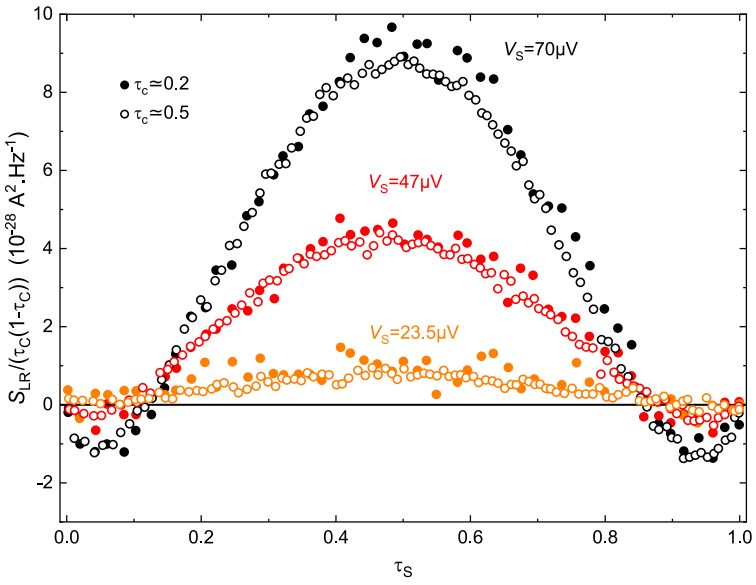

Figure 6.19: **Cross-correlations independence from τ_c.**
Cross-correlation signal plotted versus τ_S for analyzer's transmissions $\tau_c \simeq 0.5$ (full symbols) and $\tau_c \simeq 0.2$ (full symbols). Orange, red, and black data set display data respectively measured at V_S = 23.5, 47 and 70 μV.

$V_{L(R)}$ [10] can be directly attributed to the tunneling events along the path between the left (right) source and the analyzer QPC, as illustrated in Fig. 6.20a.

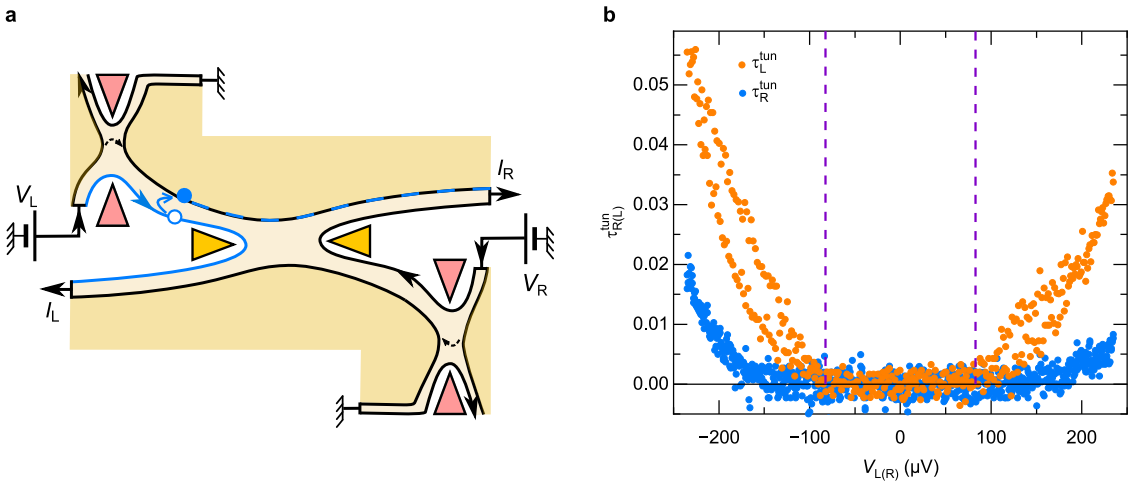

Figure 6.20: **Inter-channel tunneling characterization.**
a Device configuration: the central QPC is set on the plateau while energy is injected in the outer channel.
b Inter-channel tunneling transmission plotted versus the bias applied on source. Dashed purple vertical lines delimit the range of voltage used for the main measurement: $V_{DC} \in [-82, 82]$ μV

Quantitatively, we can define the differential inter-channel tunneling transmission as the

[10] the different injections are distinguished by lock-in measurements using distinct frequencies, see Appendix A

ratio between the current tunneling from the outer to the inner edge and the total injected current:

$$\tau^{\mathrm{tun}}_{\mathrm{L(R)}} \equiv \frac{\partial I_{\mathrm{L(R)}}/\partial V_{\mathrm{L(R)}}}{\partial (I_{\mathrm{L}} + I_{\mathrm{R}})/\partial V_{\mathrm{L(R)}}} \tag{6.22}$$

with $V_{\mathrm{L(R)}} = V_{\mathrm{S}}$ the voltage applied on the left (right) source. Figure 6.20b displays this measured inter-channel tunneling transmission versus the DC-voltage bias of the sources. It is found to be negligible at our accuracy in the DC bias range used for the main measurements $V_{\mathrm{S}} \leq 82$ µV (indicated by purple vertical lines), and to remain lower than 5% up to 200 µV. Note that $\tau_{\mathrm{R}} < \tau_{\mathrm{L}}$, which is certainly linked to the microscopic details of the sample, is more susceptible to trigger tunneling on the left than on the right paths. Besides, note that a hysteresis appears at higher voltage $V_{\mathrm{S}} > 100$ µV. These two features led us to choose 82 µV as the upper bound for the applied voltage.

6.6 Conclusion

In this chapter, we reported non-zero cross-correlations between the outputs of a source-analyzer geometry set in the integer quantum Hall regime $\nu = 2$. The observed signal is a consequence of inter-channel interactions, generating edge-magneto plasmons along the IQH edge of the system.

We have first demonstrated the presence of EMP through spectroscopic measurements. This corroborates the description of the system involving two well-separated excitations (a charged one and a neutral one), instead of a phenomenological Landauer-Büttiker picture based on interacting fermions. Second, in the case of a balanced source-analyzer set-up, the measured cross-correlations and the Fano factor are in agreement with the predictions of the EMP theory. In particular, the experimental results in the dilute regime τ_{S} points to the anyon mutual statistics of the fractional charges.

This first experimental investigation of EMP in a source-analyzer set-up paves the way to creating and studying anyons in the more readily available integer quantum Hall regime. Among the perspectives accessible in the short term, one could cite the continuous tuning of the fraction by varying the coupling between the edge states; or the implementation of "colliders" using a metallic island connected to several edge channels [46]. The latter proposal would allow to access and extensively study multiple kinds of fractional charges in the IQH regime.

General conclusion and Perspectives

This Ph.D. thesis work has explored the unconventional transport processes and braiding statistics of fractional quasiparticles emerging in the regimes of the fractional and integer quantum Hall regimes. Using the so-called "collider" geometry, composed of two opposite upstream source QPCs and one downstream central "analyzer" QPC, these unconventional properties have been evidenced through shot noise measurements, and especially via the cross-correlations of currents between the outgoing beams of quasiparticles.

Summary of the results

This manuscript has presented three main results.

First, an unconventional "Andreev-like" transport process through the analyzer QPC has been evidenced. When a dilute beam of $e/3$-charged quasiparticles impinges on the analyzer tuned to favor the transfer of e charges, an Andreev-like scattering occurs: each incident $e/3$ charge is converted into a transmitted charge e and a simultaneously reflected charge $-2e/3$. This process, predicted in 2003 by Kane and Fisher [42], has been evidenced in our sample through shot noise measurements which present a quantitative matching with the expected charges.

Second, the anyon braiding statistics of quasiparticles in the $\nu = 1/3$ Laughlin state and in the $\nu = 2/5$ Jain state have been explored. In the same "collider" geometry, when two diluted beams of quasiparticles impinge on a central analyzer QPC set in the WBS regime, negative cross-correlations were observed and attributed to anyon statistics. The effect of source imbalance on cross-correlations and the presence of super-Poissonian auto-correlations in outgoing currents provided complementary signatures of anyon braiding statistics. This work also mitigates the possibility of extracting quantitatively the exchange phase from the results recently obtained in several experiments [48, 49, 50], and demonstrates a way to distinguish the braiding from the previously evidenced Andreev-like scattering.

Finally, the statistics of fractional charges along IQH edges have been explored in a "collider" geometry. At $\nu = 2$, due to inter-channel interactions, an injected electron fractionalizes into edge magneto plasmons, i.e. a charged and a neutral modes delocalized over the two channels, as corroborated by the energy distribution spectroscopy measurements. In the strong interaction regime and at long propagating distance, resulting $e/2$ fractional charges travel along the outer channels, impinge on the "analyzer" QPC, and are investigated through the current cross-correlations between the outgoing beams. The obtained measurements are in good agreement with recently developed predictions in the edge magneto plasmon framework. In particular, the predicted negative signal in the dilute regime is found to be a signature of the anyonic braiding phase of the resulting fractional $e/2$ charges.

Outlook

This thesis provided new insights into the transport process and statistics of anyons, and it opens some important perspectives.

In the FQHE, while a relatively good agreement is found with theory in the emblematic $\nu = 1/3$ Laughlin state, further experimental and theoretical studies are needed to fully understand the more complex Jain states, like $\nu = 2/5$. Indeed, for such hierarchical states, the braiding signatures do not match with theory and the inter-channel interactions are likely to play an important role. Moreover, a family of distinct Andreev-like processes could develop in Jain series: at reach for $\nu = 2/5$, an incident e/5 quasiparticle could be converted into a hole of charge $-2e/15$ and a transmitted $e/3$ quasiparticle.

Besides, a recent theoretical study by Schiller *et al.* predicted that the scaling dimension characteristics of a quantum Hall edge could be specifically investigated through the shot noise created by a single voltage-biased QPC. The results of this thesis were compared with this prediction (see Appendix B) but, to be able to give clear conclusions, it calls for further investigations which could be implemented in the short term.

Moreover, experiments in the FQHE exhibit discrepancies with theory (such as the $I - V$ characteristics) or artifacts (such as non-local heating), impeding further manipulation of anyons. As shown in this work, the IQHE could be used as a simpler platform to create and manipulate anyons, in spite of identified artifacts such as energy relaxation with other degrees of freedom.

The recent study by Morel *et al.* proposed a setup that could allow versatile experimental studies. Using metallic islands coupled to N IQH edge channels, one could generate a full family of e/N quasiparticles to be investigated on a downstream analyzer.

Finally, a large part of the interest in these unconventional excitations is focused on the non-abelian anyons. In that case, the quasiparticles are no longer characterized by an exchange phase but by a unitary operator that transforms them into a degenerate state manifold. Advances have been made in the past years to confirm non-abelian properties of quasiparticles in the $\nu = 5/2$ state [7, 8] and the manipulation of such highly correlated objects is predicted to bring technological benefits. Indeed, non-abelian anyons are identified as good candidates to implement topologically protected qubits, with very low error rates [3].

The results of this thesis contribute to the steps needed to reach this long-term goal.

Bibliography

[1] Bernd Rosenow, Ivan P. Levkivskyi, and Bertrand I. Halperin. Current correlations from a mesoscopic anyon collider. *Phys. Rev. Lett.*, 116:156802, Apr 2016.

[2] H. Bartolomei, M. Kumar, R. Bisognin, A. Marguerite, J.-M. Berroir, E. Bocquillon, B. Plaçais, A. Cavanna, Q. Dong, U. Gennser, Y. Jin, and G. Fève. Fractional statistics in anyon collisions. *Science*, 368(6487):173–177, 2020.

[3] Chetan Nayak, Steven H. Simon, Ady Stern, Michael Freedman, and Sankar Das Sarma. Non-abelian anyons and topological quantum computation. *Rev. Mod. Phys.*, 80:1083–1159, Sep 2008.

[4] D. E. Feldman and B. I. Halperin. Fractional charge and fractional statistics in the quantum hall effects. *Rep. Prog. Phys.*, 84:076501, 2021.

[5] Frank Wilczek. Quantum mechanics of fractional-spin particles. *Phys. Rev. Lett.*, 49:957–959, Oct 1982.

[6] Yong-Shi Wu. General theory for quantum statistics in two dimensions. *Phys. Rev. Lett.*, 52:2103–2106, Jun 1984.

[7] Merav Dolev, Moty Heiblum, Vladimir I. Umansky, Ady Stern, and Diana Mahalu. Observation of a quarter of an electron charge at the $\nu = 5/2$ quantum hall state. *Nature*, 452:829–834, 2008.

[8] Mitali Banerjee, Moty Heiblum, Vladimir Umansky, Dima E. Feldman, Yuval Oreg, and Ady Stern. Observation of half-integer thermal hall conductance. *Nature*, 559:205–2010, 2018.

[9] Mark Oliver Goerbig. Quantum hall effects. *arXiv: Mesoscale and Nanoscale Physics*, 2009.

[10] L. Saminadayar, D. C. Glattli, Y. Jin, and B. Etienne. Observation of the $e/3$ fractionally charged laughlin quasiparticle. *Phys. Rev. Lett.*, 79:2526–2529, Sep 1997.

[11] R. de Picciotto, M. Reznikov, M. Heiblum, V. Umansky, G. Bunin, and D. Mahalu. Direct observation of a fractional charge. *Nature*, 389(6647):162–164, Sep 1997.

[12] Kostya S Novoselov, Andre K Geim, Sergei V Morozov, De-eng Jiang, Yanshui Zhang, Sergey V Dubonos, Irina V Grigorieva, and Alexandr A Firsov. Electric field effect in atomically thin carbon films. *science*, 306(5696):666–669, 2004.

[13] C Stampfer, E Schurtenberger, F Molitor, J Guttinger, T Ihn, and K Ensslin. Tunable graphene single electron transistor. *Nano letters*, 8(8):2378–2383, 2008.

[14] Hiske Overweg, Hannah Eggimann, Xi Chen, Sergey Slizovskiy, Marius Eich, Riccardo Pisoni, Yongjin Lee, Peter Rickhaus, Kenji Watanabe, Takashi Taniguchi, , Vladimir Fal'ko, Thomas Ihn, and Klaus Ensslin. Electrostatically induced quantum point contacts in bilayer graphene. *Nano letters*, 18(1):553–559, 2018.

[15] Péter Kun, Bálint Fülöp, Gergely Dobrik, Péter Nemes-Incze, István Endre Lukács, Szabolcs Csonka, Chanyong Hwang, and Levente Tapasztó. Robust quantum point contact operation of narrow graphene constrictions patterned by afm cleavage lithography. *npj 2D Materials and Applications*, 4(1):43, 2020.

[16] Corentin Déprez, Louis Veyrat, Hadrien Vignaud, Goutham Nayak, Kenji Watanabe, Takashi Taniguchi, Frédéric Gay, Hermann Sellier, and Benjamin Sacépé. A tunable fabry–pérot quantum hall interferometer in graphene. *Nature nanotechnology*, 16(5):555–562, 2021.

[17] B. J. van Wees, H. van Houten, C. W. J. Beenakker, J. G. Williamson, L. P. Kouwenhoven, D. van der Marel, and C. T. Foxon. Quantized conductance of point contacts in a two-dimensional electron gas. *Phys. Rev. Lett.*, 60:848–850, Feb 1988.

[18] M. Büttiker. Quantized transmission of a saddle-point constriction. *Phys. Rev. B*, 41:7906–7909, Apr 1990.

[19] R. Landauer. Spatial variation of currents and fields due to localized scatterers in metallic conduction. *IBM Journal of Research and Development*, 1(3):223–231, 1957.

[20] R. A. Webb, S. Washburn, C. P. Umbach, and R. B. Laibowitz. Observation of $\frac{h}{e}$ aharonov-bohm oscillations in normal-metal rings. *Phys. Rev. Lett.*, 54:2696–2699, Jun 1985.

[21] D A Wharam, T J Thornton, R Newbury, M Pepper, H Ahmed, J E F Frost, D G Hasko, D C Peacock, D A Ritchie, and G A C Jones. One-dimensional transport and the quantisation of the ballistic resistance. *Journal of Physics C: Solid State Physics*, 21(8):L209, mar 1988.

[22] M. Büttiker, Y. Imry, R. Landauer, and S. Pinhas. Generalized many-channel conductance formula with application to small rings. *Phys. Rev. B*, 31:6207–6215, May 1985.

[23] M. Büttiker. Four-terminal phase-coherent conductance. *Phys. Rev. Lett.*, 57:1761–1764, Oct 1986.

[24] Rolf Landauer. The noise is the signal. *Nature*, 392(6677):658–659, 1998.

[25] Ya M Blanter and Markus Büttiker. Shot noise in mesoscopic conductors. *Physics reports*, 336(1-2):1–166, 2000.

[26] Y.X. Liang, Q. Dong, U. Gennser, A. Cavanna, and Y. Jin. Input noise voltage below $1\,\mathrm{nv/hz^{1/2}}$ at 1 khz in the hemts at 4.2 k. *J. Low Temp. Phys.*, 167(5-6):632–637, 2012.

[27] S. Jezouin, F. D. Parmentier, A. Anthore, U. Gennser, A. Cavanna, Y. Jin, and F. Pierre. Quantum limit of heat flow across a single electronic channel. *Science*, 342(6158):601–604, 2013.

[28] Sébastien Jézouin. *Transport à travers un canal quantique élémentaire: action du circuit, quantification de la charge et limite quantique du courant de chaleur*. Phd thesis, Université Pierre et Marie Curie - UPMC (Paris 6), 2014.

[29] Kensuke Kobayashi and Masayuki Hashisaka. Shot noise in mesoscopic systems: From single particles to quantum liquids. *Journal of the Physical Society of Japan*, 90(10):102001, 2021.

[30] J. B. Johnson. Thermal agitation of electricity in conductors. *Phys. Rev.*, 32:97–109, Jul 1928.

[31] H. Nyquist. Thermal agitation of electric charge in conductors. *Phys. Rev.*, 32:110–113, Jul 1928.

[32] Rolf Landauer. Johnson-nyquist noise derived from quantum mechanical transmission. *Physica D: Nonlinear Phenomena*, 38(1-3):226–229, 1989.

[33] P. Dutta and P. M. Horn. Low-frequency fluctuations in solids: $\frac{1}{f}$ noise. *Rev. Mod. Phys.*, 53:497–516, Jul 1981.

[34] Laure-Hélène Bize-Reydellet. *Bruit quantique électronique et photons micro-ondes*. PhD thesis, Université Pierre et Marie Curie, 2003. Thèse de doctorat dirigée par Glattli, Denis-Christian Physique du solide Paris 6 2003.

[35] Richard Deblock, Eugen Onac, Leonid Gurevich, and Leo P. Kouwenhoven. Detection of quantum noise from an electrically driven two-level system. *Science*, 301(5630):203–206, 2003.

[36] A. A. Clerk, M. H. Devoret, S. M. Girvin, Florian Marquardt, and R. J. Schoelkopf. Introduction to quantum noise, measurement, and amplification. *Rev. Mod. Phys.*, 82:1155–1208, Apr 2010.

[37] Walter Schottky. Über spontane stromschwankungen in verschiedenen elektrizitätsleitern. *Annalen der physik*, 362(23):541–567, 1918.

[38] Th. Martin and R. Landauer. Wave-packet approach to noise in multichannel mesoscopic systems. *Phys. Rev. B*, 45:1742–1755, Jan 1992.

[39] M. Büttiker. Scattering theory of current and intensity noise correlations in conductors and wave guides. *Phys. Rev. B*, 46:12485–12507, Nov 1992.

[40] T. Martin. Course 5 noise in mesoscopic physics. In H. Bouchiat, Y. Gefen, S. Guéron, G. Montambaux, and J. Dalibard, editors, *Nanophysics: Coherence and Transport*, volume 81 of *Les Houches session LXXXI*, pages 283–359. Elsevier, 2005.

[41] M. Reznikov, R. de Picciotto, T.G. Griffiths, M. Heiblum, and V. Umansky. Observation of quasiparticles with one-fifth of an electron's charge. *Nature*, 399:238–241, 1999.

[42] C. L. Kane and Matthew P. A. Fisher. Shot noise and the transmission of dilute laughlin quasiparticles. *Phys. Rev. B*, 67:045307, Jan 2003.

[43] E. Comforti, Y. C. Chung, M. Heiblum, V. Umansky, and D. Mahalu. Bunching of fractionally charged quasiparticles tunnelling through high-potential barriers. *Nature*, 416(6880):515–518, Apr 2002.

[44] Pierre Glidic, O Maillet, C Piquard, A Aassime, A Cavanna, Y Jin, U Gennser, A Anthore, and F Pierre. Quasiparticle andreev scattering in the ν= 1/3 fractional quantum hall regime. *Nature Communications*, 14(1):514, 2023.

[45] J. Nakamura, S. Liang, G. C. Gardner, and M. J. Manfra. Direct observation of anyonic braiding statistics. *Nat. Phys.*, 16(9):931–936, Sep 2020.

[46] Tom Morel, June-Young M. Lee, H.-S. Sim, and Christophe Mora. Fractionalization and anyonic statistics in the integer quantum hall collider. *Phys. Rev. B*, 105:075433, Feb 2022.

[47] June-Young M. Lee and H.-S. Sim. Non-abelian anyon collider. *Nature Communications*, 13:6660, 11 2022.

[48] M. Ruelle, E. Frigerio, J.-M. Berroir, B. Plaçais, J. Rech, A. Cavanna, U. Gennser, Y. Jin, and G. Fève. Comparing fractional quantum hall laughlin and jain topological orders with the anyon collider. *Phys. Rev. X*, 13:011031, Mar 2023.

[49] P. Glidic, O. Maillet, A. Aassime, C. Piquard, A. Cavanna, U. Gennser, Y. Jin, A. Anthore, and F. Pierre. Cross-correlation investigation of anyon statistics in the $\nu = 1/3$ and 2/5 fractional quantum hall states. *Phys. Rev. X*, 13:011030, Mar 2023.

[50] June-Young M. Lee, Changki Hong, Tomer Alkalay, Noam Schiller, Vladimir Umansky, Moty Heiblum, Yuval Oreg, and H. S. Sim. Partitioning of diluted anyons reveals their braiding statistics. *Nature*, 617:277–281, 2023.

[51] K. v. Klitzing, G. Dorda, and M. Pepper. New method for high-accuracy determination of the fine-structure constant based on quantized hall resistance. *Phys. Rev. Lett.*, 45:494–497, Aug 1980.

[52] D. C. Tsui, H. L. Stormer, and A. C. Gossard. Two-dimensional magnetotransport in the extreme quantum limit. *Phys. Rev. Lett.*, 48:1559–1562, May 1982.

[53] N. Bouarissa and H. Aourag. Effective masses of electrons and heavy holes in inas, insb, gasb, gaas and some of their ternary compounds. *Infrared Physics and Technology*, 40(4):343–349, 1999.

[54] B. I. Halperin. Quantized hall conductance, current-carrying edge states, and the existence of extended states in a two-dimensional disordered potential. *Phys. Rev. B*, 25:2185–2190, Feb 1982.

[55] R. B. Laughlin. Anomalous quantum hall effect: An incompressible quantum fluid with fractionally charged excitations. *Phys. Rev. Lett.*, 50:1395–1398, May 1983.

[56] T. G. Griffiths, E. Comforti, M. Heiblum, Ady Stern, and V. Umansky. Evolution of quasiparticle charge in the fractional quantum hall regime. *Phys. Rev. Lett.*, 85:3918–3921, Oct 2000.

[57] Aveek Bid, N. Ofek, M. Heiblum, V. Umansky, and D. Mahalu. Shot noise and charge at the 2/3 composite fractional quantum hall state. *Phys. Rev. Lett.*, 103:236802, Dec 2009.

[58] M. Kapfer, P. Roulleau, M. Santin, I. Farrer, D. A. Ritchie, and D. C. Glattli. A josephson relation for fractionally charged anyons. *Science*, 363(6429):846–849, 2019.

[59] Remi Bisognin, Hugo Bartolomei, Manohar Kumar, Inès Safi, J-M Berroir, Erwan Bocquillon, Bernard Placais, Antonella Cavanna, Ulf Gennser, Yong Jin, et al. Microwave photons emitted by fractionally charged quasiparticles. *Nature communications*, 10(1):1708, 2019.

[60] D. T. McClure, W. Chang, C. M. Marcus, L. N. Pfeiffer, and K. W. West. Fabry-perot interferometry with fractional charges. *Phys. Rev. Lett.*, 108:256804, Jun 2012.

[61] F. E. Camino, Wei Zhou, and V. J. Goldman. $e/3$ laughlin quasiparticle primary-filling $\nu = 1/3$ interferometer. *Phys. Rev. Lett.*, 98:076805, Feb 2007.

[62] V. J. Goldman and B. Su. Resonant tunneling in the quantum hall regime: Measurement of fractional charge. *Science*, 267(5200):1010–1012, 1995.

[63] Jens Martin, Shahal Ilani, Basile Verdene, Jurgen Smet, Vladimir Umansky, Diana Mahalu, Dieter Schuh, Gerhard Abstreiter, and Amir Yacoby. Localization of fractionally charged quasi-particles. *Science*, 305(5686):980–983, 2004.

[64] June-Young M. Lee, Cheolhee Han, and H.-S. Sim. Fractional mutual statistics on integer quantum hall edges. *Phys. Rev. Lett.*, 125:196802, Nov 2020.

[65] Noam Schiller, Yuval Oreg, and Kyrylo Snizhko. Extracting the scaling dimension of quantum hall quasiparticles from current correlations. *Phys. Rev. B*, 105:165150, Apr 2022.

[66] C. de C. Chamon, D. E. Freed, S. A. Kivelson, S. L. Sondhi, and X. G. Wen. Two point-contact interferometer for quantum hall systems. *Phys. Rev. B*, 55:2331–2343, Jan 1997.

[67] Bertrand I Halperin, Ady Stern, Izhar Neder, and Bernd Rosenow. Theory of the fabry-pérot quantum hall interferometer. *Physical Review B*, 83(15):155440, 2011.

[68] K. T. Law, D. E. Feldman, and Yuval Gefen. Electronic mach-zehnder interferometer as a tool to probe fractional statistics. *Phys. Rev. B*, 74:045319, Jul 2006.

[69] Gabriele Campagnano, Oded Zilberberg, Igor Gornyi, Dmitri Feldman, Andrew Potter, and Yuval Gefen. Hanbury brown–twiss interference of anyons. *Physical Review Letters*, 109:106802, 04 2012.

[70] James Nakamura, Shuang Liang, Geoffrey C. Gardner, and Michael J. Manfra. Fabry-perot interferometry at the $\nu = 2/5$ fractional quantum hall state, 2023.

[71] D. T. McClure, W. Chang, C. M. Marcus, L. N. Pfeiffer, and K. W. West. Fabry-perot interferometry with fractional charges. *Phys. Rev. Lett.*, 108:256804, Jun 2012.

[72] F. E. Camino, Wei Zhou, and V. J. Goldman. $e/3$ laughlin quasiparticle primary-filling $\nu = 1/3$ interferometer. *Phys. Rev. Lett.*, 98:076805, Feb 2007.

[73] R. L. Willett, C. Nayak, K. Shtengel, L. N. Pfeiffer, and K. W. West. Magnetic-field-tuned aharonov-bohm oscillations and evidence for non-abelian anyons at $\nu = 5/2$. *Phys. Rev. Lett.*, 111:186401, Oct 2013.

[74] James Nakamura, Saeed Fallahi, H. Sahasrabudhe, Rajib Rahman, S. Liang, G. Gardner, and M. Manfra. Aharonov–bohm interference of fractional quantum hall edge modes. *Nature Physics*, 15:1, 03 2019.

[75] B Rosenow and BI Halperin. Influence of interactions on flux and back-gate period of quantum hall interferometers. *Physical review letters*, 98(10):106801, 2007.

[76] Nissim Ofek, Aveek Bid, Moty Heiblum, Ady Stern, Vladimir Umansky, and Diana Mahalu. Role of interactions in an electronic fabry–perot interferometer operating in the quantum hall effect regime. *Proceedings of the National Academy of Sciences*, 107(12):5276–5281, 2010.

[77] J. K. Jain. Composite-fermion approach for the fractional quantum hall effect. *Phys. Rev. Lett.*, 63:199–202, Jul 1989.

[78] J. K. Jain. Theory of the fractional quantum hall effect. *Phys. Rev. B*, 41:7653–7665, Apr 1990.

[79] D. Ferraro, A. Braggio, M. Merlo, N. Magnoli, and M. Sassetti. Relevance of multiple quasiparticle tunneling between edge states at $\nu = p/(2np + 1)$. *Phys. Rev. Lett.*, 101:166805, Oct 2008.

[80] Xiao-Gang Wen. Topological orders and edge excitations in fractional quantum hall states. *Advances in Physics*, 44(5):405–473, 1995.

[81] X. G. Wen. Theory of the edge states in the fractional quantum hall effects. *Int. J. Mod. Phys. B*, 6:1711–1762, 1992.

[82] Thierry Giamarchi. *Quantum Physics in One Dimension*. Oxford University Press, 12 2003.

[83] Sin-itiro Tomonaga. Remarks on bloch's method of sound waves applied to many-fermion problems. *Progress of Theoretical Physics*, 5(4):544–569, 1950.

[84] JM Luttinger. An exactly soluble model of a many-fermion system. *Journal of mathematical physics*, 4(9):1154–1162, 1963.

[85] I. Safi and H. J. Schulz. Transport in an inhomogeneous interacting one-dimensional system. *Phys. Rev. B*, 52:R17040–R17043, Dec 1995.

[86] Claudio de C. Chamon and Eduardo Fradkin. Distinct universal conductances in tunneling to quantum hall states: The role of contacts. *Phys. Rev. B*, 56:2012–2025, Jul 1997.

[87] J. Dubois, T. Jullien, C. Grenier, P. Degiovanni, P. Roulleau, and D. C. Glattli. Integer and fractional charge lorentzian voltage pulses analyzed in the framework of photon-assisted shot noise. *Phys. Rev. B*, 88:085301, Aug 2013.

[88] E. Berg, Y. Oreg, E.-A. Kim, and F. von Oppen. Fractional charges on an integer quantum hall edge. *Phys. Rev. Lett.*, 102:236402, Jun 2009.

[89] Ivan P. Levkivskyi and Eugene V. Sukhorukov. Dephasing in the electronic mach-zehnder interferometer at filling factor $\nu = 2$. *Phys. Rev. B*, 78:045322, Jul 2008.

[90] Matteo Acciai, Matteo Carrega, Jérôme Rech, Thibaut Jonckheere, Thierry Martin, and Maura Sassetti. Probing interactions via nonequilibrium momentum distribution and noise in integer quantum hall systems at $\nu = 2$. *Phys. Rev. B*, 98:035426, Jul 2018.

[91] Ines Safi. A dynamic scattering approach for a gated interacting wire. *The European Physical Journal B-Condensed Matter and Complex Systems*, 12:451–455, 1999.

[92] Inès Safi and H. J. Schulz. Interacting electrons with spin in a one-dimensional dirty wire connected to leads. *Phys. Rev. B*, 59:3040–3059, Jan 1999.

[93] P. Degiovanni, Ch. Grenier, G. Fève, C. Altimiras, H. le Sueur, and F. Pierre. Plasmon scattering approach to energy exchange and high-frequency noise in $\nu = 2$ quantum hall edge channels. *Phys. Rev. B*, 81:121302, Mar 2010.

[94] Claire Wahl, Jérôme Rech, Thibaut Jonckheere, and Thierry Martin. Interactions and charge fractionalization in an electronic hong-ou-mandel interferometer. *Phys. Rev. Lett.*, 112:046802, Jan 2014.

[95] Ivan P. Levkivskyi and Eugene V. Sukhorukov. Energy relaxation at quantum hall edge. *Phys. Rev. B*, 85:075309, Feb 2012.

[96] D. L. Kovrizhin and J. T. Chalker. Equilibration of integer quantum hall edge states. *Phys. Rev. B*, 84:085105, Aug 2011.

[97] Hiroyuki Inoue, Anna Grivnin, Nissim Ofek, Izhar Neder, Moty Heiblum, Vladimir Umansky, and Diana Mahalu. Charge fractionalization in the integer quantum hall effect. *Phys. Rev. Lett.*, 112:166801, Apr 2014.

[98] Yasuhiro Hatsugai. Chern number and edge states in the integer quantum hall effect. *Phys. Rev. Lett.*, 71:3697–3700, Nov 1993.

[99] J Cayssol and J N Fuchs. Topological and geometrical aspects of band theory. *Journal of Physics: Materials*, 4(3):034007, apr 2021.

[100] C. L. Kane and Matthew P. A. Fisher. Transport in a one-channel luttinger liquid. *Phys. Rev. Lett.*, 68:1220–1223, Feb 1992.

[101] C. L. Kane and Matthew P. A. Fisher. Transmission through barriers and resonant tunneling in an interacting one-dimensional electron gas. *Phys. Rev. B*, 46:15233–15262, Dec 1992.

[102] FP Milliken, CP Umbach, and RA Webb. Indications of a luttinger liquid in the fractional quantum hall regime. *Solid State Communications*, 97(4):309–313, 1996.

[103] M Grayson, DC Tsui, LN Pfeiffer, KW West, and AM Chang. Continuum of chiral luttinger liquids at the fractional quantum hall edge. *Physical review letters*, 80(5):1062, 1998.

[104] AM Chang, MK Wu, CC Chi, LN Pfeiffer, and KW West. Plateau behavior in the chiral luttinger liquid exponent. *Physical Review Letters*, 86(1):143, 2001.

[105] A. M. Chang. Chiral luttinger liquids at the fractional quantum hall edge. *Rev. Mod. Phys.*, 75:1449–1505, Nov 2003.

[106] A. Anthore, Z. Iftikhar, E. Boulat, F. D. Parmentier, A. Cavanna, A. Ouerghi, U. Gennser, and F. Pierre. Circuit quantum simulation of a tomonaga-luttinger liquid with an impurity. *Phys. Rev. X*, 8:031075, Sep 2018.

[107] Liam A. Cohen, Noah L. Samuelson, Taige Wang, Takashi Taniguchi, Kenji Watanabe, Michael P. Zaletel, and Andrea F. Young. Universal chiral luttinger liquid behavior in a graphene fractional quantum hall point contact, 2022.

[108] Xin Wan, Kun Yang, and E Rezayi. Reconstruction of fractional quantum hall edges. *Physical review letters*, 88:056802, 03 2002.

[109] Yogesh Joglekar, Hoang Nguyen, and Ganpathy Murthy. Edge reconstructions in fractional quantum hall systems. *Physical Review B*, 68, 03 2003.

[110] D. B. Chklovskii, B. I. Shklovskii, and L. I. Glazman. Electrostatics of edge channels. *Phys. Rev. B*, 46:4026–4034, Aug 1992.

[111] AH MacDonald. Edge states in the fractional-quantum-hall-effect regime. *Physical review letters*, 64(2):220, 1990.

[112] M. Hilke, D. C. Tsui, M. Grayson, L. N. Pfeiffer, and K. W. West. Fermi liquid to luttinger liquid transition at the edge of a two-dimensional electron gas. *Phys. Rev. Lett.*, 87:186806, Oct 2001.

[113] O. M. Auslaender, A. Yacoby, R. de Picciotto, K. W. Baldwin, L. N. Pfeiffer, and K. W. West. Experimental evidence for resonant tunneling in a luttinger liquid. *Phys. Rev. Lett.*, 84:1764–1767, Feb 2000.

[114] C. L. Kane and Matthew P. A. Fisher. Nonequilibrium noise and fractional charge in the quantum hall effect. *Phys. Rev. Lett.*, 72:724–727, Jan 1994.

[115] P. Fendley, A. W. W. Ludwig, and H. Saleur. Exact nonequilibrium dc shot noise in luttinger liquids and fractional quantum hall devices. *Phys. Rev. Lett.*, 75:2196–2199, Sep 1995.

[116] Y. C. Chung, M. Heiblum, Y. Oreg, V. Umansky, and D. Mahalu. Anomalous chiral luttinger liquid behavior of diluted fractionally charged quasiparticles. *Phys. Rev. B*, 67:201104, May 2003.

[117] A.F. Andreev. Thermal conductivity of the intermediate state of superconductors. *Zh. Eksperim. i Teor. Fiz.*, 46, 1964.

[118] Pierre Gilles de Gennes and Daniel Saint-James. Elementary excitations in the vicinity of a normal metal-superconducting metal contact. *Physics Letters*, 4:151–152, 1963.

[119] Max Hays. *Andreev Reflection, Andreev Levels, and the Josephson Effect*, pages 69–80. Springer International Publishing, Cham, 2021.

[120] M. Hashisaka, T. Jonckheere, T. Akiho, S. Sasaki, J. Rech, T. Martin, and K. Muraki. Andreev reflection of fractional quantum hall quasiparticles. *Nat. Commun.*, 12:2794, 2021.

[121] Nancy P. Sandler, Claudio de C. Chamon, and Eduardo Fradkin. Andreev reflection in the fractional quantum hall effect. *Phys. Rev. B*, 57:12324–12332, May 1998.

[122] Moty Heiblum and D. E. Feldman. Edge probes of topological order. *Int. J. Mod. Phys. A*, 35(18):2030009, 2020.

[123] Ya.M. Blanter and M. Büttiker. Shot noise in mesoscopic conductors. *Phys. Rep.*, 336(1):1–166, 2000.

[124] D. E. Feldman and Moty Heiblum. Why a noninteracting model works for shot noise in fractional charge experiments. *Phys. Rev. B*, 95:115308, Mar 2017.

[125] Maëlle Kapfer. *Dynamic of excitations of the Fractional quantum Hall effect : fractional charge and fractional Josephson frequency.* Phd thesis, Université Paris-Saclay, SPEC, CEA-Saclay, 91191 Gif-sur-Yvette, France, 2018.

[126] Edvin G. Idrisov, Ivan P. Levkivskyi, Eugene V. Sukhorukov, and Thomas L. Schmidt. Current cross correlations in a quantum hall collider at filling factor two. *Phys. Rev. B*, 106:085405, Aug 2022.

[127] Hiroyuki Inoue, Anna Grivnin, Nissim Ofek, Izhar Neder, Moty Heiblum, Vladimir Umansky, and Diana Mahalu. Charge fractionalization in the integer quantum hall effect. *Phys. Rev. Lett.*, 112:166801, Apr 2014.

[128] T Ota, M Hashisaka, K Muraki, and T Fujisawa. Negative and positive cross-correlations of current noises in quantum hall edge channels at bulk filling factor. *Journal of Physics: Condensed Matter*, 29(22):225302, apr 2017.

[129] Christophe Mora. Anyonic exchange in a beam splitter, 2022.

[130] K. Iyer, T. Martin, J. Rech, and T. Jonckheere. Quasiparticle andreev reflection in the laughlin fractions of the fractional quantum hall effect, 2023.

[131] Hugo Bartolomei. *Collision Experiments in Quantum Hall Conductors.* Phd thesis, Sorbonne Université, LPENS, 70005 Paris, France, 2022.

[132] T. Jonckheere, J. Rech, B. Grémaud, and T. Martin. Anyonic statistics revealed by the hong-ou-mandel dip for fractional excitations, 2022.

[133] E. Bocquillon, V. Freulon, J.-M Berroir, P. Degiovanni, B. Plaçais, A. Cavanna, Y. Jin, and G. Fève. Coherence and indistinguishability of single electrons emitted by independent sources. *Science*, 339(6123):1054–1057, 2013.

[134] Byeongmok Lee, Cheolhee Han, and H.-S. Sim. Negative excess shot noise by anyon braiding. *Phys. Rev. Lett.*, 123:016803, Jul 2019.

[135] Cheolhee Han, Jinhong Park, Yuval Gefen, and H.-S. Sim. Topological vacuum bubbles by anyon braiding. *Nat. Commun.*, 7(1):11131, mar 2016.

[136] Vivek Venkatachalam, Sean Hart, Loren Pfeiffer, Ken West, and Amir Yacoby. Local thermometry of neutral modes on the quantum hall edge. *Nat. Phys.*, 8(9):676–681, Aug 2012.

[137] A. Bid, N. Ofek, H. Inoue, C.L. Kane, V. Umansky, and D. Mahalu. Observation of neutral modes in the fractional quantum hall regime. *Nature*, 466:585–590, 2010.

[138] C. Altimiras, H. le Sueur, U. Gennser, A. Anthore, A. Cavanna, D. Mailly, and F. Pierre. Chargeless heat transport in the fractional quantum hall regime. *Phys. Rev. Lett.*, 109:026803, Jul 2012.

[139] Hiroyuki Inoue, Anna Grivnin, Yuval Ronen, Moty Heiblum, Vladimir Umansky, and Diana Mahalu. Proliferation of neutral modes in fractional quantum hall states. *Nat. Commun.*, 5(1), jun 2014.

[140] T. Krähenmann, S. G. Fischer, M. Röösli, T. Ihn, C. Reichl, W. Wegscheider, K. Ensslin, Y. Gefen, and Yigal Meir. Auger-spectroscopy in quantum hall edge channels and the missing energy problem. *Nat. Commun.*, 10(1), Sep 2019.

[141] Carles Altimiras, Hélène le Sueur, Ulf Gennser, Antonella Cavanna, Dominique Mailly, and Frédéric Pierre. Non-equilibrium edge channel spectroscopy in the integer quantum hall regime. *Nat. Phys.*, 6:34, 2009.

[142] E. Sivre, H. Duprez, A. Anthore, A. Aassime, F.D. Parmentier, A. Cavanna, A. Ouerghi, U. Gennser, and F. Pierre. Electronic heat flow and thermal shot noise in quantum circuits. *Nat. Commun.*, 10:5638, 2019.

[143] O.S. Lumbroso, L. Simine, A. Nitzan, D. Segal, and O. Tal. Electronic noise due to temperature differences in atomic-scale junctions. *Nature*, 562:240–244, 2018.

[144] Samuel Larocque, Edouard Pinsolle, Christian Lupien, and Bertrand Reulet. Shot noise of a temperature-biased tunnel junction. *Phys. Rev. Lett.*, 125:106801, Sep 2020.

[145] Xiao-Gang Wen. *Quantum Field Theory of Many-Body Systems: From the Origin of Sound to an Origin of Light and Electrons*. Oxford University Press, 09 2007.

[146] Jainendra K. Jain. *Composite Fermions*. Cambridge University Press, 2007.

[147] Y. Takagaki, K. J. Friedland, J. Herfort, H. Kostial, and K. Ploog. Inter-edge-state scattering in the spin-polarized quantum hall regime with current injection into inner states. *Phys. Rev. B*, 50:4456–4462, Aug 1994.

[148] I. Taktak, M. Kapfer, J. Nath, P. Roulleau, M. Acciai, J. Splettstoesser, I. Farrer, D. A. Ritchie, and D. C. Glattli. Two-particle time-domain interferometry in the fractional quantum hall effect regime. *Nat. Commun.*, 13:5863, 2022.

[149] Matteo Acciai, Preden Roulleau, Imen Taktak, D. Christian Glattli, and Janine Splettstoesser. Influence of channel mixing in fermionic hong-ou-mandel experiments. *Phys. Rev. B*, 105:125415, Mar 2022.

[150] D. Kovrizhin. private communication, in preparation, 2023.

[151] Erez Berg, Yuval Oreg, E-A Kim, and F Von Oppen. Fractional charges on an integer quantum hall edge. *Physical Review Letters*, 102(23):236402, 2009.

[152] Izhar Neder. Fractionalization noise in edge channels of integer quantum hall states. *Physical Review Letters*, 108(18):186404, 2012.

[153] Mirco Milletarì and Bernd Rosenow. Shot-noise signatures of charge fractionalization in the $\nu = 2$ quantum hall edge. *Phys. Rev. Lett.*, 111:136807, Sep 2013.

[154] Ch Grenier, Julie Dubois, Thibaut Jullien, Preden Roulleau, DC Glattli, and Pascal Degiovanni. Fractionalization of minimal excitations in integer quantum hall edge channels. *Physical Review B*, 88(8):085302, 2013.

[155] Erwann Bocquillon, Vincent Freulon, J-M Berroir, Pascal Degiovanni, Bernard Plaçais, A Cavanna, Yun Jin, and Gwendal Fève. Separation of neutral and charge modes in one-dimensional chiral edge channels. *Nature communications*, 4(1):1839, 2013.

[156] V Freulon, A Marguerite, J-M Berroir, B Plaçais, A Cavanna, Y Jin, and Gwendal Fève. Hong-ou-mandel experiment for temporal investigation of single-electron fractionalization. *Nature communications*, 6(1):6854, 2015.

[157] Masayuki Hashisaka, Naoaki Hiyama, Takafumi Akiho, Koji Muraki, and Toshimasa Fujisawa. Waveform measurement of charge-and spin-density wavepackets in a chiral tomonaga–luttinger liquid. *Nature Physics*, 13(6):559–562, 2017.

[158] D. L. Kovrizhin and J. T. Chalker. Relaxation in driven integer quantum hall edge states. *Phys. Rev. Lett.*, 109:106403, Sep 2012.

[159] M. J. Rufino, D. L. Kovrizhin, and J. T. Chalker. Solution of a model for the two-channel electronic mach-zehnder interferometer. *Phys. Rev. B*, 87:045120, Jan 2013.

[160] H. le Sueur, C. Altimiras, U. Gennser, A. Cavanna, D. Mailly, and F. Pierre. Energy relaxation in the integer quantum hall regime. *Phys. Rev. Lett.*, 105:056803, Jul 2010.

[161] Kyrylo Snizhko and Vadim Cheianov. Scaling dimension of quantum hall quasiparticles from tunneling-current noise measurements. *Phys. Rev. B*, 91:195151, May 2015.

Appendix A

Experimental Setup and techniques

A.1 Elements concerning the nanofabrication process

The samples used in this thesis have been nanofabricated in the clean room of the Center for Nanoscience and Nanotechnologies. For the sample used in Chapters 3 to 5 and for the one used in Chapter 6 , the nanofabrication process followed the same standard techniques divided into the five following e-beam lithography steps:

1. First, alignment marks made of a Ti-Au bilayer are deposited through a Poly(methyl methacrylate) (PMMA) mask. They allow us to align the electron beam for all the following steps.

2. The mesa is defined by using a ma-N 2403 protection mask and by wet etching the unprotected parts in a solution of $H_3PO_4/H_2O_2/H_2O$ (deeper than the Si δ-doping layer).

3. To allow the electrical connection with the buried 2DEG, Ni-Au-Ge Ohmic contacts are defined. They are realized by successive depositions of Ni (10 nm) - Au (10 nm) - Ge (90 nm) - Ni (20 nm) - Au (170 nm) - Ni (10 nm) through a PMMA mask, followed by a 440°C annealing for 50s.

4. Then, the 40 nm high aluminum split gates are deposited through a PMMA mask.

5. Finally, we deposit through a PMMA mask the large bonding ports and their connection with Al gates. In the first sample, the successive metallic layers are Ni (20 nm) - Au (380 nm). In the second sample, this has been made three times to patch disconnected areas resulting in a Cr (5 nm) - Au (400 nm) - Cr (5 nm) - Au (400 nm) - Cr (5 nm) - Au (145 nm) stack.

Figure A.1 summarizes the nanofabrication process.

A.2 Experimental setup

This section briefly presents the technical details of the experimental setup used during this Ph.D. work. It was acquired, wired, and optimized before the beginning of this thesis.

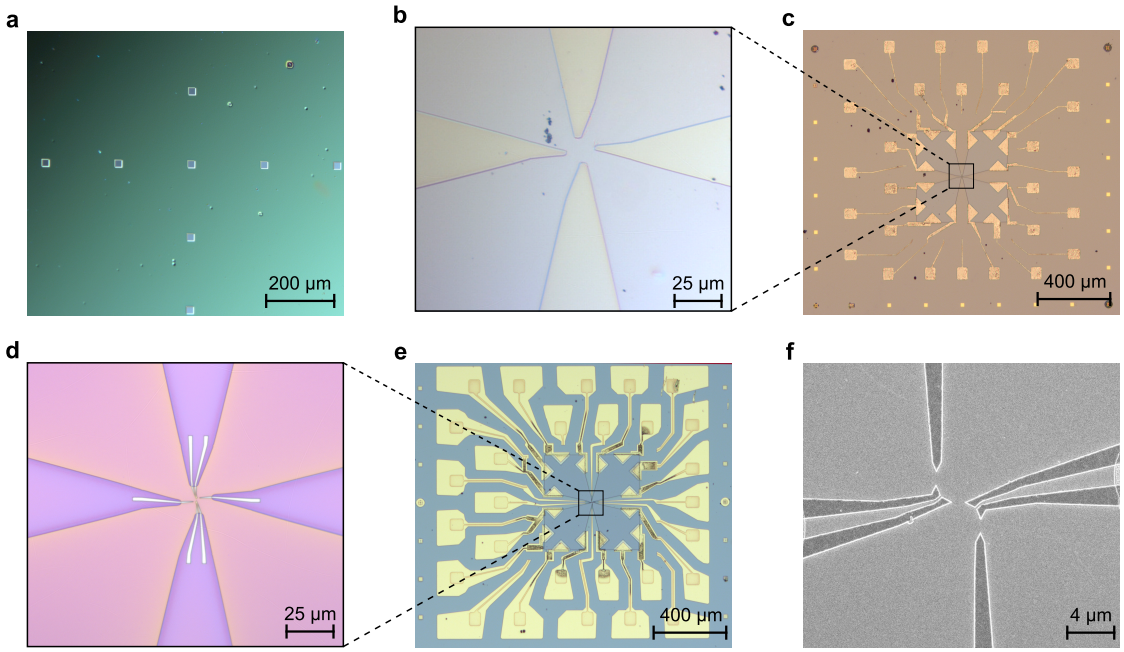

Figure A.1: **Sample fabrication process**
Optics and SEM picture of the successive nanofabrication steps for the first sample studied in this thesis: deposition of alignment marks (a), definition of the mesa (b), elaboration of the Ohmic contacts (c), deposition of the aluminum split gates (d) and deposition of the connections between bonding ports and gates (e). A SEM picture of the central part is given in (f)

A.2.1 Equipment

The samples have been measured in a commercial cryo-free dilution refrigerator with extensive filtering and thermalization of the electrical lines [27].

The DC-voltage biases applied on the injection Ohmic contacts are imposed by Yokogawa 7621 voltage sources. The DC-voltage V_g of split gates is applied thanks to a Bilt BE105 voltage source, with BE2102 modules. Finally, the low-frequency current signals are amplified (preamplifier Celian EPC1-B) and then measured via standard lock-in measurements (Stanford SR810) at frequencies below 100 Hz. The lock-in measurements are done by applying an ac modulation with an Agilent 33220A waveform generator, of rms amplitude always below $k_B T/e$ on the injection line (typically 0.5 to 1 µV on chip for $T \sim 20$ mK). In practice, the DC-currents I_{DC} are obtained by integrating with the source bias voltage the corresponding lock-in signal:

$$I_{DC}(V_{DC}) = \int_0^{V_{DC}} \frac{\partial I}{\partial V_{DC}} dV_{DC}, \tag{A.1}$$

A.2.2 DC and low-frequency wiring

The samples of interest are connected to the injection and measurement instruments through three distinct types of lines: injection lines (connected to DC-voltage biased Ohmic contacts), measurement lines (connected to measurements Ohmic contacts) and gate lines (connected to the metallic split gates defining the QPCs). Specific cold RC filters located within the same metallic enclosure are included near the device: 200 kΩ-200 nF for gate lines, 10 kΩ-47 nF for injection lines, 10 kΩ-1 nF for low-frequency measurement lines.

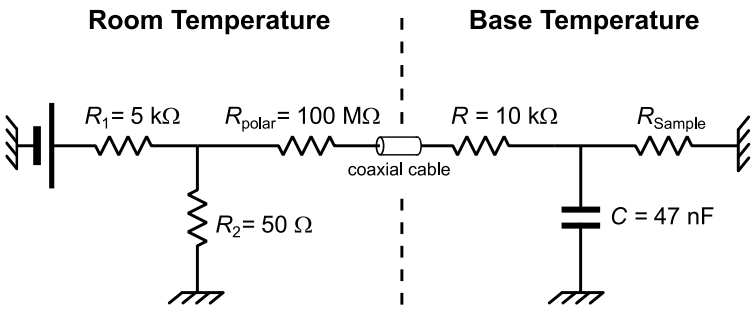

Figure A.2: **DC-injection line**
The source of voltage is connected to the injection through large Ohmic contact on the sample via a voltage divider ($R_1 \parallel R_2$), a polarization resistance R_{polar} and a RC circuit.

Besides, note that the imposed voltage bias is beforehand divided ($R_1 \parallel R_2$) following the circuit presented in Fig. A.2.

A.2.3 MHz noise measurement line

During this thesis, all the noise measurements have been performed using two cryogenic high-electron-mobility transistors (HEMT) amplifiers [26, 27], located at the 4 K stage of the fridge. These two HEMTs are labeled 1 and 2 for the following. The noise signal is integrated near 1 MHz, in a bandwidth $[0.84, 0.88]$ MHz for $\nu = 1/3$, $\nu = 2/5$ and $[0.8, 0.92]$ MHz at $\nu = 2$. Note that in practice, for the measurements presented in the manuscript, we integrate the noise signal for 10 s and we average typically 10 consecutive voltage sweeps.

Description of the line

The noise measurements are made near the MHz range which requires a specific measurement line schematized in Fig. A.3.

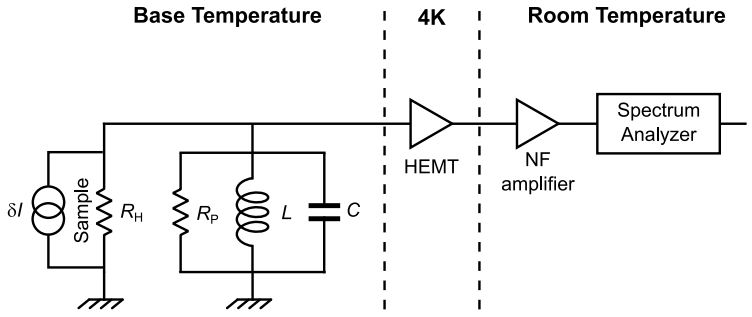

Figure A.3: **Noise amplification line**
Electrical model of the noise amplification line near 1 MHz. Current fluctuations from the sample flow in a RLC resonant circuit put in parallel with the sample. The resulting voltage fluctuations are amplified by a cryo-HEMT and a NF amplifier before being numerically analyzed.

The HEMTs are connected to the device through two RLC tank circuits of essentially identical resonant frequency ≈ 0.86 MHz. The RLC tanks are composed of home-made su-

perconducting coils of inductance $L \approx 250$ µH, a capacitance $C \approx 135$ pF developing along the interconnect coaxial cables, and an effective resistance $R_{\rm p} \approx 150$ kΩ (in parallel with $R_{\rm H}$) due to the resistance of the coaxial cables at the lowest temperature stage of the refrigerator [27, 28]. The signal is amplified at low temperature by the HEMTs of gain $G_{\rm HEMT}$ and at room temperature by NF amplifiers of gain $G_{\rm NF} \approx 200$.

At equilibrium, the noise measured through the amplification chains 1 and 2 is:

$$S(\omega) = G_{1,2}^{\rm eff}\left[4k_{\rm B}T{\rm Re}(Z(\omega)) + S_{\rm amp}(\omega)\right] \tag{A.2}$$

with $Z(\omega) = \left(\frac{1}{R_{\rm H}} + \frac{1}{R_{\rm P}} + \frac{1}{jL\omega} + jC\omega\right)$ the impedance of the circuit and $S_{\rm amp}(\omega)$ is the noise added by the amplifiers. $G_{1,2}^{\rm eff}$ are the effective gains of the full amplification chains 1 and 2.

Gain calibration

These effective gains $G_{1,2}^{\rm eff}$ have to be calibrated, which is done in two successive steps: first, we determine the tank circuit parameters; and then we apply a linear fit on $S(T)$ using the fluctuation-dissipation theorem.

First, the tank circuit modeled in Eq. (A.2) is characterized through the value of the resonant frequency together with the evolution of the noise bandwidth of the tank in parallel with the known $R_{\rm H}$ at different filling factors. The bandwidth data are measured at sufficiently high temperature ($T \gtrsim 150$ mK), such that the amplifier impact (which can deform the resonance at large $R_{\rm H}$) remains negligible with respect to thermal noise. The obtained tank parameters are summarized in the table within Fig. A.4a, which also displays the fits of the bandwidth vs $R_{\rm H}$.

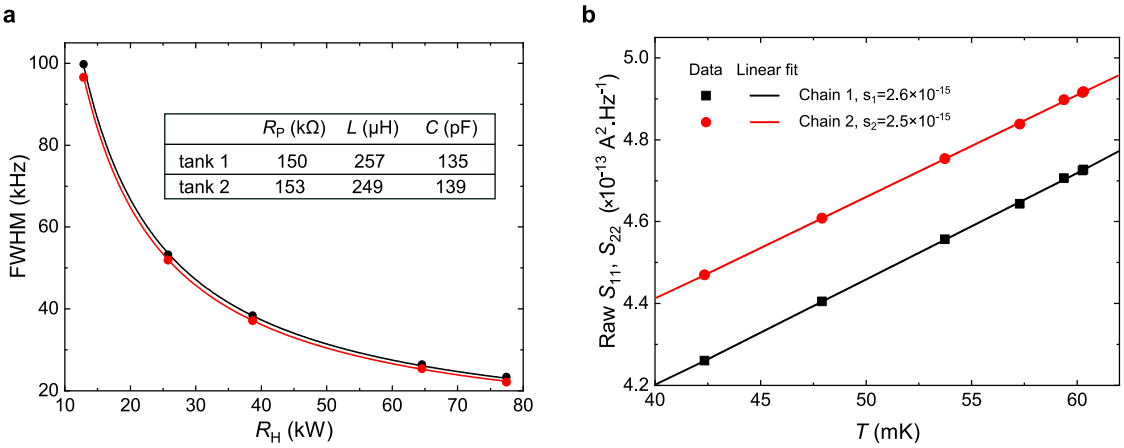

Figure A.4: **HEMT calibration at** $\nu = 2$
a Tank circuits characterization. Full Width at Half Maximum (FWHM) of the measured tank resonance in the noise signal, versus $R_{\rm H}$. Black (red) dots corresponds to tank 1 (2) measured at known $R_{\rm H}$ ($\nu \in \{2, 1, 2/3, 2/5, 1/3\}$). Solid lines display $1/2\pi CR$, with $1/R \equiv 1/R_{\rm H} + 1/R_{\rm P}$.
b HEMT gain calibration. Raw auto-correlation noise is plotted versus the temperature measured with a RuO_2 thermometer. The slopes $s_{1(2)}$ from linear fits of data from tank 1 (2) displayed as black (red) symbols allow us to calculate the gain $G_{1(2)}^{\rm eff}$ via Eq. (A.3)

In a second step, given our fixed choice of integration bandwidth (which impacts $G^{\text{eff}}_{1,2,12}$), the raw integrated noise is measured at different temperatures T_{RuO2} >40 mK given by a RuO_2 thermometer thermally anchored to the mixing chamber and pre-calibrated. The result in the representative case $\nu = 2$ is plotted in Fig. A.4b. The fluctuation-dissipation relation gives:

$$G^{\text{eff}}_{1,2} = \frac{s_{1,2}}{4k_{\text{B}}(1/R_{\text{P}}^{1,2} + 1/R_{\text{H}})}, \tag{A.3}$$

with $s_{1(2)}$ the temperature slope of the raw integrated noise on measurement port 1(2) (see fit in Fig. A.4b), and $R_{\text{P}}^{1(2)}$ the effective parallel resistance describing the dissipation in the corresponding tank circuit.

Note that the cross-correlation gain G^{eff}_{12} can be reduced by an imperfect matching between the tanks. But in our case, this reduction is negligible ($< 0.5\%$) and $G^{\text{eff}}_{12} \simeq \sqrt{G^{\text{eff}}_1 G^{\text{eff}}_2}$.

Besides, we checked that the above calibrations at $\nu = 1/3$ and $\nu = 2$ (where the relative impact of R_{P} is reduced) matched. Indeed, using the simple RLC model of the tank circuits as recapitulated in the table in Fig. A.4a, the $\nu = 2$ calibration can be converted into $G^{\text{eff}}_{1,2}$ at $\nu = 1/3$ taking into account the different integration bandwidth and R_{H}. This control procedure gave an accuracy better than 7%.

A.3 Thermometry

The temperatures of electrons in the sample at $T > 40\,\text{mK}$ are obtained from a calibrated RuO_2 thermometer thermally anchored to the mixing chamber of the fridge. As mentioned in the previous section, in this range, the thermal noise varies linearly with the RuO_2 temperature. This validates both the high-quality thermalization of electrons in the device with the mixing chamber and the calibration of the RuO_2 probe. At $T \leq 40\,\text{mK}$, the known robust linear dependence of $S(T)$ (see Fig. A.4b) is used to extrapolate from the measured noise slope in the other range.

The two amplification chains gave consistent temperatures.

Appendix B

Analytic shot noise expression in the FQHE

In the following, we present insights concerning the intriguing shape of shot noise thermal rounding observed when QPC_c is directly biased.

B.1 Experimental discrepancy with the standard shot noise formula

For a single QPC of transmission ratio τ biased by a dc voltage V (see Fig. B.1) the standard shot noise expression has been derived for non-interacting fermions in the Landauer-Büttiker framework [25]:

$$S_{\rm sn} = 2e\frac{\tau(1-\tau)V}{R_{\rm H}}\left[\coth\frac{eV}{2k_{\rm B}T} - \frac{2k_{\rm B}T}{eV}\right] \tag{B.1}$$

Therefore, this prediction is a priori not valid for FQH states described by Luttinger liquid theory. However, it has been phenomenologically used for decades in FQH states by experimentalists to characterize the charges of a quasiparticle tunneling across a QPC set in the WBS regime, just by replacing e with e^*. Indeed, in the Poissonian regime $(1-\tau) \ll 1$ and in the limit $T \to 0$ K, this prediction reduces to $S_{\rm sn} = 2e^* I_{\rm T}$ (with $I_{\rm T} = (1-\tau)V/R_{\rm H}$ the tunneling current through the bulk and e^* the charge of the tunneling quasiparticles, equal to νe for Laughlin's fractions).

This shows that, at high voltage compared to $k_{\rm B}T/e^*$, the slope is sufficient to characterize the charge of the tunneling quasiparticle. This is the criterion used in this Ph.D. work, for which we especially need to ascertain the value of the charge impinging on the analyzer QPC.

Nonetheless, as mentioned in Chapters 3 and 4 deviations with this prediction have been observed during our measurements [1]. Let us focus on the simplest $\nu = 1/3$ case at $T = 35$ mK. In the WBS regime, while the source QPCs were always in good agreement with Eq. (B.1), the central QPC_c direct shot noise measurement (in the configuration illustrated in Fig. B.1a) presented a high voltage slope compatible with the expected charges but also an intriguing shape in the thermal rounding region (see symbols in Fig. B.1b). Besides, the gate voltages required to deplete the 2DEG at QPC_c were significantly larger than the source one. We

[1] Note that the electronic temperature T is separately determined, as specified in Appendix A

attributed these specificities of QPC_c to its different orientation with respect to the crystalline structure [2], which could result in different strain from the metallic gates because of thermal contraction. Note that such shapes have also been measured in other laboratories (see e.g. Fig. 3.23 in Ref. [131]).

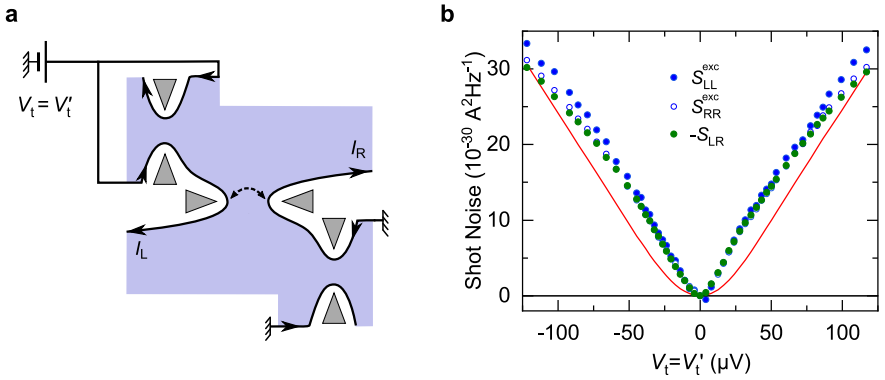

Figure B.1: **Shot noise measurement on directly biased QPC_c in the WBS regime at $\nu = 1/3$**
a Setup configuration for QPC_c tunneling charge characterization. The same voltage $V_t = V_t'$ is applied on both sides of the upstream source QPC so the central QPC_c is directly biased.
b Cross (S_{LR}) and excess auto-correlations ($S^{exc}_{LL,RR}$) shot noise are plotted versus the applied voltage $V_t = V_{t'}$. Red continuous line displays predictions of Eq. (B.1) with $e^* = e/3$ at $T = 35$ mK

Even though it does not change our conclusions because the charges of impinging quasiparticles are well established, this intriguing feature calls for a deeper investigation.

B.2 A recent prediction to probe the scaling dimension

Recently, a complete derivation of shot noise at a QPC in the fractional quantum Hall edge framework was performed by Schiller *et al.* [65, 161]. For a single QPC set in the WBS regime and biased by a DC voltage V, the shot noise is predicted to be:

$$S_{sn} = 2e^* I_T \left[\frac{2}{\pi}\mathrm{Im}\left(\psi\left(2\Delta + i\frac{e^*V}{2\pi k_B T}\right)\right)\right], \tag{B.2}$$

where $I_T = (1-\tau)V/R_H$ is the tunneling current across the QPC and Δ is the scaling dimension characteristic of the edge channel (see Sec. 2.4.6). ψ is the so-called *digamma function*, i.e. the logarithmic derivative of the Euler's gamma function[3] $\psi = \Gamma'/\Gamma$. Note that this prediction has been specifically derived in the WBS regime but in the following, it will be naively extended beyond this regime by applying the multiplicative factor τ:

$$S_{sn} = 2e^* \tau I_T \left[\frac{2}{\pi}\mathrm{Im}\left(\psi\left(2\Delta + i\frac{e^*V}{2\pi k_B T}\right)\right)\right] \tag{B.3}$$

[2] QPC_c is aligned with the primary axis of the GaAs wafer and the sources are orthogonal to QPC_c
[3] defined on $\mathbb{C}$ by $\Gamma(z) = \int_0^\infty t^{z-1}e^{-t}dt$

While this result reduces to Eq. (B.1) in the case of electrons ($e^* = e$ and $\Delta = 1/2$), the two formula are in significant contrast in other cases. Fig. B.2 displays the phenomenological formula and the recently derived prediction for the Laughlin's case $\nu = 1/3$ ($e^* = e/3$, $\Delta = 1/6$). Note that the slopes at large I_T are the same.

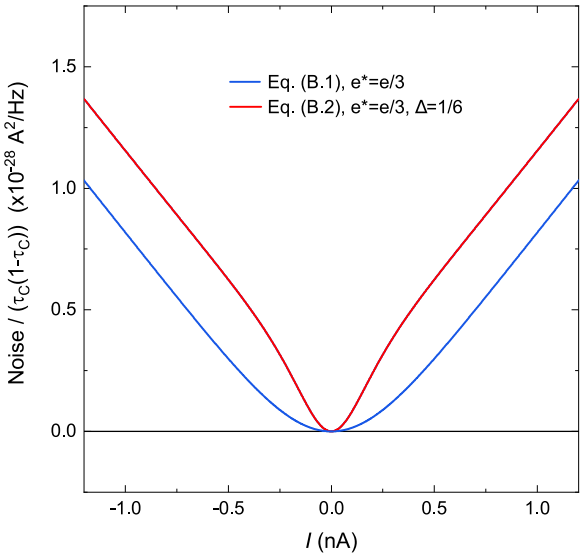

Figure B.2: **Comparison between the two shot noise formula**
Red and blue continuous line respectively display predictions of Eq. (B.1) and (B.2) renormalized by $\tau_c(1-\tau c)$ and at $T = 35$ mK

Therefore, this prediction could explain the observed discrepancy in our system. Note that, knowing the value of the tunneling charge e^* with a linear fit at high voltage, adjusting data to this formula (especially in the thermal rounded part) gives a way to directly infer the scaling dimension Δ in this simple setup made of one single dc-biased QPC.

B.3 Comparison of this prediction with the QPC_c direct shot noise measurement

In Fig. B.3a, we show an illustrative example at $\nu = 1/3$ of the shot noise resulting from the central QPC_c biased by a direct voltage V (dots) and the prediction of Eq. (B.3) without fit parameter (black dashed line). Linear fits performed at $|V|$ >30 µV (for positive and negative voltages), give a tunneling charge $e^*_{\rm fit} \simeq 0.26 \times e$. The purple line displays a nonlinear fit obtained with this fixed $e^*_{\rm fit}$ and with Δ as a single fit parameter. The obtained value of the scaling dimension in this illustrative example is $\Delta = 0.11$, reasonably close to the theoretical value 1/6. The Red dashed line indicates the phenomenological formula (B.1).

In contrast, Fig. B.3b displays an illustrative example of the source noise S_Σ obtained when the left source QPC_L is the directly biased[4]. A linear fit on the slope at high current I_T gives $e^* \sim 0.3e$. It shows a better matching of data with the phenomenological formula (B.1) than the recent analytical prediction Eq. (B.3). Then, the sources seem to exhibit a thermal rounding in disagreement with theory (note that this better matching with Eq. (B.1) is usual in

[4]the right source gave comparable results

experiments). As previously mentioned, this could be linked to a difference in QPC orientations with the crystalline structure.

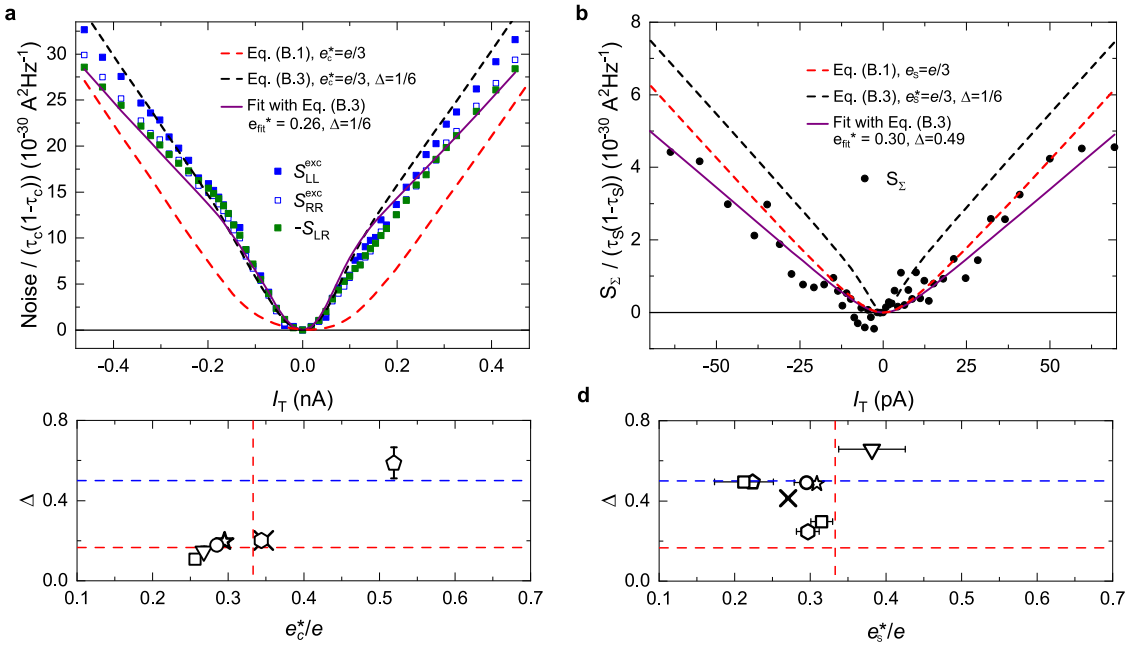

Figure B.3: **Comparison of data with the prediction of [65]**
a (b) QPC_c (QPC_S) shot noise when directly biased versus the tunneling current. Full blue, open blue, and full green (full black) symbols respectively display the signals S_{LL}^{exc},S_{RR}^{exc} and S_{LR} (S_Σ). Dashed lines displays Eq. (B.1) (red) and (B.3) (black) for the corresponding transmissions at $e^* = e/3$, $\Delta = 1/6$ and $T = 35$ mK. The purple line fits data with Eq. (B.3) where Δ is used as a non-linear fit parameter, e^* being fixed to the slope value.
c (d) Fit values of Δ plotted versus the charge $e^*_{c(S)}$ (obtained by an independent linear fit at high voltage) for all the operating points of transmissions greater than 0.6. The red dashed lines display the theoretical values of $e^* = e/3$ (vertical) and $\Delta = 1/6$ (horizontal). The horizontal dashed line indicates $\Delta = 1/2$ (corresponding to the phenomenological expression of Eq. (B.1)

Similar measurements were attempted in the SBS regime but the strong variations of the transmissions impeded solid conclusions.

Figure B.3c (d) synthesizes the values of e^* (from linear fits in the high voltage range) and Δ (from distinct fit) when QPC_c (QPC_L) is directly biased, obtained from all the explored operating points in the regime $\tau \geq 0.6$. The symbols match with the one used along Chap. 4. When greater than the symbol size, we plot error bars corresponding to the difference between measurements at negative and positive voltages (horizontal) and the standard deviation resulting from the fit over the three noise signals S_{LL}^{exc}, S_{RR}^{exc} and S_{LR} (vertical). The dashed lines indicate the respective theoretical values for $e^* = e/3$ (vertical) and $\Delta = 1/6$ (horizontal).

On the one hand, in the case of QPC_c (panel c), the correspondence between an impinging charge $e^* = e/3$ and a scaling dimension $\Delta = 1/6$ seems corroborated by these measurements, with experimental data in the vicinity of the ($e/3$, $1/6$) point. On the other hand, in the case of QPC_L (panel c), the experimental points are further from the point ($e/3$, $1/6$): while the

charge is reasonably close to $e/3$, the fitted scaling dimensions are mostly close to $\Delta = 1/2$, which is consistent with a better matching with the phenomenological formula (B.1).

B.4 Conclusion and outlook

The recent theoretical predictions are in good agreement with the observed intriguing thermal rounding in our experimental data at $\nu = 1/3$. It also gives first strong hints that a single QPC could be used to measure the scaling dimension of a FQH edge. However, the difference between the source and the central QPC prevents us from giving clear conclusions. Exploring such single QPC systems with several orientations, different temperatures, different scaling factors, and with an ALD deposed HfO_2 layer to avoid strains will be the objective of a future experiment.

Appendix C

Articles published during this thesis

The first article focuses on the Andreev-like scattering process presented in Chapter 3.

Title: Quasiparticles Andreev scattering in the $\nu = 1/3$ fractional quantum Hall effect

Co-authors: Pierre GLIDIC, Olivier MAILLET, Colin PIQUARD, Abdelhanin AASSIME, Antonnella CAVANA, Yong JIN, Ulf GENNSER Anne ANTHORE, Frédéric PIERRE

Status: Published

Journal: Nature Communications

Year: 2023

nature communications

Article

https://doi.org/10.1038/s41467-023-36080-4

Quasiparticle Andreev scattering in the $\nu = 1/3$ fractional quantum Hall regime

Received: 14 June 2022

Accepted: 12 January 2023

Published online: 31 January 2023

Check for updates

P. Glidic[1,3], O. Maillet[1,3], C. Piquard[1], A. Aassime[1], A. Cavanna[1], Y. Jin[1], U. Gennser[1], A. Anthore[1,2] ✉ & F. Pierre[1] ✉

The scattering of exotic quasiparticles may follow different rules than electrons. In the fractional quantum Hall regime, a quantum point contact (QPC) provides a source of quasiparticles with field effect selectable charges and statistics, which can be scattered on an 'analyzer' QPC to investigate these rules. Remarkably, for incident quasiparticles dissimilar to those naturally transmitted across the analyzer, electrical conduction conserves neither the nature nor the number of the quasiparticles. In contrast with standard elastic scattering, theory predicts the emergence of a mechanism akin to the Andreev reflection at a normal-superconductor interface. Here, we observe the predicted Andreev-like reflection of an $e/3$ quasiparticle into a $-2e/3$ hole accompanied by the transmission of an e quasielectron. Combining shot noise and cross-correlation measurements, we independently determine the charge of the different particles and ascertain the coincidence of quasielectron and fractional hole. The present work advances our understanding on the unconventional behavior of fractional quasiparticles, with implications toward the generation of novel quasi-particles/holes and non-local entanglements.

How do exotic quasiparticles modify when one tries to manipulate them? A conventional free electron incident upon a local barrier can be either elastically transmitted or reflected with different probability amplitudes, matching a beam splitter behavior with electron quantum optics applications[1]. However, this simple picture may be drastically altered with unconventional quasiparticles, such as the emblematic anyons in the fractional quantum Hall (FQH) regime[2]. Fractional quasiparticles could undergo markedly different transmission mechanisms across a barrier, where the number and even the nature of the quasiparticles may change. Such behaviors emerge when the barrier is set to favor the transmission of a type of particles that is different from the incident ones. This is specifically expected in the fractional quantum Hall regime at filling factor $\nu = (2n+1)^{-1}$ ($n \in \mathbb{N}$), when individual quasiparticles of charge νe are impinging on an opaque barrier transmitting quasielectrons of charge e. In a dilute beam, where no multiple quasiparticles are readily available for bunching into a quasielectron, theory predicts that the missing $(1-\nu)e$ can be supplied in an Andreev-like scenario involving the correlated reflection of $a-(1-\nu)e$ quasihole[3]. This can also be seen as the quasiparticle transmission coinciding with the excitation of $(1/\nu-1)\nu e$ quasiparticle-quasihole pairs split between the two outputs (see Fig. 1a for an illustration at $\nu = 1/3$).

A versatile investigation platform is realized by two quantum point contacts (QPC) in series along a fractional quantum Hall edge channel, combined with noise characterizations[4–9]. The first QPC here implements a source of dilute quasiparticles, impinging one at a time on the second 'analyzer' QPC playing the role of the barrier.

We presently investigate at $\nu = 1/3$ such Andreev-like behavior schematically illustrated in Fig. 1a,b. Fractional quasiparticles of charge $e/3$ are separately emitted at the upstream source QPC, which is set to this aim in the so-called weak back-scattering (WBS) regime[3,10,11] and submitted to a voltage bias. After propagating along a short chiral edge path, the quasiparticles individually arrive at the analyzer QPC set in the opposite strong back-scattering (SBS) regime that favors the

[1]Université Paris-Saclay, CNRS, Centre de Nanosciences et de Nanotechnologies, 91120 Palaiseau, France. [2]Université Paris Cité, CNRS, Centre de Nanosciences et de Nanotechnologies, F-91120 Palaiseau, France. [3]These authors contributed equally: P. Glidic, O. Maillet.
✉e-mail: anne.anthore@c2n.upsaclay.fr; frederic.pierre@cnrs.fr

https://doi.org/10.1038/s41467-023-36080-4

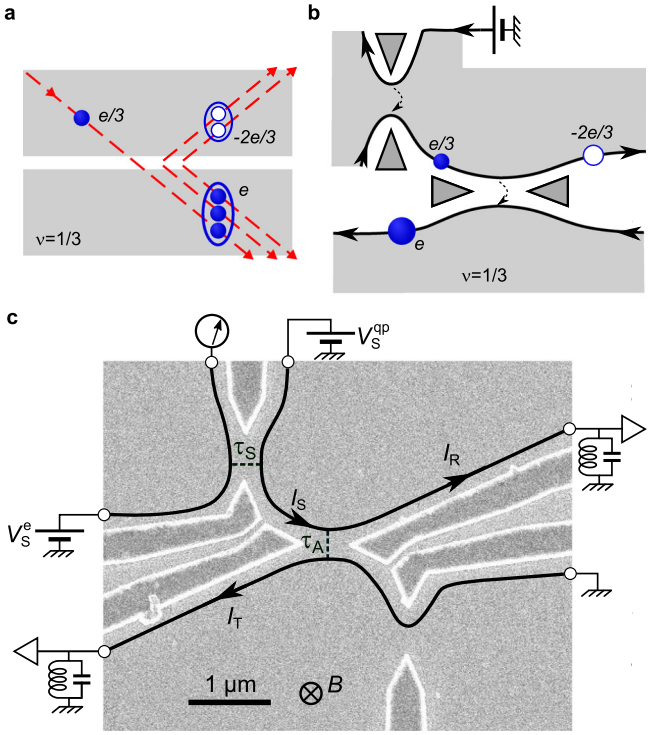

Fig. 1 | Quasiparticle Andreev reflection in a source-analyzer setup at $\nu = 1/3$. **a** Andreev mechanism. An incident $e/3$ quasiparticle is transmitted as an e quasielectron and Andreev reflected as a $-2e/3$ quasihole. The Andreev process can be pictured as the excitation of two $e/3$ quasiparticle-quasihole pairs and the incident quasiparticle bunching together. **b** Setup schematic in Andreev reflection configuration. The top-left `source' QPC is set in the weak back-scattering (WBS) regime and voltage biased from the top to emit $e/3$ quasiparticles toward the central `analyzer' QPC. The latter is tuned in the strong back-scattering (SBS) regime favoring the transmission of quasielectrons. **c**, Electron micrograph of the measured Ga(Al)As device. The current propagates along chiral edge channels shown as black lines. The gate defined QPCs are tuned by field effect. The source is biased with V_S^{qp} at $V_S^e = 0$ and $1 - \tau_S \ll 1$ (V_S^e at $V_S^{qp} = 0$ and $\tau_S \ll 1$) to produce a dilute current of quasiparticles $I_S = (1 - \tau_S)V_S^{qp}/(3h/e^2)$ (of quasielectrons $I_S = \tau_S V_S^e/(3h/e^2)$). Setting $V_S^{qp} = V_S^e$ allows for a direct voltage bias of the analyzer.

transmission of quasielectrons[3,10,11]. Whereas for a directly voltage biased QPC in the SBS regime, a quasielectron can be formed from the bunching of three available $e/3$ quasiparticles, we are here in the presence of a single incident quasiparticle that carries only a third of the required electron charge. In principle, individual $e/3$ quasiparticle tunneling could emerge as the dominant process. However, as presently observed, a different scenario akin to Andreev reflection is expected, where the missing $2e/3$ charge is sucked in from the incident edge channel to form the transmitted quasielectron. The incident fractional quasiparticle is effectively converted into a quasielectron and a $-2e/3$ fractional hole.

This mechanism was coined 'Andreev'[3], by analogy with the standard Andreev reflection of an electron into a hole to transmit a Cooper pair across a normal metal-superconductor interface[12]. Note however that the QPC is not here at an interface with a superconductor, nor with a different fractional quantum Hall state (see Refs. [13–15] for another, different kind of Andreev-like reflection at such interfaces submitted to a voltage bias). Furthermore, whereas in a standard Andreev reflection electron and hole excitations have the same energy, here energy conservation imposes that the energy of the incident quasiparticle redistributes between transmitted quasielectron and reflected quasihole. The energy of the reflected quasihole is thus lower than that of the incident quasiparticle. Finally, we point out that the present Andreev-like mechanism takes place in a fully spin-polarized electronic fluid, in contrast with a standard Andreev reflection where two electrons of opposite spins are combined to form a spin-singlet Cooper pair.

Experimentally, an earlier source-analyzer investigation appeared to contradict this scenario[16]. Indeed, the transmitted charge was there found to approach $e/3$ across the opaque barrier, identical to the charge of the incident quasiparticles, instead of e for Andreev processes (see Ref. [17] for a follow-up paper that mitigates this conclusion, by the observation of an increase in the transmitted charge as the temperature is reduced). Possibly, the $e/3$ quasiparticles have been altered during the very long propagation distance of ~100 μm between source and analyzer QPCs. Here, with a short 1.5 μm path (see Fig. 1c), we recover the predicted transmitted charge e, three times larger than the simultaneously determined charge of the incident quasiparticles. Moreover, we directly observe the Andreev correlations between transmitted quasielectron and reflected $-2e/3$ fractional hole, through the revealing measurement of the current cross-correlations between the two outputs of the analyzer QPC.

Results

Device and setup

The measured sample is shown in Fig. 1c (see Methods for large-scale pictures). It is patterned on a high-mobility Ga(Al)As two-dimensional electron gas (2DEG) of density 1.2×10^{11} cm^{-2}. The device is cooled at a temperature $T \approx 35$ mK (see Methods for supplementary data at $T \approx 15$ and 60 mK), and immersed in a perpendicular magnetic field $B \approx 13.5$ T near the center of a 2 T wide quantum Hall resistance plateau $R_H = 3h/e^2$ ($\nu = 1/3$). In this FQH regime, the electrical current propagates along each edge in a single chiral channel, as schematically depicted by black lines with arrows in Fig. 1b,c (see Methods for tests of this picture). These edge channels are measured and biased through large ohmic contacts of negligible resistance located 150 μm away from the central part (symbolized as open black circles, see Methods for the actual shape). The heart of the device is composed of two active QPCs (out of three nanofabricated ones) separately tuned by field effect with the voltages applied to the corresponding aluminum split gates deposited at the surface (darker areas with bright edges). The top-left QPC (or, alternatively, the bottom-right QPC) plays the role of the quasiparticle source, whereas the central QPC is the downstream analyzer. The auto- and cross-correlations of the currents I_T and I_R emitted from the analyzer QPC are capital for the separate tunneling charge characterization across source and analyzer, as well as for providing direct signatures of Andreev processes. They are measured using homemade cryogenic amplifiers[18,19], in a 40 kHz bandwidth centered on the resonant frequency 0.86 MHz of essentially identical tank circuits along the two amplification chains.

Quantum point contact characterization

We first determine the characteristic tunneling charges across the source and analyzer through standard shot noise measurements[20–22], involving a direct voltage bias of the considered QPC (as opposed to a dilute beam of quasiparticles, see below). For the analyzer, such characterization must therefore be performed in a specific measurement, distinct from the observation of Andreev processes. This is achieved without changing any gate voltages susceptible to impact the analyzer's tuning, by using the same bias voltage for the two input channels of the source QPC ($V_S^{qp} = V_S^e$, see Fig. 1c). In the present work, the analyzer QPC is set in the SBS regime, i.e. with a low transmission ratio $\tau_A \equiv I_T/I_S$ for which theory predicts the transmission of quasielectrons[10,11]. Accordingly, we focus here on tunings of the analyzer displaying this canonical behavior, such as shown in Fig. 2b. The filled (open) blue circles display the measured excess transmitted (reflected) noise $\langle \delta I^2_{T(R)} \rangle_{exc} \equiv \langle \delta I^2_{T(R)} \rangle (V_S^{qp} = V_S^e) - \langle \delta I^2_{T(R)} \rangle (0)$ versus bias

https://doi.org/10.1038/s41467-023-36080-4

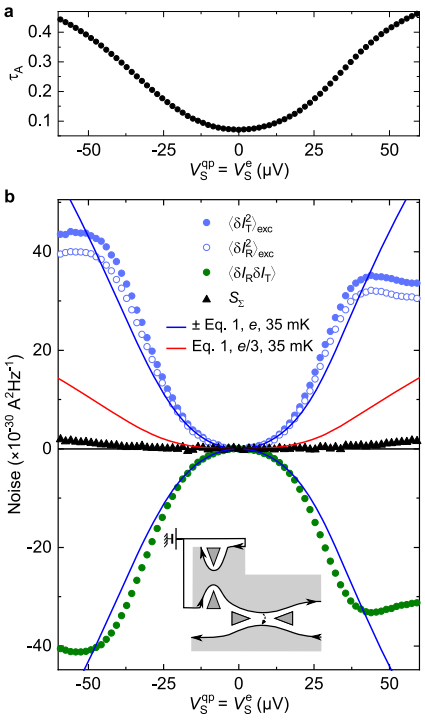

Fig. 2 | Characterization of analyzer QPC, from transmission (a) and noise (b) vs direct voltage bias $V_S^{qp} = V_S^e$. a Transmission ratio $\tau_A \equiv I_T/I_S$. **b** Measurements of the auto- and cross-correlations of the transmitted (I_T) and reflected (I_R) currents are shown as symbols. For small enough $\tau_A \lesssim 0.3$ ($|V_S^{qp}| < 35\,\mu$V, see (**a**)), the different noise signals corroborate the expected tunneling charge e (blue lines) in marked difference with $e/3$ predictions (red line). At higher $\tau_A \gtrsim 0.3$, the relatively smaller noise is consistent with the onset of the expected transition toward $e/3$. The noise sum $S_\Sigma \equiv \langle \delta I_T^2 \rangle_{exc} + \langle \delta I_R^2 \rangle_{exc} + 2\langle \delta I_T \delta I_R \rangle$, corresponding to the excess shot noise across the presently unbiased source, remains essentially null.

voltage. The tunneling charge e^* is determined by comparing with the standard shot noise expression[22,23]:

$$S_{sn} = 2e^* \frac{\tau(1-\tau)V}{R_H}\left[\coth\frac{e^*V}{2k_BT} - \frac{2k_BT}{e^*V}\right], \quad (1)$$

with τ the ratio of transmitted over incident dc currents. The positive blue and red continuous lines display the predictions of Eq. (1) for $e^* = e$ and $e/3$, respectively, at $T = 35$ mK and using the simultaneously measured τ_A shown in Fig. 2a. The negative blue line shows $-S_{sn}$ for $e^* = e$. Note that τ_A strongly increases with the applied bias voltage, which also usually drives a transition from $e^* = e$ (at $\tau_A \ll 1$) to $e/3$ (at $1 - \tau_A \ll 1$)[10,11,24]. Correspondingly, an agreement is here found with $e^* = e$ only at low enough bias voltages ($|V| < 35\,\mu$V), for which τ_A is not too large ($\tau_A \lesssim 0.3$). An important experimental check consists in confronting $\langle \delta I_T^2 \rangle_{exc}$ with both the reflected excess noise $\langle \delta I_R^2 \rangle_{exc}$ and the possibly more robust cross-correlation signal[25] $\langle \delta I_T \delta I_R \rangle$. We find that the three measurements match each other, within the experimental gain calibration accuracy (Methods), thereby corroborating the extracted value of e^*. Equivalently, the sum $S_\Sigma \equiv \langle \delta I_T^2 \rangle_{exc} + \langle \delta I_R^2 \rangle_{exc} + 2\langle \delta I_T \delta I_R \rangle$ (black symbols) mostly does not depend on bias voltage, as expected in the absence of shot noise across the upstream source QPC. Indeed, local charge conservation and the chirality of electrical current directly imply the identity $S_\Sigma = \langle \delta I_S^2 \rangle_{exc}$, independently of the downstream analyzer (the weak positive S_Σ that can be seen at large bias is in fact a small noise induced at the source, see Methods). In the source-analyzer configuration, this identity will be essential for the characterization of the tunneling charge across the source QPC simultaneously with the measurement of the main cross-correlation signal, by confronting S_Σ with Eq. (1) (see Fig. 3a,b, and also Methods)[26].

Observation of Andreev-like reflection of fractional quasiparticles

The source is now activated with the device set in the regime where Andreev reflections are predicted, and direct signatures of this process are observed. For this purpose, the source QPC is tuned in the WBS regime and biased through V_S^{qp} ($V_S^e = 0$). As shown in Fig. 3a, the backscattering probability $1 - \tau_S = I_S R_H / V_S^{qp}$ (inset) remains very small (<0.05), and S_Σ (symbols in main panel) matches the prediction of Eq. (1) for $e^* = e/3$ using $T = 35$ mK (red line). As a side note, we point out the decrease of τ_S with I_S and thus the applied bias, which although not expected theoretically[11,27] is frequently observed experimentally at high transmission (see Methods and e.g. ref. [28]).

With the upstream generation of a highly dilute beam of $e/3$ quasiparticles established, we turn to the characterization of the transport mechanism across the downstream analyzer kept in the SBS regime previously characterized. The blue symbols in Fig. 3c display the measured excess shot noise on the current transmitted across the analyzer $\langle \delta I_T^2 \rangle_{exc}$, over a range of I_T corresponding to that of I_S in panel (a) ($I_T = \tau_A I_S$, see inset for τ_A). The shot noise data closely follow the slope of $2e|I_T|$ (dashed blue line at $|I_T| > 1$ pA) denoting the Poissonian transfer of $1e$ charges, different from the $e/3$ charge of the incident quasiparticles. This corresponds to Andreev processes, in marked contrast with the slope of $2(e/3)|I_T|$ (dashed red line) approached in the dilute beam limit in the pioneer experiment ref. [16], and consistent with the different trend described in the follow-up article ref. [17]. Note that the small thermal rounding, at $|I_T| < 1$ pA, matches the displayed generalization of Eq. (1) where we used the source bias voltage (V_S^{qp}) and tunneling charge ($e/3$) in the e^*V/k_BT ratios (see Eq. (5) in Methods).

As emphasized in ref. [3], a key feature of Andreev processes is that the transmitted and reflected currents are correlated, for which the measurement of $\langle \delta I_R \delta I_T \rangle$ provides an unambiguous signature. Since the Andreev transfer of a charge e is associated with the reflection of a charge $-2e/3$, theory predicts the straightforward connection[3]:

$$\langle \delta I_R \delta I_T \rangle = -(2/3)\langle \delta I_T^2 \rangle_{exc}, \quad (2)$$

where the factor of $-2/3$ directly corresponds to the ratio between tunneling and reflected charges. Accordingly, the slope of $-(2/3)2e|I_T|$ (dashed black line at $|I_T| > 1$ pA) is compared in Fig. 3c with the measurements of $\langle \delta I_R \delta I_T \rangle$ shown as green symbols. The observed quantitative match most directly attests of the underlying Andreev-like mechanism (see Methods for different device tunings and temperatures).

Noise signal with incident quasielectrons

An instructive counterpoint, clarifying the specificity of the above Andreev signatures, is obtained by tuning the source QPC in the SBS regime with a tunneling charge $e^* = e$. In this configuration, the source is voltage biased by V_S^e (with $V_S^{qp} = 0$). As shown in Fig. 3b, the source shot noise obtained from S_Σ follows the prediction of Eq. (1) for $e^* = e$ and $T = 35$ mK (blue line) as long as the transmission remains low enough ($\tau_S \lesssim 0.3$). Noise data points displayed as full (open) symbols in Fig. 3b, d correspond to $\tau_S < 0.3$ ($\tau_S > 0.3$). Whereas $\langle \delta I_T^2 \rangle_{exc} \approx 2e|I_T|$ indicates the same $1e$ tunneling charge across the analyzer as in the previously discussed Andreev regime, it here also trivially corresponds to the charge of the incident particles. In marked contrast to Andreev processes, the cross-correlations $\langle \delta I_R \delta I_T \rangle$ are no longer negative, but relatively small and positive. The continuous blue and green lines in (d) display the predictions for non-interacting electrons at $T = 35$ mK (see Eqs. (6) and (7) in Methods). While no signal would be expected in the Poisson limit, note the prediction of appreciable negative cross-correlations (green line). This results from the rapidly growing τ_S (see

https://doi.org/10.1038/s41467-023-36080-4

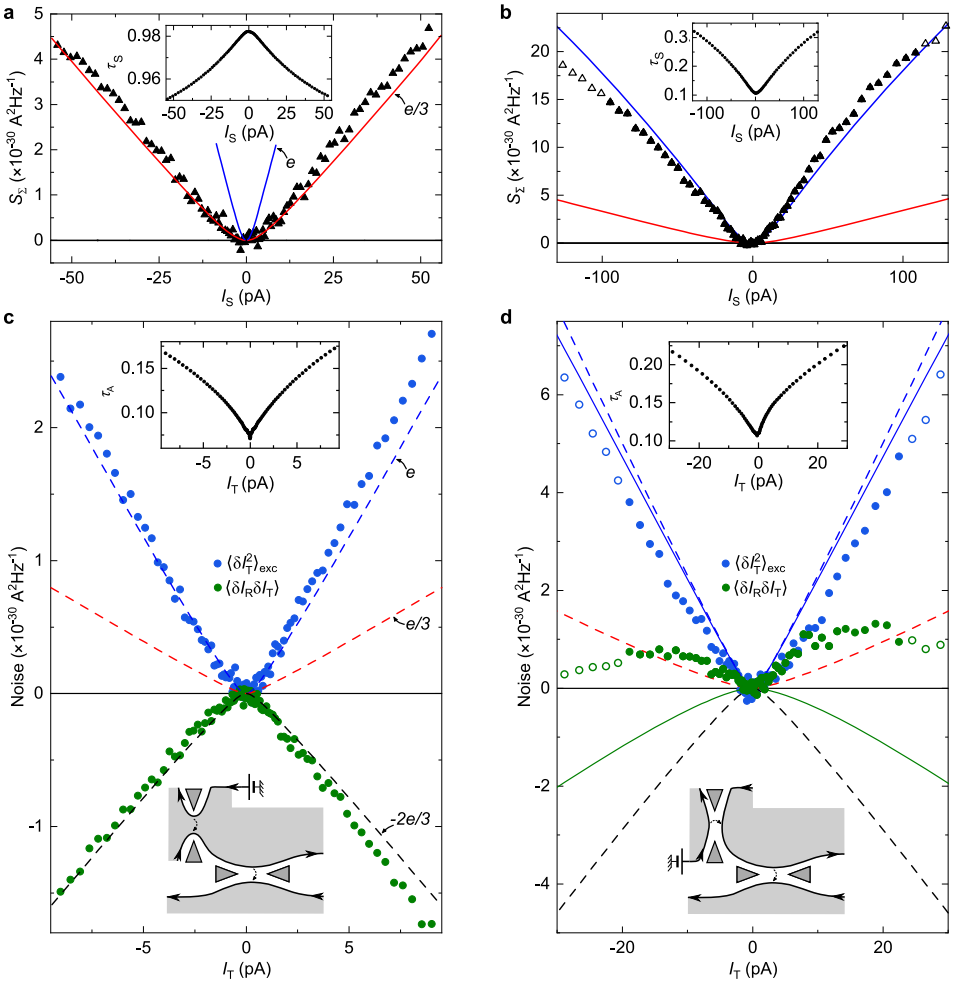

Fig. 3 | Noise observation of Andreev reflection. a, b Simultaneous characterization of the source set in the WBS (**a**) or SBS (**b**) regime (see illustrative bottom inset in (**c**) or (**d**), respectively). Continuous blue and red lines represent the shot noise predictions of Eq. (1) for tunnelings of charge e and $e/3$, respectively, using the measured transmission ratio τ_S across the source QPC (inset) and $T = 35$ mK. Symbols display measurements of S_Σ, corresponding to the shot noise across the source. **c, d** Transport mechanism across the analyzer with incident fractional quasiparticles (**c**, using the WBS source shown in (**a**)) or incident quasielectrons (**d**, using the SBS source shown in (**b**)). The simultaneous measurements of $\tau_A \lesssim 0.2$ are shown in the respective top insets (note the higher noise at low I_T due to the reduced signal). Blue and green symbols in the main panels show, respectively, the excess auto-correlations of the transmitted current and the cross-correlations between transmitted and reflected currents. Open symbols in panels (**b**) and (**d**) correspond to data with $\tau_S \geq 0.3$, for which the source notably deviates from the SBS regime. Dashed blue, red and black lines represent, respectively, a $1e$ shot noise, a $e/3$ shot noise and $-(2/3)$ times the $1e$ shot noise all in the dilute incident beam limit. Continuous lines in (**d**) display the noninteracting electrons' predictions valid at any $\tau_{A,S}$ for $\langle\delta I_T^2\rangle$ (blue) and $\langle\delta I_R\delta I_T\rangle$ (green), calculated using the measured $\tau_{A,S}$ (see Eqs. (6) and (7) in Methods).

inset of Fig. 3b), which makes it difficult to remain well within the dilute incident beam regime. Whereas the observed positive cross-correlations are not accounted for, suggesting that the role of interactions cannot be ignored (see ref. [29] for positive cross-correlations predicted in the different case of multiple copropagating channels), the contrast with the Andreev signal given by Eq. (2) (dashed black line) is even more striking.

Additivity of Andreev cross-correlations from opposite sources

Recently, it was predicted and observed that negative cross-correlations can also develop with dilute incident quasiparticles when both source and analyzer QPCs are set in the same WBS limit[8,26]. This results from the non-trivial braid (double exchange) phase of $2\pi/3$ between $e/3$ quasiparticles[8,30,31], in contrast with the braid phase between quasielectrons and $e/3$ anyons, which has the trivial value 2π, and thus plays no role in Andreev processes (with the analyzer QPC in the SBS limit)[32,33]. We will now show that, beside the fact that they take place in different regimes, exchange-driven and Andreev-like mechanisms can be qualitatively distinguished by using a second source QPC feeding the same analyzer from the opposite side (bottom-right QPC in Fig. 1c, see schematics in Fig. 4). Indeed, in the exchange-driven tunneling mechanism, each incident quasiparticle leaves behind a trace that affects the tunneling current contribution of the following ones, including in the limit of highly dilute incident beams[2,8,30,31,34]. Specifically, quasiparticles from opposite sources are associated with anyons braiding processes of opposite winding directions that cancel each other (if within a small enough time window) in the relevant total braid phase[30,31]. This results in a dependence of the exchange-driven mechanism on the symmetry between sources. In the language of refs. [8,26], the normalized cross-correlation slope ('P') is reduced by a factor of $\simeq$1.5 with two symmetric sources. In contrast, the successive Andreev tunnelings are predicted to be independent in the limit of highly diluted incident beams[3]. Consequently, the cross-correlation contributions from the two sources on opposite sides should here simply add up. This distinctive property is demonstrated in Fig. 4. The black symbols display the cross-correlations measured in the presence of two nearly symmetrical diluted beams of $e/3$ quasiparticles impinging on the central analyzer QPC set in the SBS regime.

https://doi.org/10.1038/s41467-023-36080-4

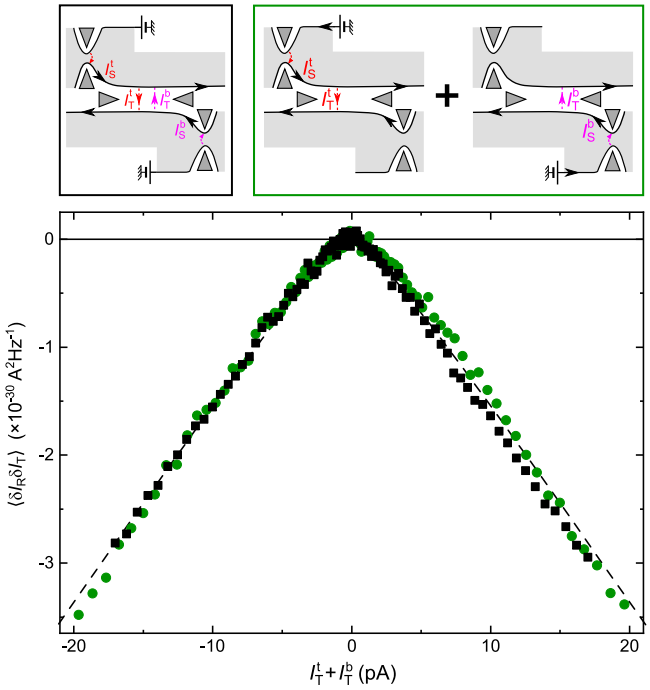

Fig. 4 | Additivity of Andreev cross-correlations from opposite sources. The black squares represent the cross-correlations measured with two similar beams of $e/3$ quasiparticles impinging from opposite sides on the central QPC set in the SBS regime (see top-left schematic). The green circles display the sum of the cross-correlations measured sequentially, using separately the top-right or bottom-right QPC as a single source (see top-right schematic). The dashed line shows the predicted cross-correlations for Andreev scatterings, independent of the symmetry between opposite sources. This contrasts with another, symmetry-dependent mechanism based on the unconventional anyon exchange phase occurring with both source and analyzer in the WBS regime[8,26].

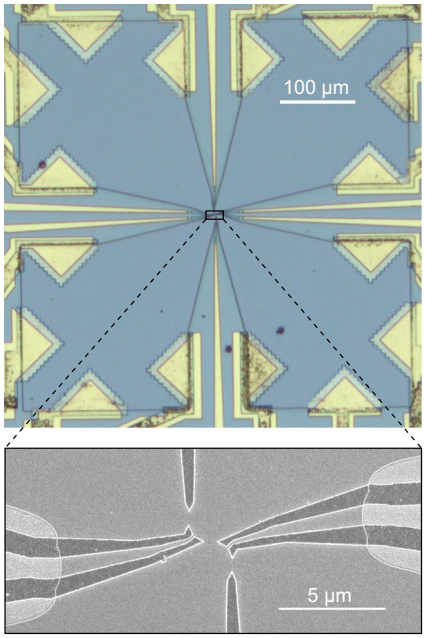

Fig. 5 | Large-scale sample pictures. Optical (top) and SEM (bottom) images of the measured device.

The data is plotted as a function of the sum of the dc tunneling currents originating from the top-left (I_T^t) and bottom-right (I_T^b) source QPCs, separately determined by lock-in techniques. For a first comparison, the same Andreev prediction previously shown in Fig. 3c is displayed as a dashed line, and found in identically good agreement with the measurement in the presence of two sources. For a most straightforward demonstration, the green symbols display the sum of the two separately measured cross-correlation signals when using solely for the source either the top-left QPC or the bottom-right QPC. The matching between green and black symbols directly shows that the contributions of the two sources simply add up, in qualitative difference with predictions[8] and observations[26] for exchange-driven tunneling processes when all the QPCs are set in the WBS regime.

Discussion

The present work investigates the emergence of markedly different transport mechanisms for fractional quasiparticles. In the observed Andreev-like scattering at $\nu = 1/3$, one $e/3$ quasiparticle impinging on a QPC in the SBS regime transforms into a correlated pair made of a transmitted quasielectron and a reflected hole of charge $-2e/3$. In stark contrast with the prominent electron beam splitter picture of QPCs, the number and nature of the quasiparticles are not conserved, with notable implications for envisioned anyonic analogues of quantum optics experiments. Remarkably, the complementary fractional charges of the Andreev-reflected holes might be associated with a distinctive exchange statistics[32,33,35], expanding the range of available exotic quasiparticles for scrutiny and manipulations, and their correlation with the transmitted particle could provides a new knob to generate non-local quantum entanglements. The multiplicity of quasiparticles accessible through the tunings of the fractional filling factor and of the QPCs, suggests that the present observation may generalize into a family of Andreev-like mechanisms, calling for further theoretical and experimental investigations. An illustration at reach is the possible Andreev reflection at $\nu = 2/5$ of an incident $e/5$ quasiparticle into a hole of charge $-2e/15$ and a transmitted $e/3$ quasiparticle.

Methods

Sample

The sample is patterned on a Ga(Al)As heterostructure forming a 2DEG of density $n = 1.2 \times 10^{11}$ cm^{-2} and mobility 1.8×10^6 cm^2 V^{-1}s^{-1} at a depth of 140 nm below the surface. Large-scale pictures are shown in Fig. 5. The mesa is defined by wet etching over a depth of about 100 nm (deeper than the Si δ-doping located 65 nm below the surface), using a protection mask made of a ma-N 2403 positive resist patterned by e-beam lithography and etching the unprotected parts in a solution of $H_3PO_4/H_2O_2/H_2O$. The electrical connection to the buried 2DEG is made through large ohmic contacts, realized by the successive deposition of Ni (10 nm) - Au (10 nm) - Ge (90 nm) - Ni (20 nm) - Au (170 nm) - Ni (40 nm) followed by an annealing at 440°C for 50 s in a ArH atmosphere. The lithographic tip to tip distance of the Al split gates used to define the QPCs is 600 nm.

Experimental setup

The device is operated in a cryofree dilution refrigerator with extensive filtering and thermalization of the electrical lines (see ref. [36] for details). Specific cold *RC* filters are included near the device, located within the same metallic enclosure screwed onto the mixing chamber: 200 kΩ-100 nF for gate lines, 10 kΩ-47 nF for injection lines, 10 kΩ-1 nF for low-frequency measurement lines.

The lock-in measurements are performed at frequencies below 100 Hz, applying an ac modulation of rms amplitude always below k_BT/e. The dc currents I_S and I_T are obtained by integrating with the source bias voltage the corresponding lock-in signal. As an illustrative example, the tunneling current associated with the top-left source (I_T^t) is obtained (separately from the tunneling current I_T^b originating from the bottom-right source when the two sources are used

simultaneously) using:

$$I_T^t(V_S^{qp}) = \int_0^{V_S^{qp}} \frac{\partial I_T}{\partial V_S^{qp}} dV_S^{qp}, \quad (3)$$

where the differential conductance at finite bias voltage is directly given by the lock-in signal measured on port T at the frequency of the ac modulation added to V_S^{qp}.

The auto- and cross-correlation noise measurements are performed using two cryogenic amplifiers (see supplementary material of ref. [19] for details) connected to the T and R ports of the device through closely matched RLC tank circuits of essentially identical resonant frequency ≈ 0.86 MHz (see schematic representation in Fig. 1c). The RLC tanks include home-made superconducting coils of inductance $L_{tk} \approx 250\,\mu$H in parallel with a capacitance $C_{tk} \approx 135$ pF developing along the interconnect coaxial cables, and an effective resistance $R_{tk} \approx 150\,k\Omega$ (in parallel with R_H) essentially resulting from the resistance of the coaxial cables at the lowest temperature stage of the refrigerator. In practice, we integrate the noise signal for 10 s and perform several consecutive voltage bias sweeps (except for temperature calibration), typically between 2 and 12. The displayed noise data is the mean value of these sweeps for the same biasing conditions. Note that the scatter between nearby points adequately indicates the standard error of the displayed mean separately obtained from the ensemble of averaged noise data points (not shown).

Thermometry

The electronic temperatures at $T > 40$ mK are obtained from a calibrated RuO_2 thermometer thermally anchored to the mixing chamber of the dilution refrigerator. In this range, the thermal noise from the sample is found to change linearly with the RuO_2 temperature (see also gain calibration of the noise amplification chains). This confirms the good thermalization of electrons in the device with the mixing chamber, as well as the calibration of the RuO_2 thermometer. At $T \lesssim 40$ mK, we use the known robust linear dependence of the noise with the electronic temperature to extrapolate from the observed noise slope. The two amplification chains give consistent temperatures, although the difference grows as temperature reduces further away from the calibrated slope, up to 2 mK at the lowest used temperatures $T \approx 15$ mK.

Noise amplification chains calibration

The gain factors $G^{eff}_{T,R,TR}$, between the power spectral density of current fluctuations of interest and the raw auto/cross-correlations, are obtained from the measurement of the equilibrium noise at different temperatures combined with a determination of the tank circuit parameters.

In a first step, we characterize the tank circuits connected to the device contacts labelled T and R. This is achieved through the value of the resonant frequency together with the evolution of the noise bandwidth of the tank in parallel with the known R_H at different filling factors. As a technical note, we mention that correlations between voltage and current noises generated by the cryogenic amplifier can deform the resonance at large R_H and thereby impact the tank parameters extraction. For this purpose, the bandwidth data are taken at sufficiently high temperature ($T \gtrsim 150$ mK) such that these amplifier-induced correlations remain negligible with respect to thermal noise. The obtained tank parameters are summarized in the table within Fig. 6, also showing the fits of the bandwidth vs R_H.

In a second step, for our fixed choice of noise integration bandwidth [0.84, 0.88] MHz (which impacts $G^{eff}_{T,R,TR}$), the raw integrated noise is measured at different temperatures $T_{RuO2} > 40$ mK given by a pre-calibrated RuO_2 thermometer thermally anchored to the mixing chamber (see Thermometry above). From the fluctuation-dissipation relation, we have:

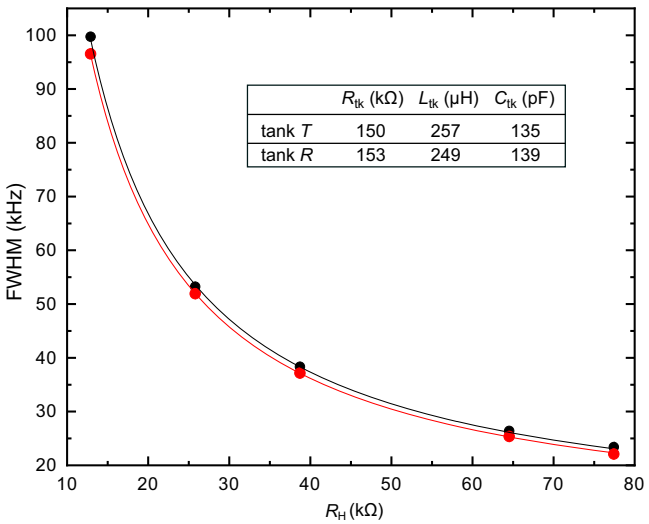

Fig. 6 | Tank circuits characterization. Full Width at Half Maximum (FWHM) of the measured tank resonance in the noise signal, as a function of the sample's resistance R_H. Black (red) dots represent the FWHM of tank T (R) measured with the device set on resistance plateaus of known R_H ($\nu \in \{2, 1, 2/3, 2/5, 1/3\}$). Solid lines show $1/2\pi C_{tk}R$, with $1/R \equiv 1/R_H + 1/R_{tk}$. The values of R_{tk} and C_{tk} used as fit parameters are recapitulated in the table together with the inductances L_{tk} given by the resonant frequencies.

$$G^{eff}_{T,R} = \frac{s_{T,R}}{4k_B\left(1/R^{T,R}_{tk} + 1/R_H\right)}, \quad (4)$$

with $s_{T(R)}$ the temperature slope of the raw integrated noise on measurement port T (R), and $R^{T(R)}_{tk}$ the effective parallel resistance describing the dissipation in the tank circuit connected to the same port. Note that the only required knowledge of the tank is here R_{tk}, whose impact remains relatively small compared to that of R_H even at $\nu = 1/3$. In particular, the relation Eq. (4) does not involve the tank bandwidth nor our choice of frequency range used to integrate the noise signal (although the slopes $s_{T,R}$ depend on these parameters). In contrast, the cross-correlation gain G^{eff}_{TR} can also be reduced by an imperfect matching between the tanks (see e.g. the supplementary material of ref. [26] for a detailed presentation). However, for our tank parameters this reduction is negligible (< 0.5%) and $G^{eff}_{TR} \simeq \sqrt{G^{eff}_T G^{eff}_R}$.

The above main calibration is checked with respect to a thermal calibration at $\nu = 2$ where the relative impact of R_{tk} is reduced. Then, using the simple RLC model of the tank circuits as recapitulated in the table in Fig. 6, the $\nu = 2$ calibration can be converted into $G^{eff}_{T,R}$ at $\nu = 1/3$ for the corresponding (different) integration bandwidth and R_H. This control procedure, relying in its first (second) step less (more) heavily on the knowledge of the tank circuits, gives compatible $G^{eff}_{T,R}$ at an accuracy better than 7%: Through this procedure $G^{eff}_{T(R)}$ is found to be 6.8% (2.0%) higher than with the main calibration above (note that this could account for the small difference between the auto-correlations in the transmitted and reflected current in Fig. 2b). In a second cool-down of the same sample, this check calibration at $\nu = 2$ was used to correct for a small ($\lesssim 2\%$) change in the gains of the cryogenic amplifiers.

Quantum point contacts

Typical sweeps of the transmission ratio at zero dc bias voltage as well as the differential fraction of the transmitted current in the presence of a dc bias of ≈ 40 μV are shown in Fig. 7 versus gate voltage for the two sources and the analyzer QPCs. The down and up

https://doi.org/10.1038/s41467-023-36080-4

arrows points to the regions used for tuning the QPCs in, respectively, the SBS and WBS regime. Note that the actual tuning of each QPC is also impacted by the choice of voltages of the other nearby gates. Note also that whereas both gates are simultaneously swept for the analyzer, only the upper (lower) gate is swept for the source top-left (bottom-right) QPC. This reduces the impact on the central analyzer QPC of changing the source's tuning from SBS to WBS. Intriguingly, the central analyzer QPC requires more negative gate voltages to be fully closed than the two rather similar source QPCs. This different behaviour, systematically observed on several devices of the same chip, may be due to the different orientation of the analyzer QPC with respect to the underlying crystalline structure, together with strain induced by the metal gates. As frequently observed in other labs (see e.g. Fig. 5 in ref. [28]), we find that the

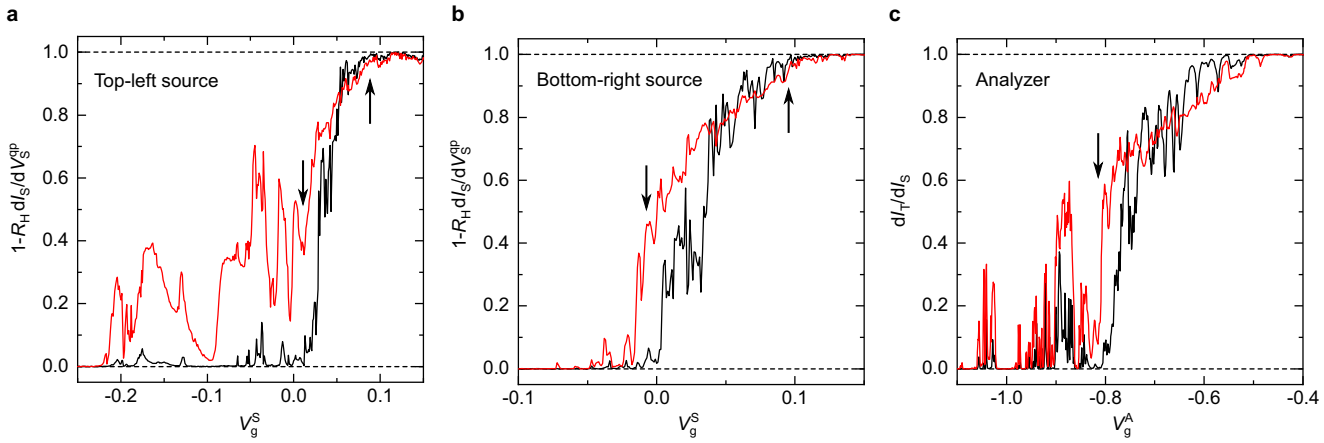

Fig. 7 | Quantum point contacts vs gate voltage. a b Differential transmission ratio $1-R_H dI_S/dV_S^{qp}$ of the top-left (bottom-right) source QPC, as a function of the voltage V_g^S applied to the source QPC gate located the furthest from the analyzer QPC. The black and red continuous lines correspond to measurements in the presence of a dc voltage bias $V_S^{qp}=0\,\mu$V and $V_S^{qp}=-43\,\mu$V, respectively. **c** Analyser differential transmission ratio dI_T/dI_S as a function of the gate voltage V_g^A applied to the two gates controlling the analyzer QPC. The black and red continuous lines correspond to measurements in the presence of a direct dc voltage bias $V_S^{qp}=V_S^e=0\,\mu$V and $-43\,\mu$V, respectively. The arrows indicate the approximate working points in the SBS (down arrows) and WBS (up arrow) regimes.

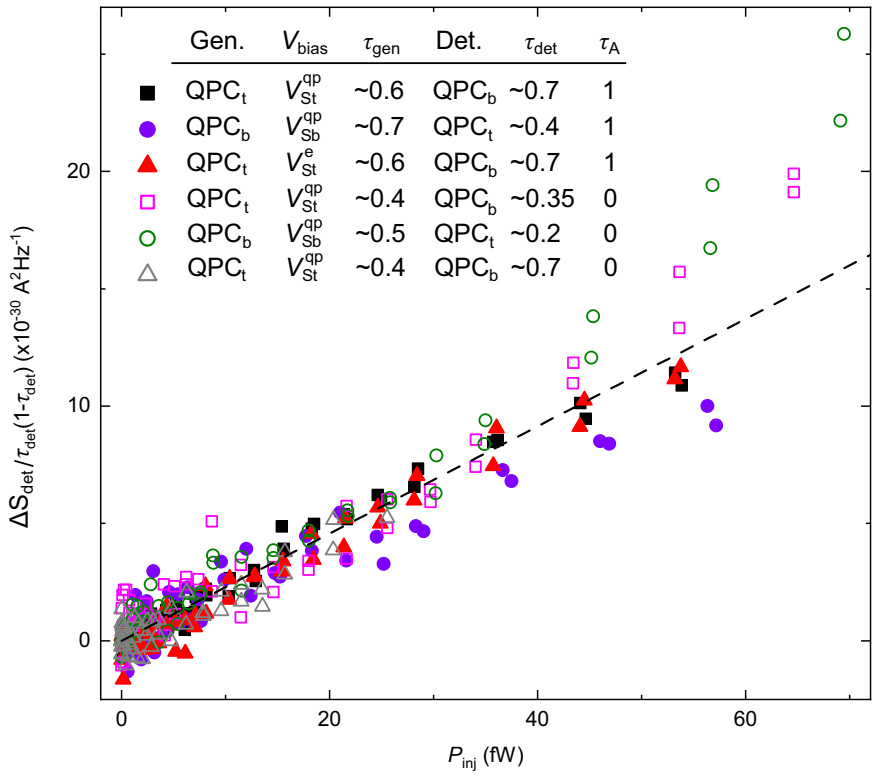

Fig. 8 | Nonlocal heating. The normalized noise increase $\Delta S_{det}/(\tau_{det}(1-\tau_{det}))$ emitted from an un-biased `detector' source $QPC_{t(b)}$ of transmission $\tau_{det}$ is plotted as a function of the power $P_{inj}$ injected at a second `generator' source $QPC_{b(t)}$ of transmission τ_{gen} (t and b indexes stand for the top-left and bottom-right QPCs, respectively). The detector and generator are electrically separated by chirality, and by an incompressible fractional quantum Hall state ($\tau_A=1$) or a depleted 2DEG ($\tau_A=0$). The measurements are here performed at $T\simeq 35$ mK, with $P_{inj}=2V_{bias}\tau_{gen}(1-\tau_{gen})e^2/3h$. The voltage bias V_{bias} is indexed by 'St' or 'Sb' depending on whether it is applied on QPC_t or QPC_b. The straight dashed line corresponds to $2.3\,10^{-16}P_{inj}$.

evolution of the transmission with the applied bias changes direction around $\tau \sim 0.8$, thus τ monotonously decreases with the bias in the WBS regime in contrast with predictions[11,37] (see the diminishing τ_S with the applied bias in the inset of Fig. 3a where $1-\tau_S \ll 1$, compared to the increasing τ_S with the bias in the inset of Fig. 3b where the source QPC is in the SBS regime).

Absence of a channel substructure along the $\nu = 1/3$ edge

At $\nu = 1/3$, the fractional quantum Hall edge is expected to be composed of a single channel[38]. Although it is also the case at $\nu = 1$, it was previously observed that an additional substructure could emerge[39], possibly due to the smoothness of the edge confinement potential combined with Coulomb interactions. Here we check for the absence of signatures of a substructure along the edge channels connecting the source QPCs to the central, analyzer QPC.

A first indication of a single channel structure is the absence of obvious plateaus at intermediate transmission (see Fig. 7). However, there would be no plateaus if the sub-channels were imperfectly separated at the QPCs. The principle of the substructure test is to compare the transmissions across the analyzer QPC as measured when a small ac voltage is directly applied or when the impinging ac electrical current first goes through a source QPC (see e.g. refs. [39,40]). In the absence of a substructure and at zero dc bias voltage, the two values must be identical whatever the tunings of the upstream and downstream QPCs. In contrast, a sub-structure robust along the 1.5 μm edge path that is associated with any imbalance in the transmission across the source and analyzer QPCs, would result in different values.

At our experimental accuracy, the two signals are systematically found to be identical (data not shown), which corroborates in our device the expected absence of a channel substructure at $\nu = 1/3$.

Absence of contact noise

A poor ohmic contact quality or other artifacts (electron thermalization in contacts, dc current heating in the resistive parts of the measurement lines...) could result in an unwanted, voltage-dependant noise sometimes refereed to as 'source' noise. Such a noise could spoil the experimental excess noise. Here we checked for any such source noise, and saw that it was absent at our experimental accuracy on the complete range of applied dc voltage bias, both with the device set to have all its QPCs fully open or fully closed.

Non-local heating

In a canonical description of the fractional quantum Hall effect at $\nu = 1/3$, the two source QPCs would be completely disconnected from one

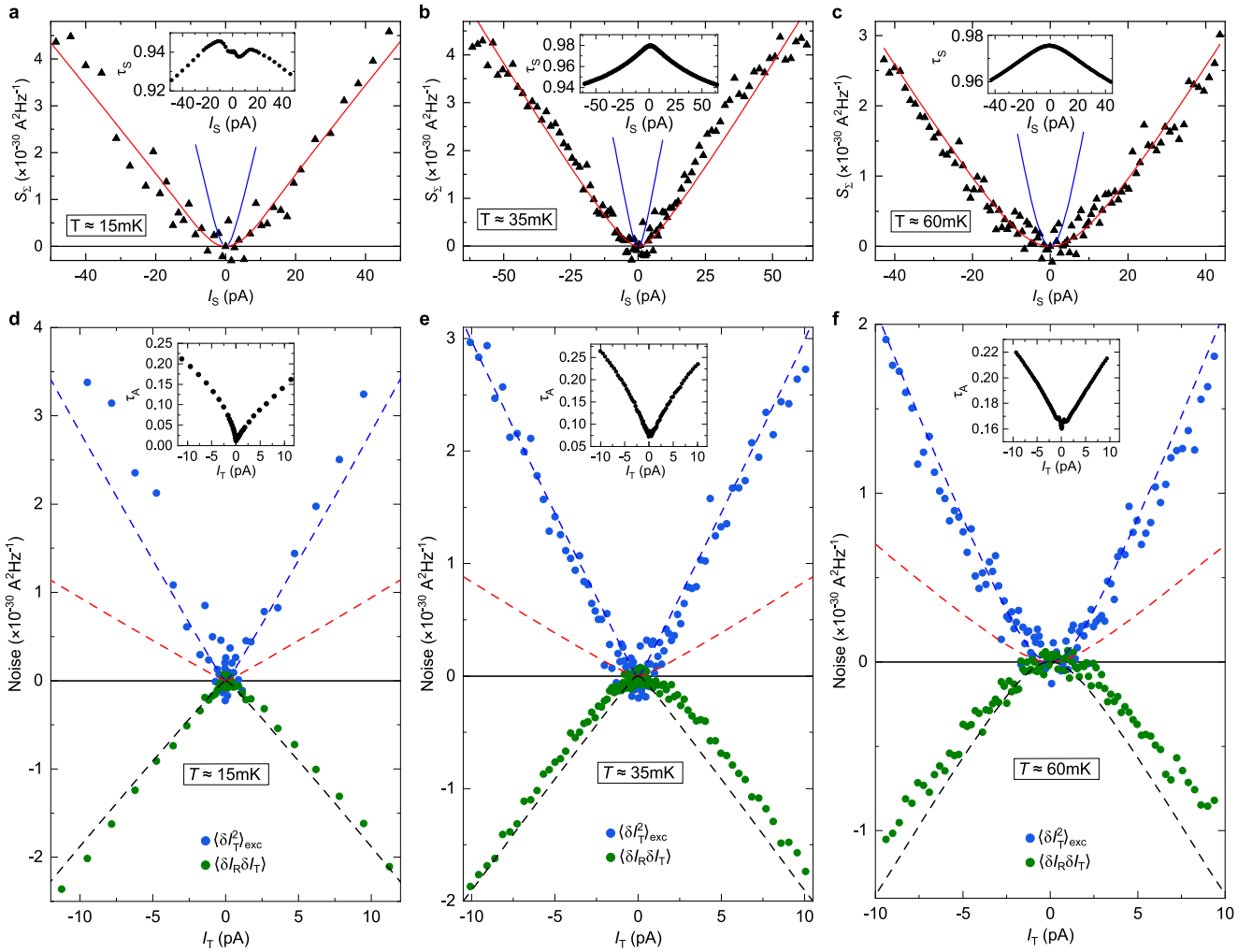

Fig. 9 | Supplementary Andreev observations, in the source WBS - analyzer SBS regime. The source QPC is here located on the opposite side of the analyzer than for the data shown in Fig. 3a,c, and measurements at the different temperatures $T \approx 15$ mK (**a, d**) and 60 mK (**c,f**) are displayed. The data in (**a**) and (**d**), in (**b**) and (**e**), and in (**c**) and (**f**) were measured simultaneously. **a, b, c** The top panels show the measured S_Σ (black symbols) for the simultaneous characterization of the source tunneling charge, similarly to Fig. 3a but at different temperatures and with another source QPC (bottom-right in Fig. 1c). The red (blue) lines are the shot noise predictions of Eq. (1) for $e/3$ at the corresponding T. **d, e, f** The bottom panels show the auto-correlations in the transmitted current (blue symbols) as well as the cross-correlations between transmitted and reflected current (green symbols), similarly to Fig. 3c. The dashed lines are the predictions of Eq. (5) at the indicated T.

another and would not be influenced by the downstream analyzer QPC due to the chirality of the edge transport. Whereas the electrical current obeys the predicted chirality, we observe signatures that it is not the case for a small fraction of the heat current. Although discernible (see e.g. the deviations from zero of the black symbols in Fig. 2b), this effect is essentially negligible in the WBS and SBS configurations of present interest. We nevertheless provide here a characterization of this phenomenon.

The non-local heating notably manifests itself as a small noise generated at one of the source QPCs when set to an intermediate transmission ratio, in response to a power injected at the other source QPC. This noise persists even at $\tau_A = 0$, where the two source QPCs are not only separated by the chirality but also by a depleted 2DEG area. This shows that it cannot result from (unexpected) neutral modes going upstream along the edges or through the fractional quantum Hall bulk[41,42]. Instead, we attribute it to a non-local heat transfer involving the long-range Coulomb interaction[39,43].

For the present non-local heating characterization, we set $\tau_A = 0$ or 1, such that the measured electrical noise $\langle \delta I_T^2 \rangle$ and $\langle \delta I_R^2 \rangle$ directly correspond to the noise originating from the corresponding uphill source QPC. A voltage bias is applied to only one of the sources, referred to as the 'generator' here. The signal is the concomitant noise increase measured on the amplification line connected to the other, unbiased source QPC referred to as the 'detector'. We can generally observe an unexpected increase of the noise from the detector, except if any of the two source QPCs is set to a perfect transmission or reflection, which can be understood as follows. If the transmission ratio across the voltage biased generator QPC is $\tau_{gen} = 0$ or 1, then there is no power locally injected along the edge at the location of this QPC ($\propto \tau_{gen}(1-\tau_{gen})$, see e.g. supplementary materials in ref. [44]) and the edge channel remains cold downstream from the generator. Consequently, there is no available energy source to heat up the detector and thereby to induce an excess electrical noise. If the transmission ratio across the detector QPC is $\tau_{det} = 0$ or 1, it is now the detector that would not be sensitive to a non-local heating. In particular, there would be no related partition noise (such as the so-called delta-T noise $\propto \tau_{det}(1-\tau_{det})$, see e.g. refs. [45–47]).

In general, one could expect that such heating would depend on the power P_{inj} locally injected at the generator QPC and that, for a given heating, the induced partition noise generated at the detector would scale as $\tau_{det}(1-\tau_{det})$. Accordingly, we show in Fig. 8 the detector excess noise normalized by $\tau_{det}(1-\tau_{det})$ as a function of the power injected at the generator, measured at a temperature $T \simeq 35$ mK. In this representation, the data obtained in different configurations fall on top of each other. It mostly does not depend on which of the source QPCs plays the role of the generator or the detector, on which dc voltage is used to bias the source, on whether $\tau_A = 0$ or 1, or on the values of τ_{det} and τ_{gen}. Based on this observation and interpretation, it is possible to estimate the impact of such non-local heating assuming a non-chiral noise on an unbiased QPC to be $\sim P_{inj}\tau_{det}(1-\tau_{det}) \times 2.3\,10^{-16}\,A^2/Hz$ (dashed line). Note that such heating should also take place between the analyzer and the upstream sources, which

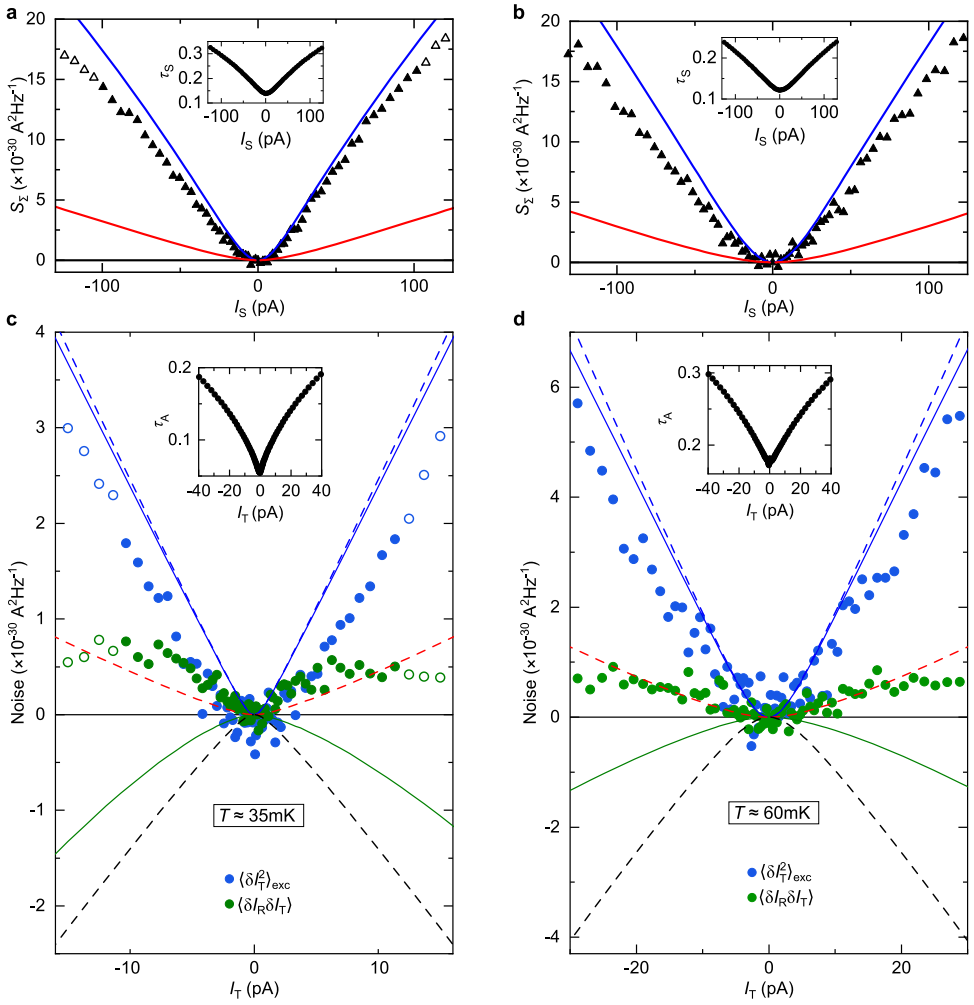

Fig. 10 | Supplementary observations in the source SBS - analyzer SBS regime. a, b, c, d The displayed data (symbols) corroborate the observations shown in Fig. 3b,d for distinct device tunings, and also at the higher temperature $T \approx 60$ mK (**b, d**). The data in (**a**) and (**c**), and in (**b**) and (**d**) were measured simultaneously.

corresponds to the small increase of S_Σ at high bias in Fig. 2b. In that specific case, a (unexpected) neutral counter-propagating heat flow could also take place, in principle, however the smallness of the heating signal rules out a substantial additional contribution to the above non-local heating. Importantly, in the main configurations with the sources set to or near a transmission of 0 or 1, we typically expect a negligible impact of only a few percent or less on the auto- and cross-correlations of interest. Moreover, when the detector QPC of tunneling charge e^* is a quasiparticle source itself voltage biased at $V_{\rm bias}$, we expect that the noise resulting from a non-local heating vanishes (in the limit of a small heating with respect to $e^*V_{\rm bias}/k_B$, see Eq. (1)).

Fit expressions

Here we provide the specific expressions used to fit the auto/cross-correlation data in the different configurations, when not explicitly given in the main text.

In the source-analyzer configurations shown in Fig. 3c, d and Fig. 4 (as well as in Fig. 9d, e, f and Fig. 10c, d in Methods), the different slopes of the dashed lines are associated with the thermal rounding of the source QPC. Explicitly, the displayed dashed lines correspond to:

$$S = 2e^* I_T \left[\coth \frac{e_S^* V}{2k_B T} - \frac{2k_B T}{e_S^* V} \right], \tag{5}$$

with $e_S^* V = (e/3) V_S^{qp}$ for Fig. 3c and Fig. 4 (as well as Fig. 9d, e, f in Methods), $e_S^* V = eV_S^e$ for Fig. 3d (as well as Fig. 10c, d in Methods), and the prefactor $e^* = e, e/3$ and $-2e/3$ for the blue, red and black dashed lines, respectively.

The noninteracting electron expressions for a source-analyzer configuration, which are displayed as continuous lines in Fig. 3d (as well as in Fig. 10c, d in Methods), are provided below. The auto-correlations of the transmitted current (continuous blue line) is given by:

$$\langle \delta I_T^2 \rangle_{\rm exc} = 2eI_T(1 - \tau_A\tau_S) \left[\coth \frac{eV_S^e}{2k_B T} - \frac{2k_B T}{eV_S^e} \right], \tag{6}$$

and the cross-correlations (continuous green line) is given by:

$$\langle \delta I_R \delta I_T \rangle = -2eI_T(1 - \tau_A)\tau_S \left[\coth \frac{eV_S^e}{2k_B T} - \frac{2k_B T}{eV_S^e} \right]. \tag{7}$$

Andreev observations for different temperatures and tunings

The robustness of our observations is ascertained by repeating the measurements at different temperatures, by using a different QPC for the source, and by using different tunings of the source and analyzer QPCs.

Figure 9 shows such additional measurements in the Andreev configuration of a source in the WBS regime and an analyzer in the SBS regime. The main changes compared to Fig. 3c are that a different QPC (located on the opposite side of the analyzer) is used for the source, and the additional temperatures of $T \approx 15$ mK and 60 mK. Note that at the lowest 15 mK temperature, the very fast increase with direct bias voltage of the transmission τ_A across the analyzer set in the SBS regime makes it difficult to unambiguously ascertain, separately, its $1e$ characteristic tunneling charge (data not shown).

Figure 10 shows additional measurements when the source and analyzer are both set in the SBS regime. A similar signal as in Fig. 3b,d is observed for a different tuning of the device and at the higher temperature $T \approx 60$ mK.

Data availability

The data that support the findings of this study are available from the corresponding authors upon reasonable request.

References

1. Bäuerle, C. et al. Coherent control of single electrons: a review of current progress. *Rep. Prog. Phys.* **81**, 056503 (2018).
2. Feldman, D. E. & Halperin, B. I. Fractional charge and fractional statistics in the quantum Hall effects. *Rep. Prog. Phys.* **84**, 076501 (2021).
3. Kane, C. L. & Fisher, M. P. A. Shot noise and the transmission of dilute Laughlin quasiparticles. *Phys. Rev. B* **67**, 045307 (2003).
4. Safi, I., Devillard, P. & Martin, T. Partition Noise and Statistics in the Fractional Quantum Hall Effect. *Phys. Rev. Lett.* **86**, 4628–4631 (2001).
5. Vishveshwara, S. Revisiting the Hanbury Brown–Twiss Setup for Fractional Statistics. *Phys. Rev. Lett.* **91**, 196803 (2003).
6. Kim, E.-A., Lawler, M., Vishveshwara, S. & Fradkin, E. Signatures of Fractional Statistics in Noise Experiments in Quantum Hall Fluids. *Phys. Rev. Lett.* **95**, 176402 (2005).
7. Campagnano, G. et al. Hanbury Brown–Twiss Interference of Anyons. *Phys. Rev. Lett.* **109**, 106802 (2012).
8. Rosenow, B., Levkivskyi, I. P. & Halperin, B. I. Current Correlations from a Mesoscopic Anyon Collider. *Phys. Rev. Lett.* **116**, 156802 (2016).
9. Lee, B., Han, C. & Sim, H.-S. Negative Excess Shot Noise by Anyon Braiding. *Phys. Rev. Lett.* **123**, 016803 (2019).
10. Kane, C. L. & Fisher, M. P. A. Nonequilibrium noise and fractional charge in the quantum Hall effect. *Phys. Rev. Lett.* **72**, 724–727 (1994).
11. Fendley, P., Ludwig, A. W. W. & Saleur, H. Exact Nonequilibrium dc Shot Noise in Luttinger Liquids and Fractional Quantum Hall Devices. *Phys. Rev. Lett.* **75**, 2196–2199 (1995).
12. Andreev, A. F. Thermal conductivity of the intermediate state of superconductors. *Zh. Eksperim. i Teor. Fiz.***46,** 713–728 (1964).
13. Safi, I. & Schulz, H. J. Transport in an inhomogeneous interacting one-dimensional system. *Phys. Rev. B* **52**, R17040–R17043 (1995).
14. Sandler, N. P., Chamon, Cd. C. & Fradkin, E. Andreev reflection in the fractional quantum Hall effect. *Phys. Rev. B* **57**, 12324–12332 (1998).
15. Hashisaka, M. et al. Andreev reflection of fractional quantum Hall quasiparticles. *Nat. Commun.* **12**, 2794 (2021).
16. Comforti, E., Chung, Y. C., Heiblum, M., Umansky, V. & Mahalu, D. Bunching of fractionally charged quasiparticles tunnelling through high-potential barriers. *Nature* **416**, 515–518 (2002).
17. Chung, Y. C., Heiblum, M., Oreg, Y., Umansky, V. & Mahalu, D. Anomalous chiral Luttinger liquid behavior of diluted fractionally charged quasiparticles. *Phys. Rev. B* **67**, 201104 (2003).
18. Liang, Y., Dong, Q., Gennser, U., Cavanna, A. & Jin, Y. Input Noise Voltage Below 1 nV/Hz$^{1/2}$ at 1 kHz in the HEMTs at 4.2 K. *J. Low. Temp. Phys.* **167**, 632–637 (2012).
19. Jezouin, S. et al. Quantum Limit of Heat Flow Across a Single Electronic Channel. *Science* **342**, 601–604 (2013).
20. Saminadayar, L., Glattli, D. C., Jin, Y. & Etienne, B. Observation of the e/3 Fractionally Charged Laughlin Quasiparticle. *Phys. Rev. Lett.* **79**, 2526–2529 (1997).
21. de Picciotto, R. et al. Direct observation of a fractional charge. *Nature* **389**, 162–164 (1997).
22. Feldman, D. E. & Heiblum, M. Why a noninteracting model works for shot noise in fractional charge experiments. *Phys. Rev. B* **95**, 115308 (2017).
23. Blanter, Y. & Büttiker, M. Shot noise in mesoscopic conductors. *Phys. Rep.* **336**, 1–166 (2000).
24. Griffiths, T. G., Comforti, E., Heiblum, M., Stern, A. & Umansky, V. Evolution of Quasiparticle Charge in the Fractional Quantum Hall Regime. *Phys. Rev. Lett.* **85**, 3918–3921 (2000).
25. Kapfer, M.*Dynamic of excitations of the Fractional quantum Hall effect : fractional charge and fractional Josephson frequency*. Phd thesis, Université Paris-Saclay, SPEC, CEA-Saclay, 91191 Gif-sur-Yvette, France. https://tel.archives-ouvertes.fr/tel-01978045 (2018).

26. Bartolomei, H. et al. Fractional statistics in anyon collisions. *Science* **368**, 173–177 (2020).
27. Kane, C. L. & Fisher, M. P. A. Transport in a one-channel Luttinger liquid. *Phys. Rev. Lett.* **68**, 1220–1223 (1992a).
28. Heiblum, M. & Feldman, D. E. Edge probes of topological order. *Int. J. Mod. Phys. A* **35**, 2030009 (2020).
29. Idrisov, E. G., Levkivskyi, I. P., Sukhorukov, E. V. & Schmidt, T. L. Current cross correlations in a quantum Hall collider at filling factor two. *Phys. Rev. B* **106**, 085405 (2022).
30. Morel, T., Lee, J.-Y. M., Sim, H.-S. & Mora, C. Fractionalization and anyonic statistics in the integer quantum Hall collider. *Phys. Rev. B* **105**, 075433 (2022).
31. Lee, J.-Y. M. & Sim, H.-S. Non-Abelian Anyon Collider. *Nat. Commun.* **13**, 6660 (2022).
32. Lee, J.-Y. M., Han, C. & Sim, H.-S. Fractional Mutual Statistics on Integer Quantum Hall Edges. *Phys. Rev. Lett.* **125**, 196802 (2020).
33. Schiller, N., Oreg, Y. & Snizhko, K. Extracting the scaling dimension of quantum Hall quasiparticles from current correlations. *Phys. Rev. B* **105**, 165150 (2022).
34. Jonckheere, T., Rech, J., Grémaud, B. & Martin, T. Anyonic statistics revealed by the Hong-Ou-Mandel dip for fractional excitations (2022). *ArXiv*: 2207.07172.
35. Wen, X. G. Theory of the edge states in the fractional quantum Hall effects. *Int. J. Mod. Phys. B* **06**, 1711–1762 (1992).
36. Iftikhar, Z. et al. Primary thermometry triad at 6 mK in mesoscopic circuits. *Nat. Commun.* **7**, 12908 (2016).
37. Kane, C. L. & Fisher, M. P. A. Transmission through barriers and resonant tunneling in an interacting one-dimensional electron gas. *Phys. Rev. B* **46**, 15233–15262 (1992b).
38. Laughlin, R. B. Anomalous Quantum Hall Effect: An Incompressible Quantum Fluid with Fractionally Charged Excitations. *Phys. Rev. Lett.* **50**, 1395–1398 (1983).
39. Venkatachalam, V., Hart, S., Pfeiffer, L., West, K. & Yacoby, A. Local thermometry of neutral modes on the quantum Hall edge. *Nat. Phys.* **8**, 676–681 (2012).
40. van Wees, B. J. et al. Anomalous integer quantum Hall effect in the ballistic regime with quantum point contacts. *Phys. Rev. Lett.* **62**, 1181–1184 (1989).
41. Altimiras, C. et al. Chargeless Heat Transport in the Fractional Quantum Hall Regime. *Phys. Rev. Lett.* **109**, 026803 (2012).
42. Inoue, H. et al. Proliferation of neutral modes in fractional quantum Hall states. *Nat. Commun.* **5**, 4067 (2014).
43. Krähenmann, T. et al. Auger-spectroscopy in quantum Hall edge channels and the missing energy problem. *Nat. Commun.* **10**, 3915 (2019).
44. Altimiras, C. et al. Non-Equilibrium Edge Channel Spectroscopy in the Integer Quantum Hall Regime. *Nat. Phys.* **6**, 34 (2009).
45. Lumbroso, O., Simine, L., Nitzan, A., Segal, D. & Tal, O. Electronic noise due to temperature differences in atomic-scale junctions. *Nature* **562**, 240–244 (2018).
46. Sivre, E. et al. Electronic heat flow and thermal shot noise in quantum circuits. *Nat. Commun.* **10**, 5638 (2019).
47. Larocque, S., Pinsolle, E., Lupien, C. & Reulet, B. Shot Noise of a Temperature-Biased Tunnel Junction. *Phys. Rev. Lett.* **125**, 106801 (2020).

Acknowledgements

This work was supported by the European Research Council (ERC-2020-SyG-951451), the European Union's Horizon 2020 research and innovation programme (Marie Skłodowska-Curie grant agreement 945298-ParisRegionFP), the French National Research Agency (ANR-16-CE30-0010-01 and ANR-18-CE47-0014-01) and the French RENATECH network. The authors thank C. Mora and H.-S. Sim for illuminating discussions.

Author contributions

O.M. and P.G. contributed equally to this work; O.M. and P.G. performed the experiment and analyzed the data with inputs from A.Aa., A.An., C.P. and F.P.; A.C. and U.G. grew the 2DEG; A.Aa, F.P., O.M. and P.G. fabricated the sample; Y.J. fabricated the HEMT used in the cryogenic noise amplifiers; F.P., O.M. and P.G. wrote the manuscript with contributions from A.Aa., A.An., C.P. and U.G.; A.An. and F.P. led the project.

Competing interests

The authors declare no competing interests.

Additional information

Supplementary information The online version contains supplementary material available at https://doi.org/10.1038/s41467-023-36080-4.

Correspondence and requests for materials should be addressed to A. Anthore or F. Pierre.

Peer review information *Nature Communications* thanks Jinhong Park and the other, anonymous, reviewer(s) for their contribution to the peer review of this work. Peer reviewer reports are available.

The second article presents the anyon braiding signatures discussed in Chapter 4 and in Chapter 5.

Title: Cross-Correlation Investigation of Anyon Statistics in the $\nu = 1/3$ and $2/5$ Fractional Quantum Hall States

Co-authors: Pierre GLIDIC, Olivier MAILLET, Colin PIQUARD, Abdelhanin AASSIME, Antonnella CAVANA, Yong JIN, Ulf GENNSER Anne ANTHORE, Frédéric PIERRE

Status: Published

Journal: Physical Review X

Year: 2023

Cross-Correlation Investigation of Anyon Statistics in the $\nu = 1/3$ and $2/5$ Fractional Quantum Hall States

P. Glidic,[1,*] O. Maillet,[1,*] A. Aassime,[1] C. Piquard,[1] A. Cavanna,[1] U. Gennser,[1] Y. Jin,[1] A. Anthore,[1,2,†] and F. Pierre[1,‡]

[1]*Université Paris-Saclay, CNRS, Centre de Nanosciences et de Nanotechnologies, 91120, Palaiseau, France*

[2]*Université Paris Cité, CNRS, Centre de Nanosciences et de Nanotechnologies, F-91120 Palaiseau, France*

(Received 4 October 2022; revised 14 December 2022; accepted 6 January 2023; published 3 March 2023)

Recent pioneering works have set the stage for exploring anyon braiding statistics from negative current cross-correlations along two intersecting quasiparticle beams. In such a dual-source-analyzer quantum point contact setup, also referred to as "collider," the anyon exchange phase of fractional quantum Hall quasiparticles is predicted to be imprinted into the cross-correlations characterized by an effective Fano factor P. In the case of symmetric incoming quasiparticle beams, conventional fermions result in a vanishing P. In marked contrast, we observe signatures of anyon statistics in the negative P found both for the $e/3$ Laughlin quasiparticles at filling factor $\nu = 1/3$ ($P \approx -2$, corroborating previous findings) and for the $e/5$ quasiparticles in the hierarchical state $\nu = 2/5$ ($P \approx -1$). Nevertheless, we argue that the quantitative connection between a numerical value of $P \neq 0$ and a specific fractional exchange phase is hampered by the influence of the analyzer conductance dependence on the voltages used to generate the quasiparticles. Finally, we address the important challenge how to distinguish at $\nu = 1/3$ between negative cross-correlations induced by a fractional braid phase and those resulting from a different Andreev-like mechanism. Although with symmetric sources P does not exhibit signatures of a crossover when the analyzer is progressively detuned to favor Andreev processes, we demonstrate that changing the balance between sources provides a means to discriminate between the two mechanisms.

DOI: 10.1103/PhysRevX.13.011030

Subject Areas: Condensed Matter Physics, Mesoscopics, Strongly Correlated Materials

I. INTRODUCTION

A variety of exotic quasiparticles are predicted to emerge in low-dimensional systems, beyond classification into bosons and fermions [1–7]. In the archetypal regime of the fractional quantum Hall effect (FQHE), the presence of quasiparticles carrying a fraction of the elementary electron charge e is by now firmly established [8–21]. These quasiparticles are furthermore predicted to exhibit unconventional behaviors upon interexchange, different from bosons and fermions, and were accordingly coined any(-)ons [22]. Such a possibility results from the topological modification introduced by a double exchange (a braiding) under reduced dimensionalities [23]. Exchanging two fractional quasiparticles can either add a factor $\exp(i\theta)$ with an exchange phase θ smaller than the fermionic π (Abelian anyons) or result in a drastic change of the wave function not possible to reduce to a simple phase factor (non-Abelian anyons). Notably, the Laughlin FQHE series at electron filling factor per flux quantum $\nu = 1/(2p+1)$ ($p \in \mathbb{N}$) is predicted to host fractional quasiparticles of charge νe and exchange phase $\theta = \nu\pi$ as elementary excitations [24–26]. Even more exotic non-Abelian anyons of charge $e/4$ are expected at $\nu = 5/2$ [7,27,28] (see Refs. [29,30] for heat conductance measurements supporting the non-Abelian character). Providing experimental evidence of a fractional exchange phase proves more challenging than the fractional charge. It is only recently that the first convincing signatures were detected at $\nu = 1/3$, from $2\pi/3$ phase jumps in an electronic interferometer [31] and through negative cross-correlations in a source-analyzer setup [32].

The two methods are complementary, and, specifically, the second [33] promises to be remarkably adaptable to different platforms, including fractional charges propagating along integer quantum Hall channels [3,34,35].

*These authors contributed equally to this work.

†anne.anthore@c2n.upsaclay.fr

‡frederic.pierre@cnrs.fr

The present work builds upon this source-analyzer approach, by exploring the discerning character of cross-correlation signatures and by expanding the investigation to a different type of anyon.

We first reexamine the $\nu = 1/3$ Laughlin fractional quantum Hall state. The observations of Ref. [32] are corroborated over an extended range of analyzer tunings as well as to lower temperatures. Remarkably, the qualitative signatures of anyon statistics are found to be robust to the setting of the analyzer. This insensitivity even blurs the frontier with a distinct Andreev-like mechanism [36,37] that does not involve an unconventional braid phase. Nevertheless, we show that it is possible to distinguish anyon braiding by changing the symmetry between sources. In addition, the remarkable data-theory quantitative agreement previously observed is reproduced here. However, we show that it relies on a specific normalization choice of the cross-correlation signal. In essence, extracting direct quantitative information regarding the value of the exchange phase θ, beyond its fractional character, is impeded by the accompanying influence of the analyzer conductance. Then, we investigate the hierarchical (Jain) $\nu = 2/5$ state, where $e/5$ quasiparticles are predicted to have a different fractional exchange phase of $3\pi/5$. The $\nu = 2/5$ observation of negative cross-correlations with symmetric sources provides a qualitative signature for the anyon character of these quasiparticles.

II. PROBING ANYON STATISTICS WITH CROSS-CORRELATIONS

The setup probing unconventional anyon statistics is schematically illustrated in Fig. 1(a). It is composed of two random sources of quasiparticles impinging on both sides of a central "analyzer" constriction. Signatures of unconventional exchange statistics are encoded into the cross-correlations between current fluctuations along the two outgoing paths $\langle \delta I_L \delta I_R \rangle$. In the limit of dilute sources of anyon quasiparticles and of a nearly ballistic short central constriction, theory predicts negative cross-correlations that depend on the balance between the two sources and persist at symmetry [3,33,34]. In this section, we first discuss the theoretical origin of the connection between cross-correlations and exotic anyon exchange phase θ. Then, the discriminating character of this signal, to attest of a non-trivial fractional phase, is assessed by comparing with expectations in different configurations.

How do cross-correlations connect with anyon statistics? Initially, an intuitive interpretation of the predicted cross-correlations was proposed in terms of a partial bunching of colliding quasiparticles [33]. However, a collision involves two almost simultaneously incoming quasiparticles, and it was recently pointed out that this contribution becomes negligibly small for sources in the considered limit of dilute, randomly emitted quasiparticles [3,34] (a rapidly diminishing signal, as the square of the dilution ratio, is

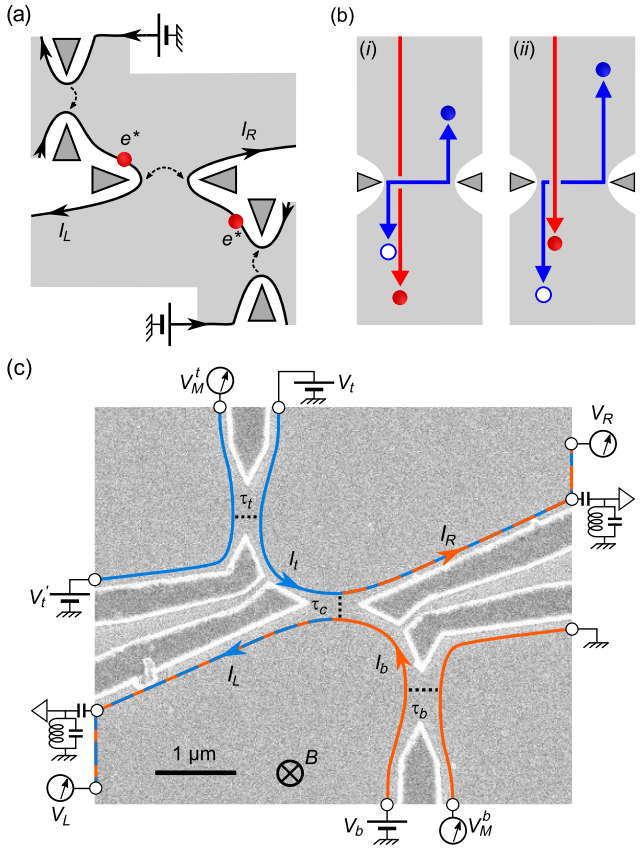

FIG. 1. (a) Source-analyzer setup. Quantum point contacts (pairs of facing triangles) at the top left (QPC_t) and bottom right (QPC_b) in the weak backscattering (WBS) regime constitute sources of quasiparticles of fractional charge e^*. The emitted quasiparticles propagate toward the central analyzer QPC_c along quantum Hall edge channels depicted by lines with arrows (inactive channels not shown). Cross-correlations $\langle \delta I_L \delta I_R \rangle$ inform on the statistics. (b) Braid-induced mechanism. Analyzer tunnelings [double arrow in (a)] result from interferences between the generation of a quasiparticle-quasihole pair across QPC_c (blue double arrow) after (i) or before (ii) the passing of incident quasiparticles (one represented with a red arrow). The process cancels for a trivial braid phase 2π. (c) Sample e-beam micrograph. Metallic gates on the surface of a Ga(Al)As heterojunction appear darker with bright edges. $QPC_{t,b}$ are tuned to matching transmission ratios $\tau_t \approx \tau_b$ of the active channel. The source imbalance $I_- \equiv I_t - I_b$ is controlled with $V_t - V_b$. We set $V_t' = 0$ except for the separate shot noise characterization of the central analyzer QPC_c, which is performed with a direct voltage bias ($V_t' = V_t$ and $V_b = 0$).

also expected from a classical model [33]). The *same* theoretical prediction was instead attributed to a different interference mechanism, between two different processes labeled (i) and (ii) in Fig. 1(b). These correspond to the thermal excitation of a quasiparticle-quasihole pair across the analyzer constriction before, or after, the transmission of quasiparticles emitted from the sources [3,34,38]. This is schematically illustrated in Fig. 1(b) in the presence of a

single incident quasiparticle. Importantly, such an interference can be mapped onto a braiding between incident and thermally excited anyons [39], and it cancels for a trivial braid phase $2\theta = 0 \pmod{2\pi}$. The pairs generated across the analyzer constriction through this braiding mechanism directly result in a current cross-correlation signal, whose mere existence for symmetric incoming beams constitutes a first marker of unconventional anyon statistics. Moreover, incident quasiparticles from opposite sources are associated with a braiding along inverse winding directions and, therefore, contribute with opposite signs to the relevant total braid phase [3,34]. For example, two quasiparticles incident from opposite sides within a time window shorter than h/k_BT (with T the temperature) are associated with a null total braid phase, leading to a breakdown of this transport mechanism across the analyzer (see Ref. [38] for the detailed dependence in the time delay). Consequently, the cross-correlations resulting from a nontrivial braiding depend on the balance between the beams of incoming, randomly emitted quasiparticles, which constitutes a second complementary marker. As recapitulated in Table I, these two markers combined together provide a strong qualitative signature of an underlying nontrivial anyon statistics.

III. EXPERIMENTAL IMPLEMENTATION

The device shown in Fig. 1(c) is realized on a Ga(Al)As two-dimensional electron gas of density 1.2×10^{11} cm^{-2} located 140 nm below the surface. It is cooled at a temperature $T \simeq 35$ mK (if not stated otherwise) and immersed in a strong perpendicular magnetic field B corresponding to the middle of the quantum Hall effect plateau at filling factors $\nu = 1/3$, $2/5$, and 2 (see Appendix C for $\nu = 2$). In the quantum Hall regime, the current flows along chiral edge channels are depicted as lines with arrows indicating the propagation direction. At $\nu = 2/5$ and 2, there are two copropagating quantum Hall channels with the same chirality, although, for clarity, only the active one in which nonequilibrium quasiparticles are injected is displayed in Fig. 1.

TABLE I. Cross-correlations with dilute beams of incident quasiparticles. Both the cross-correlation sign and evolution between symmetric sources (Sym.) and a single source (Asym.) are compulsory to distinguish between different transport mechanisms involving tunneling quasiparticles of charge $e_{t,b,c}$. Parentheses indicate a signal that emerge for nondilute incident beams, and a $--$ signifies a larger amplitude. See Ref. [35] for the predictions of positive cross-correlations with two interacting channels of the integer quantum Hall effect (IQHE) and Refs. [36,37] for the prediction and observation of an Andreev mechanism giving rise to symmetry-independent negative cross-correlations when the analyzer is set to favor the tunneling of quasielectrons.

System			Cross-correlation	
Platform (mechanism)	$e_{t,b}$	e_c	Sym.	Asym.
Laughlin FQHE (braiding)	νe	νe	$-$	$--$
Laughlin FQHE (Andreev)	νe	e	$-$	$-$
Free fermions	e	e	0	$(-)$
Interacting IQHE channels	e	e	$+$	$(-)$

The sources and analyzer constrictions are realized by voltage-biased quantum point contacts (QPCs) tuned by field effect using metal split gates (darker with bright edges). The source QPCs located in the top left and bottom right in Fig. 1(c) are referred to as QPC$_t$ and QPC$_b$, respectively. The central analyzer QPC is referred to as QPC$_c$. The sources are connected to the downstream QPC$_c$ by an edge path of approximately 1.5 μm.

In the following, we first discuss the characterization of the current fraction going through the source and analyzer. Then, we detail the determination of the fractional charges of the tunneling quasiparticles and whether this characterization can be performed simultaneously with the measurement of the main cross-correlation signal or separately.

A. QPC transmission

QPC$_{t,b,c}$ are first characterized through the fractions $\tau_{t,b,c}$ of (differential) current in the active channel transmitted across the constriction:

$$\tau_{t(b)} \equiv \frac{\nu}{\nu_{\text{eff}}}\left(\frac{\partial V_M^{t(b)}}{\partial V_{t(b)}} - 1\right) + 1, \tag{1}$$

$$\tau_c \equiv \frac{\nu}{\nu_{\text{eff}}}\left(\frac{\partial V_R/\partial V_b}{2(1-\tau_b)} + \frac{\partial V_L/\partial V_t}{2(1-\tau_t)}\right), \tag{2}$$

with the partial derivatives given by lock-in measurements and where ν_{eff} is the effective filling factor associated with the conductance $\nu_{\text{eff}}e^2/h$ of the active channel ($\nu_{\text{eff}} = \nu$ if there is a single channel, $\nu_{\text{eff}} = 1/15$ for the inner channel at $\nu = 2/5$, and $\nu_{\text{eff}} = 1$ for each channel at $\nu = 2$). Note that we follow the standard convention for the definition of the transmission direction across the QPCs' split gates, as indicated by dashed lines in Fig. 1(c). The so-called strong backscattering (SBS) and weak backscattering (WBS) regimes correspond to $\tau \ll 1$ and $1 - \tau \ll 1$, respectively. As discussed below and illustrated in Fig. 1(a), the sources and analyzer are normally set in the WBS regime to emit and probe the statistics of fractional quasiparticles. The top-right inset in Fig. 2(c) displays such $\tau_{t,b,c}$ measurements.

B. Quasiparticle sources

Applying a voltage bias $V_{t(b)}$ excites the quantum Hall edge channel at the level of QPC$_{t(b)}$ (except for $\tau_{t(b)} \in \{0, 1\}$), hence generating a quasiparticle carrying current $I_{t(b)}$ propagating toward the analyzer. The nature of these quasiparticles depends on the tuning of the QPCs. For Laughlin fractions ν, their charge is predicted to be e at

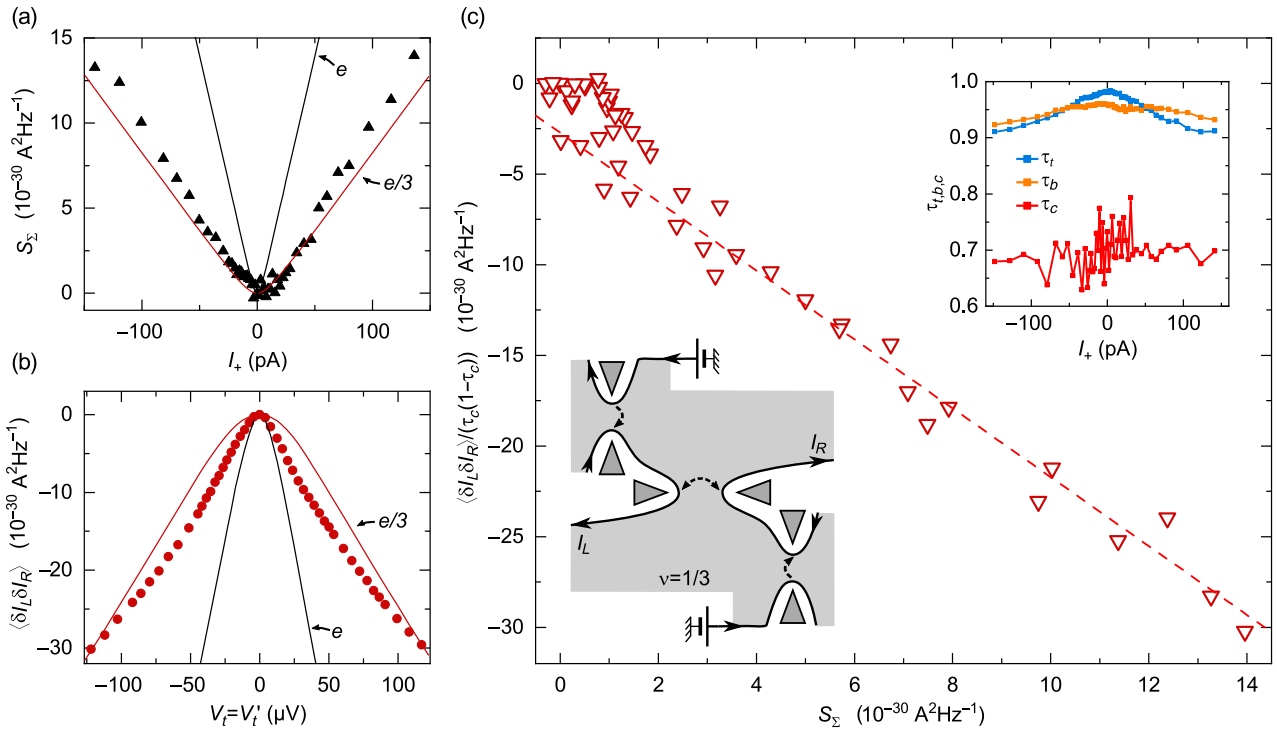

FIG. 2. Cross-correlation signature of anyons at $\nu = 1/3$ with symmetric sources. All QPCs are in the WBS regime ($\tau_{t,b} \approx 0.96$, $\tau_c \simeq 0.7$; see schematic illustration and inset in (c)]. (a),(b) Shot noise characterization of (a) the charge of the quasiparticles emitted from the sources QPC$_{t,b}$ [$I_+ \equiv I_t + I_b$, S_Σ given by Eq. (4)] and (b) the tunneling charge across the analyzer QPC$_c$. A source bias $V_t = V_b$ ($V_t' = 0$) is applied for the simultaneous measurements in (a) and (c), whereas $V_t = V_t'$ ($V_b = 0$) implements a direct voltage bias of QPC$_c$ in (b). The noise data (symbols) match the predictions for $e/3$ (red lines). (c) Cross-correlations in the symmetric source-analyzer configuration. The effective Fano factor P is obtained from a linear fit (dashed line) of the slope of the normalized cross-correlation data (symbols) plotted as a function of S_Σ. Here, $P \simeq -1.9$. Inset: QPC transmission.

$\tau \ll 1$ and νe at $1 - \tau \ll 1$ [10,11]. We characterize the charge $e_{t(b)}$ of the quasiparticles emitted at QPC$_{t(b)}$ by confronting the fluctuations of $I_{t(b)}$ with the standard, phenomenological expression for the excess shot noise [40,41]:

$$\langle \delta I^2 \rangle_{\rm exc} = 2e^* \tau^{\rm dc}(1-\tau^{\rm dc}) \frac{\nu_{\rm eff} e^2}{h} V \left[\coth \frac{e^* V}{2k_B T} - \frac{2k_B T}{e^* V} \right], \quad (3)$$

where $\delta I \equiv I - \langle I \rangle$, $\langle \delta I^2 \rangle_{\rm exc} \equiv \langle \delta I^2 \rangle(V) - \langle \delta I^2 \rangle(0)$, $I = I_{t(b)}$, $e^* = e_{t(b)}$, $V = V_{t(b)}$, and $\tau^{\rm dc}$ is an alternative definition of $\tau_{t(b)}$ with the derivative in Eq. (1) replaced by the ratio of the dc voltages. Note that the charge e^* is extracted focusing on $e^* V \gg k_B T$, while the coth transient is only a rough approximation to the predicted low-voltage behavior [42,43]. In practice, we measure the auto- and cross-correlations of $\delta I_{L,R}$ and not directly the current fluctuations emitted by the sources. The main approach here used to determine the shot noise from the sources is to consider the measured noise sum defined as

$$S_\Sigma \equiv \langle \delta I_L^2 \rangle_{\rm exc} + \langle \delta I_R^2 \rangle_{\rm exc} + 2\langle \delta I_L \delta I_R \rangle. \quad (4)$$

Current conservation ($I_t + I_b = I_L + I_R$) together with the absence of current correlations between sources expected from chirality ($\langle \delta I_t \delta I_b \rangle = 0$) imply

$$\langle \delta I_t^2 \rangle_{\rm exc} + \langle \delta I_b^2 \rangle_{\rm exc} = S_\Sigma. \quad (5)$$

This approach is systematically used simultaneously with the measurement of the anyon statistics cross-correlation signal. With two active sources in this case (both $V_{t,b} \neq 0$), S_Σ informs us on the weighted average of e_t and e_b [see, e.g., Fig. 2(a)]. Such an approach is also applied with a single active source, sweeping $V_{t(b)}$ at fixed $V_{b(t)} = 0$. For perfectly independent sources, the increase of S_Σ then corresponds to the excess shot noise across QPC$_{t(b)}$, providing us separately with the quasiparticles' charge $e_{t(b)}$. (As discussed later, some imperfections may, however, develop.) Note that, when possible, we check the consistency of the extracted charges $e_{t,b}$ with the values obtained by setting the analyzer to a full transmission or a full reflection ($\tau_c \in \{0, 1\}$), where there is a straightforward one-to-one correspondence between $I_{t,b}$ and $I_{L,R}$.

C. Analyzer tunneling charge

The individual shot noise characterization of QPC_c requires the application of a direct voltage bias, as opposed to incident currents composed of nonequilibrium quasiparticles. Hence, it must be performed in a dedicated, separate measurement. In practice, we set $V_t' = V_t$ at $V_b = 0$ [see Fig. 1(c); elsewhere, $V_t' = 0$] without changing the gate voltage tuning of any of the QPCs, and we measure the resulting cross-correlations $\langle \delta I_L \delta I_R \rangle$ (see Fig. 14 in Appendix E for the less robust autocorrelation signal). Fitting the noise slopes with the negative of the prediction of Eq. (3) provides us with the characteristic charge e_c of the quasiparticles transmitted across QPC_c [see Figs. 2(b) and 7(b)].

D. Experimental procedure

With these tools, the device is set to have two sources of transmission probabilities that remain symmetric $\tau_t \approx \tau_b$ and with the same fractional quasiparticle charges $e_t \simeq e_b \simeq e^*$, over the explored range of bias voltages of typically $V_{t,b} \lesssim 100$ μV. At $\nu = 1/3$, $2/5$, and 2, we focus on $e^*/e \simeq 1/3$, $1/5$, and 1, respectively. The symmetry between the two quasiparticle beams impinging on the analyzer is then controlled through V_t and V_b and characterized by the ratio $|I_-/I_+|$ with $I_\pm \equiv I_t \pm I_b$. The analyzer QPC_c is normally set to the same tunneling charge $e_c \simeq e^*$ to investigate the fractional exchange phase of e^* quasiparticles, although a broader range of e_c is also explored at $\nu = 1/3$ by tuning the analyzer QPC_c away from the WBS regime.

IV. THEORETICAL PREDICTIONS

We recapitulate the cross-correlation predictions for free electrons [40] and anyons of the Laughlin series [33,34,44]. Other related theoretical developments include the recent extensions to copropagating integer quantum Hall channels in interactions [35], to fractional charge injected in integer quantum Hall channels [3], to non-Abelian anyons [34], to high frequencies [45], and to Laughlin quasiparticles with a controlled time delay [38].

A. Effective Fano factor

The statistics is specifically investigated through the effective Fano factor P defined as

$$P \equiv \frac{\langle \delta I_L \delta I_R \rangle}{S_\Sigma \tau_c (1-\tau_c)}, \tag{6}$$

with a denominator chosen to minimize the direct, voltage-dependent contribution of the shot noise from the sources, thus focusing on the signal of interest generated at the analyzer. This expression generalizes the definition of P introduced in Ref. [33] beyond the asymptotic limits $1-\tau_{t,b,c} \ll 1$ (where at large bias $S_\Sigma \approx 2e^* I_+$), in the same spirit as in Ref. [32]. Note that τ_c in the denominator remains the simultaneously measured differential transmission probability given by Eq. (2) including in the presence of asymmetric incident quasiparticle beams. This is in contrast to Ref. [33] with quantitative consequences for asymmetric sources as further discussed in Sec. IV C.

B. Fermions

In the Landauer-Büttiker framework for noninteracting electrons, the cross-correlations can be written as [40]

$$\langle \delta I_L \delta I_R \rangle = -2\tau_c(1-\tau_c)(e^2/h) \int d\epsilon [f_t(\epsilon) - f_b(\epsilon)]^2, \tag{7}$$

where $f_{t,b}$ are the energy distribution functions of electrons incoming on QPC_c from the top (t) and bottom (b) paths. The cross-correlations and, consequently, P are, thus, expected to robustly vanish in the symmetric limit, whenever $f_t \simeq f_b$ (positive cross-correlations are expected within the bosonic density wave picture emerging for interacting, adjacent integer quantum Hall channels [35]). Furthermore, in the dilute incident beam limit where $|f_t - f_b| \ll 1$, P remains asymptotically null even in the presence of an asymmetry. In this limit and for symmetric configurations, the contrast is, thus, particularly striking with the cross-correlations predicted for anyons.

C. Anyons

Theoretical solutions for the source-analyzer setup were obtained for Laughlin fractions $\nu = 1/(2p+1)$ at low temperatures ($e^* V_{t,b} \gg k_B T$), in the WBS regime of the source $\mathrm{QPC}_{t,b}$ ($1-\tau_{t,b} \ll 1$), and in both the WBS ($1-\tau_c \ll 1$) [33] and SBS ($\tau_c \ll 1$) [36] regimes for the analyzer QPC_c.

1. Braiding

We consider configurations with all QPCs in the WBS regime ($1-\tau_{t,b,c} \ll 1$), where the occurrence of a nontrivial fractional exchange phase θ between anyons is predicted to play a crucial role [33,34,44]. The prediction for the effective Fano factor P defined in Eq. (6) with τ_c given by Eq. (2) reads [33]

$$\begin{aligned} P_{\mathrm{thy}}^{\mathrm{WBS}}(I_-/I_+) = {} & -4\Delta/(1-4\Delta) \\ & + |I_-/I_+| \left\{ \left(\tan 2\pi\Delta + \frac{(1-4\Delta)^{-1}}{\tan 2\pi\Delta} \right) \right. \\ & \left. \times \tan\left[(4\Delta - 2) \arctan \frac{|I_-/I_+|}{\tan 2\pi\Delta} \right] \right\}, \end{aligned} \tag{8}$$

with $I_\pm \equiv I_t \pm I_b$ and Δ the quasiparticles' scaling dimension, which is related to the exchange phase through $\theta = 2\pi\Delta$ and, for Laughlin fractions, given by $\Delta = \nu/2$

(see, e.g., Ref. [43]). Note that the above formulation ignores possible nonuniversal complications, such as edge reconstruction (see Ref. [33] for a discussion of such artifacts and Ref. [34] for an alternative formulation of $P_{\rm thy}^{\rm WBS}$ at $I_- = 0$ separating the different contributions of braiding phase, topological spin, and tunneling exponent). In the symmetric case ($I_- = 0$), Eq. (8) simplifies into $P_{\rm thy}^{\rm WBS}(0) = -4\Delta/(1-4\Delta)$, which gives $P_{\rm thy}^{\rm WBS}(0) = -2$ at $\nu = 1/3$ and progressively less negative values for lower ν in the Laughlin series.

As mentioned below Eq. (6), the dependence in I_-/I_+ of $P_{\rm thy}^{\rm WBS}$ is different from Ref. [33]. This stems from a different definition for τ_c at $I_- \neq 0$. Indeed, multiple definitions are possible for τ_c, corresponding to different quantitative predictions for this transmission and, consequently, a different P (see Table II). In particular, it could be defined as the differential transmission of the current originating from the electrode voltage biased at $V_{t,b}$ [τ_c given by Eq. (2)] or from the other, grounded electrode feeding the source QPCs ($\tau_c^{\rm ter}$ in Table II). With sources in the WBS regime, the former τ_c corresponds to the transmission across the analyzer of dilute quasiparticles of energy $\sim e^*V$, whereas the latter $\tau_c^{\rm ter}$ is essentially the transmission of a thermal current. As the transmission is predicted to strongly depend on energy in the FQHE regime, using these different definitions in Eq. (6) for P clearly results in strongly different theoretical values, as summarized in Table II (see also Fig. 5). Note that, in Ref. [33], the alternative definition $\tau_c^{\rm bis}$ relies on the same expression [Eq. (2)] but for $I_- = 0$, even for cross-correlations measured at $I_- \neq 0$. As τ_c is expected to depend on I_-, this impacts the prediction for $P(I_-/I_+ \neq 0)$.

2. Andreev reflection

We consider here the "Andreev" configuration where $\mathrm{QPC}_{t,b}$ remain in the WBS regime while QPC_c is set in the SBS regime ($\tau_c \ll 1$). In this case, quasielectrons of charge e are tunneling across QPC_c [10,11,37,46]. As the braid phase between such a quasielectron and the impinging fractional quasiparticles is a trivial 2π for the Laughlin quantum Hall fractions [4,43], the previously discussed transport mechanism driven by unconventional anyon statistics here cancels out. Instead, a different Andreev-like process takes place, involving independent tunnelings of e accompanied by the simultaneous reflection of a hole of charge $-e(1-\nu)$ [36], as recently observed at $\nu = 1/3$ [37]. As a result, the cross-correlations are simply $-(1-\nu)$ times the shot noise on the tunneling current given by $2eI_+\tau_c$ and, at high bias $\nu eV \gg k_BT$, $P_{\rm thy}^{\rm SBS} \simeq -(1-\nu)/\nu$ independently of the ratio I_-/I_+ [36]. At $\nu = 1/3$, this gives $P_{\rm thy}^{\rm SBS} \simeq -2$, identical to the exchange-induced prediction at symmetry $P_{\rm thy}^{\rm WBS}(0) = -2$. Note that this matching is specific to $\nu = 1/3$ and does not apply to other Laughlin fractions. Importantly, a qualitatively distinctive feature of the Andreev-like process is its independence in I_-/I_+ [36,37].

TABLE II. Predicted $P_{\rm thy}^{\rm WBS}$ at $\nu = 1/3$ for alternative definitions of τ_c and different source settings (symmetric when $I_- = 0$ or fully asymmetric when $I_- = \pm I_+$, with $I_\pm \equiv I_t \pm I_b$). τ_c is the transmission ratio of incident quasiparticles, $\tau_c^{\rm bis}$ the same transmission ratio but at $I_- = 0$, and $\tau_c^{\rm ter}$ the transmission ratio of thermal excitations. The corresponding values of $P_{\rm thy}^{\rm WBS}$ are obtained, respectively, from Eq. (8) and Eqs. (F1) and (F2) in Appendix F.

	$P_{\rm thy}^{\rm WBS}$	
τ_c variants	$(I_- \ll I_+)$	$(I_- = I_+)$
$\tau_c(I_-, I_+)$ from Eq. (2)	−2	−4.9
$\tau_c^{\rm bis} \equiv \tau_c(I_- = 0, I_+)$ [33]	−2	−3.1
$\tau_c^{\rm ter} \equiv \tau_t^{-1}\partial V_L/\partial V_t'$ [34]	−0.8	−1.3

V. ANYON SIGNATURES AT $\nu = 1/3$

A. Representative anyon signature with symmetric sources

Figure 2 displays some of the QPC characterization data as well as the cross-correlation anyon signature for a representative WBS device tuning, with symmetric sources ($I_-/I_+ \ll 1$) at $T \simeq 35$ mK. The data shown as symbols in Figs. 2(a) and 2(c) are measured simultaneously, whereas the shot noise characterization of QPC_c shown in Fig. 2(b) is performed separately, slightly before, as it involves a direct voltage bias of the analyzer.

The sources $\mathrm{QPC}_{t,b}$ are set in the WBS limit, at $1 - \tau_{t,b} < 0.1$ for all the data in this section [see illustrative schematic and inset in Fig. 2(c)]. The charge $e_{t,b} \approx e/3$ of the emitted quasiparticles is attested by the comparison in Fig. 2(a) with the standard shot noise expression Eq. (3). The measured noise sum S_Σ [Eq. (4)], corresponding to the shot noise from both sources, is found in close agreement with $e^* = e/3$ at $T = 35$ mK (a similar matching is obtained from individual source characterizations performed separately). Note that we limit the applied bias voltage to $|V_{t,b}| \lesssim 100$ μV.

The analyzer QPC_c transmission $\tau_c \approx 0.7$ simultaneously measured in the source-analyzer configuration, with impinging dilute quasiparticle beams, is shown in the inset in Fig. 2(c). The larger experimental noise, particularly marked at low I_+, simply reflects the lower amount of current probing τ_c at the corresponding low values of $1 - \tau_{t,b}$. The shot noise characterization in Fig. 2(b) is separately performed from the cross-correlations measured in the presence of a direct voltage bias (see Appendix E for autocorrelations and S_Σ data). A good agreement is observed with the negative of Eq. (3) for $e^* = e/3$ and $T = 35$ mK. Note that, at relatively low voltages

($e^*V \sim k_BT$), the data exhibit a noticeably larger slope than the phenomenological Eq. (3), which is expected from exact predictions for the thermal rounding [42,43]. In practice, following standard procedures, we extract the tunneling charge e_c by fitting the cross-correlations at voltages above the thermal rounding [$e_cV \gtrsim 3k_BT$, with here $e_c \simeq 0.30e$; see also Fig. 3(a)].

The main cross-correlation signal in the presence of symmetric beams of incident quasiparticles is normalized by $\tau_c(1-\tau_c)$ and plotted in the main panel in Fig. 2(c) as a function of the noise sum S_Σ. In this representation, the experimental value of P is straightforwardly obtained from a linear fit of the data. The dashed line corresponds to $P \simeq -1.9$.

Although the quantitative agreement with the prediction $P_{\rm thy}^{\rm WBS}(0) = -2$ is striking and corroborates the pioneer observation [32], it is nevertheless counterbalanced by the strong dependence of $P_{\rm thy}^{\rm WBS}$ on the specific definition of τ_c (see Table II). This is in contrast with the weakly dependent experimental P. Indeed, we observe in practice $\tau_c \sim \tau_c^{\rm bis} \sim \tau_c^{\rm ter}$ (with discrepancies smaller than 10%, of the order of our *in situ* experimental resolution on τ_c), thus leaving P mostly unchanged, as opposed to the different predictions. This situation can be traced back to the bias voltage dependence of τ_c that sharply differs from the expected power law $1-\tau_c \propto V^{2\nu-2}$ [47] [see the inset in Fig. 2(c) for a representative weak dependence of τ_c and also Appendix E for a measurement as a function of a direct voltage bias]. Nevertheless, the qualitative observation of a nonzero, negative P in the WBS regime with symmetric quasiparticle beams remains a significant, robust feature. This constitutes in itself a key marker of unconventional exchange statistics.

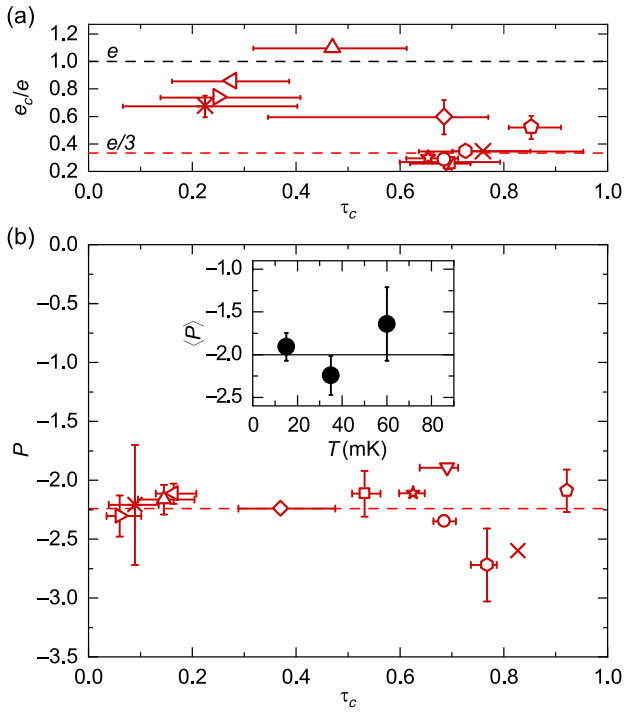

FIG. 3. $P(I_- \approx 0)$ versus analyzer tuning at $\nu = 1/3$. Identical symbols represent measurements for the same device tuning [τ_c differs in (a) and (b) because of the different biasing]. Error bars are shown if larger than symbols. The horizontal error bars encompass the variation of τ_c in the range of biases where e_c (a) or P (b) are extracted. The vertical error bars encompass the difference between measurements at negative and positive voltages. (a) Analyzer crossover from $e_c \approx e/3$ to e. (b) Indiscernible crossover in $P(I_- \approx 0, \tau_c)$. The horizontal dashed line displays the mean value $\langle P\rangle \simeq -2.2$. Inset: mean value $\langle P\rangle$ versus temperature. The vertical error bars show the standard deviation between values of P for individual analyzer settings.

B. Intriguing robustness of $P(I_- \approx 0)$ versus analyzer tuning

Figure 3 synthesizes our measurements of P at $\nu = 1/3$ while broadly changing the tuning of QPC_c from WBS to SBS (with the sources remaining in the WBS regime and symmetric, $I_- \ll I_+$). As detailed below, whereas the predicted underlying mechanism changes from anyon braiding to Andreev, no signature of this crossover is discernible in $P(I_- \approx 0, \tau_c)$. Although there is no contradiction with theory, this calls for additional ways to directly distinguish the two mechanisms.

The crossover from $e_c \approx e/3$ to e as τ_c is reduced is established in Fig. 3(a) [10,11,46]. Accordingly, a different Andreev transport mechanism is expected to dominate at $\tau_c \lesssim 0.5$, as predicted [36] and recently observed on the same sample [37]. Although an identical value $P = -2$ is asymptotically predicted for both WBS and SBS tunings of the analyzer, signatures of the crossover between different underlying mechanism could have emerged at intermediate τ_c. This is not the case. Instead, a remarkable robustness of P versus τ_c is observed, as shown in the main panel in Fig. 3(b) for $T \simeq 35$ mK. This observation is confirmed at $T \simeq 15$ and 60 mK as can be inferred from the mean and standard deviation of P displayed for different T in the inset. With no signature of a change of an underlying mechanism materializing along the crossover from WBS to SBS, it is highly desirable to have a direct signature that differentiates between braiding and Andreev processes.

C. Distinguishing anyon braiding and Andreev mechanisms

A distinctive feature of the unconventional anyon braiding mechanism, contrasting with the Andreev process, is that different incident quasiparticles do not contribute independently to the cross-correlations. A straightforward test confirming this discriminating property is displayed in Fig. 4.

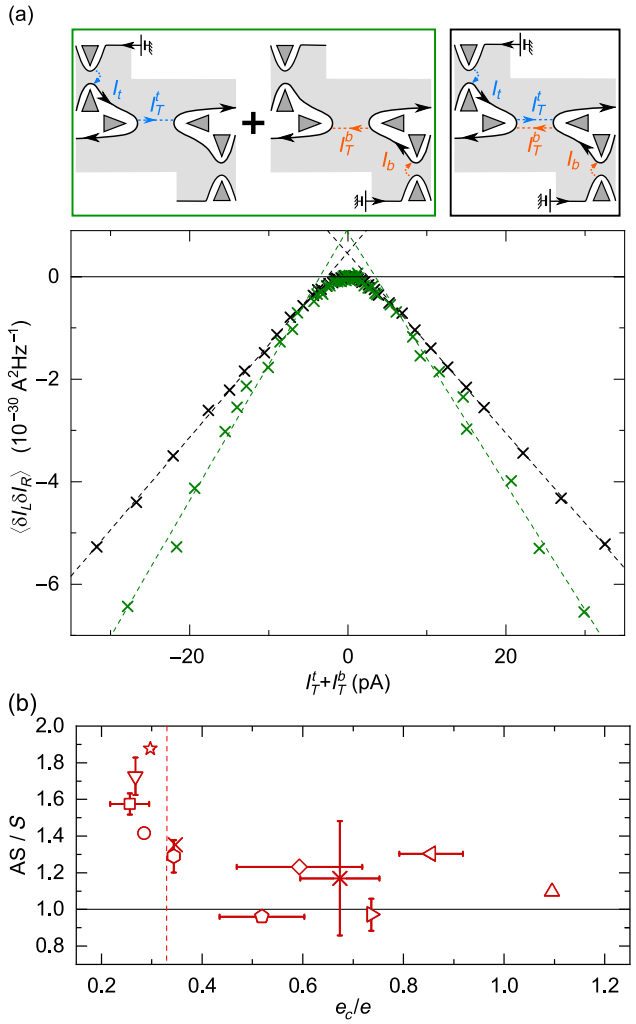

FIG. 4. Discriminating anyons braiding from Andreev mechanisms. (a) Cross-correlations with QPC_c set to $e_c \approx e_{t,b} \approx e/3$. The data (symbols, corresponding to those in Fig. 3) are displayed as a function of the sum $I_T^t + I_T^b$ of tunneling currents from the top and bottom sources (see the inset; arrows indicate the sign + convention). Black crosses are obtained with two symmetric incident beams $I_t \approx I_b$. Green crosses show the sum of independent measurements $\langle \delta I_L \delta I_R \rangle(I_t) + \langle \delta I_L \delta I_R \rangle(I_b)$, using either QPC_t or QPC_b as a single source, versus $I_T^t(I_t) + I_T^b(I_b)$. Dashed lines are linear fits. The significantly larger slope in the asymmetric case (green) rules out Andreev processes and is consistent with the predicted anyon exchange mechanism. (b) Symbols represent the ratio (AS/S) of the slopes $\langle \delta I_L \delta I_R \rangle / (I_T^t + I_T^b)$ between asymmetric [one source at a time (AS)] and symmetric [two sources (S)] incident quasiparticle beams versus separately characterized e_c/e. Error bars encompass the difference between values extracted at negative and positive applied voltages for the same device setting. A ratio close to unity is found for $e_c \gtrsim 0.5 > e_{t,b} \approx e/3$, where the charge mismatch favors Andreev processes.

As graphically illustrated in Fig. 4(a), we compare, on the one hand, the sum of the cross-correlation signals measured alternatively with a single active source ($V_t \neq 0$ with $V_b = 0$, and $V_b \neq 0$ with $V_t = 0$; green) with, on the other hand, the cross-correlations measured when both sources are symmetrically biased ($V_t = V_b \neq 0$; black). For Andreev processes, the two match, as previously observed [37]. This is not the case when the underlying mechanism is the unconventional anyon exchange phase. A representative comparison is displayed in Fig. 4(a) for the analyzer set in the WBS regime ($\tau_c \simeq 0.83$ with $e_c \simeq 0.34e$) where the anyon exchange mechanism is expected. The marked difference between symmetric (black) and fully asymmetric (green) incident quasiparticle beams confirms that the underlying mechanism is not the Andreev process.

Figure 4(b) presents a systematic comparison for different analyzer tunings along the crossover between unconventional anyon exchange and Andreev mechanisms. It is quantified by the displayed asymmetric to symmetric ratio AS/S between fitted linear slopes [e.g., dashed lines in Fig. 4(a)], plotted as a function of the parameter e_c/e driving the crossover. When $e_c \approx e/3$ (vertical dashed line), we systematically observe substantially larger cross-correlations in the asymmetric configuration, whereas for larger values of e_c the asymmetric to symmetric configuration ratio approaches 1. This signals a change of underlying transport mechanism when increasing e_c, providing experimental support to the theoretical expectations of a crossover from unconventional exchange to Andreev processes.

The important dependence in the symmetry between incident beams of dilute quasiparticles, specifically observed when $e_c \approx e/3$, constitutes a second qualitative marker of the unconventional exchange phase of the quasiparticle.

D. P versus I_-/I_+

We now confront quantitatively $P(I_-/I_+)$ data and the Eq. (6) prediction.

The experimental values of P obtained for the analyzer QPC_c set to $\tau_c \simeq 0.7$ with $e_c \simeq 0.3e$ are displayed versus I_-/I_+ in Fig. 5. For each data point, the ratio V_t/V_b is kept fixed while sweeping $V_{t,b}$. Note that the variation of $|I_-/I_+|$ during each sweep, represented by the horizontal error bars, results from the unequal evolutions of $\tau_t(V_t)$ and $\tau_b(V_b)$. The theoretical prediction of Eq. (6) is shown as a red continuous line. For a more complete assessment, the predictions for $P_{\mathrm{thy}}^{\mathrm{WBS}}$ with the alternative definitions τ_c^{bis} and τ_c^{ter} (see Table II) are also displayed as, respectively, black and blue dashed lines.

Theory predicts weak changes of P at low $|I_-/I_+|$, progressively becoming stronger for higher asymmetries, consistent with experimental observations. The expected ratio $P_{\mathrm{thy}}^{\mathrm{WBS}}(1)/P_{\mathrm{thy}}^{\mathrm{WBS}}(0) \simeq 2.5$ is in order-of-magnitude agreement with the experimental value $P(1)/P(0) \sim 1.5$.

Overall, the observed reasonable agreement between data and theory further corroborates the underlying presence of anyons of fractional exchange phase.

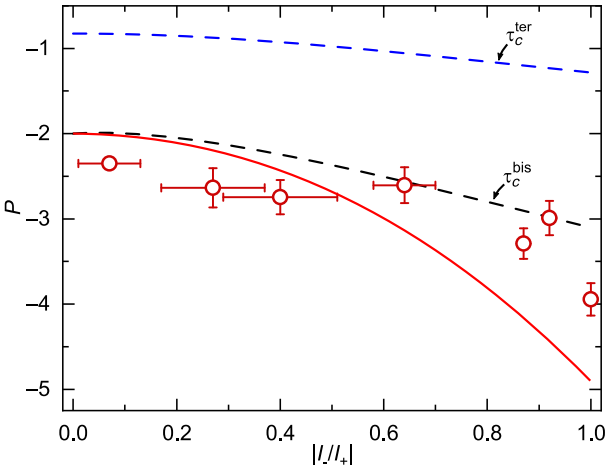

FIG. 5. P versus source imbalance at $\nu = 1/3$. Symbols display the effective Fano factor P as a function of the relative difference in incident currents I_-/I_+, for the same device tuning. Horizontal error bars encompass variations in I_-/I_+ over the range of applied voltages. Vertical error bars represent the difference between values of P separately extracted at negative and positive voltages. The prediction of Eq. (8) is shown as a red continuous line. The alternative predictions shown as dashed lines involve the different definitions τ_c^{bis} (black) and τ_c^{ter} (blue) (see Table II and Appendix F).

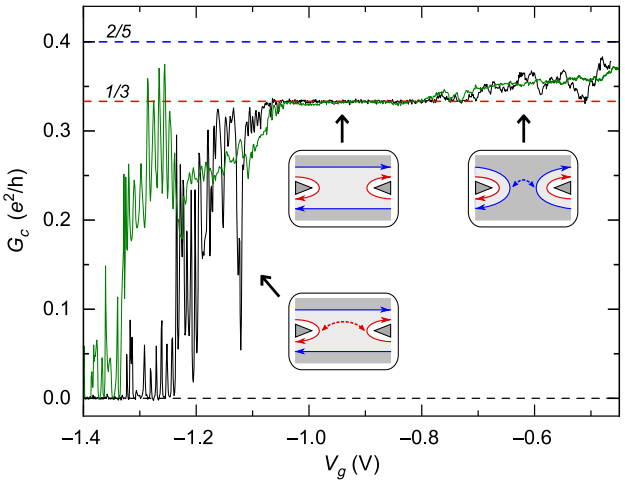

FIG. 6. Differential conductance G_c through the analyzer QPC_c at $\nu = 2/5$ as a function of the applied gate voltage V_g (detailed features may vary with overall device configuration). The black and green continuous lines display measurements, respectively, in the absence of a dc bias ($V_t = V_t' = V_b = 0$) and in the presence of a direct dc voltage bias ($V_t = V_t' = -90$ μV, $V_b = 0$). The robust $e^2/3h$ plateau, where the absence of excess noise is separately checked, ascertains the sequential channel opening illustrated schematically. Note the relatively weak voltage bias dependence at $G_c > e^2/3h$, when the inner (outer) edge channel is partially (fully) transmitted.

VI. ANYON SIGNATURES AT $\nu = 2/5$

A. Edge structure

At $\nu = 2/5$, two adjacent channels are predicted to propagate in the same direction along each edge. Quasiparticles of charge $e^* = e/5$ have been observed along the inner channel of conductance $\nu_{\rm eff} e^2/h$ with $\nu_{\rm eff} = 1/15$ [14]. These quasiparticles are predicted to have a fractional exchange phase $\theta = 3\pi/5$ [$\theta = 2\pi\Delta$ with $\Delta = (e^*/e)^2/2\nu_{\rm eff}$; see, e.g., Ref. [43]].

This edge structure is first attested by the dependence $G_c(V_g)$ of the differential conductance G_c across the analyzer QPC_c with the voltage V_g applied to the metallic split gates controlling this constriction. Figure 6 shows $G_c(V_g)$ measured both at zero dc bias voltage (black line) and at 90 μV (green line). The robust intermediate plateau at $G_c = e^2/3h$ corresponds to the full transmission of the outer edge channel, of conductance $e^2/3h$, and the total reflection of the inner edge channel. For less negative V_g, the higher $G_c > e^2/3h$ reflects the subsequent opening of the inner edge channel of present interest. The sequential, separated opening of the two channels is confirmed by the absence of excess noise when applying a dc voltage bias to QPC_c set on the $e^2/3h$ plateau. The current transmission ratio of the inner edge channel at $G_c \geq e^2/3h$ hence reads $(G_c - e^2/3h)/(e^2/15h)$ [corresponding to τ_c given by Eq. (2) in that direct voltage bias case]. Note that G_c does not reach the maximum value of $(2/5)e^2/h$ (horizontal blue dashed line), as it is not possible to fully open the inner channel across any of the QPCs. The maximum inner channel transmission achieved is $\tau_c \approx 0.9$ [see the inset in Fig. 11(d)]. We refer to Appendix E for checks of the chirality of the electrical current in the central part of the device.

In the presence of two channels copropagating along each edge, a transfer (tunneling) of charges between adjacent channels along the source-analyzer paths could occur. As this results in an additional negative contribution to the measured cross-correlations $\langle \delta I_L \delta I_R \rangle$, its amplitude is carefully calibrated (see Appendix D). The tunneling current, made of $e/3$ quasiparticles as predicted [48], approaches at most 20% of the injected inner channel current. A systematic procedure is set to estimate and subtract the tunneling current contribution to the cross-correlation signal (see Appendix D). Importantly, the qualitative markers of braiding are not affected by this contribution; only the quantitative value of P is modified, by at most 20%.

B. Representative anyon signature with symmetric $e/5$ sources

Apart from interchannel tunneling, the QPC characterization and P extraction procedures are similar to those at $\nu = 1/3$, as illustrated in Fig. 7. A charge $e_{t,b} \simeq e/5$ for the quasiparticles emitted by the sources is obtained simultaneously with the measurement of P, by comparing the

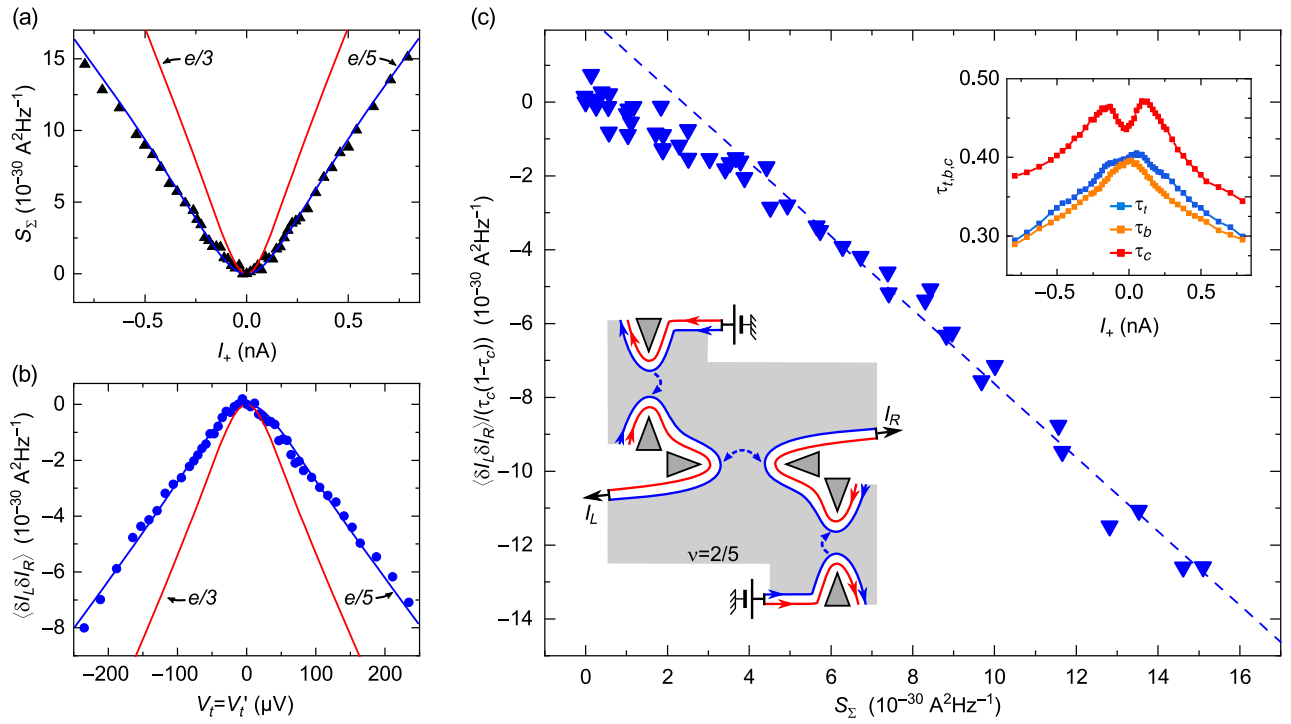

FIG. 7. Cross-correlation signature of anyons in the inner edge channel at $\nu = 2/5$. The sources are symmetrically voltage biased ($V_t = V_b$, $V_t' = 0$) except for the separate analyzer characterization in (b), where $V_t = V_t'$ ($V_b = 0$) implements a direct voltage bias. (a),(b) Shot noise characterization of the charges $e_{t,b}$ emitted from the sources (a) and of the tunneling charge e_c across the analyzer (b). The shot noise data (symbols) are compared with the predictions for $e^* = e/5$ (blue lines) and $e/3$ (red lines). (c) Experimental determination of P. The normalized cross-correlation data, from which the estimated interchannel tunneling contribution (see Appendix D) is removed, are plotted as symbols as a function of the same S_Σ also shown in (a). $P \simeq -1.0$ is obtained from a linear fit of the slope (blue dashed line). Inset: simultaneous measurements of $\tau_{t,b,c}$.

noise sum S_Σ with the standard shot noise expression Eq. (3) [see Fig. 7(a) for the simultaneous characterization of the sources]. Note that S_Σ is not directly impacted by interchannel tunnelings, as these processes preserve the overall current downstream from the sources. The characterization of $e_c \simeq e/5$ is performed separately, analogous to $\nu = 1/3$, from the cross-correlations measured in the presence of a direct voltage bias applied to QPC$_c$ [see Fig. 7(b)]. Note that, unexpectedly, the noise sum S_Σ [not shown in Fig. 7(b); see Fig. 14(c)] is far from negligible, although no voltage bias is applied to the sources in this configuration. This might be related to a nonlocal heating, with most likely little impact on our conclusions (see Appendix E for further discussion). The extraction of P from the slope of the cross-correlation signal normalized by $\tau_c(1-\tau_c)$ versus S_Σ is shown in the main panel in Fig. 7(c). We obtain in this representative example $P \simeq -1.0$ (dashed line; we extract $P \simeq -1.07$ from the raw data including interchannel tunneling). Qualitatively, the observed negative P at symmetry indicates an unconventional anyon exchange phase. Quantitatively, this is a markedly weaker value than the observed $P \approx -2$ at $\nu = 1/3$.

C. P for symmetric $e/5$ quasiparticle sources

Here, we recapitulate the experimental effective Fano factor P obtained for $e/5$ quasiparticles on five different device configurations (see Fig. 8).

The analyzer displays a rather stable characteristic charge of $e_c \approx e/5$, adapted to investigate the statistics of the corresponding quasiparticles, over a relatively broad explored range $\tau_c \in [0.2, 0.8]$ [see Fig. 8(a)]. Note that, for each tuning of QPC$_c$, the sources QPC$_{t,b}$ require gate voltage adjustments in order to preserve their symmetry. In practice, the sources exhibit similar shot noise signatures of $e/5$ emitted quasiparticles, in comparably good agreement with Eq. (3) than in the representative Fig. 7(a). Note that the transmissions across QPC$_{t,b}$ remain here within the range $\tau_{t,b} \in [0.25, 0.5]$, away from the dilute quasiparticle source limit that is experimentally not accessible. The extracted values of P are recapitulated in Fig. 8(b), with symbols matching those in Fig. 8(a) for identical device configurations (the different τ_c result from the different biasing of QPC$_c$). The blue symbols represent P obtained from the corrected cross-correlation signal, from which the contribution of interchannel tunneling is subtracted. The green symbols are the values of P extracted from the raw

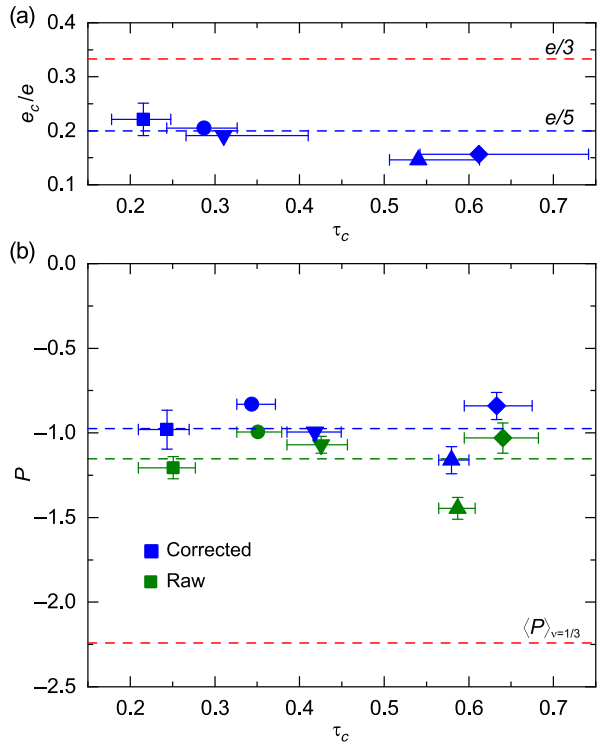

FIG. 8. Effective Fano factor for $e/5$ quasiparticles at $\nu = 2/5$. (a) Separately characterized analyzer tunneling charge e_c versus τ_c. (b) Experimental value of P with (blue symbols) and without (green symbols) correcting for interchannel tunneling. The same symbol as in (a) represents an identical device tuning (τ_c changes due to a different biasing). The horizontal dashed lines indicate the corresponding mean values $\langle P \rangle \simeq -0.97$ (blue) and $\langle P \rangle \simeq -1.15$ (green), together with the $\nu = 1/3$ observation $\langle P \rangle \simeq -2.24$ (red). Error bars are displayed in (a) and (b) when larger than the symbols. Horizontal error bars display the variation of τ_c during the measurement. Vertical error bars show the difference between values obtained separately for negative and positive applied voltages.

cross-correlations. The effect of interchannel tunneling remains relatively small (approximately 20%) with respect to the overall value of P, and it does not introduce any noticeable trend. Similarly to $\nu = 1/3$, P does not exhibit a significant dependence on τ_c. However, in contrast, no crossover to a different Andreev-like mechanism could develop, as there is here no mismatch between $e_{t,b}$ and e_c. The simple observation of negative cross-correlations (much higher than from interchannel tunnelings), thus, points to a unconventional anyon exchange phase for the investigated $e/5$ quasiparticles. Note that an exploration of the influence of an asymmetry between sources, used at $\nu = 1/3$ to distinguish with Andreev physics, is here impeded by the high minimum values of experimentally accessible $1 - \tau_{t,b} \gtrsim 0.5$, for which an applied asymmetry corresponds to a complex combination of incident quasiparticles and direct voltage bias.

Quantitatively, we find an average value of $\langle P \rangle \simeq -0.97$ represented by a blue horizontal dashed line in Fig. 8(b) ($\langle P \rangle \simeq -1.15$ from the raw data including interchannel tunneling). The theory developed for Laughlin fractions [33], and recently extended to a non-Abelian channel [34], does not yet fully encompass hierarchical states such as $\nu = 2/5$. Nevertheless, assuming that the outer channel of conductance $e^2/3h$ can be ignored, the same prediction $P = -4\Delta/(1 - 4\Delta)$ applies with the corresponding scaling dimension of the $e/5$ quasiparticles $\Delta = (e^*/e)^2/2\nu_{\text{eff}} = 0.3$ [49]. The resulting $P = 6$ is, however, much larger than observed and, intriguingly, positive. The culprit for the sign change in this generalized prediction is not the cross-correlations, which remain negative as measured, but a differential transmission τ_c becoming negative for dilute beams of such quasiparticles [33]. Here, we observe conventional, positive transmissions [see the inset in Fig. 7(c)]. The important role of τ_c in the theoretical value of P, with even more drastic consequences than at $\nu = 1/3$, impedes the extraction of quantitative information on the specific anyon exchange phase. It remains that the observation of strong negative cross-correlations constitutes a qualitative marker of unconventional exchange statistics.

VII. CONCLUSION

Noise evidence of exotic anyon braiding statistics for fractional quasiparticles of charge $e/3$ and $e/5$ are observed in a source-analyzer setup. This signature holds provided the analyzer QPC favors the transmission of the same type of quasiparticles as those emitted at the sources and for relatively weak interchannel tunnelings along the source-analyzer paths. Different values for the cross-correlation effective Fano factor $P \approx -2$ and $P \approx -1$ are obtained, respectively, for $e/3$ quasiparticles at $\nu = 1/3$ and $e/5$ quasiparticles along the inner channel at $\nu = 2/5$ (in contrast with $P \approx 0$ observed at $\nu = 2$; see Appendix C). It is tempting to attribute this difference to the distinct predicted exchange phases $\pi/3$ and $3\pi/5$. However, the quantitative connection to P is not direct but involves the dependence of the analyzer transmission τ_c on the voltages $V_{t,b}$ used to generate the quasiparticles. In practice, as generally observed experimentally in the fractional quantum Hall regime [50,51], the transmission across QPCs does not follow the predicted voltage bias dependence, which impedes any quantitative information on the exchange phase beyond its unconventional character. A promising alternative to overcome this limitation is to combine such a source-analyzer setup with a quantum circuit implementation of Luttinger liquids [3,52] where QPCs are found to accurately follow the theoretical predictions [53,54].

ACKNOWLEDGMENTS

This work was supported by the European Research Council (ERC-2020-SyG-951451), the European Union's

Horizon 2020 research and innovation program (Marie Skłodowska-Curie Grant Agreement No. 945298-ParisRegionFP), the French National Research Agency (ANR-16-CE30-0010-01 and ANR-18-CE47-0014-01), and the French RENATECH network. We thank A. Kolli and C. Loup-Forest for their help in the $\nu = 2$ measurements and C. Mora, H.-S. Sim, D. C. Glattli, C. Han, T. Jonckheere, D. Kovrizhin, and I. Safi for helpful discussions.

O. M. and P. G. performed the experiment and analyzed the data with inputs from A. Aassime, A. Anthore, C. P., and F. P.; A. C. and U. G. grew the 2DEG; A. Aassime, F. P., O. M., and P. G. fabricated the sample; Y. J. fabricated the HEMT used in the cryogenic noise amplifiers; F. P., O. M., and P. G. wrote the manuscript with contributions from A. Aassime, A. Anthore, C. P., and U. G.; A. Anthore and F. P. led the project

Note added.—Our results are consistent with the independent investigation by Ruelle *et al.* [55] submitted simultaneously with the present work. Relatively small quantitative discrepancies in P for the inner channel at $\nu = 2/5$ may be attributed to a different normalization procedure, where the measured S_Σ here [see Eq. (6)] is replaced by the ideal Poissonian noise $2(e/5)I_+$ in Ref. [55]. Recently, we also became aware of the related work Ref. [49], supporting anyon braiding statistics at $\nu = 1/3$ from a quantitative analysis of the autocorrelations in a single-source-analyzer setup.

APPENDIX A: DEVICE

The measurements are performed on the same device previously used to evidence Andreev-like processes [37]. Note that the Ga(Al)As heterojunction hosting the 2D electron gas is similar to that used in the pioneer "collider" experiment [32] and is grown in the same MBE chamber at a different time.

The nanofabrication followed standard e-beam lithography steps (see Methods in Ref. [37] for further details and large-scale pictures of the sample): (i) Ti-Au mark deposition through a PMMA mask. (ii) Wet mesa etching in a solution of $H_3PO_4/H_2O_2/H_2O$ through a positive ma-N 2403 mask. (iii) Contact Ohmic deposition of Ni-Au-Ge through a PMMA mask, followed by a 440 °C annealing for 50 s. (iv) Al gate deposition through a PMMA mask. (v) Deposition of Ti-Au bonding ports and large-scale interconnects through a PMMA mask.

Figure 9 shows the two-wire measurement at $T \sim 100$ mK of the resistance between an Ohmic contact and cold grounds as a function of the magnetic field (a fixed wiring and filtering resistance of 10.35 KΩ is subtracted). The experiments are performed in the center of the plateaus at $\nu = 1/3$, $2/5$, and 2, at the values indicated by vertical arrows. Note that the effective magnetic field range for the plateaus is, on the one hand, slightly reduced by density gradients over the sample and, on the other hand, increased by the temperature reduction when probing the anyon statistics.

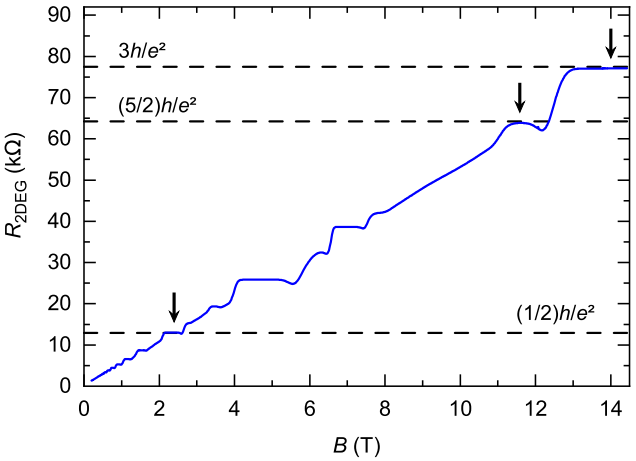

FIG. 9. Quantum Hall resistance plateaus. Two-wire resistance between an Ohmic contact and cold grounds measured as a function of the applied perpendicular magnetic field B at low temperature ($T \sim 100$ mK). Dashed lines show the fractional quantum Hall resistances $h/\nu e^2$ for the investigated fractions $\nu = 1/3$, $2/5$, and 2. Vertical arrows indicate the magnetic field at which the measurements are performed.

The Ohmic contacts have a large perimeter of approximately 200 μm with the 2D electron gas to ascertain an essentially perfect electrical connection (usually already achieved for perimeters of about 10 μm with our recipe). The Ohmic contact quality together with the robustness of edge transport chirality in the 2DEG is attested by (i) the accurate resistance of the quantum Hall plateaus, (ii) the absence of current reflected from Ohmic contacts connected to a cold ground, and (iii) the absence of excess shot noise when closing all the QPCs and applying a voltage bias.

APPENDIX B: EXPERIMENTAL SETUP

1. Measurement setup

Measurements are performed in a cryofree dilution refrigerator, where the sample is connected through electrical lines including several thermalization and filtering stages (see Ref. [56] for comprehensive technical details).

Auto- and cross-correlations of current fluctuations are measured near 1 MHz using two homemade cryogenic HEMT amplifiers (see supplemental material in Ref. [57] for further information), respectively, connected to the L and R ports of the sample as schematically depicted in Fig. 1(c).

All other measurements are performed with standard lock-in techniques, using ac modulation of rms amplitude below k_BT/e and at frequencies lower than 25 Hz. The transmitted dc currents are obtained by integrating the

corresponding lock-in differential signal with respect to the applied bias voltage (explicit expressions are provided in Methods in Ref. [37]).

2. Thermometry

At $T > 40$ mK, the electronic temperature is determined using a calibrated RuO_2 thermometer, thermally anchored to the mixing chamber of the dilution refrigerator. In this range, the thermal noise of the sample changes linearly with T, confirming both the RuO_2 thermometer calibration and the good thermalization of the charge carriers in the device.

To obtain an *in situ* electronic temperature below 40 mK, we measure the thermal noise and extrapolate the noise-temperature slope determined at higher T.

3. Noise amplification chain calibration

The gain factors $G^{\text{eff}}_{L,R,LR}$ relating the raw auto- and cross-correlations with the power spectral density of current fluctuations of interest is calibrated in two steps.

First, the nearly identical tank circuits connected to the Ohmic contacts labeled L and R are characterized. This is achieved by measuring the variation of the noise bandwidth of each of the tank circuits in parallel with the quantum Hall resistance of the sample at several filling factors, which informs on the parallel tank resistance $R_{\text{tk}} \approx 150$ kΩ and capacitance $C_{\text{tk}} \approx 135$ pF. The resonant frequency (0.86 MHz) then provides the parallel tank inductance $L_{\text{tk}} \approx 250$ μF.

Second, with our choice of noise integration bandwidth ([0.84, 0.88] MHz at $\nu = 2/5$ and $1/3$), we measure the slopes s_{tk} of raw integrated noise versus temperature at $T > 40$ mK (see Appendix B2). The robust fluctuation-dissipation relation then gives the gain factors $G^{\text{eff}}_{L,R} = s_{\text{tk}}/[4k_B(1/R_{\text{tk}} + \nu e^2/h)]$, whereas the nearly identical tanks imply for the cross-correlation $G^{\text{eff}}_{LR} = \sqrt{G^{\text{eff}}_L G^{\text{eff}}_R}$. See Ref. [37] for a more thorough presentation including checks with alternative methods.

APPENDIX C: CROSS-CORRELATION INVESTIGATION OF THE STATISTICS AT $\nu = 2$

As a counterpoint to anyons, we present here measurements of P with the device set in the integer quantum Hall

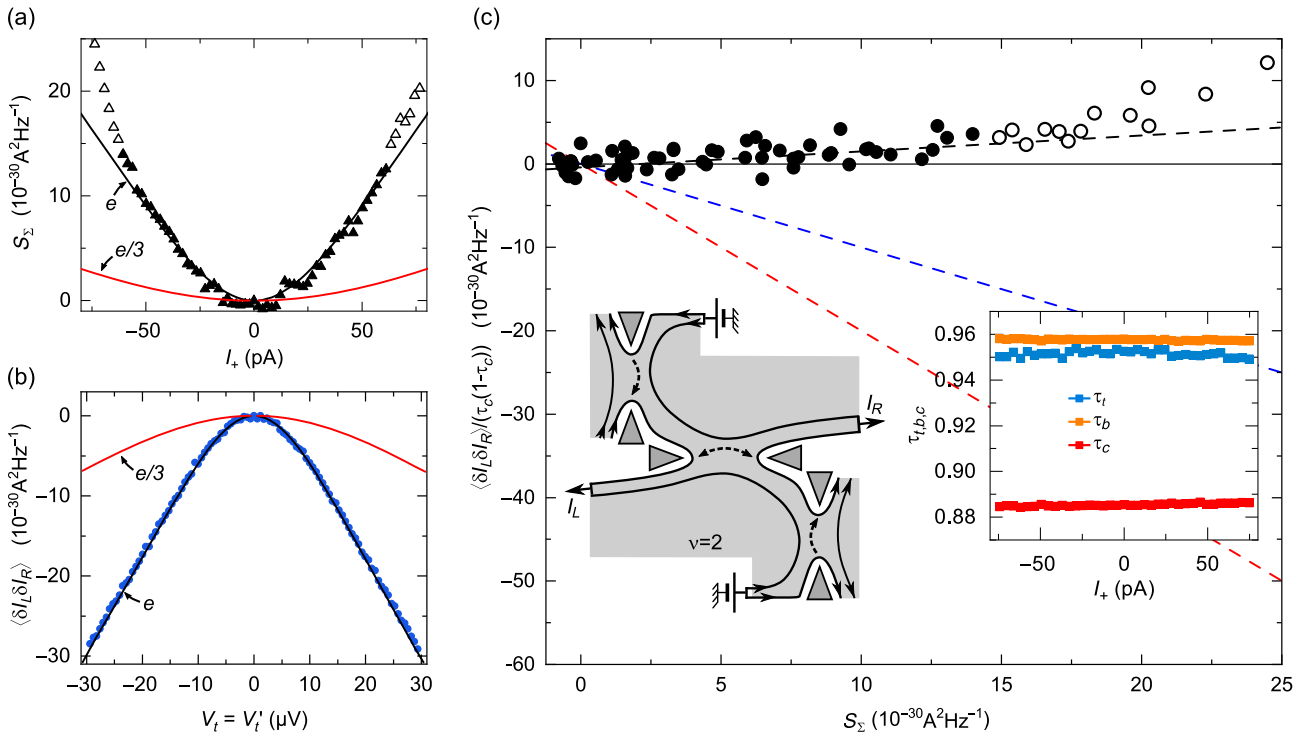

FIG. 10. Cross-correlations at $\nu = 2$ with symmetric sources. All QPCs are set in the WBS regime [$\tau_t \simeq \tau_b \simeq 0.96$ and $\tau_c \simeq 0.88$; see the inset in (c)] with $V_t = V_b$ and $V_t' = 0$, except for the analyzer characterization in (b), where $V_t = V_t'$ and $V_b = 0$ corresponding to a direct voltage bias applied to QPC_c. (a),(b) Shot noise characterization of the tunneling charges $e_{t,b}$ (a) and e_c (b). Symbols display the noise data, in close match with the prediction for a tunneling charge e (black lines) at $S_\Sigma \lesssim 15 \times 10^{-30}$ A^2/Hz (full symbols). (c) Cross-correlations measured in the symmetric source-analyzer configuration (symbols) are plotted versus source shot noise S_Σ. A linear fit at $S_\Sigma < 15 \times 10^{-30}$ A^2/Hz (black dashed line) gives $P \simeq +0.2$. The red and blue dashed lines represent the Fano factor obtained at $\nu = 1/3$ and $\nu = 2/5$, respectively. Inset: transmission probabilities of top (blue symbols), bottom (orange symbols), and central (red symbols) QPCs as a function of I_+.

regime at filling factor $\nu = 2$ ($B = 2.4$ T). In this regime, electrons with a Fermi statistics are emitted at the source QPCs and transmitted across the analyzer QPC. Note that interactions between the two copropagating channels are predicted to drive a transition of the propagating excitations from Fermi quasiparticles to bosonic density waves, resulting in the emergence of positive cross-correlations in the source-analyzer setup [35]. However, for the present short propagation distance of 1.5 μm and in the accessible small voltage bias range before artifacts develop $|V| \lesssim 30$ μV, the interactions between the two copropagating channels are essentially negligible [58,59]. Note also that interchannel tunneling is here completely negligible.

Figure 10 displays representative data obtained at $\nu = 2$, with symmetric sources emitting in the outer edge channel toward the analyzer. The procedure is identical to in the FQHE regime. Figures 10(a) and 10(b) show the tunneling charge characterization of the sources and analyzer, respectively, found to match the shot noise predictions for e in both cases. Note that a huge noise develops at high bias [emerging for the highest I_+ in Fig. 10(a)], thus limiting the investigated range. Figure 10(c) represents the cross-correlation signal in the source-analyzer configuration with symmetric incident dilute beams, normalized by $\tau_c(1-\tau_c)$ and plotted versus S_Σ. A linear fit of the data displayed as full symbols for which $S_\Sigma < 15 \times 10^{-30}$ A^2/Hz (black dashed line) gives $P \simeq 0.2$.

Although not exactly null, P is here very small with respect to the observed $P \simeq -2$ (red dashed line) and $P \simeq -1$ (blue dashed line) at $\nu = 1/3$ and $2/5$, respectively. The slight positive value may result from the essentially but not fully negligible interchannel interactions, which progressively change the nature of electronic excitations along the source-analyzer paths. The present small and positive $\nu = 2$ data, hence, corroborate the predicted link between negative cross-correlations and unconventional anyon statistics.

APPENDIX D: INTERCHANNEL TUNNELING AT $\nu = 2/5$

As illustrated in Fig. 11(a), interchannel tunnelings, if any, result in an additional negative contribution to the measured cross-correlations $\langle \delta I_L \delta I_R \rangle$, thereby impacting P. Indeed, a tunnel-induced current fluctuation δI in the outer channel is correlated to an opposite fluctuation $-\delta I$ in the inner channel. With a downstream QPC$_c$ of inner channel transmission ratio τ_c and perfectly transmitted outer channel, the resulting total current fluctuation (summed over both channels) in the transmitted and

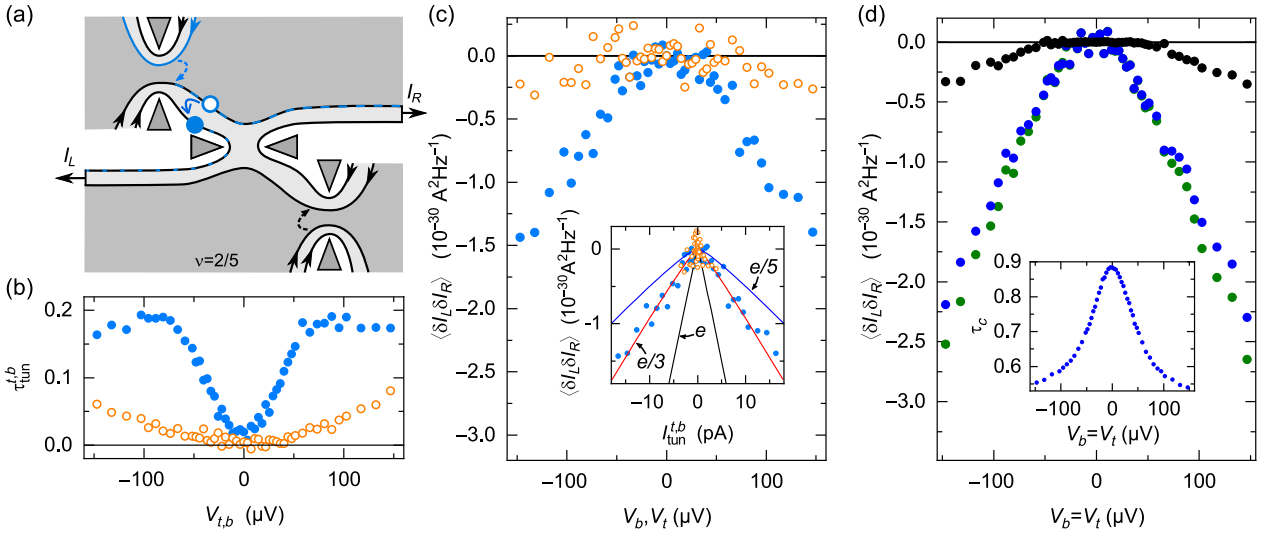

FIG. 11. Interchannel tunneling at $\nu = 2/5$. (a) Schematics of interchannel tunneling along the top source-analyzer path. For a separate characterization, QPC$_c$ is set to $\tau_c = 0$ (and a full transmission of the outer channel). (b) Interchannel tunneling fraction. Symbols display the ratio between tunneling and emitted current along the top ($\tau^t_{\rm tun}$, blue) and bottom ($\tau^b_{\rm tun}$, orange) paths, obtained at $\tau_c = 0$ from Eq. (D1). The displayed values approaching 20% are the highest observed in all investigated configurations. (c) Interchannel tunneling cross-correlations at $\tau_c = 0$. Symbols represent the separately obtained signals for tunnelings along the top (blue) and bottom (orange) paths, as a function of the dc bias voltage of the corresponding source V_t (with $V_b = 0$) and V_b (with $V_t = 0$), respectively. Inset: The same cross-correlations are plotted as a function of the corresponding interchannel tunneling current $I^{t,b}_{\rm tun}$ and compared with the shot noise predictions of Eq. (3) (lines). (d) Cross-correlations measured with QPC$_c$ tuned back to the inner channel analyzer ($\tau_c > 0$), with both sources symmetrically biased ($V_t = V_b$), are shown as green symbols. Black symbols display the interchannel tunneling contribution estimated from (c) [sum of data in (c) times $(1-\tau_c)^2$; see the text]. The resulting "corrected" cross-correlations (raw data reduced by tunneling estimate) are shown as blue symbols. Inset: simultaneously measured τ_c.

reflected L, R paths is $\delta I - \delta I\tau_c$ and $-\delta I(1-\tau_c)$, respectively, corresponding to a cross-correlation signal of $-\delta I^2(1-\tau_c)^2$. Note that the fluctuation δI depends on the charge of the tunneling quasiparticles, here between two markedly different channels. With the procedure described below, we find (i) that interchannel tunnelings can occur when some power is locally injected into the inner channel at the corresponding upstream source QPC (set at $0 < \tau_{t,b} < 1$, but note that no tunneling is here observed at $\tau_{t,b} = 0$); and (ii) that the noise in the interchannel tunneling current is consistent with the predicted tunneling charge of $e/3$ (determined by the local filling factor of $1/3$ of the incompressible stripe separating the two channels; see Ref. [48]); but (iii) that this contribution here remains relatively small with respect to the cross-correlation signal of present interest, generated at the analyzer QPC$_c$.

Figure 11 illustrates the experimental procedure to address interchannel tunneling, in the device configuration where it is found to be the strongest, at $T \simeq 25$ mK. The central QPC$_c$ is first detuned from the inner channel analyzer operating point ($\tau_c > 0$) and set to the $e^2/3h$ plateau ($\tau_c = 0$). In order to minimize any cross-talk artifacts, we change only the voltage applied to the QPC$_c$ gate located the furthest away from the separately considered path [the gate along $I_{L(R)}$ for the path originating from QPC$_{b(t)}$; see Fig. 1(c)]. The differential tunneling transmission ratio $\tau_{\rm tun}^{t(b)}$ of the inner channel current into the outer channel along the top (bottom) source-analyzer path simply reads, at $\tau_c = 0$ and for a sequential channel opening of the QPCs,

$$\tau_{\rm tun}^{t(b)} = \frac{\partial I_{L(R)}/\partial V_{t(b)}}{\partial (I_L + I_R)/\partial V_{t(b)}}. \tag{D1}$$

As shown in Fig. 11(b), the tunneling ratio along the top path can here approach 20% of the injected inner channel current (the maximum value observed in all the device configurations investigated), markedly higher than along the bottom path. The simultaneously measured cross-correlations $\langle \delta I_L \delta I_R \rangle$ are displayed in Fig. 11(c) as a function of the applied voltage V_t (blue symbols) or V_b (orange symbols) in the main panel and as a function of the dc interchannel tunneling current $I_{\rm tun}^t$ (blue) or $I_{\rm tun}^b$ (orange) in the inset. As seen in the inset, the cross-correlations resulting from interchannel tunneling match the shot noise prediction of Eq. (3) for the expected $e^* = e/3$.

QPC$_c$ is then set back to the inner channel analyzer operating point $\tau_c > 0$ [approximately 0.9 at zero bias here; see the inset in Fig. 11(d)], and the cross-correlation signal is measured in the presence of symmetric beams of quasiparticles generated at the source QPCs now simultaneously biased at the same $V_t = V_b$. The green symbols in the main panel represent the raw signal, which includes the additional negative contribution from interchannel tunnelings. The estimate of this unwanted contribution (black symbols) is obtained by simply applying the reduction factor $(1-\tau_c)^2$ to the interchannel cross-correlations previously measured at $\tau_c = 0$. Note that interchannel tunneling also changes the relation providing τ_c. The impact is generally found to be relatively small (of at most 0.04 at high bias for the present example); however, Eq. (2) should be modified by substituting $(1-\tau_{t(b)})$ with $(1-\tau_{t(b)})(1-\tau_{\rm tun}^{t(b)})$ to account for the reduction of the incident inner channel current. In this work, we extract the effective Fano factor P from both the measured cross-correlation signal ignoring interchannel tunnelings (green symbols) and by removing the estimated interchannel tunneling contribution from the measurements (blue symbols). Confronting the two obtained values of P allows one to straightforwardly appreciate the relatively small influence of interchannel tunnelings [see Fig. 8(b)].

APPENDIX E: SUPPLEMENTAL DATA

1. Bias dependence of QPC transmission at $\nu = 1/3$

In the FQHE regime, the current transmission ratio τ across a QPC is predicted to depend on bias voltage [11,47]. This energy dependence on the analyzer transmission τ_c influences the quantitative prediction for P, as discussed in the main text. However, experimentally, the QPC transmissions are generally found in disagreement with the expected voltage-biased dependence (see, e.g., Ref. [50]). The transmission versus direct voltage bias characterization of the analyzer QPC$_c$ at $\nu = 1/3$ is shown for a broad range of tuning in Fig. 12. In the WBS regime of present main interest, we find that the transmission τ_c is reduced, getting further away from the ballistic limit as the direct voltage bias

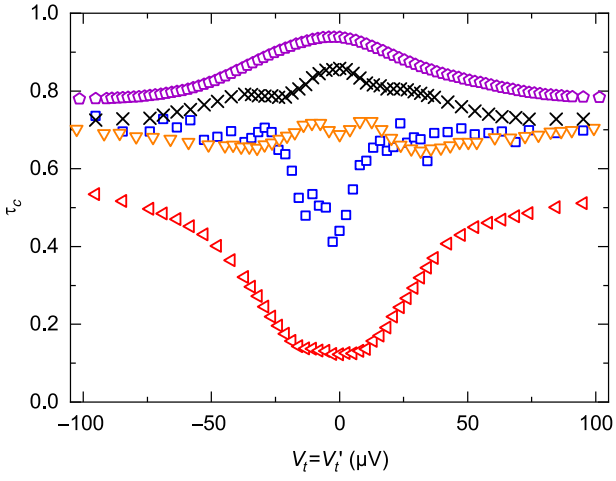

FIG. 12. Analyzer QPC$_c$ transmission τ_c versus direct voltage bias $V_t = V_{t'}$ at $\nu = 1/3$. Different symbols correspond to different tunings of QPC$_c$. An identical device tuning to Fig. 3 is represented here by the same symbol.

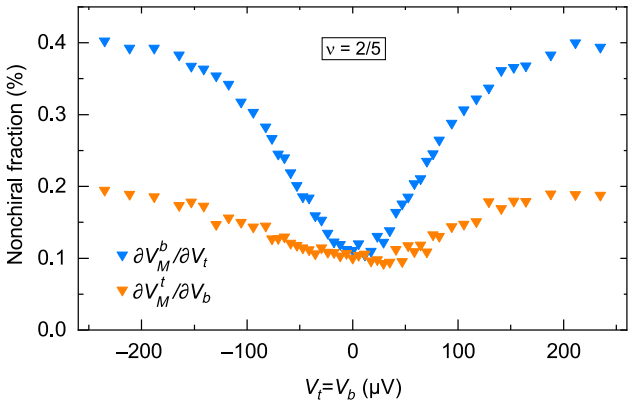

FIG. 13. Nonchiral signal at $\nu = 2/5$. The displayed differential emitted or detected current (voltage) ratios $\partial V_M^{t(b)}/\partial V_{b(t)}$ should be null for a perfectly chiral system.

is increased. Similar observations are made by other teams (see, e.g., Ref. [51]), as well as for both source QPCs and for the outer $e^2/3h$ channel of QPC_c at $\nu = 2/5$. This contrasts with the prediction of a transmission approaching unity as the bias is increased [11,47].

2. Transport chirality

The quantum Hall chirality of the electrical current is systematically obeyed at the level of the large Ohmic contacts. Nevertheless, we find that small but discernible deviations can develop at the heart of the device for the less robust $\nu = 2/5$ fractional quantum Hall state.

The local chirality is controlled by checking that the signals $\partial V_M^t/\partial V_b$ and $\partial V_M^b/\partial V_t$ are null, as $V_M^{t(b)}$ should be disconnected from $V_{b(t)}$ by chirality whatever the device tuning. This is always the case at experimental accuracy at $\nu = 2$ and $\nu = 1/3$, but a small unexpected signal is found at $\nu = 2/5$ as illustrated in Fig. 13. If we consider that the nonchiral signal originates solely from the inner channel current, the relevant nonchiral fraction is enhanced by a factor of 6 [i.e., $(2/5)/(1/15)$], up to 2.5% in the present representative example and at most 3% in the worst case investigated.

3. Auto- versus cross-correlations in QPC_c characterization

It was pointed out that the cross-correlations could provide a more robust probe than the autocorrelations for the shot noise characterization of the tunneling charge across QPCs in the FQHE regime [60]. Here, we compare auto- and cross-correlation signals measured with a direct voltage bias applied to QPC_c, during the separate e_c characterization.

Figure 14 shows measurements of the autocorrelations and cross-correlations, as well as the corresponding noise sum S_Σ, obtained at $\nu = 2$ (a), $1/3$ (b), and $2/5$ (c). The cross-correlations (green circles) correspond to the

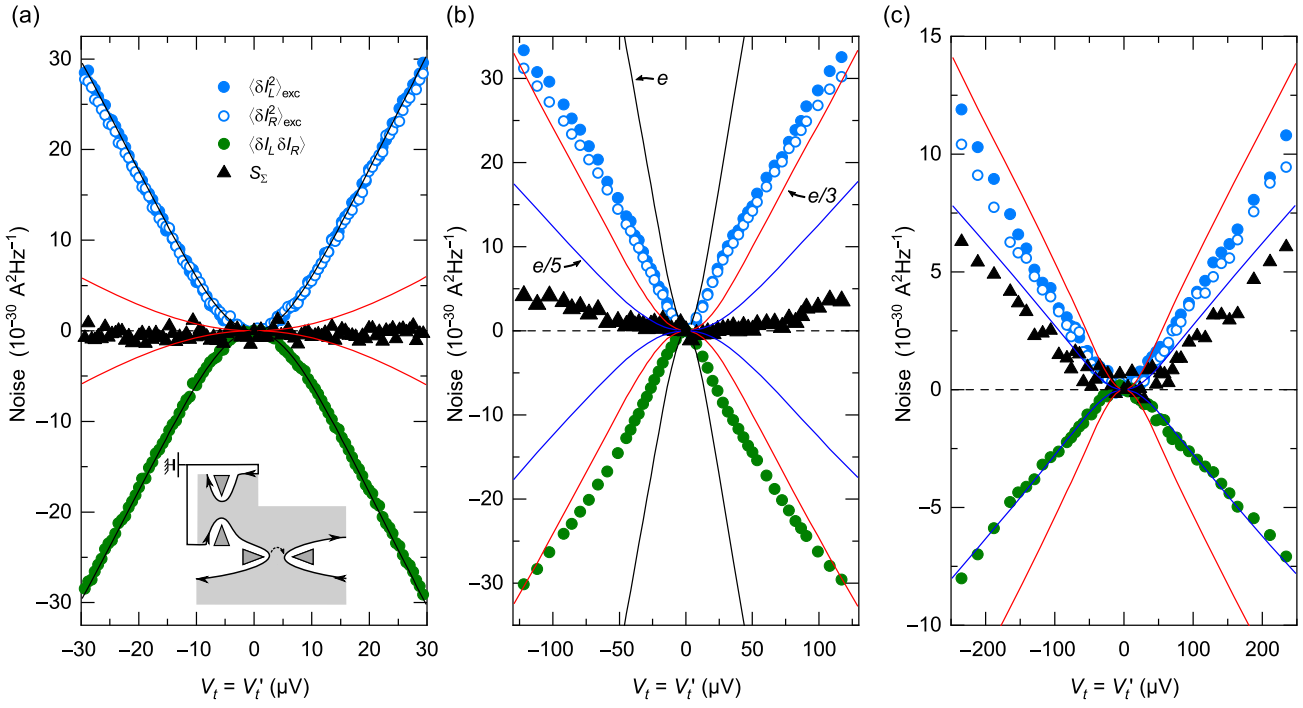

FIG. 14. Auto- and cross-correlation comparison, performed in QPC_c characterization at filling factor 2 (a), 1/3 (b), and 2/5 (c) as a function of the direct applied voltage $V_t = V_t'$ ($V_b = 0$). Full and open blue disks display the autocorrelation signal from port L and R, respectively. Green disks represents the simultaneously measured cross-correlations. S_Σ is plotted as black triangles. Continuous lines display ($\pm 1\times$) the predictions of Eq. (3) for a charge $e^* = e$ (black), $e/3$ (red), and $e/5$ (blue).

previously displayed representative data in Figs. 2(b), 7(b), and 10(b), now completed with coincidental measurements of $\langle \delta I_L^2 \rangle$ (full blue circles) and $\langle \delta I_R^2 \rangle$ (open blue circles), and with S_Σ defined in Eq. (4). Continuous lines represent the shot noise predictions of Eq. (3) (with a -1 factor when negative) at the measured $T \simeq 35$ mK for $e^* = e$ (black), $e/3$ (red), and $e/5$ (blue). At $\nu = 2$, a canonical behavior is observed, with opposite auto- and cross-correlations both corresponding to $e^* = e$ and resulting vanishing noise sum $S_\Sigma \simeq 0$. At $\nu = 1/3$, small but discernible deviations from $S_\Sigma = 0$ develop at high voltage bias, which signal the emergence of small differences between auto- and cross-correlations. These are attributed to a nonlocal heating of the source QPCs resulting in a noise increase such as the delta-T noise [61–63] (see Methods in Ref. [37] for a specific investigation on the same sample). At $\nu = 2/5$, the sum noise S_Σ is far from negligible, which might be related to the nonlocal heating observed at $\nu = 1/3$ although stronger.

One may wonder if the unexpected S_Σ signal observed at $\nu = 2/5$ with a direct voltage biased applied to QPC_c could impact our conclusions. As argued below, we believe it is unlikely. First, the doubts that this discrepancy casts on e_c would not directly impact the extracted value of P [see Eq. (6)]. Second, we point out that the cross-correlations chosen to characterize e_c were previously established to be more reliable than the autocorrelations [60]. This is even more true in the present source-analyzer setup where the incident current noise can be enhanced by a nonlocal heating of the sources. Finally, if such unexpected increase of S_Σ were to occur also in the main source-analyzer configuration, the absolute value of P involving S_Σ in the denominator would be reduced but would not vanish [Eq. (6)]. Moreover, in the source-analyzer configuration, a voltage bias is applied to the sources (as opposed to e_c characterization), which is expected to suppress the effect of a local heating on S_Σ [see Eq. (3)]. Accordingly, the reliability of S_Σ with voltage-biased sources is supported by the similar $e_{t,b}$ extracted when detuning the analyzer QPC_c to $\tau_c = 0$ and biasing the source QPCs one at a time (data not shown). These considerations suggest that the unexpectedly high S_Σ observed when applying a direct voltage bias to QPC_c is likely to have a moderate impact on $e_{t,b}$ and P, without qualitative consequences on the present anyon statistics investigation.

APPENDIX F: $P_{\mathrm{thy}}^{\mathrm{WBS}}$ WITH ALTERNATIVE τ_c

In this section, we provide the analytical expressions for the theoretical predictions of $P_{\mathrm{thy}}^{\mathrm{WBS}}$ as defined by Eq. (6), but using τ_c^{bis} and τ_c^{ter} instead of τ_c. These predictions, valid for all QPCs in the WBS limit and for large source voltages with respect to $k_B T/e^*$, are shown in Table II for $I_- = 0$ and $I_- = I_+$.

First, we consider $\tau_c^{\mathrm{bis}}(I_-, I_+) \equiv \tau_c(I_- = 0, I_+)$. This corresponds to the choice of normalization made in Ref. [33]. The effective Fano factor in the WBS regime $1 - \tau_c^{\mathrm{bis}} \ll 1$ and at large bias voltage then reads

$$P_{\mathrm{thy,bis}}^{\mathrm{WBS}} = \frac{\langle \delta I_L \delta I_R \rangle}{2e^* I_+ (1 - \tau_c^{\mathrm{bis}})} = -\frac{4\Delta}{1-4\Delta}\mathrm{Re}[X^{4\Delta-2}] + \frac{|I_-|}{|I_+|}\left[\tan(2\pi\Delta) + \frac{\tan^{-1}(2\pi\Delta)}{(1-4\Delta)}\right]\mathrm{Im}[X^{4\Delta-2}], \quad \text{(F1)}$$

with $X \equiv 1 + i(I_-/I_+)\tan^{-1}(2\pi\Delta)$. This expression reduces Eq. (8) at $I_- = 0$, since in that limit $\tau_c^{\mathrm{bis}} = \tau_c$. For $\Delta = 1/6$ at $\nu = 1/3$, it gives $P_{\mathrm{thy,bis}}^{\mathrm{WBS}}(0) = -2$ and $P_{\mathrm{thy,bis}}^{\mathrm{WBS}}(I_-/I_+ = 1) \simeq -3.1$ as shown in Table II. Equation (F1) for $\Delta = 1/6$ corresponds to the black dashed line in Fig. 5 of the present article and to the continuous line shown in the bottom right panel in Fig. 3 in Ref. [33].

Second, we consider $\tau_c^{\mathrm{ter}} \equiv \tau_t^{-1} \partial V_L / \partial V_t'$, which is the transmission ratio for thermal excitations with the sources in the WBS limit. This normalization choice is made in Ref. [34] (see the alternative Fano factor called P_{ref}). The corresponding effective Fano factor in the WBS regime $1 - \tau_c^{\mathrm{ter}} \ll 1$ and at large bias voltage reads [34]

$$P_{\mathrm{thy,ter}}^{\mathrm{WBS}} = P_{\mathrm{thy,bis}}^{\mathrm{WBS}}(I_-/I_+)\frac{\sin(4\pi\Delta)}{4\pi\Delta}. \quad \text{(F2)}$$

At $\Delta = 1/6$ ($\nu = 1/3$), the reduction factor is $P_{\mathrm{thy,ter}}^{\mathrm{WBS}}/P_{\mathrm{thy,bis}}^{\mathrm{WBS}} \simeq 0.41$, and Eq. (F2) gives $P_{\mathrm{thy,ter}}^{\mathrm{WBS}}(0) \simeq -0.83$ and $P_{\mathrm{thy,ter}}^{\mathrm{WBS}}(I_-/I_+ = 1) \simeq -1.28$ as shown in Table II. Equation (F2) at $\Delta = 1/6$ corresponds to the blue dashed line in Fig. 5 of the present article and to the black continuous line in Fig. 4 in Ref. [34].

[1] D. E. Feldman and B. I. Halperin, *Fractional Charge and Fractional Statistics in the Quantum Hall Effects*, Rep. Prog. Phys. **84**, 076501 (2021).

[2] K.-V. Pham, M. Gabay, and P. Lederer, *Fractional Excitations in the Luttinger Liquid*, Phys. Rev. B **61**, 16397 (2000).

[3] T. Morel, June-Young M. Lee, H.-S. Sim, and C. Mora, *Fractionalization and Anyonic Statistics in the Integer Quantum Hall Collider*, Phys. Rev. B **105**, 075433 (2022).

[4] June-Young M. Lee, C. Han, and H.-S. Sim, *Fractional Mutual Statistics on Integer Quantum Hall Edges*, Phys. Rev. Lett. **125**, 196802 (2020).

[5] L. Fu and C. L. Kane, *Superconducting Proximity Effect and Majorana Fermions at the Surface of a Topological Insulator*, Phys. Rev. Lett. **100**, 096407 (2008).

[6] P. L. S. Lopes, I. Affleck, and E. Sela, *Anyons in Multichannel Kondo Systems*, Phys. Rev. B **101**, 085141 (2020).

[7] G. Moore and N. Read, *Nonabelions in the Fractional Quantum Hall Effect*, Nucl. Phys. **B360**, 362 (1991).

[8] V. J. Goldman and B. Su, *Resonant Tunneling in the Quantum Hall Regime: Measurement of Fractional Charge*, Science **267**, 1010 (1995).

[9] J. Martin, S. Ilani, B. Verdene, J. Smet, V. Umansky, D. Mahalu, D. Schuh, G. Abstreiter, and A. Yacoby, *Localization of Fractionally Charged Quasi-particles*, Science **305**, 980 (2004).

[10] C. L. Kane and M. P. A. Fisher, *Nonequilibrium Noise and Fractional Charge in the Quantum Hall Effect*, Phys. Rev. Lett. **72**, 724 (1994).

[11] P. Fendley, A. W. W. Ludwig, and H. Saleur, *Exact Nonequilibrium dc Shot Noise in Luttinger Liquids and Fractional Quantum Hall Devices*, Phys. Rev. Lett. **75**, 2196 (1995).

[12] L. Saminadayar, D. C. Glattli, Y. Jin, and B. Etienne, Observation of the$e/3$ Fractionally Charged Laughlin Quasiparticle, Phys. Rev. Lett. **79**, 2526 (1997).

[13] R. de Picciotto, M. Reznikov, M. Heiblum, V. Umansky, G. Bunin, and D. Mahalu, *Direct Observation of a Fractional Charge*, Nature (London) **389**, 162 (1997).

[14] M. Reznikov, R. de Picciotto, T. Griffiths, M. Heiblum, and V. Umansky, *Observation of Quasiparticles with One-Fifth of an Electron's Charge*, Nature (London) **399**, 238 (1999).

[15] M. Dolev, M. Heiblum, V. Umansky, A. Stern, and D. Mahalu, *Observation of a Quarter of an Electron Charge at the* $\nu = 5/2$ *Quantum Hall State*, Nature (London) **452**, 829 (2008).

[16] A. Crépieux, P. Devillard, and T. Martin, *Photoassisted Current and Shot Noise in the Fractional Quantum Hall Effect*, Phys. Rev. B **69**, 205302 (2004).

[17] I. Safi, *Time-Dependent Transport in Arbitrary Extended Driven Tunnel Junctions*, arXiv:1401.5950.

[18] M. Kapfer, P. Roulleau, M. Santin, I. Farrer, D. A. Ritchie, and D. C. Glattli, *A Josephson Relation for Fractionally Charged Anyons*, Science **363**, 846 (2019).

[19] C. de C. Chamon, D. E. Freed, and X. G. Wen, *Tunneling and Quantum Noise in One-Dimensional Luttinger Liquids*, Phys. Rev. B **51**, 2363 (1995).

[20] B. Roussel, P. Degiovanni, and I. Safi, *Perturbative Fluctuation Dissipation Relation for Nonequilibrium Finite-Frequency Noise in Quantum Circuits*, Phys. Rev. B **93**, 045102 (2016).

[21] R. Bisognin, H. Bartolomei, M. Kumar, I. Safi, J.-M. Berroir, E. Bocquillon, B. Plaçais, A. Cavanna, U. Gennser, Y. Jin, and G. Fève, *Microwave Photons Emitted by Fractionally Charged Quasiparticles*, Nat. Commun. **10**, 1708 (2019).

[22] F. Wilczek, *Quantum Mechanics of Fractional-Spin Particles*, Phys. Rev. Lett. **49**, 957 (1982).

[23] J. M. Leinaas and J. Myrheim, *On the Theory of Identical Particles*, Nuovo Cimento Soc. Ital. Fis. B **37**, 1 (1977).

[24] R. B. Laughlin, *Anomalous Quantum Hall Effect: An Incompressible Quantum Fluid with Fractionally Charged Excitations*, Phys. Rev. Lett. **50**, 1395 (1983).

[25] B. I. Halperin, *Statistics of Quasiparticles and the Hierarchy of Fractional Quantized Hall States*, Phys. Rev. Lett. **52**, 1583 (1984).

[26] D. Arovas, J. R. Schrieffer, and F. Wilczek, *Fractional Statistics and the Quantum Hall Effect*, Phys. Rev. Lett. **53**, 722 (1984).

[27] S.-S. Lee, S. Ryu, C. Nayak, and M. P. A. Fisher, *Particle-Hole Symmetry and the* $\nu = \frac{5}{2}$ *Quantum Hall State*, Phys. Rev. Lett. **99**, 236807 (2007).

[28] M. Levin, B. I. Halperin, and B. Rosenow, *Particle-Hole Symmetry and the Pfaffian State*, Phys. Rev. Lett. **99**, 236806 (2007).

[29] M. Banerjee, M. Heiblum, V. Umansky, D. Feldman, Y. Oreg, and A. Stern, *Observation of Half-Integer Thermal Hall Conductance*, Nature (London) **559**, 205 (2018).

[30] B. Dutta, W. Yang, R. Melcer, H. K. Kundu, M. Heiblum, V. Umansky, Y. Oreg, A. Stern, and D. Mross, *Distinguishing between Non-Abelian Topological Orders in a Quantum Hall System*, Science **375**, 193 (2022).

[31] J. Nakamura, S. Liang, G. C. Gardner, and M. J. Manfra, *Direct Observation of Anyonic Braiding Statistics*, Nat. Phys. **16**, 931 (2020).

[32] H. Bartolomei, M. Kumar, R. Bisognin, A. Marguerite, J.-M. Berroir, E. Bocquillon, B. Plaçais, A. Cavanna, Q. Dong, U. Gennser, Y. Jin, and G. Fève, *Fractional Statistics in Anyon Collisions*, Science **368**, 173 (2020).

[33] B. Rosenow, I. P. Levkivskyi, and B. I. Halperin, *Current Correlations from a Mesoscopic Anyon Collider*, Phys. Rev. Lett. **116**, 156802 (2016).

[34] J.-Y. M. Lee and H.-S. Sim, *Non-Abelian Anyon Collider*, Nat. Commun. **13**, 6660 (2022).

[35] E. G. Idrisov, I. P. Levkivskyi, E. V. Sukhorukov, and T. L. Schmidt, *Current Cross Correlations in a Quantum Hall Collider at Filling Factor Two*, Phys. Rev. B **106**, 085405 (2022).

[36] C. L. Kane and M. P. A. Fisher, *Shot Noise and the Transmission of Dilute Laughlin Quasiparticles*, Phys. Rev. B **67**, 045307 (2003).

[37] P. Glidic, O. Maillet, C. Piquard, A. Aassime, A. Cavanna, Y. Jin, U. Gennser, A. Anthore, and F. Pierre, *Quasiparticle Andreev Scattering in the* $\nu = 1/3$ *Fractional Quantum Hall Regime*, arXiv:2206.08068.

[38] T. Jonckheere, J. Rech, B. Grémaud, and T. Martin, *Anyonic Statistics Revealed by the Hong-Ou-Mandel Dip for Fractional Excitations*, arXiv:2207.07172.

[39] C. Han, J. Park, Y. Gefen, and H.-S. Sim, *Topological Vacuum Bubbles by Anyon Braiding*, Nat. Commun. **7**, 11131 (2016).

[40] Y. Blanter and M. Büttiker, *Shot Noise in Mesoscopic Conductors*, Phys. Rep. **336**, 1 (2000).

[41] D. E. Feldman and M. Heiblum, *Why a Noninteracting Model Works for Shot Noise in Fractional Charge Experiments*, Phys. Rev. B **95**, 115308 (2017).

[42] K. Snizhko and V. Cheianov, *Scaling Dimension of Quantum Hall Quasiparticles from Tunneling-Current Noise Measurements*, Phys. Rev. B **91**, 195151 (2015).

[43] N. Schiller, Y. Oreg, and K. Snizhko, *Extracting the Scaling Dimension of Quantum Hall Quasiparticles from Current Correlations*, Phys. Rev. B **105**, 165150 (2022).

[44] B. Lee, C. Han, and H.-S. Sim, *Negative Excess Shot Noise by Anyon Braiding*, Phys. Rev. Lett. **123**, 016803 (2019).

[45] I. Safi, *Fluctuation-Dissipation Relations for Strongly Correlated Out-of-Equilibrium Circuits*, Phys. Rev. B **102**, 041113(R) (2020).

[46] T. G. Griffiths, E. Comforti, M. Heiblum, A. Stern, and V. Umansky, *Evolution of Quasiparticle Charge in the*

Fractional Quantum Hall Regime, Phys. Rev. Lett. **85**, 3918 (2000).

[47] C. L. Kane and M. P. A. Fisher, *Transport in a One-Channel Luttinger Liquid*, Phys. Rev. Lett. **68**, 1220 (1992).

[48] X. G. Wen, *Theory of the Edge States in the Fractional Quantum Hall Effects*, Int. J. Mod. Phys. B **06**, 1711 (1992).

[49] J.-Y. M. Lee, C. Hong, T. Alkalay, N. Schiller, V. Umansky, M. Heiblum, Y. Oreg, and H. S. Sim, *Partitioning of Diluted Anyons Reveals Their Braiding Statistics*, arXiv: 2209.15461.

[50] A. M. Chang, *Chiral Luttinger Liquids at the Fractional Quantum Hall Edge*, Rev. Mod. Phys. **75**, 1449 (2003).

[51] M. Heiblum and D. E. Feldman, *Edge Probes of Topological Order*, Int. J. Mod. Phys. A **35**, 2030009 (2020).

[52] I. Safi and H. Saleur, *One-Channel Conductor in an Ohmic Environment: Mapping to a Tomonaga-Luttinger Liquid and Full Counting Statistics*, Phys. Rev. Lett. **93**, 126602 (2004).

[53] S. Jezouin, M. Albert, F. Parmentier, A. Anthore, U. Gennser, A. Cavanna, I. Safi, and F. Pierre, *Tomonaga-Luttinger Physics in Electronic Quantum Circuits*, Nat. Commun. **4**, 1802 (2013).

[54] A. Anthore, Z. Iftikhar, E. Boulat, F. D. Parmentier, A. Cavanna, A. Ouerghi, U. Gennser, and F. Pierre, *Circuit Quantum Simulation of a Tomonaga-Luttinger Liquid with an Impurity*, Phys. Rev. X **8**, 031075 (2018).

[55] M. Ruelle, E. Frigerio, J.-M. Berroir, B. Plaçais, J. Rech, A. Cavanna, U. Gennser, Y. Jin, and G. Fève, following paper, *Comparing Fractional Quantum Hall Laughlin and Jain Topological Orders with the Anyon Collider*, Phys. Rev. X **13**, 011031 (2023).

[56] Z. Iftikhar, A. Anthore, S. Jezouin, F. Parmentier, Y. Jin, A. Cavanna, A. Ouerghi, U. Gennser, and F. Pierre, *Primary Thermometry Triad at 6 mk in Mesoscopic Circuits*, Nat. Commun. **7**, 12908 (2016).

[57] S. Jezouin, F. D. Parmentier, A. Anthore, U. Gennser, A. Cavanna, Y. Jin, and F. Pierre, *Quantum Limit of Heat Flow across a Single Electronic Channel*, Science **342**, 601 (2013).

[58] H. le Sueur, C. Altimiras, U. Gennser, A. Cavanna, D. Mailly, and F. Pierre, *Energy Relaxation in the Integer Quantum Hall Regime*, Phys. Rev. Lett. **105**, 056803 (2010).

[59] P. Roulleau, F. Portier, D. C. Glattli, P. Roche, A. Cavanna, G. Faini, U. Gennser, and D. Mailly, *Direct Measurement of the Coherence Length of Edge States in the Integer Quantum Hall Regime*, Phys. Rev. Lett. **100**, 126802 (2008).

[60] M. Kapfer, *Dynamic of Excitations of the Fractional Quantum Hall Effect: Fractional Charge and Fractional Josephson Frequency*, Ph.D. thesis, Université Paris-Saclay, SPEC, CEA-Saclay, 91191 Gif-sur-Yvette, France, 2018.

[61] O. Lumbroso, L. Simine, A. Nitzan, D. Segal, and O. Tal, *Electronic Noise due to Temperature Differences in Atomic-Scale Junctions*, Nature (London) **562**, 240 (2018).

[62] E. Sivre, H. Duprez, A. Anthore, A. Aassime, F. Parmentier, A. Cavanna, A. Ouerghi, U. Gennser, and F. Pierre, *Electronic Heat Flow and Thermal Shot Noise in Quantum Circuits*, Nat. Commun. **10**, 5638 (2019).

[63] S. Larocque, E. Pinsolle, C. Lupien, and B. Reulet, *Shot Noise of a Temperature-Biased Tunnel Junction*, Phys. Rev. Lett. **125**, 106801 (2020).